SiGe/Si Microwave Photonic devices and Interconnects towards Silicon-based full Optical Links

Zerihun Tegegne

To cite this version:

Zerihun Tegegne. SiGe/Si Microwave Photonic devices and Interconnects towards Silicon-based full Optical Links. Electronics. Université Paris-Est, 2016. English. NNT : 2016PESC1070 . tel-01550015

HAL Id: tel-01550015
https://theses.hal.science/tel-01550015

Submitted on 29 Jun 2017

UNIVERSITÉ PARIS-EST
École Doctorale MSTIC
Mathématiques, Sciences et Technologies de l'Information et de la Communication

Ph.D. THESIS
In order to obtain the title of Doctor of Science
Specialty: Electronics, optoelectronics and systems

Defended on May 11, 2016

Zerihun Gedeb TEGEGNE

SiGe/Si Microwave Photonic Phototransistors and Interconnects toward Silicon-based full Optical Links

Final Version June 01, 2016

Thesis Director: Prof Elodie RICHALOT
Thesis Advisor: Dr. Jean-Luc POLLEUX
Dr. Marjorie GRZESKOWIAK

JURY:

Reviewers:	Laurent VIVIEN, Pr.	UPSUD, IEF (France)
	Stavros IEZEKIEL, Pr.	University of Cyprus (Cyprus)
Advisor:	Elodie RICHALOT, Pr.	ESYCOM-UPEM (France)
	Jean-Luc POLLEUX, Dr.	ESYCOM-ESIEE (France)
	Marjorie GRZESKOWIAK, Dr.	ESYCOM-UPEM (France)
Examiners:	Catherine AlGANI, Pr.	ESYCOM-Le Cnam (France)
	Mehmet KAYNAK, Dr.	IHP GmbH (Germany)
	Pascal CHEVALIER, Dr.	STMicroelectronics (France)

Abstract

With the recent explosive growth of connected objects, for example in Home Area Networks, the wireless and optical communication technologies see more opportunity to merge with low cost MicroWave Photonic (MWP) technologies. Millimeter frequency band from 57GHz to 67GHz is used to accommodate the very high speed wireless data communication requirements. However, the coverage distance of these wireless systems is limited to few meters (10m). The propagation is then limiting to a single room mostly, due to both the high propagation attenuation of signals in this frequency range and to the wall absorption and reflections. Therefore, an infrastructure is needed to lead the signal to the distributed antennas configuration through MWP technology. Moreover, MWP technology has recently extended to address a considerable number of novel applications including 5G mobile communication, biomedical analysis, Datacom, optical signal processing and for interconnection in vehicles and airplanes. Many of these application areas also demand high speed, bandwidth and dynamic range at the same time they require devices that are small, light and low power consuming. Furthermore, implementation cost is a key consideration for the deployment of such MWP systems in home environment and various integrated MWP application.

This PhD deals with very cheap, Bipolar or BiCMOS integrated SiGe/Si MWP devices such as SiGe HPTs, Si LEDs and SiGe LEDs, and focused on the combined integration of mm wave and optoelectronic devices for various applications involving short wavelength links (750nm to 950nm).

This research focused on the study of the following points:

- The better understanding of vertical and lateral illuminated SiGe phototransistors designed in a 80 GHz Telefunken GmbH SiGe HBT technology. We draw conclusions on the optimal performances of the phototransistor. The light sensitive Si substrate and two-dimensional carrier flow effects on SiGe phototransistor performance are investigated. This study helps to derive design rules to improve frequency behavior of the HPT for the targeted applications.
- For future intra /inter chip hybrid interconnections, we design polymer based low loss microwave transmission lines and optical waveguides on low resistive silicon substrate. It is a step to envisage further Silicon based platforms where SiGe HPT could be integrated at ultra-low cost and high performances with other structures such high-speed VCSEL to build up a complete optical transceiver on a Silicon optical interposer. The polymer is used as dielectric interface between the line and the substrate for electrical interconnections and to design the core and cladding of the optical waveguide.
- The design, fabrication and characterization of the first on-chip microwave photonic links at mid infrared wavelength (0.65-0.85µm) based on 80 GHz Telefunken GmbH SiGe HBT technological processes. The full optical link combines Silicon Avalanche based Light Emitting Devices (Si Av LEDs), silicon nitride based waveguides and SiGe HPT. Such device could permit hosting microfluidic systems, on chip data communication and bio-chemical analysis applications.

Résumé

Avec la croissance forte de ces dernières années des objets connectés les technologies de communication optique et radio voient davantage d'opportunités de s'associer et se combiner dans des technologies bas-couts Photoniques-Microondes (MWP). Les réseaux domestiques en sont un exemple. La bande millimétrique notamment, de 57GHz à 67GHz, est utilisé pour contenir les exigences des communications sans fils très haut-débit, néanmoins, la couverture de ces systèmes wireless est limitée en intérieur (indoor) essentiellement à une seule pièce, à la fois du fait de l'atténuation forte de l'atmosphère dans cette bande de fréquence, mais aussi de fait de l'absorption et de la réflexion des murs. Ainsi il nécessaire de déployer une infrastructure pour diffuser l'information au travers d'un système d'antennes distribuées. Les technologiques optiques et photoniques-microondes sont une des solutions envisagées. Les technologies MWP se sont également étendues et couvrent une gamme très large d'applications incluant les communications mobiles 5G, les analyses biomédicales, les communications courtes-distances (datacom), le traitement de signal par voie optique et les interconnexions dans les véhicules et aéronefs. Beaucoup de ces applications requièrent de la rapidité, de la bande-passante et une grande dynamique à la fois, en même temps de demander des dispositifs compacts, légers et à faible consommation. Le cout d'implémentation est de plus un critère essentiel à leur déploiement, en particulier dans l'environnement domestique ainsi que dans d'autres applications variées des technologies MWP.

Ce travail de thèse vise ainsi le développement de composants photonique-microondes (MPW) intégrés en technologie BiCMOS ou Bipolaire SiGe/Si, à très bas coût, incluant les phototransistors bipolaires à hétérojonctions (HPT) SiGe/Si, les Diodes Electro-Luminescentes (LED) Si et SiGe, ainsi que l'intégration combinées des composants optoélectroniques et microondes, pour l'ensemble des applications impliquant des courtes longueurs d'ondes (de 750nm à 950nm typiquement).

Ces travaux se concentrent ainsi sur les points suivants :

- La meilleure compréhension de phototransistors SiGe/Si latéraux et verticaux conçus dans une technologie HBT SiGe 80GHz de Telefunken GmbH. Nous traçons des conclusions sur les performances optimales du phototransistor. Les effets de photodétection du substrat et de la dispersion spatiale des flux de porteurs sont analysés expérimentalement. Cette étude aide à développer des règles de dessin pour améliorer les performances fréquentielles du phototransistor HPT pour les applications visées.

- Dans l'objectif de développer de futures interconnexions intra- et inter- puces, nous concevons des lignes de transmissions faibles-pertes et des guides d'ondes optiques polymères sur Silicium faible résistivité. Il s'agit d'une étape afin d'envisager des plateformes Silicium dans lesquelles les HPT SiGe pourront potentiellement être intégrés de manière performante à très bas coût avec d'autres structures telles que des lasers à émission par la surface (VCSEL), afin de construire un transpondeur optique complet sur une interface Silicium. Le polymère est utilisé comme une interface diélectrique entre les lignes de transmission et le substrat, pour les interconnexions électriques, et pour définir le gain du guide d'onde optique dans les interconnexions optiques.

La conception, la fabrication et la caractérisation du premier lien photonique-microonde sur puce Silicium sont menées en se basant sur la même technologie HBT SiGe 80GHz de Telefunken dans la gamme de longueur d'onde 0,65µm-0,85µm. Ce lien optique complétement intégré combine des LEDS Silicium en régime d'avalanche (Si Av LED), des guides d'ondes optiques Nitrure et Silice ainsi qu'un phototransistor SiGe. Un tel dispositif pourrait permettre d'accueillir à l'avenir des communications sur-puce, de systèmes micro-fluidiques et des applications d'analyse biochimiques.

Acknowledgments

I would like to express my special appreciation and thanks to my thesis director Prof. Elodie Richalot and thesis advisors Dr. Jean Luc Polleux and Dr. M. Grzeskowiak, you have been a tremendous mentor for me. I would like to thank you for encouraging my research and for allowing me to grow as a research scientist. Your advice on both research as well as on my career have been priceless.

I would also like to thank the committee members of this thesis reviewer's Prof. Laurent Vivien and Prof. Stavros Iezekiel. My special thank also extended to the committee members of examiners Prof. Catherine Algani, Dr. Mehmet Kaynak and Dr. Pascal Chevalier. I thank you all for your participation.

A special thanks to my friends Dr. C. Viana, Dr. M. Rosales and Dr. J. Schiellein for the valuable supports and numerous stimulating discussions.

I also thank Prof. Laurent Vivien from CNRS and University of Paris-Sud for the technical helps for the dicing processes of edge illuminated HPTs at the nano-center CTU-IEF-Minerve.

At the end I would like express appreciation to my beloved family. Words cannot express how grateful I am to you for all of the sacrifices that you've made on my behalf. Your prayer for me was what sustained me thus far.

Table of contents

List of Figures

List of Tables

Acronym

BCB	Bisbenzocyclobutene
BiCMOS	Bipolar Complementary Metal Oxide Semiconductor
BS	Base Station
CEB	Common Emitter Base
CMOS	Complementary Metal Oxide Semiconductor
CO	Centeral Office
CPW	Coplanar Waveguide
DC	Direct Current
DFB	Distributed Feedback and distributed Bragg Reflected
DSB	Double Sideband
DUT	Device under Test
EEL	Edge Emitting Laser
EDA	Electronic Design Automation
eO	etched Oxide
FP	Fabry Perot
GaAs	Gallium arsenide
Ge	Germanium
GCPW	Grounded Coplanar Wavegide
GSG	Ground Signal Ground
HAN	Home Area Network
HBT	Heterojunction Bipolar Transistor
HFSS	High Frequency Structure Simulator
HPT	Heterojunction Phototransistor
IC	Integrated Circuit
IF	Intermediate Frequency
InGaAs	Indium Gallium Arsenide
InGaAsP	Indium Gallium Arsenide Phosphide
LAN	Local Area Network
LED	Light Emitting Diode
MIC	Microwave Integrated Circuit
MMF	Multimode Fiber
MMIC	Monolithic Microwave Integrated Circuit
MOEMS	Micro Optical Electro-Mechanical Sensor
MSM	Metal Semiconductor Metal
MQW	Multiple Quantum Well
MWP	Microwave Photonics
MZM	Match Zehnder Modulator
NDA	Non-Disclosure Agreement
O/E	Electrical-to-Optical
OEIC	Optoelectronic Integrated Circuits
OFDM	Orthogonal Frequency Division Multiplex
OM	Opto-Microwave
ORIGIN	Optical Radio Infrastructure for Gbit/s Indoor Network
PD	photodiode / photodetector

PGL	Planar Goubau Line
QAM	Quadrature Amplitude Modulation
QW	Quantum Well
RCE	Resonant-Cavity-Enhanced
RF	Radio Frequency
RoF	Radio over Fiber
Si	Silicon
SIC	Selectively Implanted Collector
SiGe	Silicon Garmanium
SiN	Silicon Nitride
SNOM	Scanning Near-field Optical Microscopy
SQ	Square
TE	Transverse Electric
TEM	Transverse Electromagnetic
TEOS	Tetraethyl orthosilicate
TFM	Thin Film Microstrip line
TIA	Transimpedance Amplifier
TiSi	Silicided Polysilicon (Titanium discilicite)
TWPD	Traveling Wave Photodiode
VCSEL	Vertical Cavity Surface Emitting Laser
VNA	Vector Network Analyser
VMPD	Velocity Matched Distributed Photodetector
UTC	Uni Traveling Carrier
UWB	Ultra-Wide Band
WPAN	Wireless Personal Area Network
xBC	Extended Base-Collector
xEBC	Extended Emitter-Base-Collector

General Introduction

Wireless technologies have been developed to replace wirelines installed in the Home Area Network (HAN) in the context of the recent explosive growth of new services and wireless devices. The new proposed services demand higher data rates reaching Giga bits per second. Home services using high definition video signal transmission is one example that requires such high data rate.

The conventional and popular Wi-Fi, based on the standard IEEE 802.11 [9], uses centimeter wave frequency band range and allows data rates up to 480Mbit/s. New solutions reaching higher data rates are essential for future. For this purpose, new wireless network standards arise such as the IEEE802.11.ad which is the extension of the Wi-Fi toward the millimeter wave ranges (mm wave), from 57GHz to 67GHz. Here four channels with a large bandwidth of 2GHz are used getting data rates up to 7Gbit/s. However, the coverage distance of these wireless systems is limited to few meters (10m) with the propagation limited to a single room mostly due to both the high propagation attenuation of signals at 60GHz and to the wall absorption and reflections. Therefore, an infrastructure is needed to cover the whole home area so as to distribute the signal from one room to another through Microwave photonic technology.

Microwave Photonics (MWP) is an interdisciplinary area that merges photonics and wireless technologies for signal transmission. The advantage of MWP systems is that they can benefit from the strengths of both optical and wireless technologies, such as the inherently large bandwidth of optical fiber and unused bandwidth in the mm-wave wireless spectrum. For this reason, a hybrid system has the potential to provide very high data transmission rates with minimal time delay. Cost is however an extreme constraint in this system to permit the deployment of this network in each home; this pushes pressure on the extremity devices such as the lasers and the photodetectors. Vertical Cavity Surface Emitting Laser (VCSEL) is the solution on the emitting side, while the Silicon integration is a key target for the detecting side. SiGe Microwave Photonics devices are developed for being integrated into such 60GHz WiFi Radio-over-Fiber architecture as in the ORIGIN project [10]. The vision of ORIGIN was to down-convert mm wave signal to intermediate frequency bands (5GHz) before transmitting through the fiber channel, and then to up convert the signal at the end. The use of an intermediate frequency is required to keep in the limit of the cutoff frequency of low cost optoelectronic devices. These up and down conversions of signals however introduce high noise and make the system more complex. Development of 60GHz direct-RoF system (millimeter wave over fiber) would avoid such down- and up- conversions. Millimeter-Waves over Fiber systems are thus of tremendous interest for such architecture. While this domain may still be limited to III-V or GeoSi technologies, it is an interest in investigating the rise in frequency of SiGe based ultra-low-cost phototransistors.

Edge illuminated SiGe Heterojunction Photo-Transistors (HPTs) along with Si based external optical modulator might be potential candidate to address this issue. Understanding the physics and physical structure of SiGe/Si Microwave Photonics devices and improving its performance would be a clear breakthrough, which could enable the combined integration of mm wave circuits and optoelectronic devices on silicon at low cost.

Moreover, on chip optical and mm wave integration on Si CMOS or BiCMOS technology are key issues for short range optical communication applications [11] such as intra/inter-chip interconnections, biomedical analysis or Datacom, in addition to RoF systems. The most important constituents of such a system is an effective BiCMOS compatible optical source, Bi/CMOS compatible optical waveguide, effective optical coupling to the waveguide, Bi/CMOS compatible electrical waveguide (transmission lines) and Bi/CMOS compatible optical detector, which all seem to be highly viable in regard to the present analyses and proposed technological process.

In this context, the important objectives of this thesis concern the understanding of physical behavior of SiGe/Si Microwave photonic devices including SiGe HPTs, Si LEDs and SiGe LEDs, and the proposal of mechanisms to improve their performances. We also work on the combination of optical and electrical waveguides and transmission lines to interconnect mm wave circuits and optoelectronic devices. Finally on-chip microwave photonics links have been fabricated and characterized using a SiGe Bipolar technology.

The contributions of this PhD thesis concern three axes:

- The better understanding of vertical and lateral illuminated SiGe phototransistors designed in a 80 GHz Telefunken GmbH SiGe HBT technology. We draw conclusions on the optimal performances of the phototransistor. The light sensitive Si substrate and two-dimensional carrier flow effects on SiGe phototransistor performance are investigated. This study helps to derive design rules to improve frequency behavior of the HPT for the targeted applications.

- For future intra /inter chip hybrid interconnections, we design polymer based low loss microwave transmission lines and optical waveguides on low resistive silicon substrate. It is a step to envisage further Silicon based platforms where SiGe HPT could be integrated at ultra-low cost and high performances with other structures such high-speed VCSEL to build up a complete optical transceiver on a Silicon optical interposer. The polymer is used as dielectric interface between the line and the substrate for electrical interconnections and to design the core and cladding of the optical waveguide.

- The design, fabrication and characterization of the first on-chip microwave photonic links at mid infrared wavelength (0.65-0.85µm) based on 80 GHz Telefunken GmbH SiGe HBT technological processes. The full optical link combines Silicon Avalanche based Light Emitting Devices (Si Av LEDs), silicon nitride based waveguides and SiGe HPT. Such device could permit hosting microfluidic systems, on chip data communication and bio-chemical analysis applications.

This PhD document is divided in 5 chapters:

Chapter 1: State of The Art

This chapter presents an overview on the radio networks and their limitations. It mainly focuses on the Wi-Fi technology and the arrival of the last standard for 60GHz systems. It introduces the Micro-Wave Photonic (MWP) systems and technologies, which can complement the 60GHz wireless communication to overcome its short range propagation distances.

Inter-chip and intra-chip interconnections for MWP applications are also detailed in this chapter. Different types of transmission lines used for electrical interconnections as well as Silicon-based on-chip optical interconnect techniques are presented.

We also briefly present the state-of-the-art of several types of opto-microwave transceivers. Light emission devices of III-V materials and Silicon LEDs are presented along with their performances. The trade-off between photodetector responsivity and bandwidth is discussed. Photodetector material choices for a specific application at a specific wavelength are described. Different photodetector structures are analyzed and their performances are compared. We also investigate the previous works on heterojunction bipolar phototransistors (HPTs) and Silicon-based optical modulators that could be used in the implementation of RoF systems.

Chapter 2: SiGe/Si HPT technology, Opto-microwave characterization and de-embedding techniques

This chapter is focused on preparing the further experimental analysis of opto-microwav devices, including SiGe HPTs, SiGe and Si LEDs. We first describe the 80GHz SiGe bipolar technology from Telefunken GmbH that we aim to use for all our SiGe-based optical structures. The fabrication of SiGe HPT made within this technology is explained, with a special focus on being directly integrated in the commercial process, without any adaptation of the required process flow. Opto-microwave parameters of the phototransistor (such as opto-microwave gain, cutoff frequency, optical transition frequency and optical gain) are defined and explained. The measurement bench setups for optical and opto-microwave characterizations of top and edge illuminated HPTs are then detailed. Opto-microwave measurement calibration and de-embedding techniques are also detailed to remove parasitic from the device under test. A method to compute all photocurrents in each region of the phototransistor is proposed, based on its physics, and explained. The de-embedding technique to isolate the substrate photodiode effect (response) from the intrinsic phototransistor response is then demonstrated. At the end, the methods of extracting the electrical intrinsic capacitance and transit time and their optical induced contribution within the phototransistor are proposed and detailed.

Chapter 3: Experimental Study of SiGe HPT with Top Illumination

This chapter is focused on the experimental study of vertically illuminated (top illuminated) SiGe HPTs developed using the 80 GHz Telefunken GmbH SiGe HBT technology.

We start this study with the static behavior of the phototransistor under dark and illuminated conditions. The optimum dc bias points that maximize the low frequency gain and the dynamic behavior (in terms of cutoff frequency and optical transition frequency) of the HPT are then pointed out. Different types of base terminal interconnection that improves the low frequency gain of the HPT are then studied.

The size dependency of the electrical dynamic behavior of SiGe HPTs, which shows an unusual behavior as compared to HBTs, is investigated. We thus propose a “2D extension electrical effect” that analyzes the two-dimensional and distributed nature of currents within SiGe HPT.

The variation of the DC current and of the opto-microwave frequency response versus the optical spot illumination position over the surface of the structure is studied through an Opto-Microwave Scanning-Near-field-Optical-Microscropy (OM-SNOM) technique under optimum dc bias conditions [1]. This study led to the localization of the substrate photodiode within the structure as well as the analysis of its impact under opto-microwave working condition [4] [8]. Once the behavior of the substrate photodiode is understood, the intrinsic behavior of the HPT is then extracted by removing the influence of the later.

The impact of the injected optical power level on the dc and opto-microwave performance of the SiGe HPT is studied at three different injected optical power levels. The optical transition frequency dependency on the photogenerated current is then demonstrated. The transit times and junction capacitances of the HPT under opto-microwave condition are also extracted with the aim of inserting them in an equivalent electrical circuit model in future phototransistor studies.

The impact of the optical window size on opto-microwave gain and cutoff frequency is analyzed. The optical window size dependency of the substrate photodiode and 2D carrier distribution effects are also investigated. Finally a conclusion is made regarding the design rules of SiGe/Si HPT structures.

Chapter 4: Microwave and Photonic interconnections on Silicon

In this chapter we investigate a novel method of fabricating different transmission lines and optical waveguides on low resistivity silicon substrates using polymers (SU8 negative resist, BCB and Parlyene) as a dielectric interface layer and as optical propagation medium. This topic is dealt with in order to think the integration as in an overall multi-chip circuit in a Si-interposer like structure capable of handling both millimeter wave interconnects and optical interconnects in a polymer lithographic process.

We use HFSS software to model the transmission lines in order to determine the modes of propagation and the propagation characteristics of various types of lines (Coplanar, Micro-strip and Grounded coplanar). We also investigate the inclusion techniques of RF lines and optical waveguides on a single structure. This technique could also be explored for SiGe HPTs structures to obtain high speed Traveling Wave HPT considering the active region (base-emitter-collector) as optical waveguide.

Based on the simulation results and line dimensions determined through HFSS, we developed the schematic patterns/layouts of the lines and optical waveguides using CADENCE software. The validity of the design is then demonstrated through the measurement of the fabricated lines.

We have also designed and studied optical waveguides by taking advantage of different oxide layers in the SiGe HBT technology. This enables us to develop on-chip full optical links by using a technology as presented in chapter 5.

Chapter 5: Edge illuminated SiGe HPT and on Chip microwave photonic links

This chapter has two main parts:

The first part focuses on edge illuminated SiGe HPT. We develop the first edge illuminated SiGe phototransistor based on the available commercial SiGe/Si HBT technology [2] [5]. The structure of the HPT under study is first described, and then experimentally characterized. The DC biasing values are optimized to maximize its cut-off frequency and its low frequency responsivity. Then, we perform an edge mapping / SNOM of the phototransistor by sweeping the optical fiber illumination spot in order to observe the fastest and the more sensitive areas of the structure. We characterize this HPT by using a multimode fiber (MMF) without the need of complex coupling techniques to fit with the MMF context of Home-Area-Networks. However the performance of the HPT could be greatly improved by using a single mode source at 850nm or by focusing the light with a tapered coupling structure. This work is an ongoing perspective of this PhD thesis.

The second part of this chapter focuses on on-chip full optical link, obtained in co-operation between the ESYCOM laboratory in France and both the Pr.Snymann team in the University of South-Africa (UNISA) and Tshwane University of Technology (TUT) in South Africa. Such full optical links on Silicon are directly integrated in the Telefunken GmbH SiGe HBT technological process without process modifications. The general view of Si or SiGe LEDs design approach is first analyzed from the literature and then the strategies to develop Si and SiGe LEDs from the existing bipolar technology are presented. We design a full optical link in the operating wavelength range of about 650-850nm. The involved optical link combines Silicon Avalanche based Light Emitting Devices (Si Av LEDs), Silicon-Nitride based waveguides and SiGe HPT technology. Finally we validate the full optical link design through experiment in terms of DC and RF behavior [6] [7].

Chapter 1 State of the art

1.1 Introduction

This chapter aims at giving the applicative context of the work and at providing the state-of-the-art in the microwave-photonics devices, technologies and interconnects.

Following the introduction of this chapter, the second section presents a brief overview on the radio networks, especially in the microwave range, and their limitations. It mainly focuses on the Wi-Fi technology and the arrival of the last standard based on the 60 GHz.

The third section introduces the Micro-Wave Photonic (MWP) systems and technologies, which can complement the 60 GHz wireless communication to overcome their short range propagation distances.

Inter-chip and intra-chip interconnects for MWP applications are detailed in the fourth section. Different types of transmission lines used for electrical interconnections and silicon based on chip optical interconnection techniques are discussed.

The fifth section briefly presents the state-of-the-art of different types of optical sources. In this section light emission device from III-V materials and Silicon LEDs along with their performance is presented.

The sixth section covers the performance of different photodetectors. Different types of high-speed PDs for microwave photonics application such as p-i-n photodiodes (p-i-n PD), uni-traveling- carrier photodiodes (UTC PD), metal-semiconductor-metal photodetectors (MSM PD), resonant-cavity-enhanced photodetectors (RCE PD), waveguide photodiodes (WGPD), traveling-wave photodetectors (TWPD) and velocity-matched distributed photodetectors (VMDP) will be discussed. The trade of between photodetector responsivity and bandwidth are covered in details with the state-of-the-art of those PDs.

The seventh section of this chapter will focus on heterojunction bipolar phototransistors that can be used in the implementation of MWP systems and applications. In the final section we revise few works on silicon base optical modulators.

1.2 Microwave Radio-Networks

In the past, the benefits of unmetered connectivity and high mobility have driven the demand for wireless services. However, with the proliferation of a variety of new data communication services, the demand for broadband wireless networks is increasing rapidly. With the current generation of mobile communications, the available spectral bandwidth is limited which prohibits the provision of broadband services for a large customer number. To overcome this problem, the use of smaller radio coverage areas in microcellular and picocellular wireless networks has attracted attention as a means to increase capacity by enabling more efficient use of the limited available bandwidth. Wireless communication systems operating at higher RF frequencies (>6GHz) provide larger bandwidths; however, these are still limited to only few hundred MHz in bandwidth with Orthogonal Frequency Division Multiplex (OFDM) modulation schemes [12].

As a result of the problem of spectral congestion limiting the provision of broadband services to users in mobile and fixed wireless networks operating at lower microwave frequencies, radio networks operating at higher frequencies are gaining more attention. 60 GHz wireless standards have been developed with the dedicated ISM band for high data rate Wireless Personal Area Networks (WPANs) like the ECMA-387 [13] in 2008, the 802.15.3c [14][15] and the IEEE802.11ad in 2013 [9] based on the 60 GHz unlicensed spectrum. The internationally available unlicensed spectrum surrounding the 60 GHz carrier frequency got particular interest due to the propagation characteristics and the 9 GHz available bandwidth. The standard IEEE 802.11ad presents a maximum throughput of up to 7 Gbit/s. This new generation of 60 GHz Wi-Fi systems are intended to be massively introduced in the coming years, keeping the compatibility with the current 2.4 and 5 GHz Wi-Fi solutions. Such radio networks offer the ability to provide truly broadband services to users by utilizing the enormous bandwidth available in these frequency bands. Due to the large atmospheric absorption that occurs at mm-wave frequencies (around 60GHz) [16] as shown in Figure 1-1, such radio networks operate with significantly smaller wireless coverage areas. This also enables efficient radio frequency re-use schemes, and high security communication.

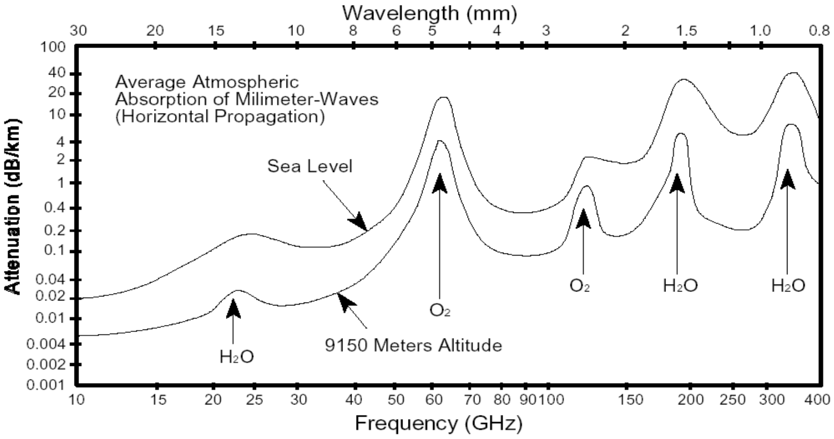

Figure 1-1: Millimeter wave atmospheric absorption spectrum [16]

1.3 Microwave photonic Systems and RoF Technologies

Signals can be transmitted in different form as analog electrical signal or in most of the cases they are digitalized beforehand. The digital signals can be transmitted directly via metal line or cables, over radio wave (high frequency carrier must be available), or via optic fibers (digital signals are transmitted through one or several optical carriers). The advantages of optical fiber as transmission medium are its low loss, large bandwidth characteristics, small size and low cable cost – it makes it the ideal solution for efficiently transporting the combined millimeter wave signals. One however has to integrate the O/E and E/O transverse that are required.

The distinctive feature of MWP links is to transmit analog or digital modulated microwave signals over the fiber. This microwave signal modulates an optical carrier, which is then guided with minimum loss over the optical fiber. The microwave signal is then detected by a photodetector.

The main applications of MWP are the distribution of microwave carrier in radar or radio astronomy systems [17], in home area wireless network or ultra-wideband (UWB) interconnections [18]. In the latter case the optical tunnels produced are capable of reaching all rooms of the house or buildings of the company, university, or diverse institutions. In home area wireless network like new Wi-Fi standard (IEEE802.11.ad), the signal distribution in each room is achieved by a 60GHz millimeter wave, which stays confined in a room due to atmospheric absorption. The optical fiber is a mean to interconnect each room through MWP access point per room. It extends the millimeter wave signal throughout the whole home area.

A MWP link has three parts:

1. Light source: a laser that emits an optical carrier, whose intensity is directly modulated inside the laser or externally by an optical modulator. The external modulator could be either Mach-Zehnder or electro-absorption modulator.
2. Optical fiber: the modulated light is then transported by single or multi-mode optical fiber. It may also include optical amplifiers.
3. Photodetector: the modulated and transmitted optical signal is then detected by a photodiode or phototransistor at the receiver.

Figure 1-2 shows the case of a MWP system with an externally modulated laser.

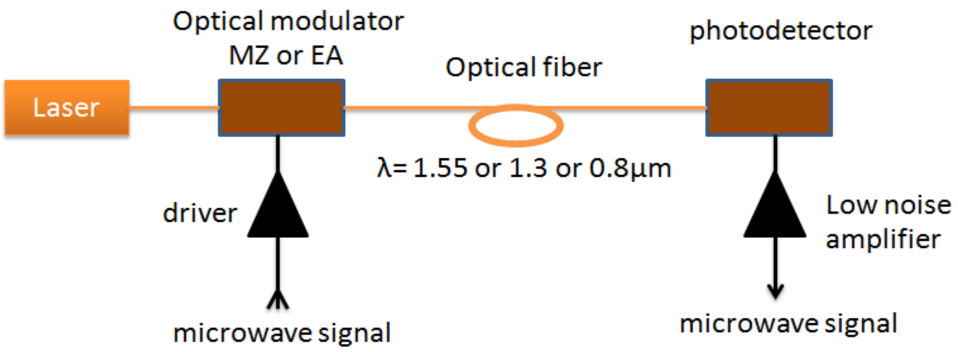

Figure 1-2: Example of externally modulated MWP link. The direct modulation link can be done by removing the external optical modulator and directly connecting the driver to the laser.

The light emitted from the laser is injected to a Mach-Zehnder or electro-absorption amplitude modulator. The microwave modulation is also applied to the modulator through a driver circuit. After passing through the optical fiber, the optical modulated signal is detected via a photodetector and then amplified by a low noise amplifier.

There are also limitations associated to each device in the link and its constituting materials. For example materials used for optical fibers, such as silica or plastic substances, are characterized by losses presented in Figure 1-3 and chromatic dispersion. The losses present two minima at 1.3 and 1.5µm, and the chromatic dispersion is zero at 1.3µm.

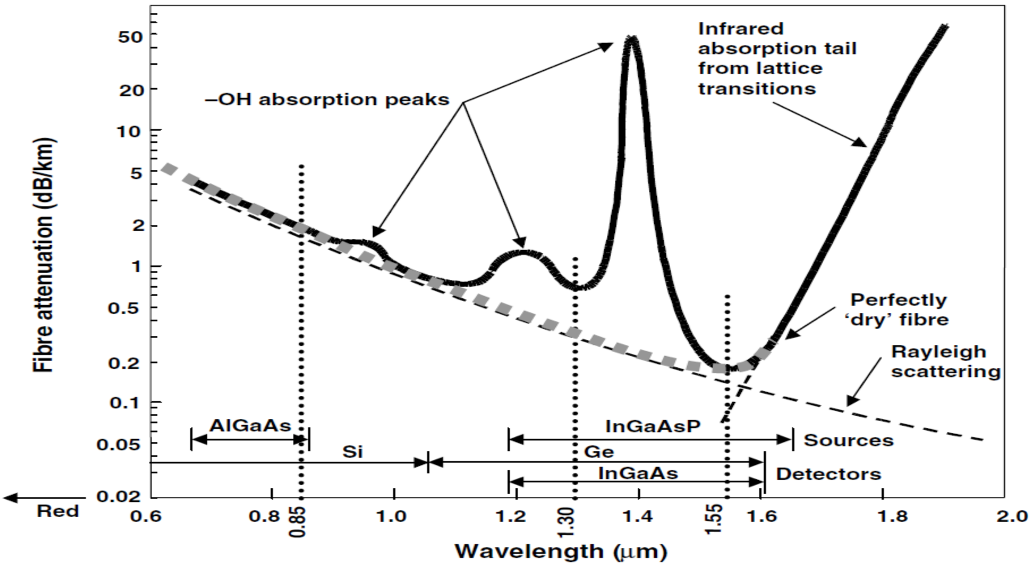

Figure 1-3: Attenuation in a single mode silica optical fiber and functional zones of the principal materials constituting the components of the link [17]

The devices used to generate, modulate, or detect optical waves are made up from semiconductors, comprise one or more heterojunction, multiple quantum wells, or stacking of different layers. For the generation of optical wave, it would be better to use InP and GaAs substrates where GaInAsP and GaInAs respectively must be grown on the top by epitaxial [20]-[22]. Silicon based optical sources are also interesting for low cost applications like on chip and inter chip systems. Photodetection at 850nm is more feasible using Si [23][24][25] and GaAs [26]-[28] as substrate. Ge and InGaAs may be grown by epitaxial in thin layer on these substrates respectively to achieve better performance at 1.55µm.

For very long links, 1.55µm wavelengths are preferred, as chromatic dispersion is low and losses are the lowest. However, for short or very short links the attenuation of the optical signal per kilometer is no longer a problem, so that it is possible to use optical wavelengths from 0.8µm to1.3µm. There are three basic approaches of MWP technologies.

1.3.1 IF over Fiber Technology

Figure 1-4 shows a schematic diagram of the basic hardware required at the transmitter and receiver for downstream signal transmission in a fiber radio system based on the distribution of the radio signal at a lower intermediate frequency (IF), the so-called 'IF-over-fiber' signal transport scheme. Here IF refers to microwave frequencies in the L and C band (such as 1– 8GHz). IF over fiber scheme requires frequency up-conversion at the receiver and down-conversion at the transmitter. The IF-over-fiber signal transport approach offers the advantage that readily available mature microwave hardware can be utilized; it requires low bandwidth opto-electric device and the chromatic dispersion at IF frequency is low. This scheme has the disadvantage that it requires frequency conversion to moves into the mm-wave frequency regime at both the receiver and transmitter which complicates the architecture. The complexity of the hardware increases since a high-frequency local oscillator (LO) and mixers for the frequency conversion processes are required (as shown in Figure 1.4). This may also be a limitation when considering the ability to upgrade or reconfigure the radio network with the provision of additional radio channels or the implementation of required changes in RF frequency. Moreover, this up and down conversions adds noise to the system.

Several commercial fiber-radio products employing IF-over-fiber are often based on the distribution of radio signals over multimode fiber (MMF) since many buildings have a legacy of optical fiber infrastructure networks based on multimode fiber (MMF). For example, the transmission of a 2 Mb/s 32-QAM signal at 2 GHz over 1 km of MMF at 1300 nm was demonstrated in [29] with very little penalty. Recent research investigations have also considered the use of new vertical cavity surface emitting lasers (VCSELs) operating at 850 nm, which are currently being developed for a range of applications including MultiGigabit [10]. VCSELs are low-cost devices and their application in analog optical links has been the subject of the thesis of Carlos VIANA [10]. He demonstrated a successful transmission at 5GHz over 2 meters of a 2.8GB/s HD QPSK modulated signal.

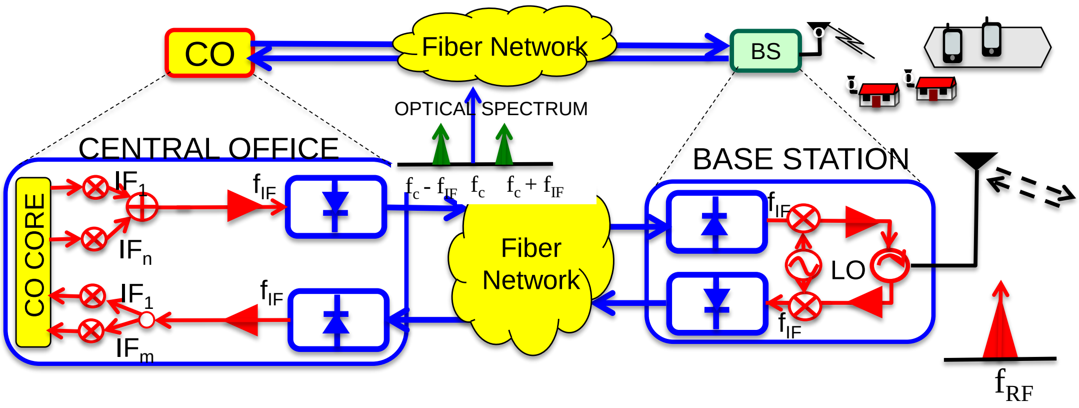

Figure 1-4: Simplified diagram of IF over fiber link.

1.3.2 RF over Fiber technology

The most straightforward approach to interconnect remote antennas in a fiber radio system is via an optical fiber feed network which can transport the wireless signals directly over the fiber at the radio carrier transmission frequency without the need of any subsequent frequency up- or down-conversion. Such a configuration is attractive in microcellular and picocellular networks operating in the mm-wave frequency region where a large number of antennas is required to provide wide geographical coverage. These applications include fixed wireless access at 38 GHz and indoor wireless LANs at 60 GHz [30].

Figure 1-5 shows the simplified block diagram of Radio over fiber link. The wireless signal at radio frequency up to millimeter wave frequencies, f_{RF}, is externally modulated onto the optical carrier, f_c usually resulting in a double sideband (DSB) signal. Sidebands are thus separated from the optical carrier by f_{RF}. Upon detection at the base station (BS) the wireless signal is recovered from the beating of the sidebands and the optical carrier via a photodetector and then amplified, filtered and directed to an antenna for free-space transmission to a customer unit.

Since no frequency translation is required this means that the BS design is very simple and thus this configuration benefits from the centralized control. It also enables multi-wireless band operation since each band is recovered after beating with the optical carrier.

The implementation of fiber radio systems based on RF-over-fiber signal transport for wireless systems operating at higher wireless transmission frequencies presents more challenges, particularly at mm-wave frequencies. One of the main issues for implementing such fiber radio architectures with RF over fiber lies in the search for both suitable high speed optical modulation techniques that have the ability to generate mm-wave modulated optical signals and also high-speed photodetection techniques that directly convert the modulated optical signals back into mm-wave signals in the electrical domain.

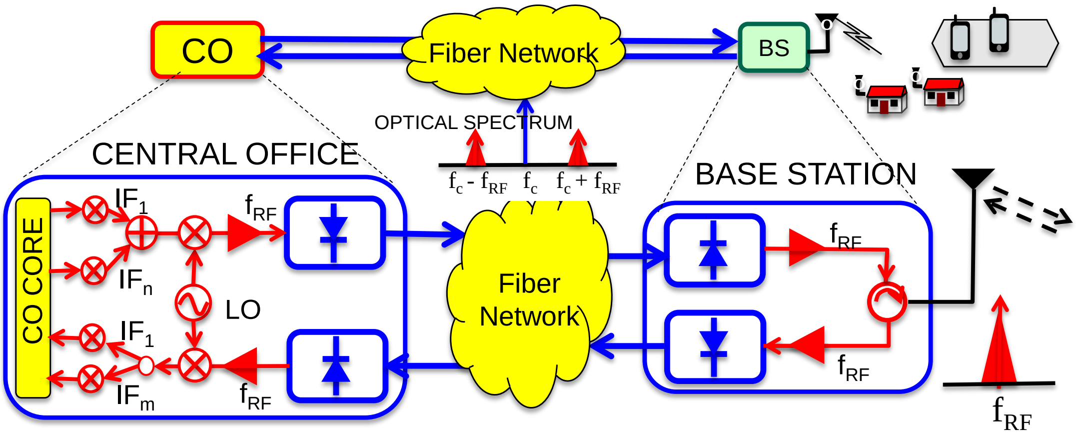

Figure 1-5: Simplified diagram of Radio over fiber.

1.3.3 Baseband over Fiber technology

The wireless signal is transported as baseband over the optical fiber link. Upon reaching the BS it is detected and converted to RF before being radiated as shown in Figure 1-6: In the baseband-over-fiber approach the radio information for the radio carriers is transported to the receiver as a time-division multiplexed data stream. The individual data channels are then demultiplexed, up-converted to intermediate frequencies and then undergo a further frequency up-conversion to the required radio frequency band via a local oscillator located at the receiver.

As with IF-over-fiber signal distribution, the effect of fiber dispersion is small, and this technology permits to use matured and reliable RF and digital hardware for signal processing. Furthermore low-cost optoelectronic devices with low bandwidth can be employed [30]. However, the need for frequency conversion at both transmitter and receiver complicates the system architecture design. The additional LO source and extensive signal processing hardware (frequency conversion, multiplexing and demultiplexing of signals) in the antenna station may also limit the upgradability of the overall fiber radio system based on baseband-over-fiber signal transport.

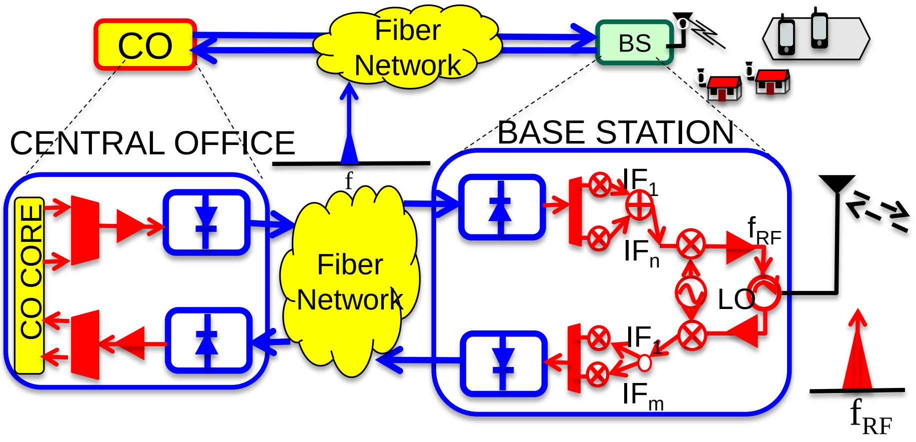

Figure 1-6: Simplified diagram of base band over fiber link.

In general, to implement RoF techniques we need high speed photodetector, optical light source, optical modulator in case of external modulated systems, as well as optical and microwave interconnections. In this chapter we are going to study the state of the art of these very important components of the RoF technology. In the first section we summarize the state of the art of optical and electrical interconnections and then optical source, photodetector and optical modulator respectively mainly based on Si technology.

1.4 Silicon-based Interconnections

The Monolithic integration of several optoelectronic and electronic devices on a single semiconductor chip has been demonstrated. III-V semiconductor materials such as GaAs, InP, and related compounds (InGaAs, InGaAsP, InAs, etec) have been frequently used to achieve this goal [31]-[35]. They are the most widely used materials in the fabrication of electronic and optoelectronic devices present in today’s microwave and fiber-optic communication systems. In addition to the well-established processes that are available for GaAs and InP electronic device and circuit fabrication, more sophisticated GaAs and InP-based multilayer heterostructures also allow the fabrication of low-loss optical waveguides that can be used to interconnect optoelectronic devices and components and hence fabricate “fully” optoelectronic or photonic integrated circuits [36], [37]. However, major drawbacks to such monolithic integration are the difficulties in optimizing the epitaxial layers for both the passive and active functions as well as limitations in the fabrication of low-loss curved waveguides, which can result in large Optoelectronic integrated circuits (OEIC’s) that make inefficient use of expensive semiconductor materials.

Integration of millimeter wave circuits with digital and analog circuits using silicon technology as well as interconnecting/ integrating optical components are then of great interest in order to have compact and cheap transceiver in RoF systems and other applications [17][18].

Since their introduction in the 1950s [38], microwave integrated circuits (MICs) have played an important role in the development of radiofrequency (RF) microwave technologies. The most noticeable and important milestone was the possibly of the emergence of monolithic microwave integrated circuits (MMICs). This progress of MICs would not have been possible without the advances in solid-state devices and planar transmission lines. Planar transmission lines refer to transmission lines that consist of conducting strips printed on surfaces of the transmission lines’ substrates. These structures are the backbone of MICs, and represent an important and interesting research topic for many microwave engineers. Along with the advances in MICs and planar transmission lines, numerous analysis methods for microwave and millimeter-wave passive structures, in general, and planar transmission lines, in particular, have been developed in response to the need for accurate analysis and design of MICs. These analysis methods have in turn helped further investigation and development of new planar transmission lines.

Si radio frequency integrated circuits are progressing rapidly into millimeter wave applications on CMOS and Bi-CMOS technologies, due in large part to significant improvements in SiGe HBTs [39]. However, RF transmission lines on Si substrate suffer from high loss unless novel transmission lines or high resistive silicon wafer are used.

We recall the internationally available unlicensed spectrum surrounding the 60 GHz carrier frequency [9] is focused in this work due to the propagation characteristics and the 9 GHz available bandwidth.

In the following section we presented the electrical interconnections at 60GHz applicable for on chip RoF systems. Different types of transmission lines such as Microstrip line, Coplanar line (CPW), Grounded Coplanar line (GCPW) and Planar Goubau line (PGL) are introduced. We are also interested to develop an integrated opto-microwave circuit on a single chip. Thus, an optical interconnection based on silicon is elaborated in the following section.

1.4.1 Electrical interconnections at 60 GHz on Si

1.4.1.1 Microstrip line

The microstrip line is the most used among all planar transmissions lines in conventional frequency bands (<20 GHz). Designed in the 1950s by Grieg and Engelmann [40], it consists of a substrate on which a metal strip is deposited on the rear face and a ground plane is deposited on the lower face of the substrate as shown in Figure 1-7. The characteristic equations of this line have been extensively studied and described particularly in the reference book "Microstrip Lines and Slot lines" of Gupta [41]. On this line, the mode of propagation is of type quasi-TEM (Figure 1-7) and the characteristic impedance for a given permittivity, is determined mainly by the w / h ratio, where w is the line width and h is the height of the dielectric substrate.

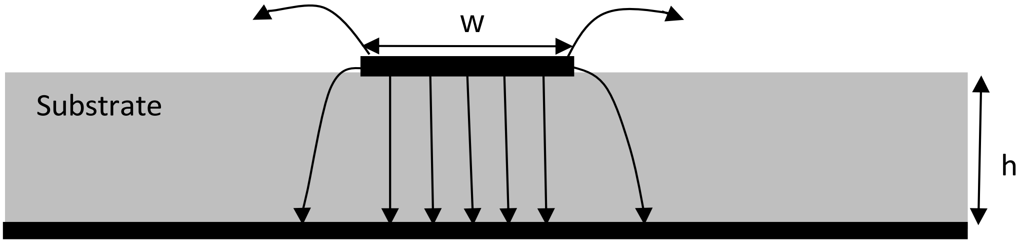

Figure 1-7: Cross section of micro strip line with associated electric field lines

Microstrip line technology offers both simplicity and ease of implementation and integration in microwave devices. They are used at frequencies ranging from a few MHz to a few tens of gigahertz. At higher frequencies, in the millimeter band, the losses in the dielectric and in the metal as well as radiation losses become important. Higher order modes also appear and cause problems. At high frequency, the manufacturing tolerances become also very difficult to meet because of the small size and the technology used. However, this type of line makes it easy to insert series elements, even though it is necessary to penetrate the substrate for the inclusion of discrete components in parallel. Of course it is not easy to do so. "Via hole" in the circuits are technologically difficult to realize at high frequency due to their small dimensions.

Several types of novel microstrip transmission lines exist to minimize losses on silicon substrate at high frequency, such as inverted micro-strip line as presented in [42] [43], Thin Film Microstrip line (TFMs) [44] [45] and Microshield line or Shielded membrane microstrip [46]. TFMs lines are created by depositing a metallic ground plane, and thin insulating layers on silicon wafer, before printing the microstrip line (Figure 1-7).

In [44], TFMs lines are characterized for strip widths of 23µm and 52µm, polyimide thickness of 11.05µm on low resistive (2Ω.cm) silicon wafer. These TFMS transmission lines have characteristic impedances of 53Ω and 31Ω respectively and a minimum attenuation of 0.3dB/mm at 20 GHz. Another TFMs work is presented in [45] on low resistive silicon wafer for a metal strip widths of 3µm and 9.2µm which leads to the characteristic impedances of 68Ω and 44Ω, and attenuations of 1.2 dB/mm and 1 dB/mm respectively.

Table 1-1: Summary of the state of the art of Microstrip lines for different technologies on silicon

Material	**Thickness (µm)**	**α(dB/mm)**	**ρ of Si (Ω.cm)**	**F(GHz)**	**reference**	**comment**
Polyimide	20	0.14	10	60	[47]	suspended
polyimide	7.4	0.4	No effect	60	[48]	
air	10	1.4	5	8	[49]	inverted
air	100	0.02	4000 (HR Si)	8	[49]	inverted

1.4.1.2 . Coplanar line (CPW)

The coplanar line (Figure 1-8) consists of a central metal strip and a pair of ground planes separated by two identical slots located on the same face of the substrate. W represents the width of the signal line, while s is the distance between the signal line and the ground conductors. This architecture has been used extensively in MMICs due to its easy fabrication and flexibility of design [50].

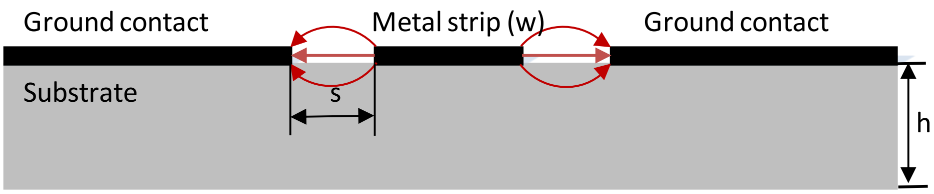

Figure 1-8: Cross section of the coplanar line with E-field lines associated to the odd mode

This structure shows two possible modes of propagation:

- An even mode, quasi-TE and dispersive.
- An odd mode, quasi-TEM and dispersive (Figure 1-8).

The odd mode is used in most of the devices. To prevent the even mode propagation, the ground planes of the coplanar line are connected by a metallic structure so that they are at the same potential, which has the effect of cancelling the even mode. The connecting devices used between ground planes are ribbons (air bridge). The coplanar line radiates weakly at high frequencies due to the uneven structure of the electric field. As indicated in Figure 1-8, there are a little field lines penetrating into the dielectric thereby line losses are reduced and it makes coplanar lines interesting at high frequencies. Another characteristic of the coplanar lines is that they are less sensitive to the thickness of the dielectric substrate than microstrip lines. Besides, the topology of this line permits an easily integration of discrete components either in series or parallel.

Coplanar transmission lines have been extensively studied in many research groups both at low and high frequencies by using different types of technologies [50]. A few works have also been done for CPW on low resistive silicon substrate [39] [51]-[53]. In CMOS and BiCMOS technologies, the quality factor of the transmission lines implemented on low resistive silicon substrate is much lower than on a semi-insulating GaAs, InP and high resistive silicon substrates. Improving the performance of such a CPW line through elevating them away from the lossy substrate, using additional layers of low loss dielectric materials, has been recently investigated [39] [51]-[53] as shown in Figure 1-9. To minimize the loss in these technologies a photolithographic process is performed by using polymers on low resistive silicon to obtain CPW line elevated with respect to the substrate.

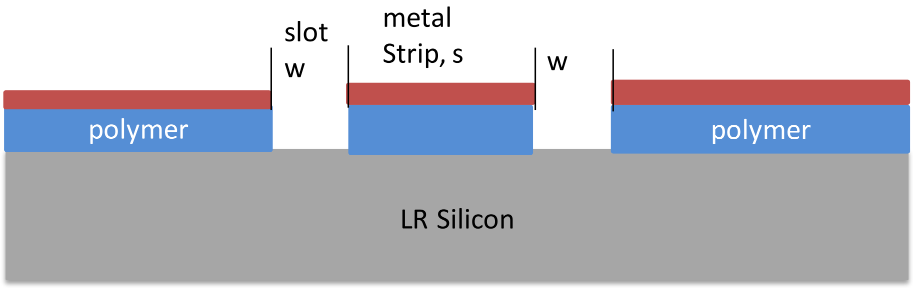

Figure 1-9: Coplanar line on low resistive silicon with a polymer layer used to elevate the conductor lines away from the substrate.

A summary of the performances of coplanar line fabricated on low resistive silicon substrate with different types of polymer interface is presented in Table 1-2. A coplanar line fabricated on 75Ω.cm resistivity silicon and elevated away from the substrate by 26µm SU8 reaches a minimum loss of 0.1mm/dB at 10GHz [53]. In [39], a coplanar line on 2Ω.cm silicon substrate with 25µm or 125µm SU8 polymer interface is presented. The minimum attenuation achieved at 60GHz frequency is 4mm/dB and 0.7mm/dB respectively. On 10Ω.cm silicon substrate with 10µm BCB dielectric interface an attenuation of 0.6dB/mm is measured at 50GHz [51].

Table 1-2: Summary of the state of the art of coplanar lines on low resistive silicon substrate with a polymer layer used to elevate the metal away from the substrate.

Polymer type	Thickness (µm)	α(dB/mm)	f(GHz)	ρ of Si (Ω.cm)	reference	comment
SU8	25	4	60	2	[39]	
	125	0.7	60	2	[39]	
	26	0.1	10	75	[53]	
BCB	10	0.6	50	10	[51]	
Parylene	15	0.56	40	10	[52]	5µm oxide on Si & then parylene
oxide	5	1.85	40	10	[52]	

1.4.1.3 Planar Goubau line (PGL)

Research efforts are continuously devoted to transmission line studies, and new types of transmission line are proposed and investigated. The original Goubau line (a single circular conductor surrounded by a uniform dielectric coating in free space) was analyzed in the 1950s [54] [55]. The dielectrics surrounding the conductor help to confine the field around the wire. Standard circular Goubau line and planar Goubau line have been studied for mm-waves (below 100GHz) and sub-millimeter waves (above 100GHz) applications [56]-[57]. They are mainly used in the field of THz (100 GHz to 10 THz) [59].[60]. Planar Goubau line [61] consists of a metallic ribbon on a dielectric, the propagation medium of the field contains several materials (substrate and air see Figure 1-10). The parameters influencing the line properties are the dielectric thickness, the substrate resistivity or tangent loss and the permittivity [62].

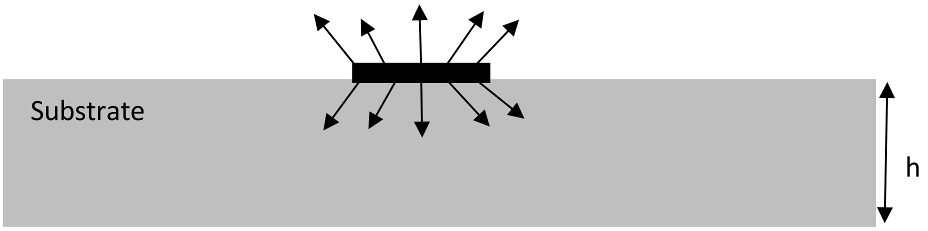

Figure 1-10: Cross section of the Planar Goubau line with E-field lines shown.

Planar Goubau lines are simple to fabricate, low cost and have wide bandwidth. PGL on an alumina ceramic substrate (relative dielectric constant 9.9 and 0.254mm thick) is used in [63] at frequencies between 40GHz and 60GHz. Low loss (0.064dB/mm @ 60GHz) Goubau line on high resistive silicone in the 57-64 GHz band was investigated in [64].

1.4.2 Optical interconnections

Optical interconnection is the technology of interconnecting various optical devices and components for the generation, focusing, splitting, combining, isolating, polarization, coupling, switching, modulation and detection of light, all on a single chip, or chip to chip, or between boards. Optical waveguides can be used to provide the connections between these components. An optical waveguide is a light conduit consisting of a slab, strip or cylinder of dielectric material surrounded by another dielectric material of lower refractive index. The light is transported through the inner medium without radiating into the surrounding medium. The most widely used of these waveguides is the optical fiber, which is made of two concentric circular cylinders of low loss dielectric materials such as glass.

In the last two to three decades, the optical interconnections have been widely employed in high-speed transmission because of their characteristics of high information capacity, no noise emissivity, transmission security, low loss, and low weight [65]-[68]. Optical interconnections are replacing the electrical interconnections not only for long distance communication but optical interconnections are also being developed for chip to chip[69]-[71], or on chip [72]-[74] communications as well.

Progress in computer technology is becoming increasingly dependent on faster data transfer between and within microchips [75]. Optical interconnections may provide a way forward, and silicon photonics has been proven to be particularly useful, once integrated on the standard silicon chips [76]-[78]. Thus, silicon based optical waveguides are hot research issues for low cost and high data transfer interconnections. The high index contrast in Si core and SiO_2 coating makes Si/SiO_2 waveguide one of the most popular components. An attempt to lower propagation loss, on a SiO_2 core waveguide was discussed in [72] at wavelength spectra of 650-1300nm.

From the viewpoint of the signal transmission rate, silicon is however not the best waveguide material. Its high refractive index (n=3.4–3.5) reduces the light speed. A polymer waveguide has a lower refractive index (n= 1.3) and produces a shorter delay than Si waveguides [74]. The use of polymer waveguides for on-chip optical interconnection also allows a multistep fabrication process whereby it is possible to first optimize the processing of the semiconductor devices and then fabricate the polymer waveguide structures for the optical signal distribution system [79]. Polymers offer high thermal, chemical and environmental stability, low optical losses, good dielectric properties, low cost, ease of processing and compatibility with semiconductor processing technology, and represent an interesting alternative to semiconductor materials as light distribution systems [80].

In 2012, IBM announced that it had achieved optical components, based on silicon photonics technology, at the 90 nanometer scale that can be manufactured using standard techniques and incorporated into conventional chips [81] [82]. It has already demonstrated optical transceivers exceeding 25 Gbit/s per channel [82]. In September 2013, Intel announced a completely integrated module that includes silicon modulators, detectors, waveguides, hybrid silicon laser and circuitry that transmits data at speeds of 100 Gigabits per second [83].

1.5 Optical Sources

We can categorize laser diodes according to device structure in three main types being Fabry Perot (FP), distributed feedback and distributed Bragg reflected laser (DFB) and vertical cavity surface emitting lasers (VCSELs). The first two are Edge Emitting lasers (EEL), whereas VCSELs are surface emitting lasers. Differences between VCSELs and the Edge Emitting lasers (EEL) are shown in figure 1.9. The main difference is the optical aperture which is on the top for a VCSEL and on the side for an EEL. As an EEL has a longer active layer it generates higher optical power. Nevertheless, the reduced active layer of the VCSELs induces a lower threshold current and higher operation speed. The small lasing cavity of the VCSEL, shown in Figure 1-11 a), requires mirrors with very high reflectivity.

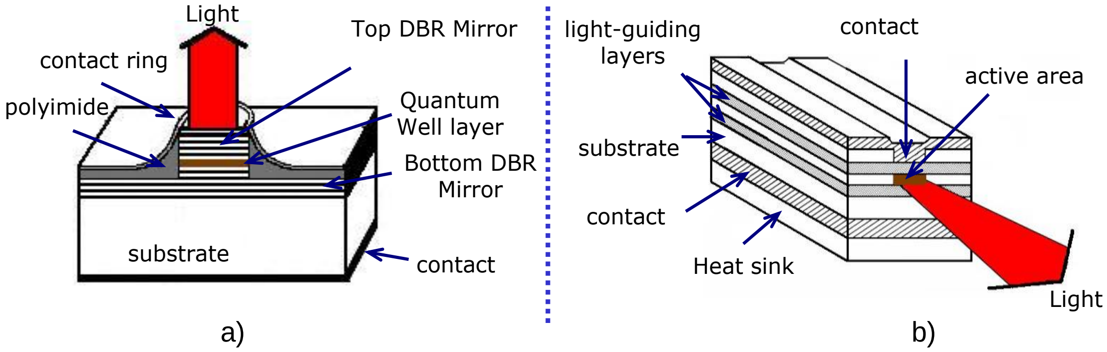

Figure 1-11: Physical structure of VCSEL (a) and EEL (b).

It is clear that VCSELs are more efficient regarding their low power consumption, single mode operation (SM), and high optical efficiency. The main advantage of the EELs is their high optical power.

VCSELs have numerous advantages. As a vertical emission laser, it gives the capability of on wafer level testability and 2-D array production which reduce the cost. Their circular and low divergent optical beam facilitates the alignment and packaging into the optical fiber. The low volume of the optical cavity allows a single mode operation and high speed operation. The low cost crops up in the development of VCSELs and Si LEDs, in particular for their implementation in short range optical interconnections (within a building and on a chip).

Many industrial companies, universities and research laboratories have focused their activities on high speed VCSELs emitting at different wavelengths and low cost Si LEDs. Moving from shorter wavelengths (650, 750, 850, 980, 1100 nm) to longer ones (1300 and 1550 nm) the VCSEL technology complexity increases as well as the cost. Thereby, in the recent years, the shorter wavelength optical sources and low cost Si LEDs with a potential to be integrated into CMOS based optical interconnect on a single chip become of a big interest [84]-[86]. Thus we will focus our discussion on low wavelengths with a special interest in 850 nm VCSEL and Si LED.

1.5.1 Light Emission device in III-V materials

850 nm is the most interesting wavelength for LAN applications and 850nm VCSEL will surely keep playing an important role in the further future of optical communications. Different materials for active region can be used and have been reported, including GaAs [87] [89]-[94], InGaAs [20]-[22] and InGaAlAs [95]. New concepts in order to increase the VCSEL performances, like the bandwidth modulation, have been applied, including optical/electrical confinement techniques: oxide aperture [93] [94], proton implantation [20] [89], Photonic Crystals (PhC) [96] [94] and a few years ago back double oxide aperture [97]-[100]. Bit rates up to 40 Gbit/s have been reached recently [97] [95] [101] using double oxide aperture and InGaAs quantum wells (QW), with an aperture diameter of 6 µm - 9µm.

In the case of 980 nm VCSELs, active region materials can be GaAs [94] [101] or InGaAs [102] [103] [104] [105]. Bit rates up to 35 Gbit/s have been achieved recently [227] using tapered-deep-oxide aperture with an aperture diameter of 3 µm and using InGaAs QW.

The most recent 1100 nm VCSEL devices make use of InGaAs [106] [107]. Bit rates up to 40 Gbit/s have been achieved [108] using tapered-deep-oxide aperture with an aperture diameter of 5µm.

1.5.2 Light Emission device in Silicon

Unfortunately, silicon is an indirect bandgap semiconductor, and, therefore, fabricating integrated lasers is a challenge. The most successful approaches to fabricate lasers on silicon are based on hybrid or heterogeneous integration of III-V materials [246].

However, various researchers have highlighted the need for small-dimension light emitters which are compatible with mainstream silicon CMOS integrated circuit technology [84]-[86]. Light emission from silicon devices has previously been performed in reverse-biased silicon p-n avalanche structures [109]-[112]. It has been postulated that light emission occurs from these structures through phonon assisted intra-band and inter-band recombination phenomena [109] [110].

In particular, Kramer et al [111] and Snyman et al [112] realized the first Si LED light emitting devices utilizing current density and surface engineering technology. Snyman et al have succeeded in obtaining practical and usable light emitting devices (Si LED’s) using standard CMOS design and processing technology [111] [112]. Recently, models have been presented which postulate that enhanced light emission can be obtained in these devices through carrier energy and carrier momentum engineering [113] [114].

In [242], an optical emission intensities of about 100nW μm^{-2} were subsequently measured on silicon avalanche LED when the total active emission areas are considered at the device surface. About 1nW μm^{-2} and 0.5nW μm^{-2} optical emission intensity on silicon LEDs were measured in [243] and in [114] respectively.

Because of the easy integration in CMOS technology, these type of devices show great potential to be integrated into CMOS based optical interconnects, optical RF connection systems and lab-on chip micro-photonic systems. Although present emission levels are sufficient in order to sustain diverse applications, a higher emission power is desirable.

1.6 Photodetectors

1.6.1 Introduction

A photodetector is the device that detects the optical power and then converts it into electrical power. Photodetector devices perform photodetection. The performance of an optical detector can be determined by its ability to detect the smallest possible optical power and to generate a maximum electric power at the output with an absolute minimum degree of distortion. Optical detection must also exhibit a wide Bandwidth and sharp response to accommodate high bit rate criteria. Besides its ability to interface with optical cables, a long operating life, cost, fast response, low noise, high reliability are desirable criteria.

In the last decade there has been a considerable interest for photodetectors bandwidth increment. This results in arrival of new types of high speed photodiodes based on InP/InGaAs for long distance communication systems. However, nowadays the bandwidth requirement of the last mile (home area networks) is increasing and thereby high cost efficiency of integrated transceivers is of great interest. As a result some researchers on this area are working on SiGe/Si technologies, which are cheap and easy to integrate [23] [115]-[119].

1.6.2 Photodetector Material Choices

High speed photodetectors are used in the implementation of the different Radio over Fiber systems as discussed in the previous section. These devices are required in telecommunication systems and in high capacity optical based networks. There are different materials that are used in the implementation of these photodetector structures. The use of the materials that are matched to a specific wavelength and optimized for high speed operation is a key activity in the research for very high speed discrete photodetectors. This is specially the case in telecoms applications where the performance is the major criterion.

Based on the operating wavelength, Semiconductor materials can be categorized into:

1. Detector materials for long-haul communication systems
    - InGaAs (slightly tunable gap) direct bandgap, ternary alloy. Excellent material for long-haul communications ($\lambda = 1.55$ µm), grown (lattice-matched) on InP substrates
    - InGaAsP (slightly tunable gap), direct bandgap, quaternary alloy. Material for long-haul communications ($\lambda = 1.55$ µm), grown (lattice-matched) on InP substrates
    - AlGaSb (tunable gap) [122], direct bandgap, ternary alloy. Material for long-haul communications ($\lambda = 1.55$ µm). Poor substrate choice (GaSb), not competitive with InP at present. Interesting material for low-bandgap (high mobility) electronics, less developed than InGaAsP
2. Detector materials for LANs communication
    - GaAs (AlGaAs), direct bandgap, somewhat tunable gap, ternary alloy. Cannot be used for long-haul communications, only suited for LAN applications ($\lambda = 0.85$µm). Excellent substrate availability (GaAs), mature technology, low-cost; compatible with AlGaAs lasers.
    - Si, indirect bandgap. Cannot be used for long-haul communications since it cannot absorb light at at related high wavelengths. Well suited for LANs, OK for avalanche photodiodes. Excellent substrate availability (Si), mature technology, low-cost.
3. Detector materials for LAN and long-haul
    - Ge, indirect bandgap, bulk material. Can be used for long-haul communications but also for LANs (high secondary absorption edge due to direct processes). Excellent possibilities for avalanche photodiodes. Good substrate availability (Ge), mature technology, medium cost. Recently revived by the emergence of high-speed SiGe technologies integration with Si-based

ICs.

- Silicon based photodetectors are commonly used for wavelengths from 400nm up to1000nm. Germanium is used for photodetectors at long wavelengths up to 1800nm. Due to the indirect bandgap of Silicon and Germanium at these wavelengths, they have relatively small bandwidth efficiency products.

As Silicon is abundant and has relatively low processing cost, there have been a lot of research activities to develop high speed photodetectors that are based on Silicon. This permits to monolithically integrate detectors with high speed electronic circuits that are needed for the processing of the detected optical signals [120]. One aspect of these researches aims to extend the spectral response of Silicon based detectors so that they can be used in the telecoms at wavelength such as 1310nm. This involves the use of Germanium [118] [121] and SiGe based photodetectors [116].

1.6.3 Photodetector Structures and frequency limitations

The bandwidth of a photodetector is mainly limited by carrier transit time and RC time constant. Carrier transit time is the time taken by the photo-generated carriers to travel across the high-field region. It is usually dominated by holes transit time as holes typically have lower drift velocity than electrons in common photodetector materials. The RC time constant is determined by the equivalent circuit parameters of the photodiode and the load circuit. Diode series resistance (due to ohmic contacts and bulk resistances), load impedance and the junction and parasitic capacitances contribute to the RC time constant. Diffusion time becomes important when the photocurrent due to carriers absorbed in the p and n contact regions within about one diffusion length at the edge of the depletion region becomes comparable to the current arising from the photo-generated carriers within the depletion region.

Generally factors that affect photodetector speed can be categorized into three mechanisms depending on the device structure.

1. Intrinsic cut-off mechanisms
   - ✓ Device capacitance (due to junction and /or parasitic)
   - ✓ Minority carrier life time (in the case of photoconductor)
   - ✓ Active region transit time (PIN, APD)
   - ✓ Avalanche build up time (APD)
   - ✓ Internal gain cut-off frequency (in phototransistors)
2. External mechanisms: external parasitic or load capacitance
3. Light and RF signal velocity mismatch: in distributed photodetectors

Based on the way of the optical signal injected into the photodetector (PD) structure, the high speed PDs may be classified in three classes: surface-illuminated, resonant-cavity-enhanced and edge coupled PDs (Figure 1-12). Besides, in regard to their microwave properties they can be divided in lumped and distributed PDs.

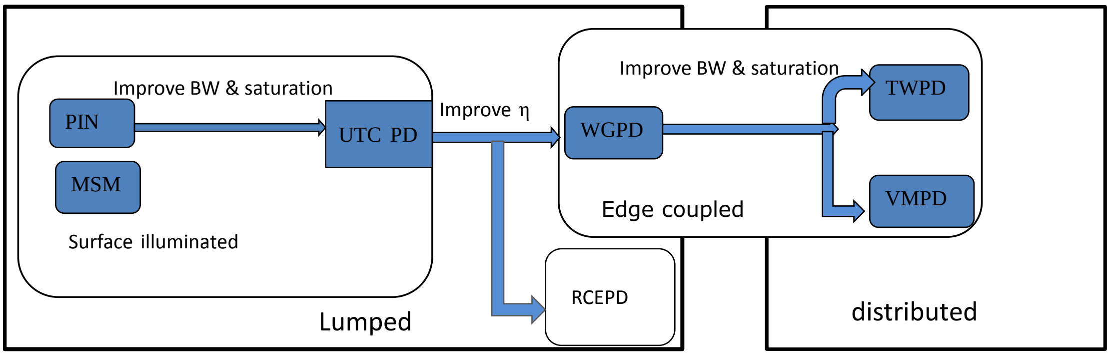

Figure 1-12: The main trends in the progress of high speed photodetectors[130]

Usually the quality of the different types of high-speed PDs is characterized by the bandwidth-efficiency product. For surface-illuminated PDs this parameter usually does not exceed 20-30 GHz (BW*efficiency) [122] due to trade-off between quantum efficiency and bandwidth. The increase of the quantum efficiency requires increasing the PD absorption layer thickness, whereas to increase the bandwidth requires reducing it. This trade-off can be overcome by means of resonant-cavity-enhanced PDs, in which PD is placed in a Fabry-Perot resonator. Optical radiation passes through the thin absorption layer many times and quantum efficiency increases at the resonant wavelength. In the edge-coupled PDs, optical wave propagates in perpendicular direction to the charge carrier transport. In this case, it is necessary to increase the device length instead of the absorption layer thickness, in order to increase the quantum efficiency.

For some novel microwave optoelectronic systems it is necessary to have high-speed PDs with large saturation current, for example, in systems using optical amplifier as a preamplifier in the photo-receiver. PDs with high saturation current are needed also for such applications as photonic generation of millimeter waves and photonic measurements of the high-speed electronic devices [216]. The saturation of a photocurrent under high optical power is connected to screening of an internal electrical field of the PD by photo-carriers (space-charge effect). To increase the PD bandwidth, in general, it is necessary to decrease the absorption layers volume. In this case the optical power density incident into the PD is increased. So there is a trade-off between bandwidth and high saturation current. This general trade-off is overcome in distributed photodetectors such as TWPD and VMDP (Figure 1-12). The bandwidth of the distributed PDs is limited by the difference between propagation velocities of light wave and microwave as well as by the microwave losses. So the length and width of the absorption layer can be made rather large compared with the lumped PDs [123] [124] [125]. On the other hand, improving the saturation current can be achieved by optimizing carrier dynamics, which has been done in UTC PDs [126]. Thus, there are two main trends in the development of high-speed PDs. The first is suited for the development of PDs with high bandwidth-efficiency product and the second is related to the development of high-speed PDs with high saturation current [127] [122] [128].

1.6.3.1 PIN Photodetector

A p-i-n photodiode consists of p and n regions separated by a very lightly doped intrinsic (i) region as indicated in Figure 1-13. The intrinsic layer contains only a very small amount of dopants and acts as a wide depletion layer. In normal operation, a sufficiently large reverse bias voltage is applied across the device so that the intrinsic region is fully depleted of carriers. At longer wavelengths, light penetrates more deeply into the semiconductor material.

Light is incident on depletion region so photo-generated carriers are generated in the depletion region. Due to the high electric field induced across the depletion region, the carriers separate and are collected by the reverse biased voltage. This causes a current flow in the external circuit which is referred as photocurrent.

The performance of p-i-n photodiodes can be improved by using a double heterostructure design. The intrinsic layer is sandwiched between p-type and n-type layers of a different semiconductor whose band gap is chosen such that light is absorbed only in the middle i-layer. As an example Figure 1-13 shows a p-i-n photodiode made of InGaAs for the intrinsic layer and InP for the p-type and n-type access layers.

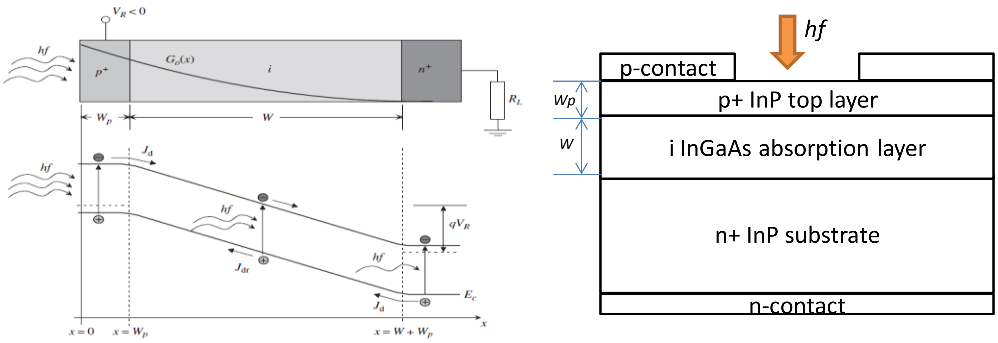

Figure 1-13: Schematic structure (right) and band diagram with structure (left) of a pin photodiode in reverse bias. Jdr and Jd are drift and diffusion current densities, respectively

Compound semiconductor pin structures are today probably among the best components available for 10 Gbps and 40 Gbps systems. Cut-off frequencies higher than 67 GHz have been demonstrated [129]. Usually, a compromise must be reached between speed and responsivity (efficiency); the device speed is dominated by transit time and the parasitic capacitance. Such limitations can be overcome in more advanced structures such as traveling-wave waveguide photodiodes.

a) The pin PD photocurrent, responsivity and efficiency

The main contribution to the photocurrent is given by the drift current associated with carriers generated inside the intrinsic depleted region; secondary contributions (which disappear in heterojunction devices) come from the diffusion regions. Due to the large width of the depletion region W, the optical generation rate will be non-uniform, according to the law:

$$G_{opt}(x) = \eta_i \frac{P_{in}(1-R)}{Ahf} \alpha e^{-\alpha x} = G_{opt}(0) e^{-\alpha x} \qquad (1.1)$$

Where η_i is the intrinsic quantum efficiency, P_{in} the total incident power on the lateral (upper) photodiode detection facet, A is the detector area, *hf* is the photon energy, α is the material absorption, G_{opt} is the optical generation and R is the power reflectivity of the detection surface.

The total photocurrent is the contribution of both the drift (from the intrinsic layer) and diffusion (from the surface and substrate layers) carriers' movement: $I_{ph} + I_{dr} + I_{dff}$.

By ignoring the dark current the photocurrent can be expressed as:

$$I_{ph} = \eta_i \frac{q}{hf} P_{in} (1-R) e^{-\alpha w_p} \left(1 - \frac{e^{-\alpha w}}{1+\alpha L_{hn}}\right) \qquad (1.2)$$

Where L_{hn} is the length of diffusion region, w_p is the width of p doped region and w is the width of the depletion region.

Thus the responsivity is:

$$R = \frac{I_{ph}}{P_{in}} = \eta_i \frac{q}{hf} (1-R) e^{-\alpha w_p} \left(1 - \frac{e^{-\alpha w}}{1+\alpha L_{hn}}\right) \qquad (1.3)$$

And external efficiency is:

$$\eta_{ext} = \frac{I_{ph}/q}{P_{in}/hf} = \eta_i (1-R) e^{-\alpha w_p} \left(1 - \frac{e^{-\alpha w}}{1+\alpha L_{hn}}\right) \qquad (1.4)$$

The diffusion contributions to currents are much smaller than the drift contributions in dynamic operation, and should be reduced to optimize the high-speed response. This can be immediately achieved in heterojunction devices, where the substrate layer below the absorption region is of wide gap and therefore does not appreciably absorb light. The maximization of η_{ext} requires that the thickness of the top layer is small, or that the top layer is of wide gap, (i.e. transparent to the incoming light). For high-speed, high-efficiency photodiodes $\alpha w_p \rightarrow 0$ and $\alpha L_{hn} \rightarrow 0$, the external device quantum efficiency and responsivity are:

$$\eta_{ext} = \eta_i \left(1-R\right)\left(1-e^{-\alpha w}\right) \tag{1.5}$$

$$R = \frac{q}{hf}\eta_i \left(1-R\right)\left(1-e^{-\alpha w}\right) \tag{1.6}$$

b) The pin PD Frequency Response

There are four main mechanisms that limit the speed of pin photodiodes under dynamic excitation [122]:

1. The effect of the total diode capacitance, including the depleted region diode capacitance and any other external parasitic capacitance.
2. The transit time of the carriers drifting across the depletion layer.
3. The diffusion time of carriers generated outside the undepleted regions (mainly in homojunction devices).
4. The charge trapping at heterojunctions (in heterojunction devices).

Transit time effects are negligible in pn junction photodiodes owing to the small depletion region width, but become a dominant mechanism in pin devices. Transit time and RC cutoff are thus the main limitations in technology-optimized pin photodiodes.

There are two extreme frequency behaviors of a transit limited bandwidth Photodiode:

- Thick diode ($\alpha W >> 1$): the frequency response is mainly limited by the velocity of minority carriers generated at the illuminated side. For p+ side illuminated pin, the 3dB electrical bandwidth is limited by electrons saturation velocity ($V_{n,sat}$) [17] [122] [130]:

$$f_{3dB,tr} = 0.443\frac{v_{n,sat}}{w} \tag{1.7}$$

For n+ side illuminated pin, the 3dB electrical bandwidth is limited by holes saturation velocity ($V_{h,sat}$) [17] [122] [130]:

$$f_{3dB,tr} = 0.443\frac{v_{h,sat}}{w} \tag{1.8}$$

Since the holes are slower than electrons, illumination should come from the p+ side to maximize the device speed.

Assuming, on the other hand, that both carriers have the same transit time we can have the approximate expression [17] [122] [130]:

$$f_{3dB,tr} = \frac{1}{2.2\tau_t} \quad where\ \tau_t\ is\ the\ electron\ or\ hole\ transit\ time$$

- The diode is thin ($\alpha W << 1$); in this case, the generation of pairs along the i layer is almost uniform and the frequency response is limited by both carriers; an approximation of the cut-off frequency is given by[17] [122] [130]:

$$f_{3dB,tr} = \frac{3.5v}{2\pi w}, \qquad where \frac{1}{v^4} = \frac{1}{2}\left(\frac{1}{v_{n,sat}^4} + \frac{1}{v_{h,sat}^4}\right) \tag{1.9}$$

From these computations it is clear that transit time limited cut-off frequency increases with decreasing the absorption region thickness w.

The cut-off frequency of pin photodiode is also highly limited by the total diode capacitance that can be deduced from the PD equivalent circuit. In Figure 1-14, C_p is the external diode parasitic capacitance and Rs the series parasitic diode resistance, R_D the parallel diode resistance, C_j the intrinsic capacitance (dominated by the intrinsic layer capacitance). Usually it is considered that $R_D >> R_s, R_L$.

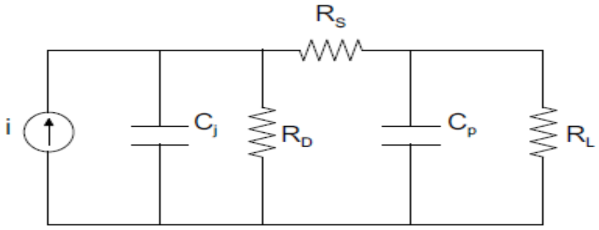

Figure 1-14: Simplified pin photodiode equivalent circuit

From the equivalent circuit we can also estimate the RC-limited cut-off frequency. Thus the 3 dB RC-limited photodiode bandwidth is given by [17][122] [130]:

$$f_{3dB,RC} = \frac{1}{2\pi RC}, where\, R = R_s + R_s\; and\; C = C_j + C_p, C_j = \frac{\epsilon_s A}{w} \tag{1.10}$$

The total cutoff frequency resulting from the transit time and RC effect can be evaluated at a circuit level. An approximate expression is:

$$f_{3dB} = \frac{1}{\sqrt{f_{3dB,RC}^{-2} + f_{3dB,tr}^{-2}}} \tag{1.11}$$

In general in PIN PD the external efficiency (η_x) and the RC limited band width ($f_{3dB,RC}$)increase with the thickness of the active region (W). However, the transit limited bandwidth ($f_{3dB,tr}$) decreases when the active area thickness increases. When the surface area (A) of the PD increases the external efficiency increases whereas RC limited bandwidth decreases. Thus, there is a tradeoff between external efficiency and bandwidth in PIN photodetector structure.

c) Bandwidth efficiency trade-off

In a vertically illuminated photodiode, optimization of the external quantum efficiency suggests W >> Lα = 1/α (absorption length); moreover, the detection area A should be large in order to improve the coupling with the external source (e.g.an optical fiber). However, increasing the active area thickness increases the RC-limited bandwidth (since it decreases the junction capacitance) but decreases the transit time-limited bandwidth. Increasing the device area has no influence on the transit time-limited bandwidth but makes the capacitance larger and therefore decreases the RC-limited bandwidth (Figure 1-15 b)). Keeping the device area A constant, we therefore have $f_{3dB,RC} \propto W$ but $f_{3dB,tr} \propto$ 1/W. Since f_{3dB} < min ($f_{3dB,RC}$,$f_{3dB,tr}$), the total bandwidth is dominated by $f_{3dB,RC} \propto$ W (low W) or $f_{3dB,tr} \propto$ 1/W (large W). The total bandwidth then first increases as a function of W, then decreases (Figure 1-15 a)). f_{3dB} therefore has a maximum, which shifts toward smaller values of W and larger cut-off frequencies with decreasing A. At the same time, the efficiency always increases with W. As a consequence, high-frequency operation (high f_{3dB}) requires small-area diodes, with small W and consequently poor efficiency (Figure 1-15 c).

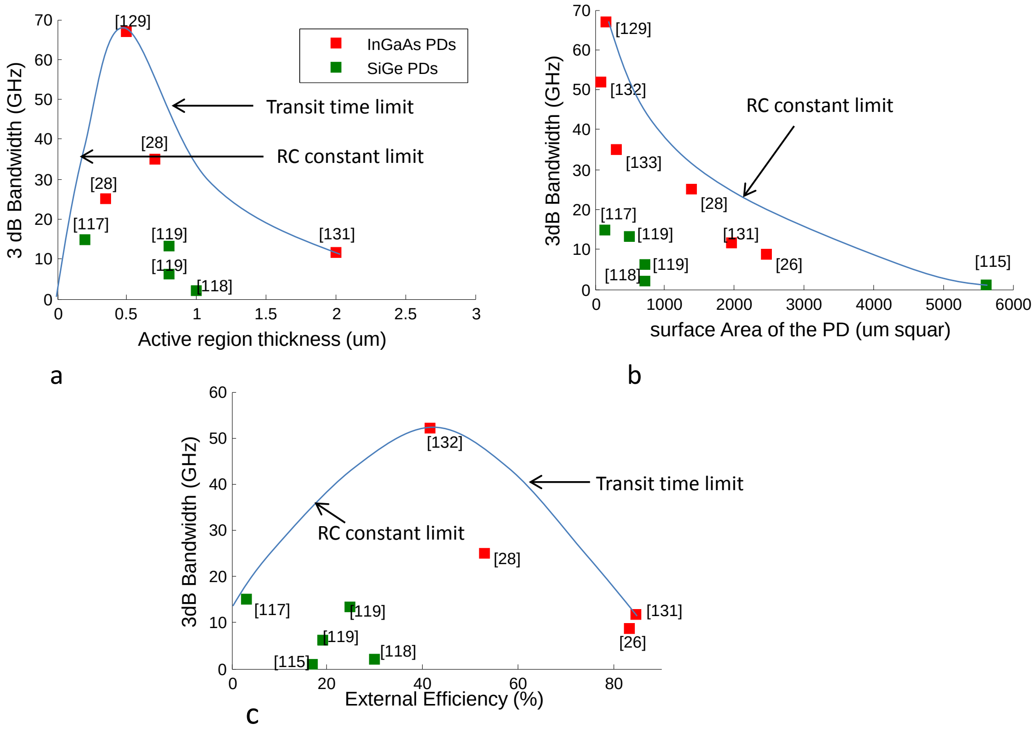

Figure 1-15: High speed pin optimization: trade-off between speed and efficiency.

1.6.3.2 Uni Travelling Carrier Photodiode-UTC PD

In PIN diode, under the effect of the applied reverse voltage electric field appears in the intrinsic region i, electrons are thus directed to the N doped zone and holes are directed to the P doped zone. These charges create a space charge region, generating an electric field .This new electric field can interfere with the internal electric field due to reverse voltage, thus carriers are delayed. Hence the carrier delay is the principal cause of non-linearity.

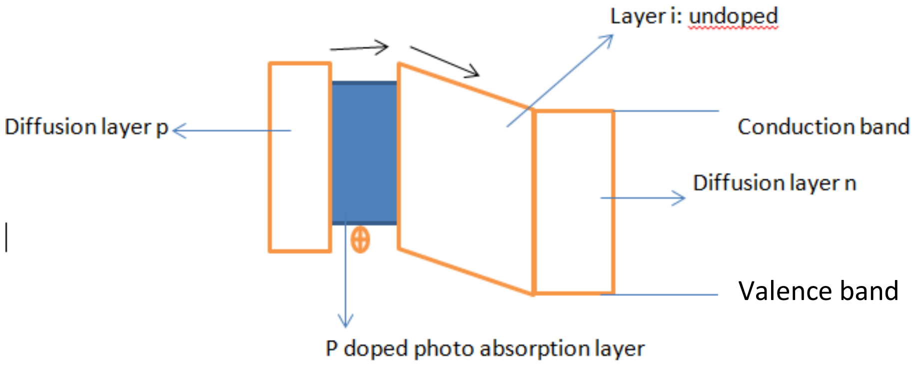

Figure 1-16: UTC photodiode energy diagram

Another way to enhance both the bandwidth and the saturation current of the traditional p-i-n PD is to use only fast electrons for charge carrier transport, that is achieved in the UTC PDs [17] [130] [134] [217] [218]. The principle of this PD is based on the fact that absorption occurs in p doped zones followed by large gap i zones. Holes generated in zone p are absorbed in the same zone with a very short relaxation time. However, electrons move via diffusion from zone p towards zone i where they are captured and drift under the effect of the electric field present in the zone. Hence the space charge in this zone is only due to electrons. Additionally, as long as the layer thickness is less than 0.2µm, a velocity overshoot phenomena in InGaAs/InP UTC PD occurs meaning that electrons can move five times the saturation velocity [17]. Therefore the transit-time limited bandwidth of the UTC PD with thin absorption layer can be as high as 200 GHz and above [130]. Moreover, usage of a graded band gap in the absorption p-layer creates an internal electric field and drift mechanism becomes dominant in the absorption p-layer that results in even greater decrease of the transit time. The saturation current of the UTC PD is determined by the space charge effect in the collector layer [17][130]. Since only photoelectrons induce space charge effect the saturation current of the UTC PD is higher than for the traditional p-i-n PD, in which both photo generated holes and electrons destroy the internal electrical field of the p-n junction.

1.6.3.3 Resonant Cavity Enhanced Photodetector –RCE PD

One technique to overcome the bandwidth–efficiency limitations of the vertically illuminated PIN is to try to increase the distance over which photons travel through the absorption region in order to maximize optical absorption, while keeping the distance that the electron-hole pairs travel as small as possible to minimize the transit time. This may be achieved through creating a resonant optical cavity in order to set up multiple passes of the optical signal through the active region [17] [27] [119] [122] [130] [137]-[139] as shown Figure 1-17, but the resonance leads to wavelength selectivity thus making these devices of more interest for use in wavelength division multiplexed (WDM) systems. Due to multiple propagation of optical radiation at the resonant wavelength through the absorbing layer, its thickness can be reduced for receiving necessary bandwidth without any efficiency penalty. In this case bandwidth-efficiency product can reach hundreds of GigaHertz [130].

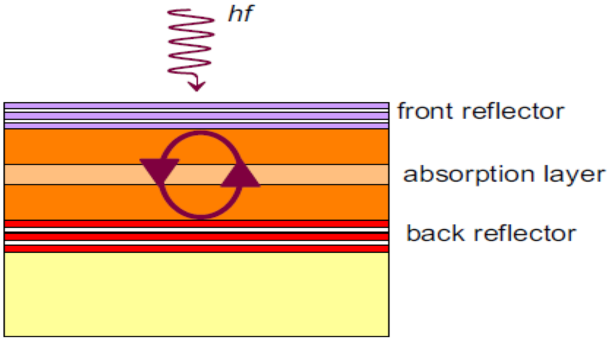

Figure 1-17: Resonate cavity enhanced Photodetector structure.

This potodetector has high speed and high quantum efficiency. It was demonstrated in [137] 36GHz 3dB bandwidth and 70% external quantum efficiency can be achieved in a GaAs photodiode.

The RCE PD quantum efficiency can be expressed by the following formula [17][130]:

$$\eta(\lambda)=\frac{\left[1-R_1(\lambda)\right]\left[1+R_2(\lambda)e^{-\alpha(\lambda)d}\right]}{\left|1-\sqrt{R_1(\lambda)R_2(\lambda)}e^{-\alpha(\lambda)d}e^{-j[4\pi(n_1d_1+n_2d_2+nd)/\lambda+\varphi_1(\lambda)+\varphi_2(\lambda)]}\right|^2}\left[1-e^{-\alpha(\lambda)d}\right] \quad (1.12)$$

where R_1, φ_1 and R_2, φ_2 are the reflection coefficients and phase shifts of the forward and reverse reflectors, n, α, d are the refractive index, absorption coefficient and thickness of the absorption layer, n_1, d_1 and n_2, d_2 are the refractive index and thickness of layers above and below the absorption layer. The quantum efficiency is maximum at wavelength λ_0 when $4\pi(n_1d_1+n_2d_2+nd)/\lambda_0+\varphi_1(\lambda_0)+\varphi_2(\lambda_0)=2\pi$. The maximum efficiency and the related spectral width at half maximum can be expressed by the following formulae [17] [130]:

$$\eta_{max}=\frac{\left[1-R_1\right]\left[1+R_2e^{-\alpha d}\right]}{\left(1-\sqrt{R_1R_2}e^{-\alpha d}\right)^2}\left[1-e^{-\alpha d}\right] \quad (1.13)$$

$$\Delta\lambda_{1/2} = \frac{\lambda_0^{\,2}\left(1-\sqrt{R_1R_2}e^{-\alpha d}\right)}{2\pi\left(n_1d_1+n_2d_2+nd\right)\sqrt{\sqrt{R_1R_2}e^{-\alpha d}}} \tag{1.14}$$

The above equations show that quantum efficiency grows with increasing of the reflection coefficients R_1 and R_2. However, in this case the spectral width ($\Delta\lambda_{1/2}$) decreases.

Since the RCE PD differs from the surface-illuminated PDs only by the optical resonator, the electrical parameters of the RCE PD, such as bandwidth, dark and saturation currents have mostly the same expressions as for the surface illuminated PD placed in the optical resonator.

1.6.3.4 Metal Semiconductor Metal Photodetector –MSM PD

A MSM photodetector consists of interdigitated metal lines deposited over a semiconducting material [24] [130] [140]-[143], as shown in Figure 1-18. The main advantage of the MSM PD is a very simple production process, which is completely compatible with production process of field-effect transistors [130]. To the best of knowledge MSM PD has reached a bandwidth of 75 GHz [141]. However, the MSM PDs suffer from lower quantum efficiency and higher dark current compared to PDs based on p-n junction. The quantum efficiency of MSM PD can be expressed by the following expression [130]:

$$\eta = \left(1-R\right)\left(1-e^{-\alpha d}\right)\frac{L}{L+w} \tag{1.15}$$

where L is the interdigital spacing, w is the finger width, d is the effective absorption thickness, R is reflection coefficient and α is absorption coefficient.

MSMs are a good choice for high-speed operation with large detection area because MSMs have lower intrinsic capacitance per unit area than P-i-Ns, but the finger electrode shadowing of conventional MSMs decreases the responsivity of the PD. To increase MSM PD’s responsivity it is possible to use inverted MSM structure as well as for the Schottky PD [144] [143]. Inverted MSM PDs are thin-film MSMs with the growth substrate removed and fingers on the bottom of the device to eliminate finger shadowing to enhance responsivity. This device optimizes the tradeoff between speed and responsivity. For the MSM PD operation it is necessary to supply bias voltage, which is sufficient for maintenance of drift mechanism of photo carriers transport.

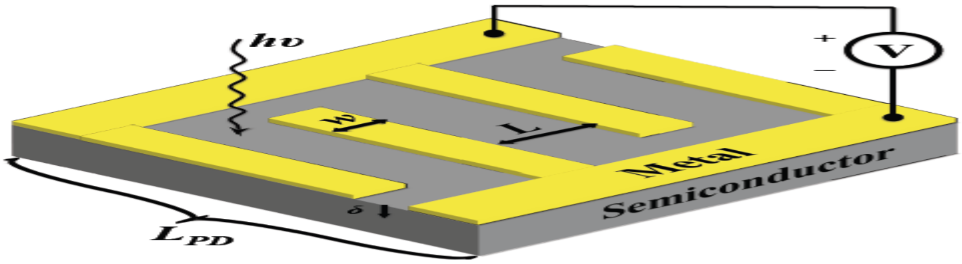

Figure 1-18: Physical schematic of MSM PD[144]

The MSM PD bandwidth, as well as for the p-i-n PD, is limited by drift time and RC-time. Although in the MSM PD optical radiation propagates perpendicular to the direction of the charge carrier transport, there is a similar trade-off between the quantum efficiency and bandwidth than with top illuminated pin PDs. To increase the transit time, the inter-digital spacing has to be reduced, and to increase the quantum efficiency it is necessary to decrease the fingers capacitance, and thus to enlarge the inter-digital spacing. Since the MSM PD has lower capacitance per unit area compared to the PDs based on p-n junction, the MSM PD bandwidth is usually limited by transit time. Besides it is necessary to note that the inter-digital spacing reduction increases both dark current and degradation probability of the MSM PDs due to high surface currents.

The nature of a saturation of a photocurrent in the MSM PD is the same as in the p-i-n PD. However, the internal electrical field of the Schottky barrier is usually lower than in the p-i-n structure and moreover there is a large barrier for holes at the metal-semiconductor interface. This result in lower saturation current of the PD based on Schottky barrier compared with the p-i-n PDs [144].

1.6.3.5 Waveguide Photodetector -WGPD

An alternative structure for increasing optical absorption and reducing the transit time impact is to use edge-coupling, thus allowing the optical input to enter directly the intrinsic region and to propagate orthogonally to the electric field. Thus the photon flux and the carrier motion are orthogonal. In this case, the structure becomes an optical waveguide, allowing the design of long but narrow absorption regions which ensure that a large fraction of the input power is absorbed while maintaining low transit times [122] [130] [146] [147][148]. Waveguide photodiodes with bandwidths larger than 100 GHz have been demonstrated [149], and typical bandwidth–efficiency products for these devices are about 55 GHz.

Light is guided by an optical waveguide made of an intrinsic narrow gap semiconductor layer, sandwiched between two highly doped wide-gap layers (see Figure 1-19).

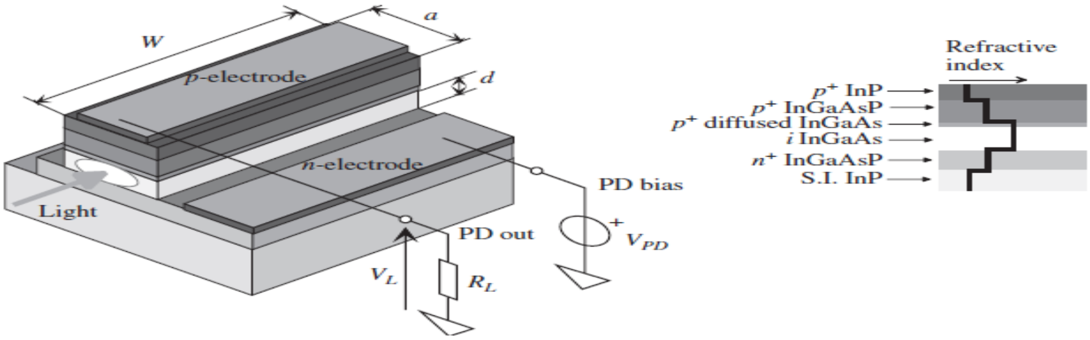

Figure 1-19: Schematic structure of an InGaAs waveguide photodiode (left) and details of the epitaxial structure (right) showing the guiding refractive index profile [122]

Applying a reverse bias voltage, photo carriers are collected by the doped layers after a very short transit time since the waveguide active region is typically thin. As the waveguide length can be designed long enough (W >> Lα), the majority of photons are absorbed, without affecting the transit time. The photodiode external efficiency and responsibivity can be expressed as: [122] [130]:

$$\eta_x = \eta_i (1-r)\left(1-e^{-\Gamma_{ov}\alpha W}\right) \tag{1.16}$$

$$R = \frac{q}{hf}\eta_i (1-r)\left(1-e^{-\Gamma_{ov}\alpha W}\right) \tag{1.17}$$

Where r_{ov} is the overlap integral or confinement factor, α is the core absorption, d is the active absorption region thickness W is the optical waveguide length and r is the input reflection coefficient.

The RC constant limited 3dB bandwidth is:

$$f_{3dB,RC} = \frac{1}{2\pi RC} \quad where\, R = R_s + R_D, C = C_j + C_p, C_j = \frac{\epsilon_s a w}{d} \tag{1.18}$$

Where C_p is the external diode parasitic capacitance, R_s is the series parasitic diode resistance, R_D is the parallel diode resistance, C_j is the intrinsic capacitance, w is the length of the active area, a is the width of the active area and d is the thickness active area.

Finally, the transit time limited cut-off frequency will be

$$f_{3dB,tr} = \frac{3.5v}{2\pi d} \qquad where \frac{1}{v^4} = \frac{1}{2}\left(\frac{1}{v^4_{n,sat}} + \frac{1}{v^4_{h,sat}}\right) \tag{1.19}$$

Where v is mean velocity, v_n and v_p are the electron and hole velocities in the intrinsic region respectively.

The waveguide photodiode has the following disadvantages:

- First, the thickness of the active layer is often less than 1 mm, leading to a significant reduction in coupling efficiency between the photodiode and single-mode fibre. This can be improved to some extent by using tapered fiber or by fabricating devices that have doped optical guiding layers around the absorption region.
- Second, the 'long and narrow' topology creates a capacitive region with a large area-to-thickness ratio, resulting in increased capacitance which causes an RC time limitation.
- Third, such structures suffer from earlier power saturation with respect to conventional photodiodes, due to the very small cross section.

1.6.3.6 Travelling Wave Photodetector -TWPD

The photodiode structures discussed above results of lumped element approaches. In order to eliminate the limitation of the RC time constant and to improve impedance matching, distributed designs were proposed. These are commonly known as travelling-wave photodetectors [30] [122] [127] [130] [135] [136] [150] and they are a natural evolution of the edge coupled waveguide PIN structure discussed above. In this case, in addition to the optical wave guiding mechanism, the device contacts are engineered to support microwave travelling waves; the approach is similar to Mach–Zehnder travelling wave modulators, and it is another example of transmission line effects in microwave photonics. Coplanar waveguide is typically chosen which supports a quasi-TEM mode; the transmission line parameters are determined by the device capacitance and the contact strip inductance. Absorption of optical power occurs in a distributed manner along the length of the device, through a travelling wave (Figure 1-20). Such a device is no longer limited by RC effects but by the velocity mismatch between the optical group velocity and electrical phase velocity. When velocity matching is achieved, then long device lengths compared to waveguide photodiodes are possible in principle. The fact that the absorption volume is increased also means that these devices will saturate at a higher power level [30] [135].

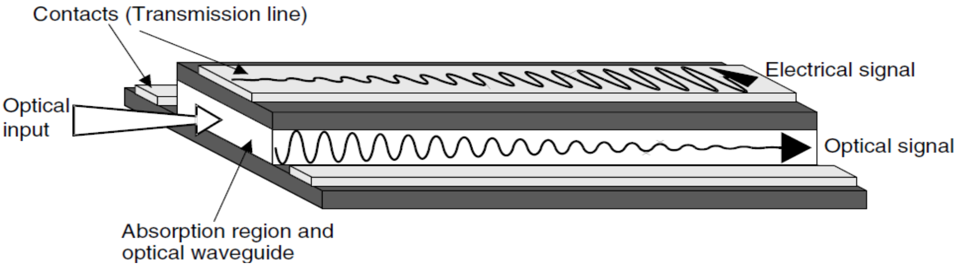

Figure 1-20: Distributed effects in a travelling wave photodetector [30] [135].

The TWPD is a device with distributed parameters. Its bandwidth is not limited by RC-time; therefore the TWPD length can be made much longer. The TWPD bandwidth is limited by the difference in the propagation velocities of light and microwave, and by parasitic RC-time and microwave losses in the transmission line. It is necessary to note that the propagation velocity of the microwave in the TWPD is 2 or 3 times smaller than the velocity of the light wave [30] [135] [144] [151]; because the velocity of the microwave signal is significantly slowed down by the capacitance of the photodiode (slow wave effect). Therefore major factor limits the bandwidth in correctly designed TWPD.

Optical radiation is absorbed in the TWPD and the photocurrent generates two microwaves propagating in opposite directions. The backward travelling microwave (in regard to the light direction of propagation) is reflected from the TWPD input edge and thus introduces additional mismatching between the light wave and microwave propagation velocities. This effect can be eliminated by means of matched load at the input edge of the TWPD microwave transmission line. However, in this case, half of the photocurrent will be absorbed by the matched load and the TWPD quantum efficiency divided by two. The TWPD bandwidth limited by the mismatch between the light wave and microwave propagation velocities can be expressed using the following expressions [122] [130] while considering two cases:

1. If the absorption region is short (ΓαW<<1) one has

$$f_{3dB} = \frac{0.44}{W} \frac{v_o v_m}{|v_m - v_o|} \tag{1.20}$$

Where v_o is the light wave propagation velocity and v_m the microwave propagation velocity in the TWPD.

In this case the cutoff frequency is inversely proportional to the device length W.

2. In a more realistic case the absorption region is long (ΓαW>>1)

$$f_{3dB} = \frac{\Gamma\alpha}{2\pi} \frac{v_o v_m}{|v_0 - v_m|} \quad \textit{for matched laod TWPD} \tag{1.21}$$

$$f_{3dB} = \frac{\Gamma\alpha}{\sqrt{2\pi}} \frac{v_m v_0{}^2}{\sqrt{5v_0{}^2 - v_m{}^2}} \cong \frac{\Gamma\alpha v_m}{3\pi} \qquad \textit{for unmached load TWPD} \tag{1.22}$$

In this case f_{3dB} is independent on W

Where, v_0 and v_m are the light wave and microwave propagation velocities in TWPD. The above two formula show that the bandwidth of matched TWPD is 2 or 3 times larger than for the unmatched TWPD. To increase the TWPD bandwidth, it is necessary to increase the Γα product. However, this results in the saturation current decrease due to non-uniformity of optical radiation absorption. Since the TWPD length is longer than for WGPD, the TWPD still has in general a larger saturation current. A large variety of travelling-wave photodiodes have been demonstrated and exhibit excellent performance such as 3dB bandwidths higher than of 210 GHz, for PIN based devices [123].

1.6.3.7 Velocity Matched Distributed Photodetector -VMPD

VMDP consists of a microwave transmission line periodically loaded by separated PDs (p-i-n PD [152], UTC PD [126], or MSM PD [153] [154]), to which optical radiation is provided by means of a passive waveguide (Figure 1-21). The key feature of the VMDP is that the microwave transmission line, the passive optical waveguide and the PDs can be designed separately with the purpose of achievement of the required characteristics. The microwave propagation velocity in a customary microwave transmission line is higher than light wave propagation velocity in semiconductor waveguide. The microwave propagation velocity can be reduced by periodical loading the microwave transmission line with capacitances, which can be p-n junction capacitances of the separated PDs. VMDP is designed so that the photocurrents from each separated PD sum in phase (matching of the microwave and light wave propagation velocities).

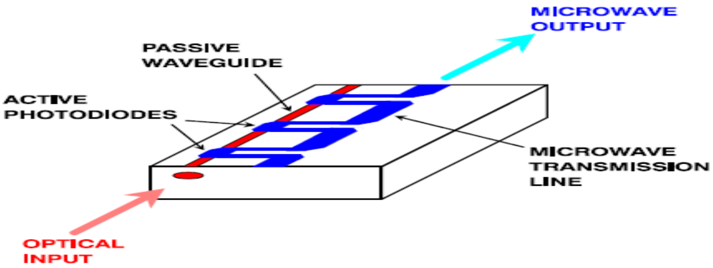

Figure 1-21: Velocity Matched PD structure

The VMDP quantum efficiency with matched loads at the ends of the transmission line can he expressed by the following formula [53]:

$$\eta = \eta_e \frac{\eta_0}{2} \frac{1-\left[\left(1-\eta_0\right)k^2\right]^N}{1-\left(1-\eta_0\right)k^2} \approx \frac{\eta_0}{2}\left[1-\left(1-\eta_0\right)^N\right] \tag{1.23}$$

Where $\eta_0 = 1 - e^{-\Gamma\alpha d}$ is the quantum efficiency of the separated PD, k is the coupling efficiency between passive waveguide and separated PDs (it is possible to achieve k value almost equals to 1), N is the number of separated PDs in the VMDP and η_e is the coupling efficiency.

$$f_{3dB} = \left[\frac{1}{\Delta f_p^{\ 2}} + \left(2\pi\left(N-1\right)\Delta l\,\frac{v_0 - v_m}{v_0 v_m}\right)^2 + \frac{1}{\Delta f_0^{\ 2}}\right]^{-1/2} \tag{1.24}$$

Where Δl is the spacing interval between the separated PDs in the VMDP, Δf_p is the parasitic RC-time limited bandwidth. The separated PD bandwidth Δf_0 can be very large (about hundreds of GigaHertz), since it is not required to have simultaneously a high quantum efficiency. Since the VMDP is designed so that $v_0 \approx v_m$, the slight mismatching between the light wave and microwave propagation velocities bandwidth influences on the VMDP bandwidth only under large number of separated PDs. Thus, in a correctly designed VMDP, the bandwidth is mostly determined by microwave losses in the transmission line and by parasitic RC-time.

For perfectly matched PDs ($v_0 \approx v_m$) and when neglecting parasitic RC time, the 3dB bandwidth is limited by the transit time of discrete PDs. Thus it can be expressed [155] [30] [144] as:

$$f_{3dB} = 0.55\frac{v_{eh}}{d} = 0.55\frac{\mu E}{d}$$

The VMDP bandwidth is limited by microwave losses, parasitic RC-time, mismatching of the microwave and light wave propagation velocities, and separated PD bandwidth. It can be expressed as [151]:

(1.25)

Where v_{eh} is the velocity of electon hole, d is the absorption thickness of each PD, μ is the carrier mobility and E is the electric field in the active region.

The global photocurrent of the VMDP is the sum of the photocurrents of the discrete PDs. Therefore to obtain a high saturation current it is necessary that each separated PDs only absorbs a small part of the incident optical power. This is easily reached by decreasing the confinement factor of each separated PD. It is necessary to notice, that on the first photodiode the maximum optical power drops. To avoid this, it is necessary to use the VMDP with parallel optical feeding of (Figure 1-22) [30] [135]. In this case, each separated PD absorbs the same optical power and the VMDP saturation current is increased. However, in this case the lengths of optical waveguides should be selected so that the photocurrents of the separated PDs sum in phase.

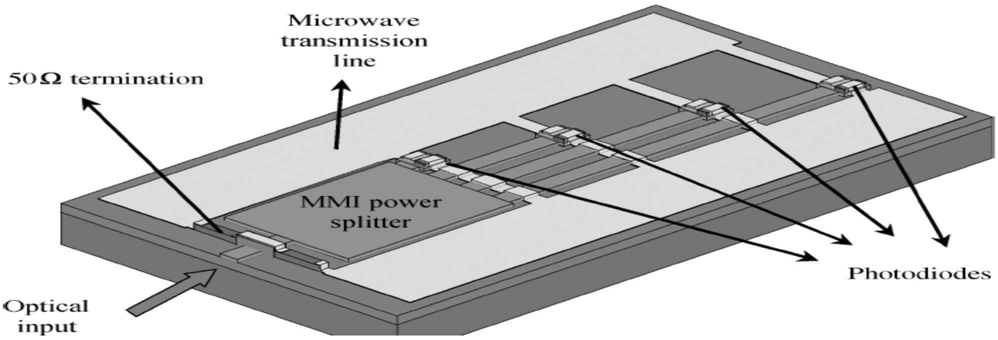

Figure 1-22: Parallel optical feed VMPD [30] [135].

1.6.3.8 Summary

To conclude, we summarize in this section the state of the art of PDs by comparing results of different publications in the previous years. The 3dB bandwidth of different types of photodetector with respect to the technology used (InP/InGaAs or SiGe/Si), active region thickness, surface area and external efficiency are plotted in Figure 1-23, Figure 1-24 and Figure 1-25. The related references are also indicated in the figures.

PDs made from InGaAs have higher efficiency and bandwidth than SiGe/Si PDs, see Figure 1-23 and Figure 1-24. This is due to the indirect bands of SiGe/Si material.

Figure 1-23 shows that waveguide PDs have better external efficiency than PIN because of large absorption length and they have poor bandwidth because of RC limitation. RCE also has good responsivity with values as high as 90% [138] (long absorption due to repeated reflection). TWPDs have the highest bandwidth with f_{3dbB} as high as 210GHz but low efficiency due to poor optical coupling. PIN photodiodes have the lowest performances because of the trade-off between efficiency and bandwidth.

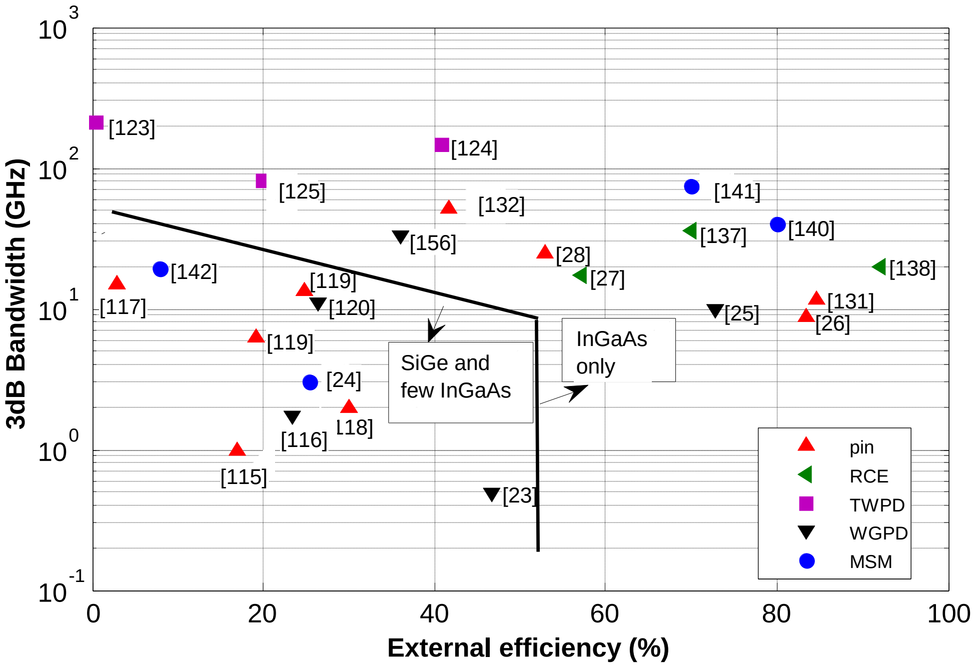

Figure 1-23: 3dB bandwidth as a function of external efficiency

From Figure 1-24, it can be observed that at an equivalent active area thickness, SiGe photodiodes are less high speed with bandwidth however as high as 15GHz [117]. Maximum active area thickness achieved with this material is less than 1µm [118] due to the mechanical instability of the layer induced by the mismatch between Si and SiGe lattice constant. This explains why achieved external efficiencies are below 46.67% [23].

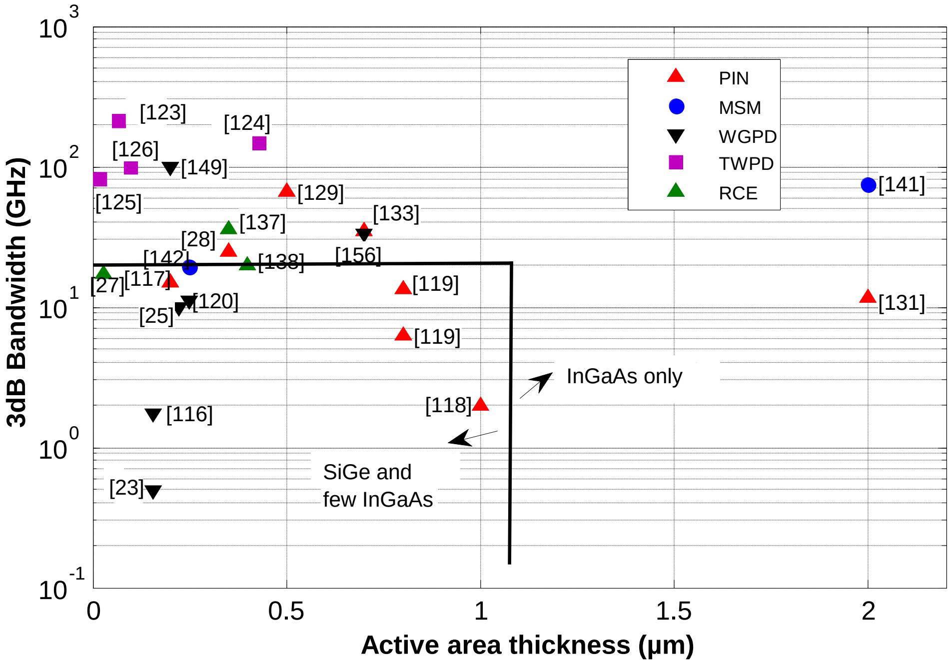

Figure 1-24: 3dB bandwidth as a function of active region thickness

Edge illuminated PDs (WGPD and TWPD) have thin absorption region thickness as shown in Figure 1-24. However, waveguide PDs have small bandwidth compared to traveling wave PD, because of the RC limitation. TWPDs have high BW at very thin absorption thickness as the transit time is highly reduced and no RC time constant effect appears. Top illuminated PDs require thick absorption thickness to improve the external efficiency, and thin active region thickness to improve the 3dB bandwidth. As indicated in Figure 1-24, the 3dB bandwidth decreases as active region thickness increases. RCE requires only thin absorption region due to multiple pass of the optical signal, as a result it has better efficiency and bandwidth than PiN PDs[27] [137] [138].

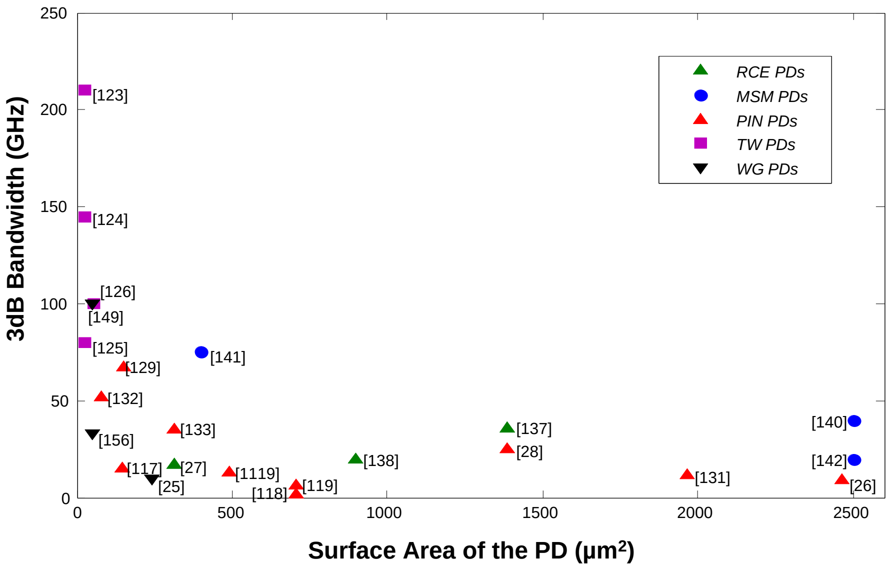

Figure 1-25: 3dB bandwidth as a function of surface area of the PD

High surface area results in low bandwidth because of RC effect. Top illuminated PDs have high surface area so that they have low BW as shown in Figure 1-25. Waveguide PDs have low surface area, but still have low BW because of the thin active region (thickness, d) capacitance ($C = \varepsilon A/d$).

Finally we conclude that advanced high-speed PDs based on compounds materials have recently been proposed for microwave photonics application. For frequencies below 50 GHz surface-lumped PDs such as p-i-n PDs, WGPDs, MSM PDs or RCEP PDs are successfully developed. For higher frequencies it is necessary to work with lumped UTC PDs and to go above 100 GHz it is more suitable to use distributed devices such as TWPDs and VMDPs [123] [124] [126]. In the applications where high-output power is required, one should use the UTC PDs, WGPDS and/or distributed absorption, TWPDs, or VMDPs.

1.7 Heterojunction Bipolar Phototransistor (HPT)

In this section we present the overview of Heterojunction bipolar Photo-Transistors (HPT) which are implemented as high-speed light detector. The principle of HPTs, the motivation to use phototransistors instead of photodiodes and light illumination techniques of HPTs are first introduced. In the second sub-section, HPTs are presented according to their technological approach, while considering both III-V material and Si-based phototransistors. Edge illuminated and traveling wave phototransistors are also pointed out.

1.7.1 HPT Principles

Heterojunction bipolar phototransistors (HPT) are based on Heterojunction Bipolar Transistors (HBTs) with the design of an optical window to enable the light path into the device and with some of its layers made of optical absorbing material, especially in the base-collector region. HPTs are good candidate as microwave photo-receivers, and could be called as microwave phototransistors, as opposed to low speed homojunction phototransistors used in sensor or opto-coupler applications.

The performance of HPTs, as any phototransistor, is supported by their internal current gain; not present in p-i-n and schottky photodiodes. In addition, unlike avalanche photodiodes, HPTs do not suffer from extensive noise due to avalanche effect. This advantage, and their process and layer compatibility to heterojunction bipolar transistor, makes them highly attractive in manufacturing single chip optical receiver [157].

Figure 1-26 shows a representative cross section of an AlGaAs phototransistor [17]. The structure of the HPT is similar to a bipolar transistor except for enlarged base and collector regions, to enable the presence of an optical window that receives the illumination spot, as given in Figure 1-26. The phototransistor structure can be illuminated vertically or laterally. Vertical illumination of the phototransistor can be achieved in different ways. A simple way is to illuminate the phototransistor between base-emitter contacts. This is simply illuminating a transistor structure [158]. The optical beam can also be injected via the emitter through an opening in the emitter contact [159] or by utilizing a transparent emitter contact [160]. Finally, one of the base contacts could be removed or omitted to allow the direct illumination of the base-collector junction [161] [162]. Another way of vertical illumination is through the backside of the phototransistor. Lateral illumination of the HPT is one method to improve the coupling efficiency to bandwidth trade-off. This allows the propagation distance before a complete optical absorption to be long enough while the absorption layer remains thin enough to ensure short transit times. Lateral illumination of phototransistors can be done by injecting the light through the cleaved side of the device. It can also be achieved by using an optical waveguide integrated in the device structure [163].

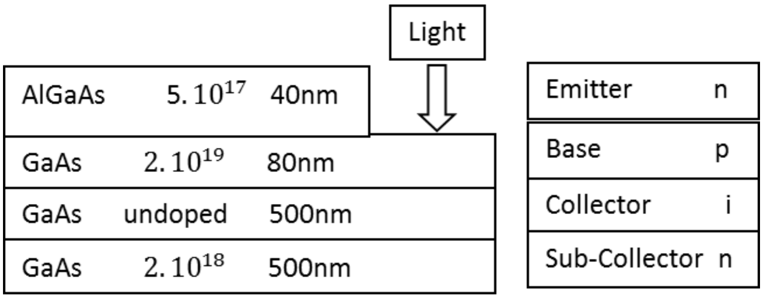

Figure 1-26: Schematic diagram of an npn GaAs/AlGaAs phototransistor.

Generally, in phototransistor, the base-collector region behaves as a p-i-n photodiode and injects the photo-generated current into the base (holes) and collector (electrons). The hole photo-generated current goes through the base and is then amplified. The phototransistor is hence usually represented by the simplified diagram given in Figure 1-27:

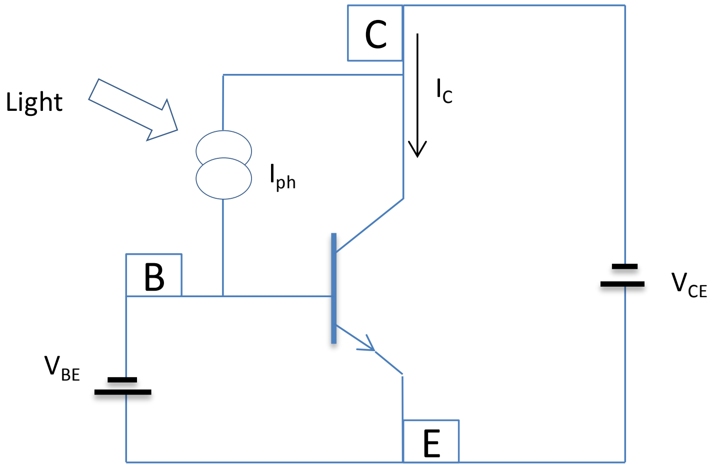

Figure 1-27: Simplified diagram of an HPT

I_C in such transistor can be written as:

$I_C = I_{ph} + \beta I_{ph}$ where β is the current gain and I_{ph} is the photogenerated current.

As the current gain of a transistor can be very high, this relation shows the benefit of using a phototransistor instead of a photodiode, which only generates I_{ph}.

This diagram is however a rough approximation and can lead to wrong interpretation results if one consider that in a voltage biasing mode, for example, all the photogenerated current should leak into the voltage source, which is only partially the case. Chapter 3 will better analyze the real HPT behavior.

Microwave bipolar transistors are mostly all n-p-n types and all have an emitter base heterojunction. In this transistor, the emitter base heterojunction has either the emitter made of a large gap semiconductor or the base made of a small band gap semiconductor. The semiconductor must be chosen in such a way that the band gap difference is in the valence band side as much as possible. This results in blocking the holes that could come from the base towards the emitter and thus increasing the emitter injection efficiency. Thus, the base can be doped more than that of homojunction transistor base and its thickness can be reduced, leading to increase the transistor operational speed, without increasing the transistor base resistance R_B [17] [157] [164].

The npn phototransistor is basically operated in the common emitter configuration where Vbe and Vce voltages are greater than 0. In this case the phototransistor is in the forward active mode. The BC junction is reverse biased and the BE junction is forward biased. The BE junction biasing could come from either the optical illumination of the HPT or by providing an external electrical base bias. The biasing of BE junction from the optical illumination is called a two terminal phototransistor operation (2T-HPT), as the base contact does not exist [165]. The base contact may however exist but is left floating [166] [168]. Providing an external bias for the base is called a three terminal HPT operation (3T-HPT) which is reported to provide enhanced HPT performances [175] [169]-[171]. For simplicity, it is assumed that no absorption occurs in the sub-collector and the collector is free of mobile charges. The photoelectric effects generate an electron-hole pair for every photon that is absorbed. The electron hole pairs generated in BC depletion region and within the diffusion lengths of the minority carriers in the base and collector will be separated and collected by the field of BC junction leading to a current flow in the external circuit. This is known as the primary photocurrent. The holes are swept into the base, thereby increasing the base potential. This in turn increases the base emitter forward bias. To maintain the charge-neutrality condition in the base, a large injection of electrons occurs from the emitter into the thin base resulting in a large electron-current flow from the emitter to the collector. This is the traditional behavior of a bipolar transistor. The amplification of the photocurrent is a purely electrical phenomenon due to the transistor action.

Finally the advantage of using a phototransistor instead of a photodiode comes from the possibility to have an internal gain into the HPT, providing a PiN + HBT like structure, but also in providing novel functionality due to the three-terminal structure, such as optical mixing and injected oscillators [172].

1.7.2 HPT Technological Approach

Based on the energy gap and lattice constant we can select the appropriate semiconductor materials to construct the HPT stacks. Heterojunction phototransistors using III-V compound have been extensively studied in the past two decades [174]-[179]. Heterojunction phototransistor using IV-IV also emerges nowadays since SiGe phototransistor proposed in 1997 with the multiple walls [173] [181], and since 2003 with SiGe HPTs integrated with the existing SiGe bipolar and BiCMOS technologies emerging for RoF applications [159] [161] [182]-[187].

1.7.2.1 GaAlAs/GaAs, InGaP/GaAs and InGaAs/InP phototransistors

Various HPTs fabricated using AlGaAs/GaAs [174] [175] [178] and InGaP/GaAs [176] [177] [179] technologies have been reported and applied to high performance optical receivers.

The first HPTs were fabricated on GaAs substrate because AlGaAs/GaAs heterojunction has lattice matching regardless of the proportion of Al and Ga. Furthermore the GaAs substrate was available elsewhere in the form of wafer with good mechanical and electrical properties. The GaAs semiconductor shows a correct absorption only for wavelength inferior to 0.85µm.

InGaP/GaAs heterojunction bipolar phototransistors (HPTs) are attractive photodetectors for optical communication and sensor applications. Those HPTs have large optical gain at low voltage bias and are compatible with heterojunction bipolar transistors (HBTs) concerning their epitaxial structures and fabrication process [188] [166]. Moreover, InGaP/GaAs HPTs have an advantage over GaAlAs/GaAs, because InGaP/GaAs HPTs have superior electrical and optical performances due to their larger valence and smaller conduction band discontinuities and a high etching selectivity between InGaP and GaAs [180]. An InGaP/GaAs HPT with a responsivity of 0.6A/W and optical gain of 45dB has been demonstrated in [179].

Another material used to realize a phototransistor is InGaAs/InP [172] [189] [190]. In this phototransistor light absorption takes place at optical wavelengths equal or inferior to 1.5µm. The proportions of Ga and In in the arrangement of InGaAs materials has to be well chosen to get good lattice matching between InP and InGaAs. The material used is actually $In_{0.53}Ga_{0.47}As$. For such phototransistor an optical transition frequency of 62GHz and responsivity of 0.4A/W has been reported in [191]

1.7.2.2 Pure Silicon Phototransistors

Pure silicon bipolar phototransistors have been studied for a long time as sensors or opto-couplers and only few as high speed detectors. High speed Si phototransistors were however fabricated in a 0.35µm commercial AMS BiCMOS technology without process modifications [187]. They have studied extended base collector phototransistors with different optical window sizes. In their work, NPN transistors are directly implemented in a 0.35µm BiCMOS technology. This technology has no silicide layers. The transistors are designed with an enlarged base collector junction area which serves as a photodiode in which the photocurrent is amplified by the intrinsic transistor part of the device. It has a base node, which is used for base biasing to help speeding up the detectors response and to slightly raise responsivity. The emitter capacitance is maintained as small as possible to avoid slowing the device by making the emitter area as small as possible. The transistors are characterized over a wide optical spectral range at 410nm, 675nm, 785nm, and 850nm, providing -3dB bandwidths up to 390MHz at 410nm and responsivities of 1.76A/W at 675nm corresponding to quantum efficiencies of 359% normalized in terms of the quantum efficiency of a silicon photodiode. Another pure silicon phototransistor obtained from a standard 180 nm CMOS process technology is presented in [192]. A responsivity of 2.89 A/W at 630 kHz and DC responsivity of 6.44 A/W is achieved. Furthermore this phototransistor reaches bandwidths up to 50.7 MHz at 850 nm, 76.9 MHz at 675 nm and 60.5 MHz at 410 nm at VCE = 10 V and floating base conditions.

1.7.2.3 SiGe/Si Phototransistors

The last type of phototransistor is the SiGe heterojunction phototransistor. In 1997 SiGe/Si multiple quantum well (MQW) HPT was proposed on SOI substrate according to SIMOX process [173]. Its base is composed of several SiGe/Si multiple quantum wells that are inserted in a vertical resonant cavity which operates at 1.3um wavelength. The SiGe/Si MQW both forces the base and the absorption layer as shown in Figure 1-28. The cavity is defined by the lower SIMOX substrate and the upper Si02/Si mirror. For a SIMOX substrate based resonant cavity photodetector with 1µm absorption layer, a calculated quantum efficiency of 18% was obtained and a cutoff frequency as high as 1GHz was calculated at input optical power of 10µW.

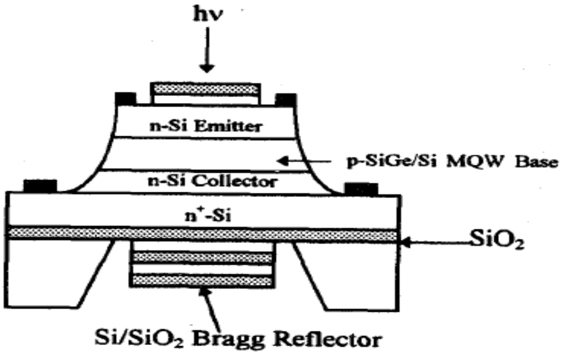

Figure 1-28: Schematic of a SiGe/Si MQW resonant cavity phototransistor using a double heterojunction [173].

In 2002, a SiGe/Si phototransistor was fabricated by placing $Si_{0.5}Ge_{0.5}$/Si multiple quantum wells (MQWs) in the base-collector region [181]. A responsivity of 1.47A/W and bandwidth of 1.25GHz at 850nm are demonstrated. In [193], the same group has been demonstrating MQW SiGe phototransistor with f_T and f_{max} of 25 GHz and an external quantum efficiency of 194%, thus a responsivity of 1.33A/W, at 850nm.

The use of MQW SiGe/Si has demonstrated a promising responsivity and high bandwidth detection at 850nm wavelength. However, this approach is not straight forward to implement in commercial SiGe-based processes and at 850nm wavelength detection, a single SiGe layer could be used as done in 2003, [182]. In that case SiGe HPTs are fully compatible with the SiGe HBT structure from commercial SiGe-based technologies. This allows monolithic integration with electronic signal processing circuits, and thus extends the existing application list of SiGe-based technologies to include opto-electric (O/E) functionalities without the addition of masks and processing steps. These microwave SiGe phototransistors provide an innovative solution for the integration of optoelectronic functions in commercial bipolar or BiCMOS process technologies, contrary to SiGe multi quantum wells structures. These devices have since been fabricated using several industrial SiGe bipolar and BiCMOS process technologies: Atmel/Telefunken [159] [161] [182] [183], TSMC [185], IBM [184] and AMS [187].

The first SiGe bipolar heterojunction phototransistor developed in a commercial available SiGe/Si technology (Atmel technologies) was presented in 2003 [182] [183]. Figure 1-29 illustrates the configuration of such a phototransistor and a photograph. This structure has a 10x10µm^2 optical window opening in the emitter through which the light penetrates. The phototransistor structure is made without any additional absorption structure and is purely based on the SiGe bipolar technology. The base profile was abrupt in shape with Ge content in range of 20 to 25%. The base doping was significantly high compared to Si HBT and typically around 10^{19}cm^{-3}. This HPT structure has a measured f_T of approximately 20 GHz. It has a lower f_T as compared to the 30GHz f_T of standard HBT devices in this process due to the enlargement of the structure to open the optical window. However it is still considerably high due to thin base and high base doping. A dc responsivity of 1.47A/W and a -3dB bandwidth of 0.4GHz were achieved at 0.94µm.

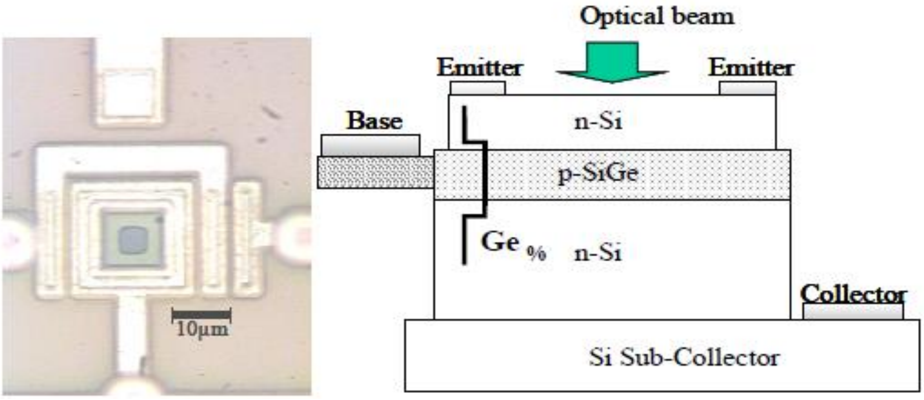

Figure 1-29: Left: Photograph of the top view of a SiGe HPT with a 10x10µm² optical window in the emitter; Right: Sketch of the vertical stack [183].

A second SiGe HPT was proposed almost simultaneously with Pie et al in [185]. It is implemented in a BiCMOS process from TSMC and exhibits a responsivity of 0.43A/W with a pass band of 3GHz. In 2004, Apsel et al [194] from Cornell University demonstrated a 0.25µm IBM BiCMOS process SiGe HPT with responsivities of 2.4A/W and 0.12A/W that were achieved under 850nm and 1060nm respectively under 2T Phototransistor operation and a bandwidth of above 500MHz for a 10x16µm^2 HPT. By modifying the commercial SiGe HBT structure in IBM 0.25µm SiGe BiCMOS process, Apsel at el [194] also implement a smaller sized 6x10µm^2 HPT. The photo detecting window was incorporated by removing silicide layers that block the optical absorption and the existing layers were manipulated. Smaller sized HPTs using the IBM BiCMOS process show that a responsivity of 2.7A/W and a cut off of 2.3GHz were measured. The optical cutoff frequencies of these devices measured from pulsed laser measurement are 2.0GHz, 2.1GHZ and 5GHz for the HPT sizes of 6x10µm^2, 5x5µm^2 and 2x2µm^2 respectively at 850nm.

Most recently at the end of 2015, a SiGe HPT fabricated by adapting the available design kit provided by CMC Microsystems with very high DC responsivity of 232A/W at 1.55µm wavelength is reported in [19].

1.7.3 Edge illuminated Phototransistor

Vertically illuminated photodetectors or HPTs are known for their ease of coupling but suffer from a trade-off between conversion efficiency and transit time limited frequency performance [195] [189] [196].

Edge-coupled devices overcome this problem by allowing the optical signal to enter through the side of the device, orthogonal to the bias field. This gives the freedom to design longer devices to ensure that a high proportion of the optical signal to be absorbed while maintaining a narrow absorption region to keep transit times low. The drawback, however, is that the device capacitance becomes significant due to the increased device area and reduced depletion layer thickness [195]. This increased capacitance gives rise to a response limited by the increased RC time constant once the device contact and load resistances are taken into account [196] [197].

1.7.4 Travelling wave phototransistors

In order to improve both the bandwidth and the conversion efficiency in a single device, topologies must move away from lumped element configurations to distributed traveling-wave structures. In 1998, it was proposed that using the transistor structure in the traveling- wave geometry would eliminate the RC limitations of the lumped devices, replacing them instead with a velocity mismatch limited response [198]. The literature is generally sparse on high-frequency characterization of traveling-wave heterojunction phototransistors (TW-HPTs); however, measured results from [198] seemed very promising, indicating a dc gain of more than 35 times that of a similar length traveling wave photodiode. While frequency response results were not presented, devices showed no saturation up to a dc photocurrent of 50 mA at 60 GHz, indicating the potential for the use of such devices in high-power applications.

In [199] the set of classical drift-diffusion device equations has been applied to fully distributed travelling-wave heterojunction phototransistor structures (TW-HPTs). In this publication a full physical model has been shown for the first time indicating that the potential RC limitations still exist for transistor in the traveling-wave regime.

Table 1-3 presents the summary of the performances of HPTs fabricated from different material type. Their performance in terms of responsivity, optical transition frequency, optical gain and external efficiency are presented. The operating wavelength, base thickness, doping level, optical window size and HPT structure are also summarized in the same table.

Table 1-3: Summary of state of the art of HPTs

Reference	year	type	material	Wb[A]	doping base[cm^{-3}]	Wc[A]	optical window[μm^2]	λ[µm]	illumination	β current gain	ft [GHz]	fmax[GHz]	R[A/W]	Gopt[dB]	ft_opt[GHz]	ηext
[200]	2004		InP-InGaAS					1,55		x	x	x	x	7,5	x	x
[191]	1999		InP-InGaAS	600	3,00E+19	5000	5x6	1,55		42	71	x	0,4	35	62	x
[182]	2003		Si-SiGe	x	1,10E+19	x	10x10	0,94		x	18.9@1.5V and 20.4@2.5V	x	1.49 [HPT]	3,46	x	x
[201]			Si-SiGe	300	x	x	10x10	1,17	latteral	5	x	x	x	30	x	x
[161]	2011		Si-SiGe				10x10	0,85		x	39	x	1.8 [HPT]		x	
[179]	2005		InGaP-GaAs	1400	4,00E+19	6000	x	0,85		x	x	x	0,64	45	x	Assumed 100%
[180]	2010		InGaP-GaAs	800	4,00E+19	8000	50x50	0,635					0,34	120,5		
[185]	2004		Si-SiGe					0,85		100			0,43			
[202]	2009	UTC-HPT	InP-InGaAS	2200	2e+18 , 1e+18 , 5e+18	4600	5x5	1,55					0,2	37	52	
[202]	2009	UTC-HPT	InP-InGaAS	2200	2e+18 , 1e+18 , 5e+18	4600	10x10	1,55					0,2	29	36	
[177]	2005	2T-HPT	InGaP-GaAs	1400	4,00E+19	6000		0,85		33				28,4		
[162]	2005	3T-HPT	InGaP-GaAs	1400	4,00E+19	6000		0,85						34		
[189]	1999	edge coupled HPT	InP-InGaAS	500	1,00E+19	4000		1,55	edge		43		100 [HPT]	400 @length=1µm		
[190]	2011	UTC-HPT	InP-InGaAS				52x52	1,55								
[203]	2005	2T-HPT	InP-InGaAS	500	3,50E+19	8000		1,55		25			0,2	20		
[204]	2008	APD-HPT	InP-InGaAS-(InAlAs charge layer	700	5,00E+17	25000		1,55					460000 [HPT+APD]	5,50E+05		66%
[159]	2012		Si-SiGe				20x20	0,85		451,8			3.53 [HPT]			
[181]	2003	MQW-HPT	Si-SiGe	600	5,00E+18		14,4	0,85		200	25	25	0.026 (1.3 in HPT)			194%
[205]			Si-SiGe				10x10	0,94					0.014 (1.5 HPT)	94	x	
[205]			Si-SiGe				10x10	1,17	latteral				0.04[HPT]	134	x	

1.8 Silicon-based Optical Modulators

The development of large bandwidth external modulators has also seen intense investigation over the past two decades. For their practical application in MWP systems, it is imperative that these devices feature the characteristics of broad bandwidth, low drive voltages, good linearity, bias stability, high optical power-handling ability and low optical insertion loss. To give the required electro–optic effect in an external modulator, materials such as lithium niobate, semiconductors or polymers can be used, and travelling-wave interferometric structures are generally used to achieve a broad frequency response.

Several research works have been carried out successfully on various Si Mach-Zehnder Modulator (MZM) [210] [211], ring modulator [207]-[209], slow wave modulator [212].

Silicon Push-Pull and traveling wave MZM compatible to CMOS integration were compared in [210] and they demonstrated the advantage of traveling modulator over push-pull in terms of bandwidth and power penalty. Figure 1-30 shows both structures.

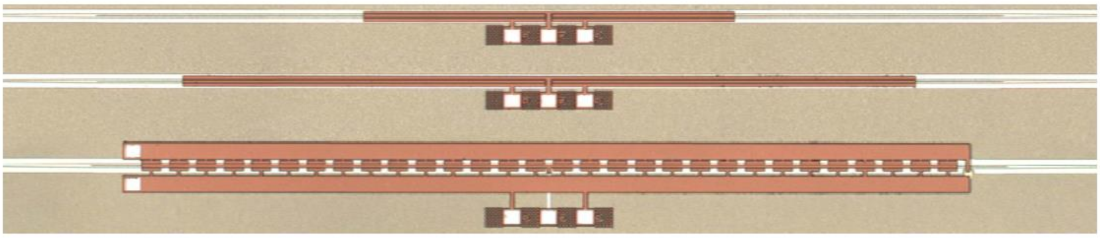

Figure 1-30: The three MZMs under test; from top to bottom the 1000-µm Push-Pull MZM, the 2000-µm Push-Pull MZM, and the 1500-µm segmented TW electrode MZM with a built-in 50Ω termination on the TWE. The TW device is self-terminated with an n+ resistor (far right of device)[210].

Furthermore, a new silicon depletion-mode vertical p-n junction phase-modulator was implemented in Mach–Zehnder modulator configuration as presented in [211], enabling an ultra-low $V_\pi L$ (π phase shift achieved with reverse bias voltage V and device length L product) of only ∼1V·cm. Further, in a 500-µm-long lumped elements device, they demonstrate a 10-Gb/s non return-to-zero data transmission with wide- open complementary output eye diagrams.

Ge/SiGe QW modulators integrated on SOI waveguide with promising performances were demonstrated in [213]. Recently, a waveguide integrated Ge electro absorption modulator operating at 1615nm wavelength with 3dB bandwidth of beyond 50GHz is reported in [214] as the structure shown in Figure 1-31. In this modulator a 2V swing enables 4.6dB DC extinction ratio for 4.1dB insertion loss.

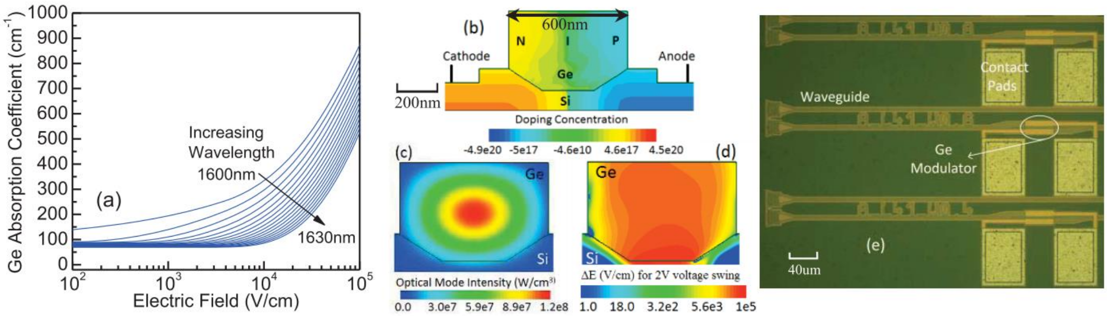

Figure 1-31: a) Modeled absorption coefficient vs applied electric field, b) Schematic of the EAM p-i-n diode, c) Approximated optical flied distribution showing good confinement in Ge, d) Change in electric field between ON and OFF state, e) Microscope image of the fabricated modulators integrated with Si waveguides and grating couplers [214].

Organic polymers have several attractive features for integrated optical applications and can be made electro–optic using high temperature poling methods. Several broadband electro–optic polymer based ring modulators have been developed [206] [207]. For ring modulators, an error free modulated signal transmission with a bandwidth of 25 Gbps has been reported with 1-V peak-to peak drive voltage [208]. Low efficiency, and low-power handling performance, and the linearity of ring modulators were reported in [209]. As demonstrated, for low-dynamic-range applications, silicon ring modulators offer a compact solution. Figure 1-32 shows an example of CMOS compatible ring modulator where a) illustrates the cross section of the pn junction and b) illustrates the schematic of the ring modulator design with n-doping at the center and surrounded by p-doping.

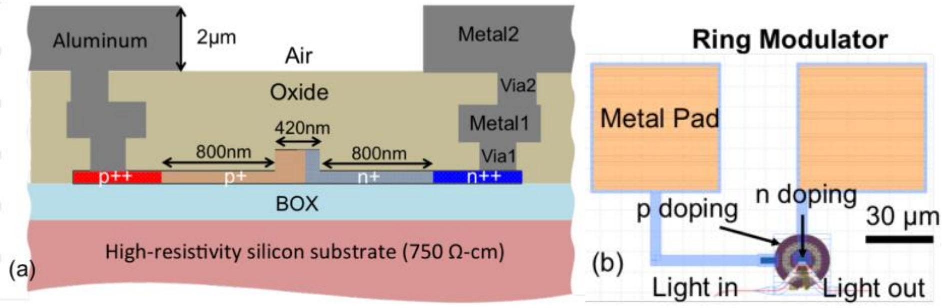

Figure 1-32: a) Schematic cross sectional diagram of ring modulator, b) Micrograph of the ring modulator [209].

1.9 Conclusion

In this chapter, we have presented the evolution on the broadband home area wireless network towards multiGbit/s data communication taking into consideration the increase of wireless devices, emerging of new services and the service quality. 60 GHz band Wi-Fi systems are intended to be massively introduced in the coming years, keeping the compatibility with the current 2.4 and 5 GHz Wi-Fi solutions. Such radio networks offer the ability to provide truly broadband services to users by utilizing the enormous bandwidth available in a number of these frequency bands. To leverage the low distance range of the 60GHz propagation, the RoF technology is a suitable solution. The different architectures and schemes within RoF systems were then discussed. Such RoF architectures should respect the constraint of ultra-low-cost as their integration gets closer and closer to the consumer. It requires then to develop some novel very low-cost high-speed OE/EO components with improved performances. The main direction for it is intended to be 850nm for the low cost nature of its optical sources, and the Silicon-based integration.

The chapter then reviewed the state-of-the-art in electrical and optical interconnects, to reach intra- and inter-chip interconnections at RF and millimetric waves, optical sources, photodetectors and modulators, with a clear focus on Silicon-based solution, but also the experience from other material in the device optimizations.

Polymer base waveguides for on-chip optical and electrical interconnections are emerging nowadays as it allows multistep fabrication process whereby it is possible to first optimize the processing of the semiconductor devices and then fabricate the polymer waveguide structures for the optical or electrical signal distribution system We have got an indication that fabricating a coplanar line on 2Ω.cm silicon substrate and 25µm SU8 polymer interface could achieve minimum attenuation at 60GHz frequency of 4mm/dB or on 10Ω.cm silicon substrate and 10µm BCB dielectric interface could achieve an attenuation of 0.6dB/mm at 50GHz.

Optical sources from III-V materials and from Silicon are summarized. Form this investigation, in recent years, the shorter wavelength optical sources and low cost Si LEDs with a potential to be integrated into CMOS based optical interconnect on a single chip become a center of a big interest.

The trade-off between bandwidth and responsivity of photodetector has also been presented. Hence various photodetectors from PIN to traveling wave structures are revised. An InGaAs/InP photodiode (in a travelling wave structure) having a bandwidth up to 210GHz, however with very low coupling coefficient, is shown to be the record up to now.

We have also revised the state of the art of Heterojunction bipolar Photo-Transistors (HPT) in terms of technology and structure. Various laboratories developed SiGe HPT by using BiCMOS technologies. The HPT realized from IBM technology achieves a maximum cutoff frequency up to 5GHz, according to through pulsed response measurement, and up to 0.4GHz, according to continuous wave opto-microwave (OM) measurement. As we believe OM measurement is the right way to characterize the opto-microwave devices, all experimental results presented in this thesis are based on OM measurement technique.

Silicon-based external modulators are also emerging in these days. Si modulator based on ring structure achieving an error free modulated signal transmission with a bandwidth of 25 Gbps has been reported with 1 V peak-to-peak drive voltage.

In general, to develop high speed RoF system at low cost, complete optical transceivers based on Si technology only, detectors, modulators included, are a clear and well developed strategy as various research groups are working on it. Developing high speed Silicon-based opto-electric devices and its further integration with mainstream Si technologies, without adding further step, is still one challenge which has not been yet covered thoroughly at short wavelength such as 850nm. Another main obstacle toward a real full silicon optical transceiver system is obviously as well the efficiency and bandwidth limitation of the Si sources. Hence integrating VCSEL technology as an optical source into low cost Silicon-based system could be a promising solution for which developing further high speed optical and electrical interconnections from chip-to-chip and intra-chip is important.

Chapter 2 SiGe/Si HPT Technology, Opto-microwave characterization and de-embedding techniques

2.1 Introduction

This chapter aims at preparing the steps of characterization and analysis of SiGe HPTs, opto-microwave (OM) devices in general. Before describing the specific OM measurement techniques that are employed, this chapter introduces the SiGe HPT samples under study and their technology.

The second section, then, gives an overview of the 80GHz SiGe bipolar technology (SiGe HBT) from Telefunken GmbH. The phototransistors we studied are essentially modified versions of SiGe HBT. The HPT structure and its various design methods are presented.

The third section starts by defining the OM characterization parameters of the HPT (such as opto-microwave gain, cutoff frequency, optical transition frequency and optical gain). Then the opto-microwave measurement bench setups for top and edge illuminated HPTs are presented. Information about the OM calibration and de-embedding techniques are also provided in this section

The fourth section focuses on the isolation of the intrinsic behavior of SiGe HPT. We observe the existence of the substrate photodiode photocurrent in SiGe HPT experimentally and then we validate this observation through physical model. The method of photocurrent computation in each region of the phototransistor is then presented. The impact of the frequency response of the substrate photodiode on intrinsic behavior of SiGe HPT is shown. The technique to de-embed the frequency response of the substrate and the model to extract the coupling coefficient is also demonstrated in this section.

In the last section, the method of extracting the intrinsic capacitance and transit time of the phototransistor is presented.

2.2 SiGe HPT Technology and structure under study

2.2.1 SiGe HPT Technology

This work is based on the HPTs that are fabricated using a Telefunken GmbH SiGe Bipolar technological process [161] [159] [168]. One key aspect of this research is to implement an HPT in such a commercial technology without the addition of masks and processing steps. We only modify layout geometries in order to create an optical window opening. This approach ensures a straight compatibility with SiGe circuits on the same chip, and makes the SiGe HPTs directly integrated into an industrial foundry.

The Telefunken SiGe2-RF Bipolar Silicon Germanium process technology exhibits f_T up to 80GHz and f_{max} up to 90GHz. This makes this technology able to provide circuits working above 10GHz and potentially up to 60 GHz in some configurations [234]. This RF bipolar technology allows the production of wafers with applications in high-speed cellular, high-speed networking, wireless LAN and high performance standard RF devices used in various applications [230]-[234].

As in the previous SiGe1RF technology of Telefunken used in [225] to create the first SiGe HPT from the team [182] [183] [225] [260], the Germanium content is high with values in the range of 20-25% and might be almost flat across the base. This process is a 0.8µm lithography double polysilicon heterojunction bipolar technology. The minimum emitter size on the layout is of 0.8x1.4µm^2 for vertical NPN HBT transistors which provides actual size after processing of 0.5x1.1µm^2 due to lateral spacers. This technology leads to two transistor types: one with a selectively implanted collector (SIC) NPN HBT and the other one without. The difference between them is the additional mask required by the SIC-transistor, influencing the high frequency performances and static characteristics. This option allows transition frequency (f_T) to reach the 80GHz value for SIC transistors, against only 50GHz for non-SIC transistor, with f_{max} of up to 90GHz in both cases. This process technology also offers PNP transistors, diodes (PN, Zener, ESD, Varactor and Schottky) and passive devices such as inductors capacitors and resistors.

In the frame of our relation with Telefunken, a Non-Disclosure Agreement (NDA) has been signed and no information about the detailed process cross-section can be given. It is however important to give the general scheme of the cross-section of the HBT as in Figure 2-1.

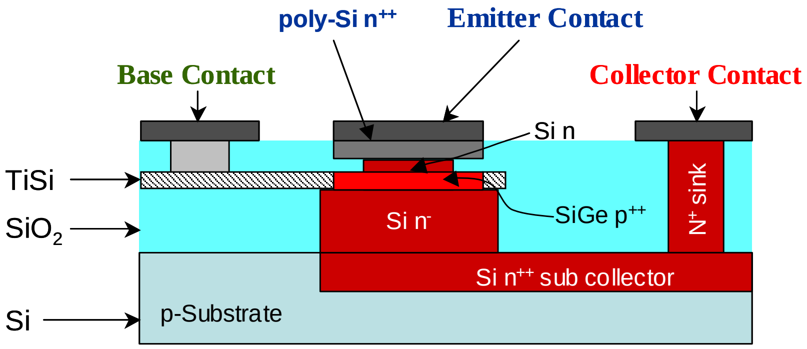

Figure 2-1:– Schematic cross-section of SiGe2RF technology from Telefunken

2.2.2 HPT structure, design variations and nomenclature

The design of the HPT using the SiGe2RF process involves the different material layers that are available to define a standard HBT using this technology. To ensure compatibility with Telefunken technological process, there are no new material layers and/or processing masks added. The HPT's are designed using the available masks and layers and are based on a common emitter base (CEB) type non-SIC HBT with a cross section as shown in Figure 2-1. The HBT structure is mostly enlarged, with the emitter contact limited to its original size, thus creating an optical window opening for a vertical illumination. The emitter contact is 1.5µm in width, while the full width of the metal above is 2.2µm. Phototransistors are designed according to two main structures named extended base-collector and extended base-emitter-collector structures. Each structure is thereby implemented into different HPT structures with the target of reducing the optical losses at the injection of light into active layers. These structures have been fabricated by Marc Rosales during his PhD [202].

2.2.2.1 Extended base-collector (xBC) Structure

The base and underneath collector region are extended to open an optical window at their top. Emitter is kept unchanged and ensures the transistor effect on the side of the HPT only (under the emitter). This way, the light is injected through the contact silicided polysilicon (TiSi) of the base into the vertical epilayers of the base and collector, as shown in Figure 2-2. TiSi reduces the base resistance but also introduces additional optical absorption and reflection losses [235].

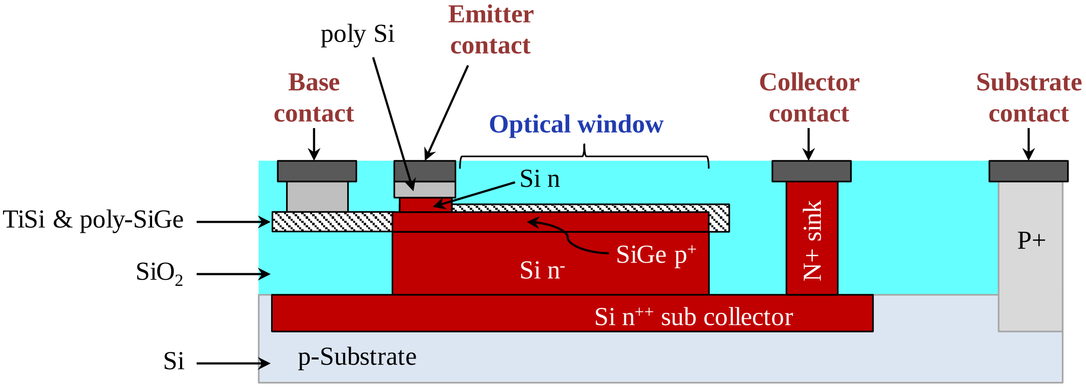

Figure 2-2 : Simplified schematic cross section of an extended Base Collector HPT (xBC)

Different variations around this HPT structures were designed to minimize the optical losses in the optical signal, coming eventually from the silicidation of poly Silicon or from the above oxide layers:

- xBC structure: This extended base-collector structure is the core of following structures.
- xBC_rT structure (removed Titanium): Silicidation process is blocked out, using an existing mask level. Therefore only polysilicon is on the top of the structure. There is no TiSi neither absorbing nor reflecting light. The removal of silicided titanium (TiSi) improves the low frequency responsivity by a factor of 5.7 and the current gain slightly decreases from 305 to 292 according to Marc Rosales PhD work [161] [235].
- xBC_eO structure: To improve the optical penetration, the superficial oxide layers at the defined optical window are removed by using a RIE step available in the process design kit for pads definition. The etching of the oxide layer provides the needed vertical stack variation to improve the low frequency responsivity by a factor of 6.7 [235].

2.2.2.2 Extended emitter-base-collector (xEBC) Structure

The second HPT structure type is designed by extending the emitter, base and collector all together. The optical opening is made through the emitter. The light goes through the oxide and polysilicon of the emitter before entering the device. This HPT is essentially one large HBT whose emitter metallization is kept limited to the edge of the device.

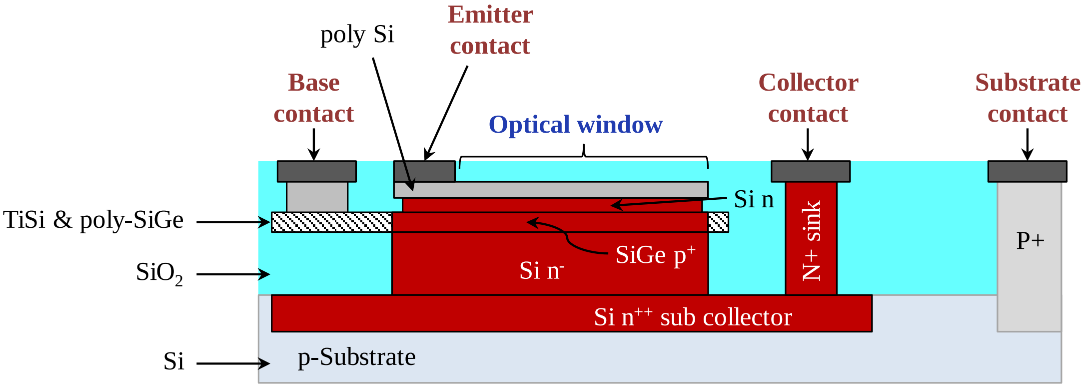

Figure 2-3 : Simplified schematic cross section of an extended Emitter Base Collector HPT (xEBC)

One variant with a reduced thickness of oxide layers on the top was fabricated to evaluate optical losses:

1. xEBC structure.
2. xEBC_eO structure: oxide layers above at the defined optical window are etched out. The oxide etching improves the optical response by 2dB [235].

Different structures were implemented in the three prototyping runs during the work of Marc Rosales. To keep the reference of the wafer lot and the design variations, we use and remind his HPT name labelling [235]:

<Prototype Run Number>-<Optical Window Size><optical window type><xBC or xEBC><extras><extras>

Reference code for HPT description is built as follows:

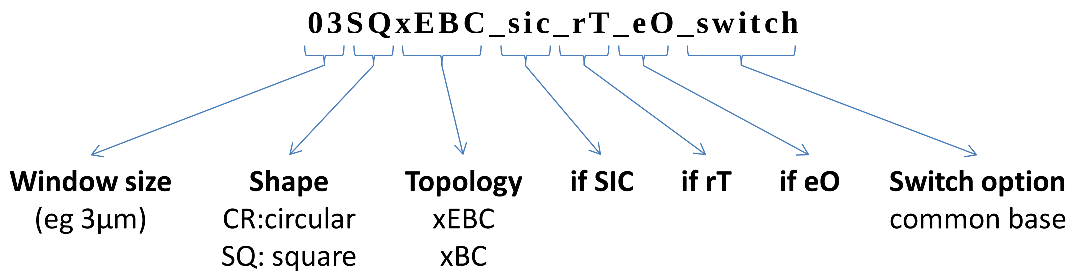

R1, R2, R3 code can be added before, to specify the run number of HPT devices.

Prototype Run Number	R1, R2, R3
Optical Window Size	03 = 3 µm x 3 µm 05 = 5 µm x 5 µm 10 = 10 µm x 10 µm 20 = 20 µm x 20 µm 30 = 30 µm x 30 µm 40 = 40 µm x 40 µm 50 = 50 µm x 50 µm
Optical Window Type	xBC = extended Base Collector xEBC = extended Emitter Base Collector
Optical Window Shape	SQ = Square CR = circular, applicable to xEBC type only
Extras	rT = removed Titanium, applicable only to xBC type eO = etched oxide sic = if the collector uses SIC.

For example, R1_10SQxBCrTeO corresponds to Prototype Run 1, with square optical window size of 10x10µm^2, extended base and collector, removed titanium and etched oxide. R2_50SQxEBC_eO corresponds to Prototype Run 2, with square optical window size of 50x50µm^2, extended emitter, base and collector, and etched oxide.

In his thesis [235], Marc Rosales focused on the validation and identification of the best structure in terms of dc biasing and opto-microwave responses. He validated that extended emitter-base-collector *(xEBC)* HPT structures on prototype run 2 shows better performance by 11dB in terms of opto-microwave gain and the cutoff frequency is improved by a 30% ratio (for both oxide etched and non-etched) when compared to extended base collector (xBC) structure. Therefore, in this thesis, we will focus on xEBC structures only for further experimental studies. It will correspond to the samples R2_03SQxEBC (3x3µm^2), R2_05SQxEBC (5x5µm^2), R2_10SQxEBC (10x10µm^2) and R2_50SQxEBC (50x50µm^2). The test results are reported in chapter 3. We have also designed an edge illuminated structure based on the same technology. The experimental results of such structure are presented in chapter 5. In the present chapter we deal with tools that are used for opto-microwave characterization of the HPTs and different approaches (physical and technical approaches) to deeply understand the behavior of SiGe/Si HPTs.

2.3 Opto-Microwave Characterization

2.3.1 Optical Microwave characteristics of phototransistor

This section is focused on the definition of parameters that characterize the phototransistor behavior as shown in Figure 2-4. This curve is extracted from S-parameter measurement of the opto-microwave link. From this figure we can extract the opto-microwave gain both in photodiode ($G_{OM,PD\ mode}$) and in phototransistor mode ($G_{OM,HPT\ mode}$), the cutoff frequency ($f_{-3dB,OM}$) and the optical transition frequency ($f_{T,opt}$). The photodiode mode is obtained by setting the base-emitter biasing dc voltage to zero, whereas the phototransistor mode is obtained by setting appropriate voltage biasing at the base-emitter contact (typically above 0.6V to activate the transistor effect).

First of all let's define the opto-microwave gain (G_{OM}). The opto-microwave gain represents the ratio of the HPT output signal power ($P_{out\text{-}hpt}$) to the output power of a photodiode with a 1A/W responsivity and loaded by 50Ω ($P_{1A/W\text{-}photodiode\text{-}over\text{-}50\Omega}$) [182] [200] [225] as presented in equation(2.1). This is of particular use as it is equal to the square of the responsivity (i.e., same value in dB) under a 50Ω loading condition. This provides an effective means of evaluating the efficiency of matching networks compared to a 50Ω loading network as reference case.

$$G_{OM} = \frac{P_{out-hpt}}{P_{1A/W-photodiode-over-50\Omega}} \tag{2.1}$$

If loaded with 50 Ohms, then it comes:

$$G_{OM}(f) = \frac{\frac{1}{2}.R_0.I_c^{\ 2}}{\frac{1}{2}.R_0.P_{opt}^{\ 2}} = R_{hpt}^{\ 2} \tag{2.2}$$

$$G_{OM}\,|_{dB} = R_{hpt}\,|_{dB} \tag{2.3}$$

Where R_{hpt} is the responsivity of the phototransistor, P_{opt} is the illumination optical power considered as equivalent to a current and I_C is the collector current.

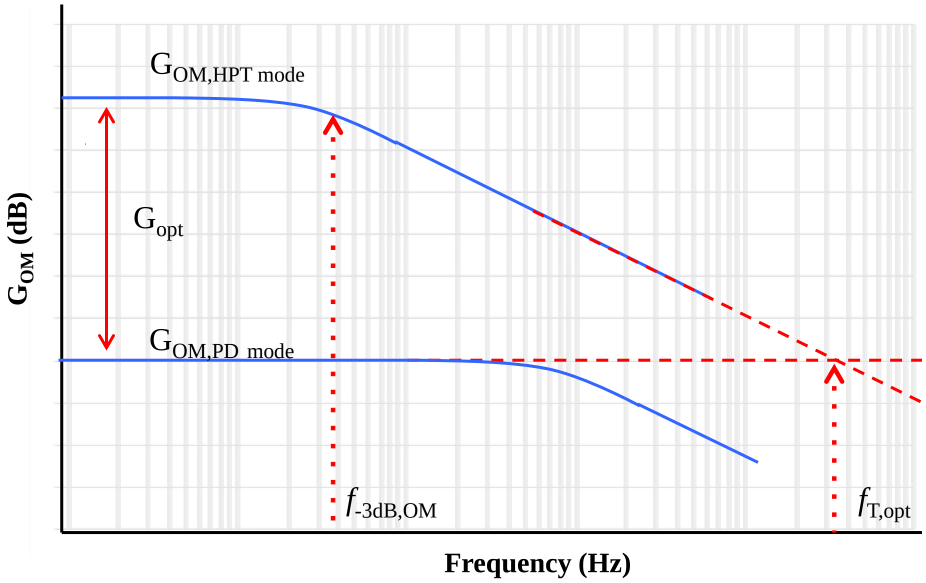

Figure 2-4: Typical phototransistor characteristics and definition of opto-microwave parameters.

The opto-microwave S-parameters are an extension into the opto-microwave domain of the scattering parameters as defined in the microwave domain [200] [225]. We can consider a phototransistor as a 3-ports device, whose accesses are labelled 1, 2 and 3, where 1 represents the base access, 2 is the optical access and 3 is the collector access as shown in Figure 2-5 a). The extension relies on the modeling of the optical port as an electrical port whose input impedance is 50Ω as shown in Figure 2-5 b). A current of the same amplitude as the modulated optical power models the optical signal. It can be considered as if the signal were detected by a virtual 1 A/W photodiode before entering the internal phototransistor. Both the amplitude and phase information and power waves theory can be transposed [200] [225]. This approach is the origin of the opto-microwave power gain definition [225] and the opto-microwave noise figure definition [10].

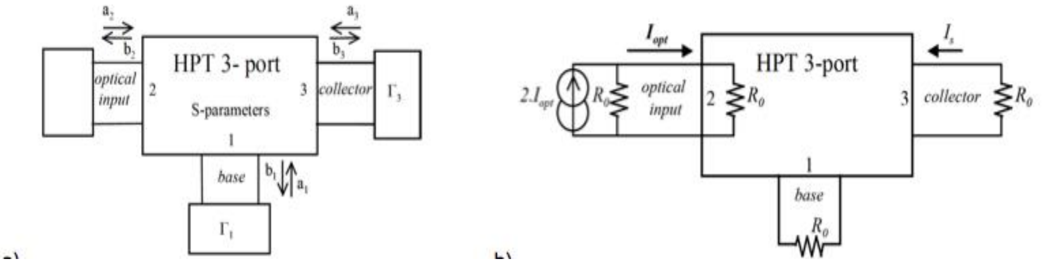

a) b)

Figure 2-5: a) Three ports schematic representation of the HPT; b) definition of the equivalent optical input port [225]

According to [200] [225], the opto-microwave gain of such a three-ports HPT can then be written as:

$$G_{OM} = G_1.G_0.G_2 = \left|\frac{1-M.\Gamma_1}{1-S_{11}.\Gamma_1}\right|^2 .\left|S_{32}\right|^2 .\frac{1-\left|\Gamma_3\right|^2}{\left|1-sp_3.\Gamma_3\right|^2} \qquad (2.4)$$

Where Γ_1 and Γ_3 are respectively the base and collector load reflection coefficients, and where M and sp_3 are given below:

$$M = S_{11} - S_{31}.\frac{S_{12}}{S_{32}} \qquad (2.5)$$

$$sp_3 = S_{33}.\frac{1-\left(S_{11}-S_{31}.\frac{S_{13}}{S_{33}}\right).\Gamma_1}{1-S_{11}.\Gamma_1} \qquad (2.6)$$

G_0 is the main transfer characteristic while G_1 is a pure Γ_1 function that describes the influence of the base load impedance on the G_{OM}. G_2 shows the influence of the collector load impedance. It is lightly influenced by Γ_1 but this dependency could be neglected.

All S-parameters are measured by using the bench setup described in section 2.3.2. The opto-microwave gain of the HPTs of various optical window sizes as a function of the frequency could then be plotted as shown in Figure 2-4 for both photodiode and phototransistor modes. From such experimental results another characteristic of phototransistors called optical gain G_{opt} can also be extracted. It is defined as the difference between the HPT G_{OM} (in dB) as a function of the frequency and the PD mode G_{OM} (in dB) at low frequency, all measured under 50Ohms load conditions. It is the current gain enhancement between the HPT and PD modes of operation (the internal gain of the phototransistor due to its amplification effect).

From this opto-microwave characteristic curve we can also extract the opto-microwave dynamic behavior of the phototransistor through the cutoff frequency in PD and HPT modes and through the optical transition frequency. The opto-microwave cutoff frequency ($f_{-3dB,OM}$) is the frequency at which the opto-microwave gain drops by 3dB from its dc response.

The optical transition frequency $f_{T\ opt}$ is the frequency at which the optical gain is unity or zero in dB. This sets the limit for the use of phototransistor as a photocurrent amplifier. It can also be seen as the frequency for which the responsivity of the phototransistor in phototransistor mode is equal to the low frequency responsivity in photodiode mode, which means that there is no more amplification. Figure 2-4 shows the graphical representations of the $f_{T\ opt}$ and $f_{-3dB,OM}$.

The optical transition frequency can also be related to the cutoff frequency, PD and HPT mode responsivities (R_{pd} and R_{hpt} respectively) through equation(2.7) assuming a 20dB/decade slope after the 3dB cutoff frequency. This provides a guideline for further design rules. Actually we can also extract the cutoff frequency and optical frequency independently on the opto-microwave gain as indicated in Figure 2-4.

$$R_{pd} \cdot f_{T,opt} = R_{hpt} \cdot f_{-3dB,OM} \tag{2.7}$$

2.3.2 Opto-Microwave Measurement Bench Setup

The test bench set up as in Figure 2-6 is used in order to measure the opto-microwave performances of top and edge illuminated HPTs. Port 1 of the Vector Network Analyzer (VNA) directly modulates a 10Gbps 850nm Vertical Cavity Surface Emitting Laser (VCSEL) from Philips ULM photonics. The direct modulated optical signal is connected to a 90/10 optical splitter. The 10% output of the coupler is continuously monitored to ensure the system is properly connected. This is also used to compute the optical power that is inserted to the optical probe. The 90% output of the coupler is injected into the phototransistor through a focusing lensed fiber vertically placed above the HPT optical window. The optical probe is mounted on a nano-positioner so as to have precise movements in the three axes and to optimize optical coupling ratio to the HPT. With the aid of 45° mirror we can observe and control the height of the optical probe above the optical windows of the HPT through the microscope. The optical probe has a lensed fiber assumed to generate a Gaussian profile optical beam. The base of the HPT is connected to a GSG probe. The base is biased using a bias tee with a 50Ω load attached to the RF input of the bias tee. Port 2 of the VNA is linked to the collector access of the HPT to bias the transistor and collect the output signal. The VNA used for the experiment is an 8753ES 40GHz VNA and it is connected to an Agilent B1500 semiconductor parametric analyzer.

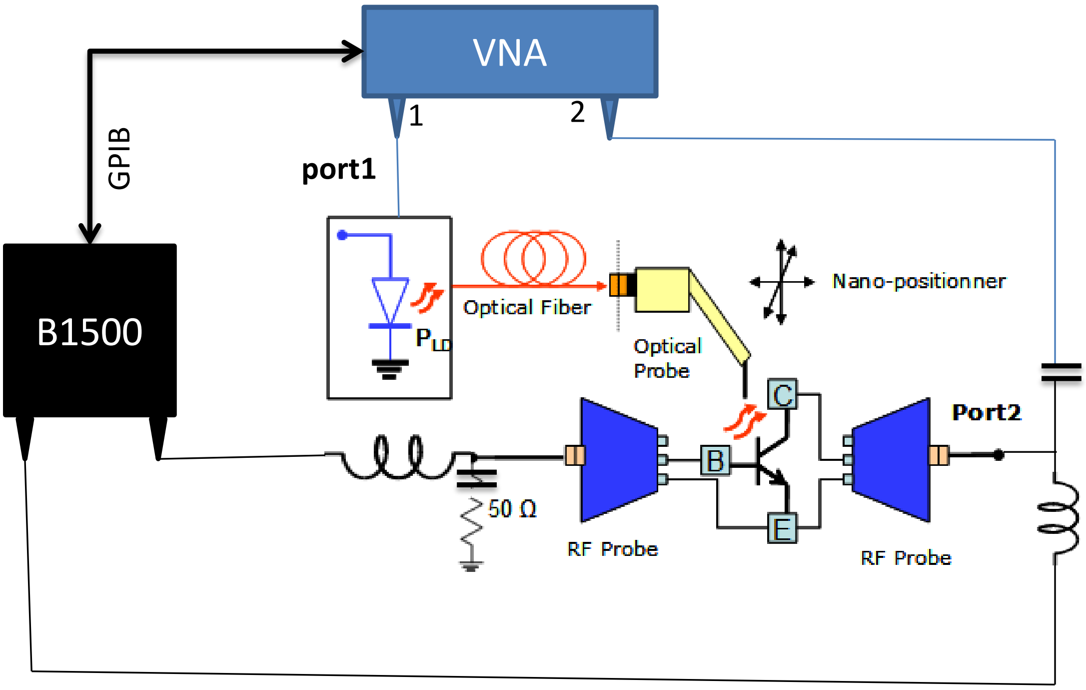

Figure 2-6: Opto-Microwave characterization bench setup

Figure 2-7 shows the photographs of the opto-microwave measurement of the R2-10SQxEBC HPT. The GSG probes are on the GSG pads and the optical probe is positioned at the top of the HPT. The center location of the HPT optical window is determined by scanning the optical probe along X and Z axes in the vicinity of the optical window. The location corresponding to the highest measured base current for the HPT operation is considered as the center of the HPT optical window.

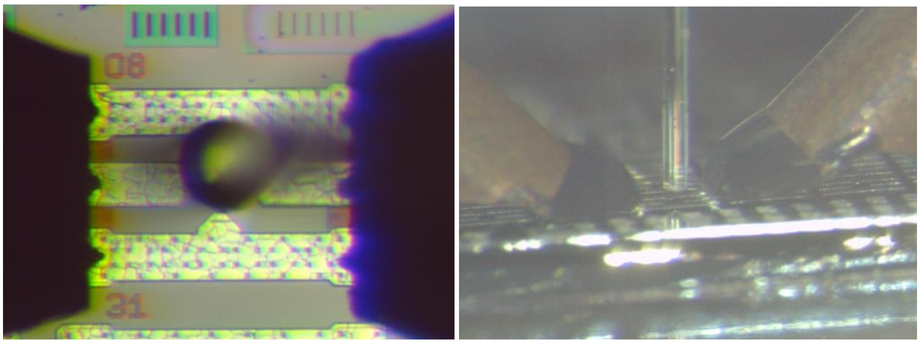

Figure 2-7: Optical probe at the top of HPT structure

Figure 2-8 shows the photographs of the bench setup with the required fiber mounting modifications to characterize edge illuminated HPTs. All the connections, except the axis of light injection, are similar to the bench setup described above. To inject light on the side, we use a horizontal optical probe supporter to point the optical probe on the side as shown in Figure 2-8 a). To control the position of illumination we attach the optical probe with the nano-positioner, so that we can move the fiber in a well-controlled way. Figure 2-8 b) shows the microscopic picture of the device under test along with the optical fiber on the side. From this view we can control the movement of the fiber along x and z axes. In the same picture we can clearly observe the base and collector contacts through RF probe. Figure 2-8 c) is a microscopic picture taken through a 45 degree mirror. By using this view we can control the movement of the optical probe along y axis.

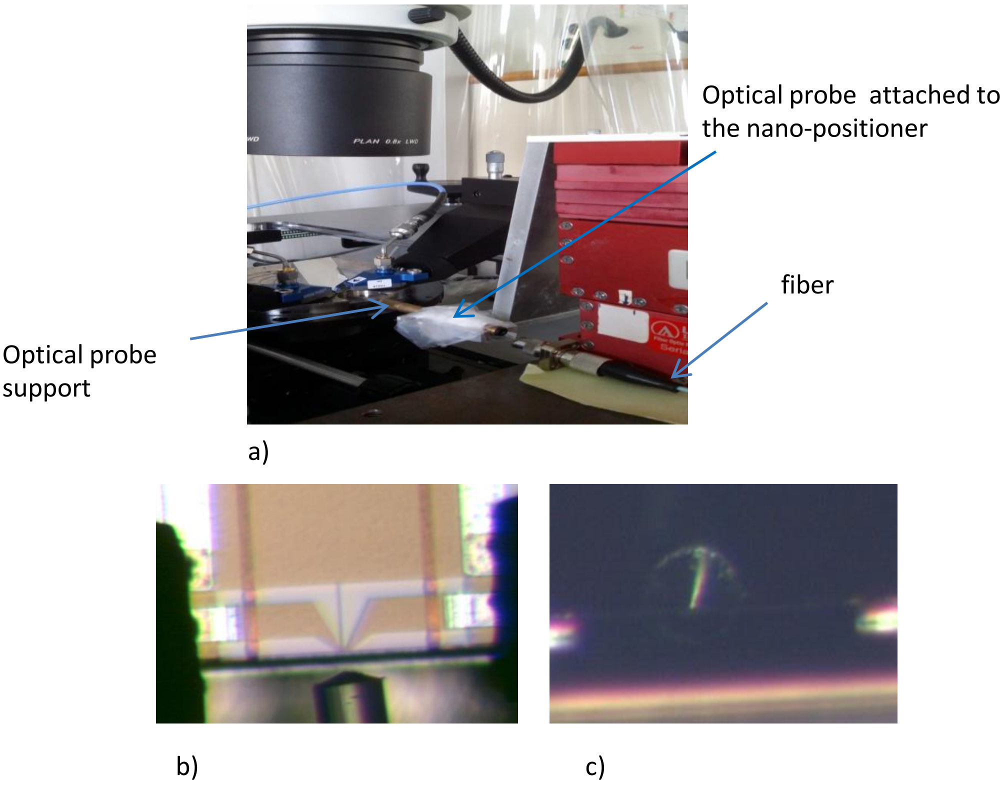

Figure 2-8: Experimental bench setup of edge illuminated HPTs. a) photograph of the bench. b) Top view microscopic picture of the device under test and the optical probe pointing on the edge side of the HPT. c) Microscopic picture taken from 45^o mirror.

It is then important to note that the measurement of the HPT is actually the measurement of the link composed of the laser, the injection fiber, the electrical connectors and the phototransistor. To characterize only the HPT, it is necessary to overcome the losses and phase shifts introduced by the test link. It is therefore necessary to correct mathematically the errors from the actual behavior of devices under test. Thus, the measurement is carried out in two steps, firstly with a reference photodetector, then with the phototransistor under test.

2.3.3 Calibration and De-embedding Techniques

The purpose of this part is to demonstrate how to extract the HPT characteristics from the test link, through hybrid calibration techniques. The implementation of one of the extraction techniques known as “T matrix” [172] will be detailed for the electrical error correction. Then the opto-microwave calibration itself will be described. Finally the test fixture de-embedding technique will be presented.

When an optical signal is introduced, we can define the opto-microwave S-parameters, and calibrations then become hybrid, using opto-microwave quantities described in section 2.3.1. It is therefore necessary to develop new calibration procedures. The problem with this kind of calibration is that the chain of elements at the input port is compatible with a coaxial cable of Type K, while the output port is in the form of a coplanar line access only compatible with a GSG probe. It is thus not possible to use a conventional SOLT calibration since the loads used for calibration (Open, short, load and Thru) cannot be connected to both ports simultaneously. Thus a proper calibration technique with a precise de-embedding technique has to be implemented.

At this point, it is necessary to define the measurement planes as shown in Figure 2-9. This shows the measurement plane where we can connect the input and the output ports simultaneously through the K-connector for microwave calibration. The device under test is then made of the laser, the optical channel offset (optical fiber, splitter and optical probe), the phototransistor and port 2 GSG RF probe.

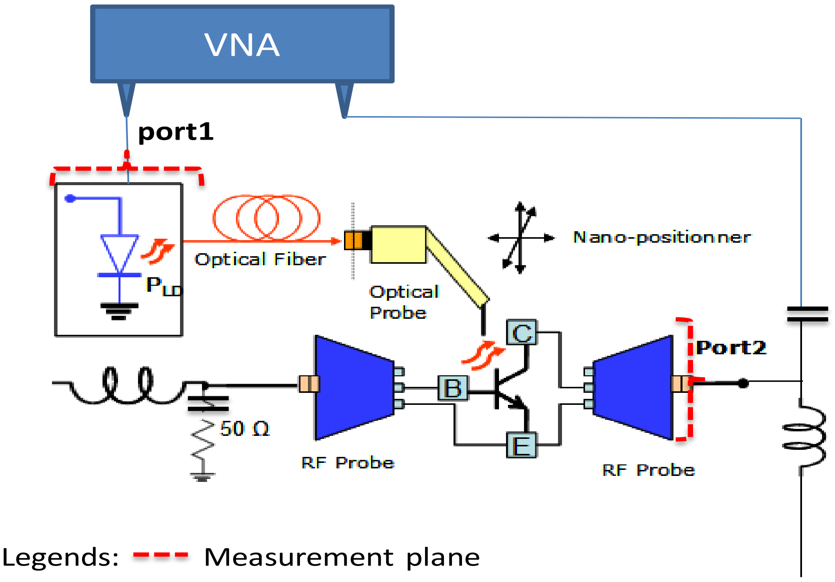

Figure 2-9 : Defining the opto-microwave measurement planes. The device under test in the link includes 850nm VCSEL, optical fiber, optical probe, the phototransistor and port 2 RF probe.

Thus, to perform this type of calibration, there are several techniques:

- The adapter removal calibration technique is described in the reference [236]. This technique is applied to study the DUT composed of the laser, fiber and HPT, which is an insertable device with K connector at the input and GSG pads at the output.
- The ghost removal technique [190] also sets the DUT to consist of the laser, fiber and HPT. The HPT under study has GSG pads as connectors for its base and another set of GSG pads for its collector. The first step for this technique involves setting up the measurement bench for full two-port on-wafer calibration and performing this calibration. This moves the measurement plane up to the tips of the GSG probe. Step two involves physically disconnecting the port 1 of the VNA that was connected to one of the GSG probes and keeping the port 2 of the VNA connected to the other GSG probe. In the third step, one connects the port 1 of the VNA to the laser and land the GSG probe on the GSG pad which is connected to the collector of the HPT. Measurements of the DUT are done on this step. These measurements include the effects of ghost parameters due to the change of measurement setup immediately after a calibration procedure. In the last step the connector is physically disconnected from

the laser input and one port measurements are performed with the Short, Open and Load standards of the calibration kit. The post processing is done in two steps. Step one permits to extract the ghost parameters and step two to extract the HPT parameters.

- In the T-matrix technique [190], the DUT is composed of the laser, fiber, HPT and GSG probe. In this configuration, the input and output ports are both K connectors. In the first step a full 2-port calibration is performed using the K SOLT calibration standards. At this step, the system is ready to perform measurements on the DUT. In the final step the GSG probes are connected and one performs Short, Open, Load and Thru measurements using the GSG probe calibration kit. The post processing is done in two steps. Step one permits to extract the GSG probes characteristics and step two to extract the HPT parameters.

The third technique, the “T matrix” technique, will be preferred here because it is proved to be easier to implement in measurements than the previous two techniques.

2.3.3.1 Implementation of “T matrix” Technique

The link corresponding to the DUT is composed of the laser, the optical channel (optical fiber, splitter and optical probe), the phototransistor and the RF probe connected to the collector. In this configuration, the input ports and output coaxial connectors are of type K as shown in Figure 2-9. For further computation and de-embedding processes it is better to define the measured link as 4 cascaded networks as shown in Figure 2-10, so that we can characterize each block independently using matrices. Using T matrix we define each block as

- 1st block = Port 1 RF cable and connectors $[T_{port1}]$
- 2nd block= Laser , splitter, optical probe and fiber $[T_{opt}]$
- 3rd block= Phototransistor $[T_{HPT}]$
- 4th block= Port 2 RF cable, probe and connectors $[T_{port2}]$

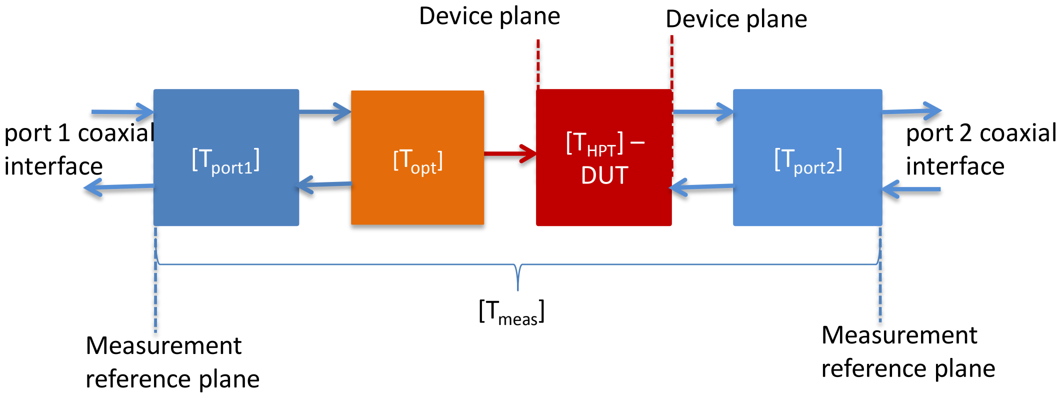

Figure 2-10 : Cascade network to represent the test fixture using four matrix blocks.

Therefore, from link measurement we have the overall characteristics of the cascade link T matrix $[T_{meas}]$ defined as the product of the matrices of each block as shown in equation (2.8)

$$\left[T_{meas}\right] = \left[T_{port1}\right]\left[T_{opt}\right]\left[T_{HPT}\right]\left[T_{port2}\right] \tag{2.8}$$

2.3.3.2 Microwave and Optical calibration techniques

The configuration of the input and output ports are coaxial connectors of type K for the total link as shown in Figure 2-9. As the system is composed of both optical and microwave components, the hybrid calibration is performed into three steps.

- ➢ The first step consists in calibrating the bench through a SOLT calibration using type K loads, as shown in Figure 2-11 a).

- In the second step one measures the loads SHORT, OPEN, LOAD, and THRU on substrate calibration kit as shown in Figure 2-11 b), to complete the T matrix extraction procedure.
- In the 3rd step the optical power is measured at the tip of the optical probe to know the intensity of the optical power injected to the HPT by using the bench shown in Figure 2-12. The measured optical power for this particular characterization of 2.38mW.

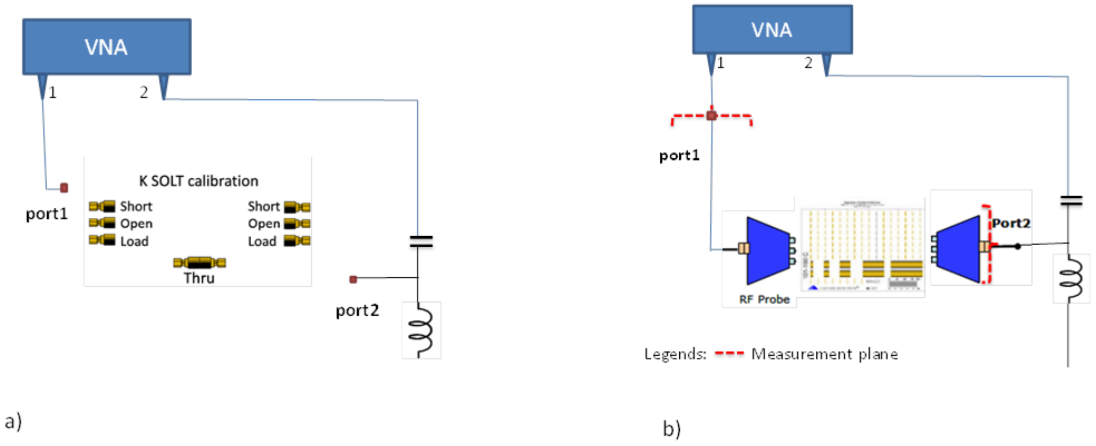

Figure 2-11 : a) K-SOLT calibration bench setup. b) Bench setup to measure microwave parasitic using a substrate standard calibration kit.

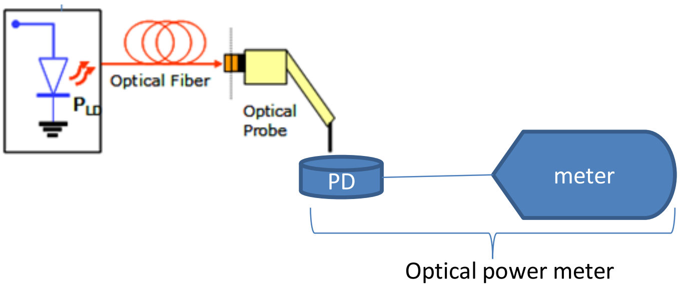

Figure 2-12 : Bench setup to measure the optical power injected into the HPT using optical power meter.

2.3.3.3 De-Embedding Techniques

After performing the link measurement, the post-processing (De-embedding) of the data is then carried out in two stages:

1. Removing of the electrical errors: The error matrix of the electrical fixtures can be determined using the data measured in the second step above. The calibration techniques are described in [172] [236]. Thus, using such techniques the electrical error matrices from port 1 and port 2 can be determined independently ($[S_{port1}]$ and $[S_{port2}]$). One then converts the S-parameters into T-matrices as it is easier for further computation. Once we know the error introduced by RF cables and GSG pads, we can extract the opto-microwave parameters which include the laser, HPT, splitter and optical probes as:

$$[T]=\left[T_{opt}\right]\left[T_{HPT}\right]=\left[T_{port1}\right]^{-1}\left[T_{meas}\right]\left[T_{port2}\right]^{-1} \qquad (2.9)$$

Where T is the opto-microwave link matrix (laser, HPT, splitter and optical probes), T_{opt} the optical link matrix (laser, splitter and optical probe), T_{meas} the measured link matrix, T_{HPT} the HPT matrix, T_{port1} and T_{oprt2} the electrical error matrices at port1 and port2.

At port 1 there is no electrical error introduced in the link measurement since the K_SOLT calibration is done at the plane where the laser is connected. Therefore, we should put T_{port1} as unity matrix for the computation. Figure 2-13 shows the electrical error induced at port 2 due to the GSG pad. It compares the measured error with the data provided by the manufacturer.

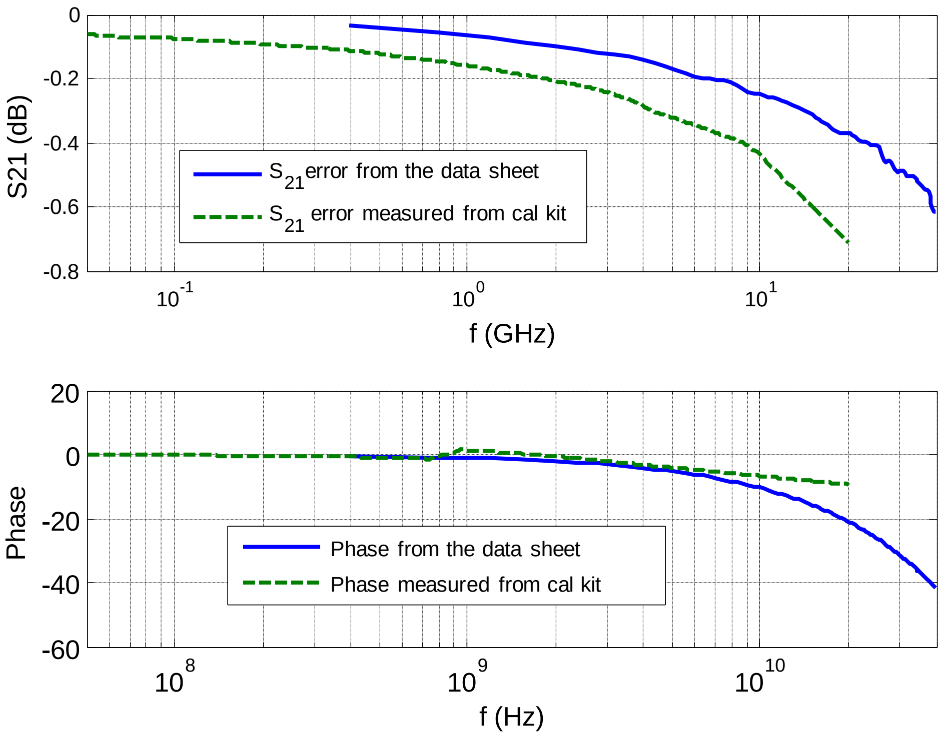

Figure 2-13: Measured and data sheet microwave errors introduced by the GSG probe at port 2. The 1st figure is in terms of magnitude and the 2nd one in terms of phase.

2. Removing of the effect of the laser and optical excitation stages (fiber, splitter): It is now necessary to remove the characteristics of the laser, the optical splitter, and the losses in lensed fiber. To characterize the behavior of the optical link including the laser we use a New Focus multimode photodiode (model 1414-50) with the specifications shown in Table 2-1 instead of the HPT.

Table 2-1: Photodiode: NFPD 1414-50 Specifications

	Units	**1414-50**
Wavelength	nm	800-1630
Bandwidth (dB)	GHz	25
Conversion gain	V/W	17
Responsivity at 850nm	A/W	0.26
Detector material		InGaAs
Output impedance	Ω	50
NEP	pW√Hz	40
Saturation power CW	mW	8
Optical Input		Multimode FC
Output Connection		K

The New Focus high Speed Photodetector shows a flat and linear response in both amplitude and phase respectively up to 25GHz and is optimized for frequency-domain applications. This information will simplify the laser frequency response extraction as the laser has a -3dB cutoff frequency of 12GHz [237]. Therefore, we replace the HPT by the New focus PD as shown in Figure 2-14 and perform the measurement.

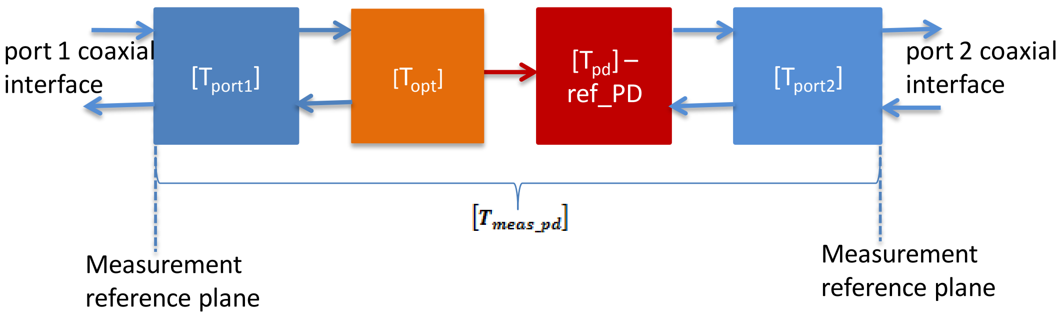

Figure 2-14: Cascade network to represent the test fixture using four blocks where NFPD is used as photodetector red block).

The opto-microwave response shown in Figure 2-15 follows the behavior of the laser used to characterize our phototransistor. The opto-microwave response of the laser is expected to be flat up to 10GHz and it has a cutoff frequency of 12GHz as it is characterized on wafer [10]. However, due to the influence of the test board (shown in Figure 2-16) which is used to supply the dc bias and RF signal into the optical source, the flatness of the response is lost at low frequency up to 0.7GHz and high frequency above 3GHz as shown in Figure 2-15. In this curve the responsivity of the New Focus PD is also included.

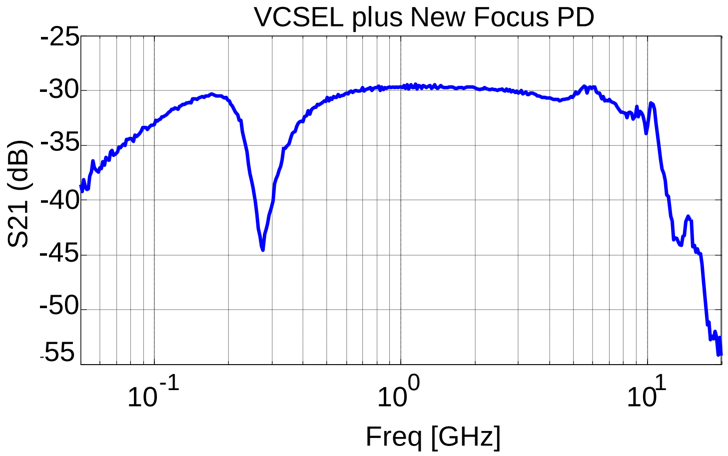

Figure 2-15: The measured link response of the optical excitation stages (including laser) plus NFPD.

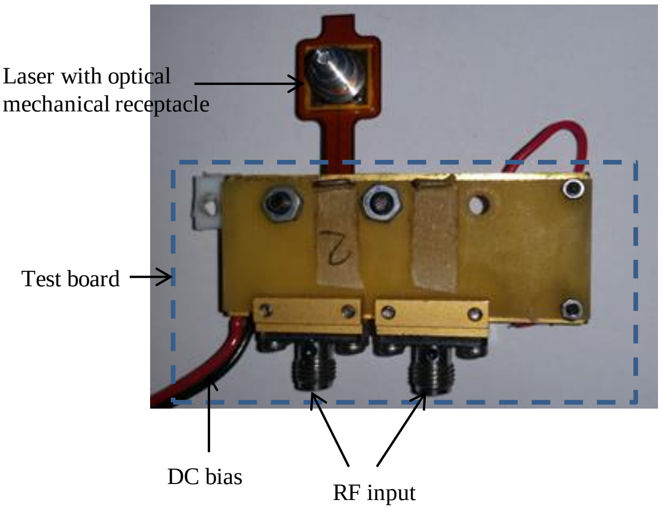

Figure 2-16: Transmitter Optical Sub-Assembly (TOSA) integration and packaging. The laser is packaged and integrated with the external DC and RF signal circuits

Thus, from this measurement we should extract the behavior of the laser along with the optical excitation stages *[T_{opt}]* by removing the New Focus PD response as follows.

Similarly to the 1st stage related to the electrical errors coming from the electrical test fixture, we remove the optical excitation stages using equation(2.10).

$$\left[T_{opt+pd}\right]=\left[T_{opt}\right]\left[T_{pd}\right]=\left[T_{port1}\right]^{-1}\left[T_{meas_{pd}}\right]\left[T_{port2}\right]^{-1} \qquad (2.10)$$

Where *[T_{pd}]* is the responsivity of the NFPD used instead of HPT, *[T_{opt+pd}]* is the link response of optical excitation stages (including laser) plus NFPD, *[T_{opt}]* the optical link matrix (laser, splitter and optical probe) and *[T_{meas_pd}]* the measured link matrix with NFPD.

According to Table 2-1, the reference photodiode has a responsivity of 0.26 A/W. This value can also be measured directly through an LIV measurement, providing the dc curve of the photogenerated current as a function of the injected optical power. The extracted slope then provides the real effective responsivity of the photodiode, which is then measured to be 0.222A/W. The opto microwave gain of the New focus Photodiode can be obtained from the responsivity by using equation (2.11) as explained in [236].

$$S_{21pd}=20\log R_{PD}=20\log(\frac{0.222}{2})=-19.093 \qquad (2.11)$$

Since we know the link response of optical excitation stages (laser, optical interconnection) plus NFPD *[T_{opt+pd}]*, it is now easy to remove the NFPD response and extract such optical excitation stages response as:

$$\left[T_{opt}\right]=\left[T_{opt+pd}\right]\left[T_{pd}\right]^{-1} \qquad (2.12)$$

It leads to the response of the optical interconnection. By using equation(2.9), we can extract the pure opto microwave response of the HPT as:

$$\left[T_{HPT}\right]=\left[T\right]\left[T_{opt}\right]^{-1} \qquad (2.13)$$

Where *T* is the opto-microwave link matrix (laser, HPT, splitter and optical probes)

All opto-microwave responses of HPTs presented in this thesis are extracted by using the above processes.

2.4 The complete and intrinsic SiGe HPT behavior

2.4.1 Introduction

The internal properties of the SiGe HPT could change due to the impact of the light sensitive Si substrate. Hence it is important to point out the existence of the substrate photodiode influence on the intrinsic HPT.

To do so, we start this investigation form the dc behavior of the HPT. Then the various components of the DC photocurrent generated in different regions of the HPT's vertical stack are computed based on its vertical structure.

The optical beam to the HPT's optical window coupling coefficient extraction model is presented. Then the impact of the substrate on OM behavior of HPT and the technique to de-embed this impact are demonstrated.

2.4.2 Intrinsic and Substrate photocurrent computation

Figure 2-17 shows the Gummel plot of 10x10mμ^2 HPT under illumination and dark conditions. Under illumination condition, at low Vbe bias, the base current Ib saturates at around -7μA flowing out of the base contact and the collector current Ic saturates at around 797μA. These currents correspond to photocurrents, which are much higher than the ones only due to biasing effect (dark condition) at this bias level.

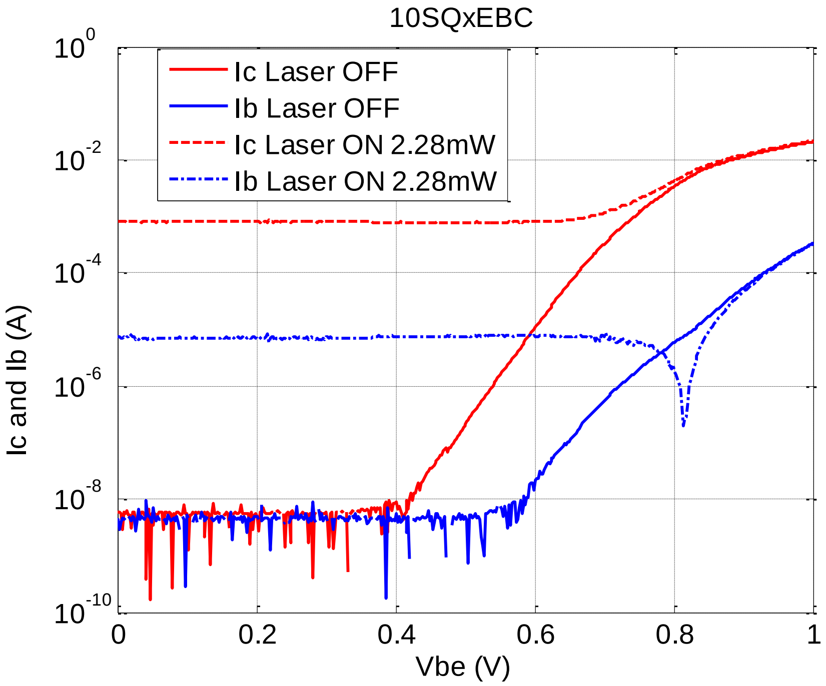

Figure 2-17: Gummel plot of 10x10µm^2 HPT under 2.28mW illumination and dark condition

The base current is plotted as the absolute value of the measured base current. The notch (Laser ON at Vbe=0.82V) shows the reversal in the direction of the base current. For a low base bias, and with adequate optical power, the holes injection into the base due to the optical absorption can exceed what is required for recombination with electrons that are injected from the emitter. This produces a net flow of holes out of the base connection. This results in illuminated base currents lower (because negative) than the dark base current. At high base-emitter bias, the holes injection due to the optical absorption is negligible compared to the one from the electrical base contact.

The difference between the values of Ic and Ib at low Vbe (unity current dc gain) shows that, under 850nm optical power illumination, the increase in collector current is due to the optical absorption in the parasitic photodiode that is formed by the HPT sub-collector and the p-type substrate. This is a clear difference with respect to InGaAs/InP HPTs undergoing no substrate absorption.

To confirm the existence of the substrate photodiode effect we perform Hydrodynamic Drift Diffusion physical modeling of SiGe/Si phototransistor, using COMSOL commercial software, without taking into account the substrate photodiode. The dimensions of the phototransistor structure are defined based on Telefunken GmbH SiGe Bipolar technology. The optical opening size of the phototransistor is 10x10 µm^2. The base profile is a 100nm thin abrupt SiGe layer with Ge content of 22% and with high p-doping of 3.10^{19}cm^{-3}. The collector has 400nm thick and low doped. The 120nm n+ Si is used in the emitter region.

Figure 2-18 shows the comparison of the experimental and physical model curves of the Gummel plot. The physical model curves follow the same behavior as the experimental ones for both base and collector current. The notch of base current also appears in the model even though it is shifted to the left compared to the experimental one. This could be related to the approximate value of doping levels and dimensions of the phototransistor compared to the fabricated one as the latter is confidential to the company.

The most interesting part of this model appears at low base emitter voltage at which the transistor has unity dc current gain. In this region, simulated Ib is nearly equal to simulated Ic. A little difference is due to the emitter current. When we compare the measured collector current and its simulated value at low Vbe, we indeed observe that the difference between the photocurrent measured at the collector and base contacts is the substrate photodiode photocurrent. Due to the presence of this current, the general physical behavior of the transistor is modified.

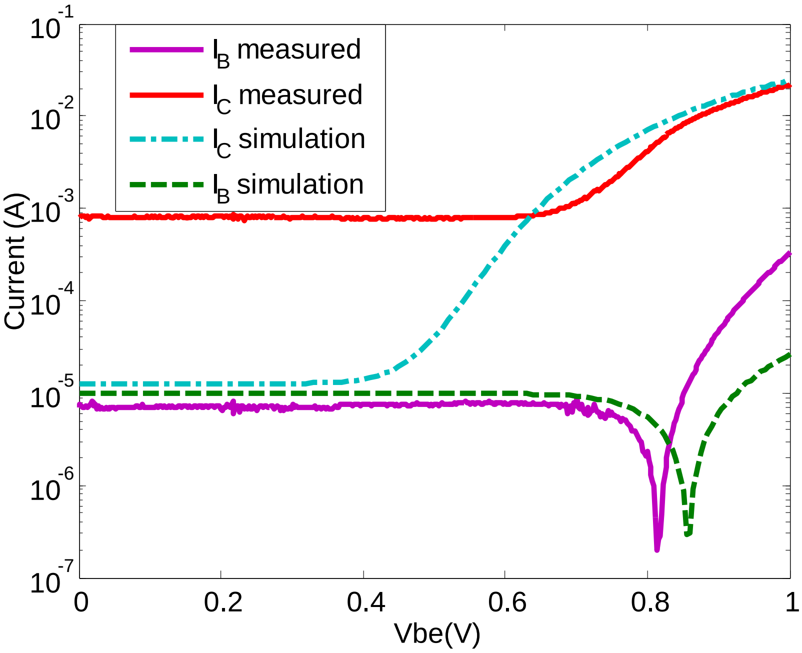

Figure 2-18: The comparison of the experimental and physical modeling Gummel plots of 10x10µm2 optical window HPT under illumination condition.

After understanding the presence of substrate photocurrent we extend our study to locate the main source of substrate photocurrent regions in the HPT structure and also to observe the intensity of the intrinsic photocurrents generated in the base-collector region through a DC Scanning Near-field Optical Microscopy (SNOM) investigation. Thus, it is better to observe both photodiode and phototransistor modes operations separately. The photodiode mode operation shows the response of the HPT without the transistor effect. In the next section, we provide a physical understanding of the origin of all photo-generated current sources within the HPT structure and we develop analytical expression for both PD and HPT modes. This model is based on the band-diagram structure of SiGe/Si HPTs.

A. In Photodiode mode

Primary photocurrent (I_{prim_ph}):

The primary photocurrent generated in the active area of the HPT, which is the total flux of carriers created by the incident optical power, is expressed as

$$I_{prim\_ph} = q\frac{P_{opt\_i}.\lambda}{h.c}\eta_{int}.(1-R).e^{-\alpha_{Si}W_{Si}}.\Gamma.(1-e^{-\alpha_{SiGe}W_{base}}) \tag{2.14}$$

Where P_{opt_i} is the input optical power, R is the input reflection coefficient, η_{int} is internal quantum efficiency, Γ is the confinement factor, α_{Si}, α_{SiGe} are the absorption coefficients of Si (in the emitter and collector) and SiGe (in the base) respectively, W_{Si}, W_{SiGe} are the thickness of the Si region (emitter plus collector) and SiGe one (base) respectively.

The primary photocurrent includes all the possible photocurrents generated by light in emitter, base and collector regions and collected at the base contact.

When base-emitter junction is not biased, the generated primary photocurrent is distributed throughout the structure as shown in Figure 2-19.

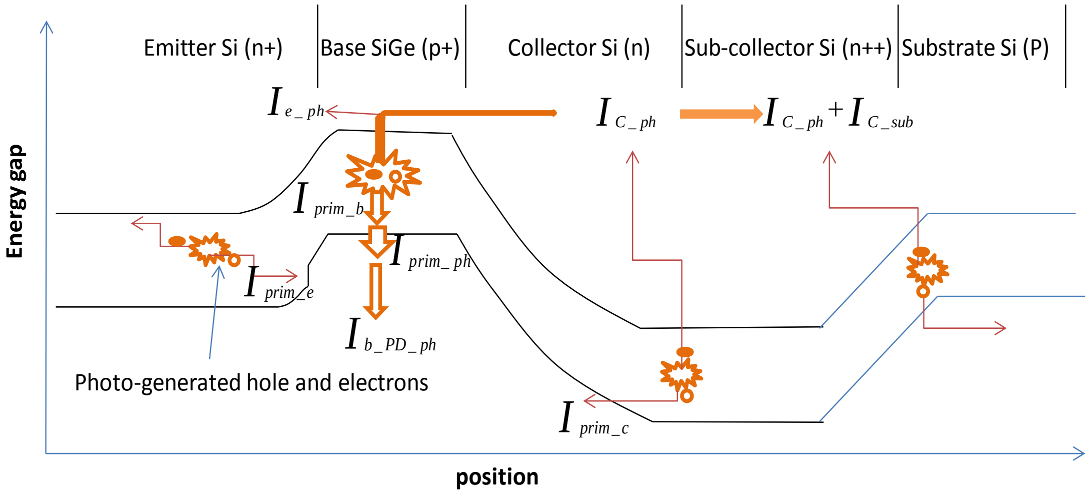

Figure 2-19 : The band gap of SiGe HPT along with distribution of photo-generated carriers, photodiode mode (Vce>0, Vbe=0).

The electrons, generated in the base and collector, are divided into two streams: a few go to the emitter, and most of them towards the collector, because of the electric potential introduced by Vce. The majority of holes in the base are discharged by the base contact. Some holes can stay in the base or may go over the potential barrier to reach the collector or emitter but this effect is very small and is neglected.

Electrons generated in the emitter are flowing to the emitter contact. Holes generated in the space charge region are moving towards the base and the base contact. Thus, holes generated in the emitter and mostly in the collector are contributing to the primary photocurrent and hence to the base current flowing out to the base contact. Moreover, photo-generated electrons in the Si substrate at the proximity of the sub-collector within the induced substrate space charge region are injected into the collector and reach the collector contact (hence contribute to the collector current) and substrate holes are flowing away by the substrate contact (not added to the primary photocurrent). Hence the current measured at the base contact are free from the substrate current.

The primary photocurrent is the photocurrent generated in the emitter, base and collector of the device due to the optical light illumination. It can thus be rewritten from Figure 2-19 as:

$$I_{prim\_ph} = I_{prim\_b} + I_{prim\_c} + I_{prim\_e} \tag{2.15}$$

Where I_{prim_b} is the primary photocurrent from the base, I_{prim_c} is the primary photocurrent from the collector and I_{prim_e} is the primary photocurrent from the emitter

Photo-generated holes that are injected from the base to the emitter are much fewer and are thus neglected. This means then that all photo-generated holes reach the base contact at some points. Thus, the primary photocurrent (I_{prim_ph}) can be measured through the photo-generated contribution of the base current ($I_{b\_PD\_ph}$) as described here after.

Total base current measured in PD mode (I_{b_PD}):

The current measured at the base contact in PD mode can be expressed in terms of the dark current and the base photocurrent as:

$$I_{b\_PD} = I_{b\_PD\_ph} + I_{b\_PD\_dar} = I_{prim\_ph} + I_{b\_PD\_dar} \tag{2.16}$$

Where I_{b_PD} is the total current measured at the base contact in PD mode operation, $I_{b\_PD\_ph}$ is the photocurrent measured at the base contact in PD mode operation, $I_{b\_PD\_dar}$ is the dark current measured at the base contact in PD mode operation and I_{prim_ph} is the primary photocurrent.

Total collector current measured in PD mode (I_{C_PD}):

In PD mode, as the base-emitter junction is turned off, the photo-generated electrons flowing from the base to the emitter are negligible. In phototransistors like InGaAs/InP ones, the collector current in PD mode is equal to the current flowing into the base ($I_{C\_PD}=I_{b\_PD}$). However, in SiGe/Si HPT the collector current in the PD mode configuration (at low Vbe) is larger than the base current as shown in Figure 2-17. This is due to the parasitic photocurrent generated in the substrate as shown here after:

The PD mode collector current is expressed in terms of dark collector current, substrate photocurrent and the electron photocurrent generated from the active region (base, and base-collector junction) of the device as:

$$I_{C\_PD} = I_{C\_ph} + I_{C\_PD\_dar} + I_{C\_sub} \tag{2.17}$$

Where I_{C_PD} is the total current measured at the collector contact in PD mode operation, I_{C_ph} is the photocurrent measured at the collector contact in PD mode operation, $I_{C\_PD\_dar}$ is the dark current measured at the collector contact in PD mode operation and I_{C_sub} is the substrate photocurrent.

Substrate photocurrent (I_{sub}):

The substrate photocurrent is then the difference between the photo-generated collector current measured in the photodiode mode ($I_{C\_PD} – I_{C\_PD\_dar}$) and the photo-generated base current ($I_{b\_PD\_ph}$) measured in the photodiode mode:

$$I_{c\_sub} = (I_{C\_PD} - I_{C\_PD-dar}) - (\left|I_{b\_PD}\right| - I_{b\_PD\_dar}) \tag{2.18}$$

The substrate photocurrent includes the photocurrent generated by the photodiode formed by n+ sub collector and p type Si substrate underneath the active region and extrinsic substrate on the side of the active region. Hence, the inherent photodetected current from the active region of the HPT without electrical effect of the transistor is:

$$I_{c\_ph} = I_{C\_PD} - I_{C\_PD\_dar} - I_{c\_sub} \tag{2.19}$$

B. In HPT mode:

In the HPT mode, the base-emitter junction is biased to active the transistor effect. The electrical current flowing through the base is injected into the emitter. It is the one responsible for the transistor effect. In fact, this current reduces the energy barrier that prevents the flow of electrons from the emitter to the collector. As a result, a collector current appears which is equal to the base current multiplied by the current gain factor β. A part of the photocurrent which is generated in the structure due to the incident optical power undergoes the same phenomenon of amplification. The primary photocurrent is distributed in the structure as shown in Figure 2-20.

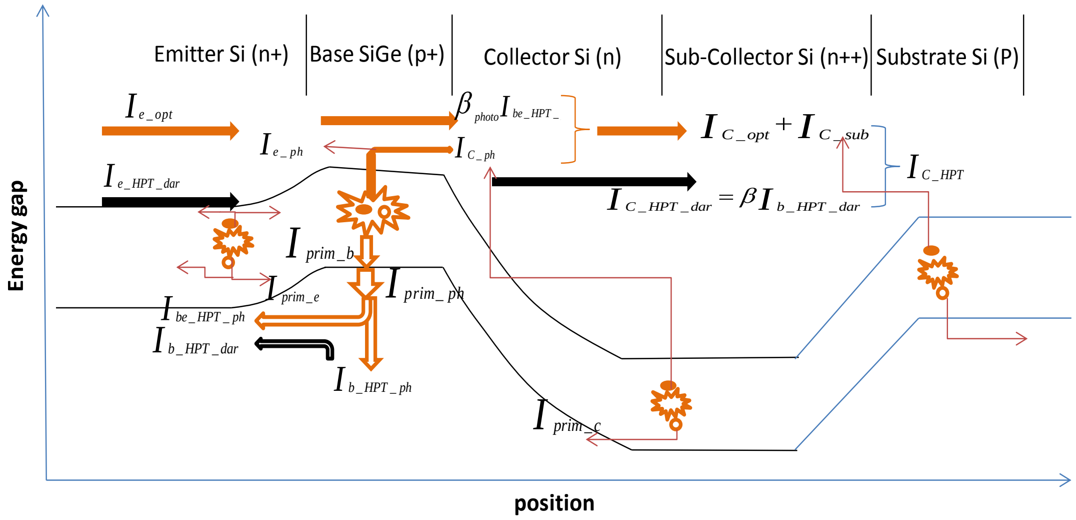

Figure 2-20: The band gap diagram of a common emitter HPT and the distribution of flows of photo-generated carriers and electrical currents, in the phototransistor mode.

In the phototransistor mode, the holes that are photo-generated in the emitter are separated into two parts. One part diffuses toward the emitter contact, and another part is injected into the base region due to both diffusion and proximity of electrical field of the base-emitter space-charge-region. Photo-generated electrons are divided into the emitter contact and the base region. As in the photodiode mode, some of the photo-generated holes in the emitter, base and collector are thus collected by the base contact. This creates the current $I_{b\_HPT\_ph}$. However, there are photo-generated holes which are injected into the emitter which creates the current called transistor effect photocurrent ($I_{be\_HPT\_ph}$). Moreover, in the case when the base-emitter diode is forward biased, the energy barrier gets reduced so that the path mostly selected by photo-generated holes is towards the emitter. In terms of equation, this means:

- Primary photocurrent in HPT mode (I_{prim_ph}): As defined in equation(2.14), the primary photocurrent is the photocurrent generated in the active region of the HPT which is exactly the same as the primary photocurrent in the PD mode. In HPT mode it is expressed as:

$$I_{prim\_ph} = I_{be\_HPT\_ph} + I_{b\_HPT\_ph} \qquad (2.20)$$

Where $I_{be\_HPT\_ph}$ is a fraction of photo-generated photocurrent flowing from the base to the emitter (activating the transistor effect), $I_{b\_HPT\_ph}$ is the photocurrent measured at the base contact in HPT mode.

There is the contribution of the primary photocurrent to the total base, emitter and collector currents of the phototransistor. Theoretically these currents have electrical and optical origins as follows:

- For the base: Total current measured at the base contact:

$$I_{b\_HPT} = I_{b\_HPT\_ph} + I_{b\_HPT\_dar} \qquad (2.21)$$

Where I_{b_HPT} is the total current measured at the base contact in HPT mode and $I_{b\_HPT\_dar}$ is the dark current measured at the base contact in HPT mode.

- For the collector: The total current measured at the collector contact is:

$$I_{c\_HPT} = I_{c\_opt} + I_{c\_HPT\_dar} + I_{C\_sub} \quad with\ I_{c\_opt} = \beta_{opt}.I_{be\_HPT\_ph} + I_{c\_ph} \qquad (2.22)$$

Where I_{c_HPT} is the total current measured at the collector contact in HPT mode, I_{c_opt} is the photo-generated contribution and $I_{c\_HPT\_dar}$ is the dark current, all measured at the collector contact in HPT mode, β_{photo} is the common emitter photocurrent gain, $I_{be\_HPT\_ph}$ is the transistor effect activating photocurrent and I_{c_ph} is the photocurrent measured at the collector contact in PD mode operation.

- For the emitter: The total current measured at the emitter contact is:

$$I_{e\_HPT} = I_{e\_opt} + I_{e\_HPT\_dar} \quad with\ I_{e\_opt} = (\beta_{opt}+1).I_{be\_HPT\_ph} - I_{e\_ph} \tag{2.23}$$

Where I_{e_HPT} is the total current measured at the emitter contact in HPT mode, I_{e_opt} is the photocurrent contribution and $I_{e\_HPT\_dar}$ is the dark current, all measured at the emitter contact in HPT mode, and I_{e_ph} is the photocurrent measured at the collector contact in PD mode operation.

Finally I_{e_opt} is evaluated from equation (2.22) and (2.23) as:

$$I_{e\_opt} = I_{c\_opt} - (I_{prim\_ph} - I_{be\_HPT\_ph}) = I_{c\_opt} - \left|I_{b\_HPT\_ph}\right| \tag{2.24}$$

Photocurrent gain (β_{opt}): the photocurrent gain of transistor is defined as the ratio between the amplified photocurrent (difference between I_{c_opt} and I_{c_ph}) and the photocurrent flowing from the base to the emitter ($I_{be\_HPT\_ph}$), responsible of activating the transistor effect:

$$\beta_{opt} = \frac{I_{c\_opt} - I_{c\_ph}}{I_{be\_\_HPT\_ph}} \tag{2.25}$$

Where $I_{be\_HPT\_ph}$ can be computed from equation 2.20. $I_{b\_HPT\_ph}$ and I_{c_opt} can be computed from equation (2.21) and (2.22) respectively as all terms in these equations are already known.

Base efficiency (γ): is the ratio of the photocurrent at the base to the primary photocurrent generated in the HPT.

$$\gamma = \frac{I_{b\_\_HPT\_ph}}{I_{prim\_ph}} \tag{2.26}$$

Photocurrents computing flow-chart: Figure 2-21 shows the summary of computing photocurrents in different regions of the phototransistor. This flow chart helps computing the previously defined currents.

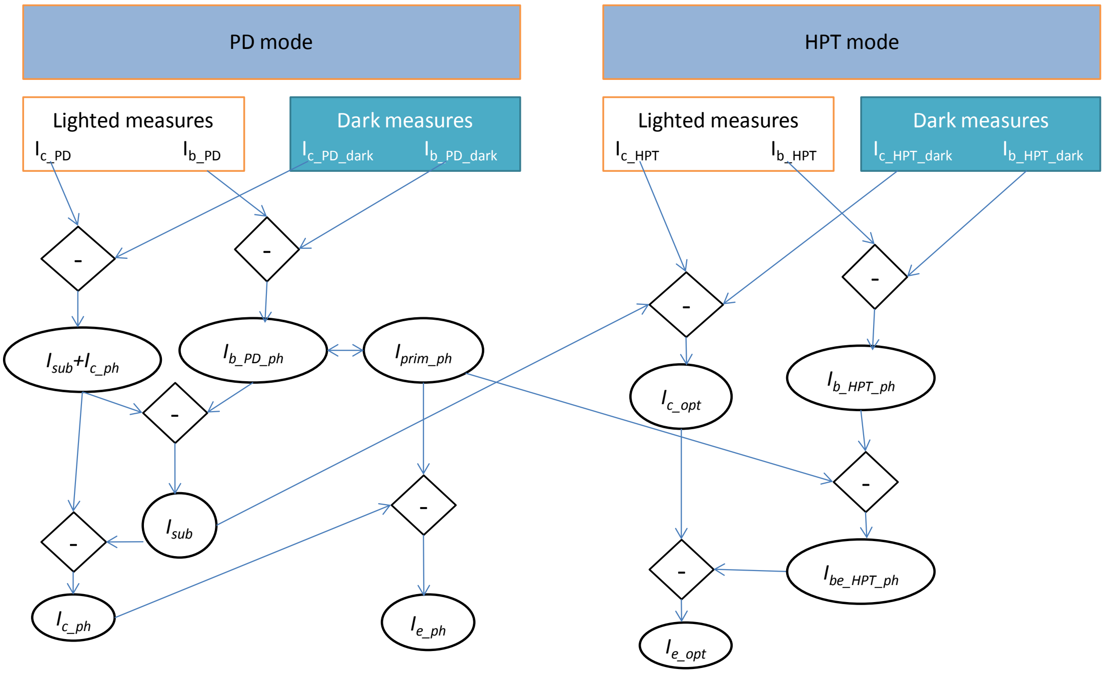

Figure 2-21: Photocurrent computation flow chart

2.4.3 Extraction of the coupling coefficient

In this section we present how to extract the coupling coefficient of the optical beam and the device under test. Among all photocurrents measured into the phototransistor, the base photocurrent is easily accessible and, as opposed to the collector one, is only due to the intrinsic structure of the HPT and does not depend on other contributions, such as the substrate photocurrent or amplification position dependent mechanisms. It is then possible to use the base photocurrent to estimate the shape of the incident optical beam directly from it.

Figure 2-22 shows the experimental topological map of the base current of a 10x10µm^2 SiGe/Si HPT in phototransistor (a) and photodiode (b) modes. It is symmetric along X and Z axes in both modes. The phototransistor mode is obtained with V_{ce}=3V and V_{be}=0.857V. The photodiode mode is obtained under the same collector emitter voltage of 3V and with the base emitter junction short-circuited with a voltage of 0V. The origin of X and Z axes is centered on the peak intensity of the photocurrent, to provide a constant and repeatable reference for all further measurements. The position of the transistor layout is then centered on the figure to guide the eye. Ib will be the reference for such an alignment in all this PhD work.

Figure 2-23 shows cross-sections of the topological map along the two transverse axes, X and Z.

The shape of the optical beam that is scanned over the HPT has a Gaussian profile in the X and Z axes. The resulting photocurrent is the correlation between the optical window and the Gaussian profile of the optical beam, leading to an Erf function shape, as given in equation (2.27).

$$f(x,z) = A*\left(\mathrm{erf}\left(\frac{X+W_X/2}{\sigma_X}\right)-\mathrm{erf}\left(\frac{X-W_X/2}{\sigma_X}\right)\right)\left(\mathrm{erf}\left(\frac{Z+W_Z/2}{\sigma_Z}\right)-\mathrm{erf}\left(\frac{Z-W_Z/2}{\sigma_Z}\right)\right) \quad (2.27)$$

Where A is the amplitude, W_X (W_z) is the optical window width along X axis (resp. Z) mean and σ_X (σ_Z) is the Gaussian beam deviation factor along X direction (resp. Z).

This is used to fit with the measurement as shown in Figure 2-23. We then estimate the full width half maximum (FWHM) power of the incident optical beam having a circular shape to be of 28µm in diameter. This is larger than the HPT window. A maximum optical coupling rate of 32.3% between the lensed fiber and 10x10µm^2 HPT and 16.5% for 5x5µm^2 HPT is then deduced. The base current is well fitted with the *erf* function as shown in Figure 2-23 at the estimated coupling coefficient.

In the phototransistor mode the sign of the base current changes from positive to negative when the optical probe moves towards the center of the optical window. We can explain this behavior as follows. Under illumination, electron-hole pairs are created in the base and collector regions of the HPT. The photo-generated electrons are swept towards the sub-collector and the photo-generated hole towards the base. Some of the photo-generated holes reaching the base region accumulate at the emitter/base junction and modify the potential barrier which causes a large electron current from the emitter to the collector. But some photo-generated holes, with a large quantity, and are eliminated via the base contact. This component of photo-generated holes does not contribute to the optical gain but are responsible of the base photocurrent which is opposite to the electrical dark current, biasing the structure. The overall base current tends to be negative then, when the coupling efficiency and the optical power are sufficient.

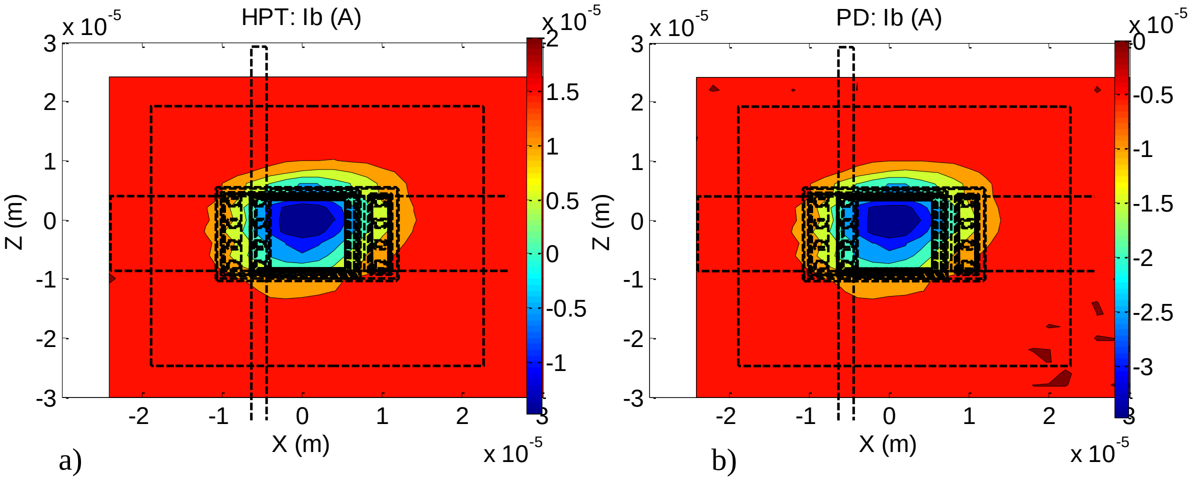

Figure 2-22: Base current mapping over the structure of the HPT by 2µm step in a) HPT mode under Vce=3V and Vbe=0.857V and b) PD mode under Vce=3V and Vbe=0V.

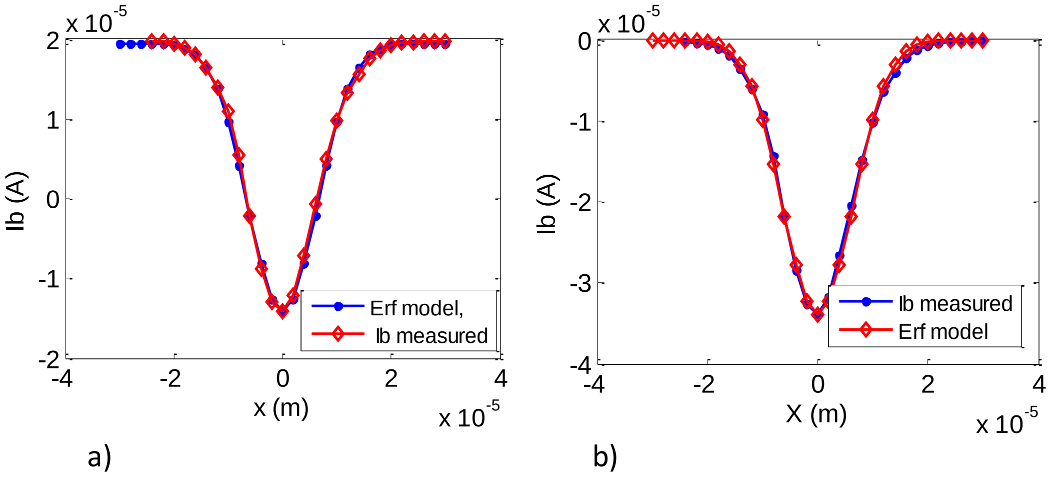

Figure 2-23: The slice of the base current at Z=0m a) HPT mode at Vce=3V and Vbe=0.857V and b) PD mode at Vce=3V and Vbe=0V. The base current is not influenced by the substrate photocurrent as the photogenerated carriers in the substrate are collected either by the substrate or collector contact intentionally.

2.4.4 Substrate photodiode impact on the Opto-microwave behavior

S-parameters and thus the opto-microwave gain are measured by using the bench setup described in section 2.3.2. Figure 2-24 shows the opto-microwave gain (G_{OM}) of the HPTs having 10µmx10µm and 50µmx50µm optical window size as a function of the frequency. In the same figure the PD and HPT modes of both devices are presented. All the parasitic effects are removed by the de-embedding procedure described in section 2.3.3. The measurements are made from 50MHz up to 20GHz.

The result shows that for a 0V Vbe biasing and 2V Collector voltage (PD mode), we observe a G_{OM} of -32 dB at 50 MHz against a peak G_{OM} value of -17 dB at 50 MHz for a base voltage of 0.857 V and 2 V collector voltage (HPT mode) for an optical window size of 10SQxEBC (10x10µm^2) HPT. For 50SQxEBC (50x50µm^2) HPT we observe a PD mode G_{OM} of -31 dB and HPT mode G_{OM} of -5 dB at 50 MHz with the same biasing as the former one. From the same figure we can also extract the optical gain, Gopt. For 10SQxEBC HPT we observe a Gopt at 50 MHz of 15 dB and for 50SQxEBC a Gopt at 50 MHz of 26 dB.

The PD mode Gom at low frequency of the 50x50µm^2 HPT was expected to be much higher than for the 10x10µm^2 HPT due to the higher optical coupling efficiency. However, they have nearly equal value. It is obvious that there is a coupling loss for 10x10µm^2 HPT, whereas for 50x50 a 100% coupling efficiency is attended. This expectation is violated here; it is due to substrate photodiode effect which is more visible into the 10x10µm² HPT and increase the overall responsivity and thus the G_{OM}.

Another observation is for frequencies less than 3GHz the slope of the Gom curve in PD mode for 10x10µm^2 HPT versus frequency is steeper than the slope of Gom curve for 50x50µm^2. The 10x10µm² do any exhibit any plateau and has an almost 10dB/decade slope which is characteristics from substrate photocurrents. The cutoff frequency of the smaller device then is smaller than the one of the 50x50µm² HPT in PD mode. Normally the bigger one should have smaller cutoff frequency. This shows that there is a great impact of the slow substrate photocurrent in PD mode on smaller HPTs. This will be investigated in detail in chapter 3.

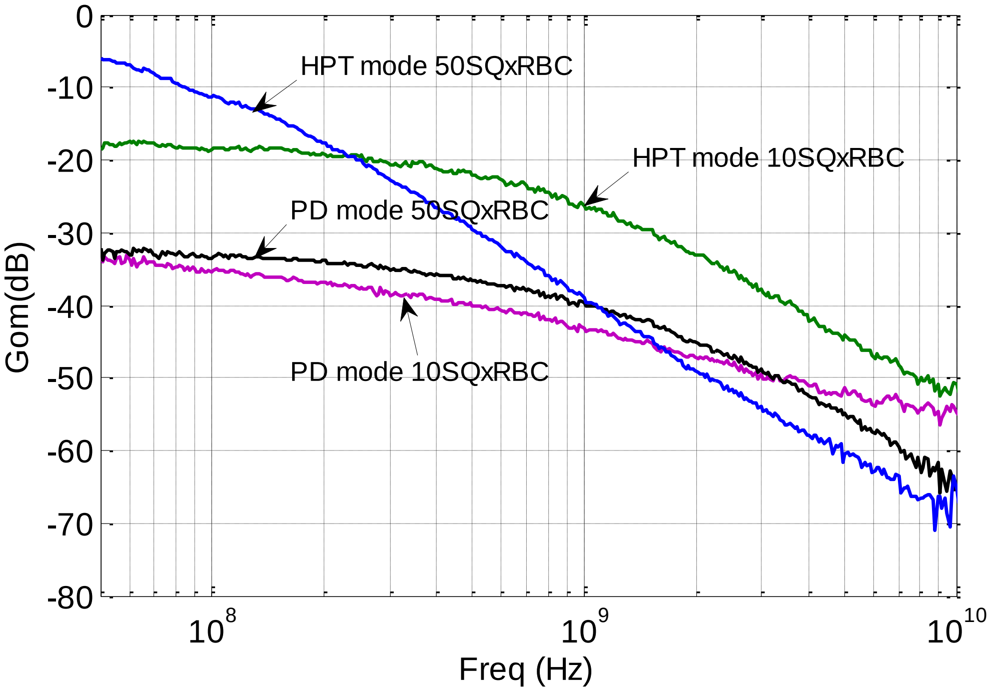

Figure 2-24: Opto microwave gain of 10SQxEBC and 50SQxEBC. At Vce=2V and Vbe=0.857V for HPT mode and Vbe=0V for PD mode

2.4.5 De-embedding the frequency response of the substrate photodiode

Figure 2-26 b) shows the topological mapping experimental result of the low-frequency responsivity of the HPT in the photodiode mode. The responsivity forms a donut shape with response higher in the substrate than in the active area. This helps us to select a position of the fiber where we can isolate the substrate response from the HPT one for further analysis. Figure 2-26 a) then shows the opto-microwave response of the substrate obtained at X=5µm and X=15µm (where the peak of the substrate response appears).

The intrinsic characteristics of the HPT are related to the behavior of the excess carriers into the emitter, base and collector regions as described previously. They may however be hidden by the substrate photodiode created by the n++ sub-collector and p type substrate at some given positions. It is then important to separate the two contributions, as well in term of frequency response.

The frequency response of these various contributions is influenced by the intensity of light reaching each layer of the structure and the distance covered by the photo-generated carriers to reach the metal contacts. Similarly the frequency response of the substrate photodiode is also dependent on the depth of the light penetration into the structure and the lateral position of the optical probe to illuminate the device:

The substrate photocurrents can thus be considered as the sum of individual photocurrents contribution each given at a specific penetration depth into the structure as shown in Figure 2-25. The magnitude and the speed of the photocurrent generated at the top surface for example (at A) is different from the ones obtained underneath (for example at B and C). This difference is related to the number of photons reaching the specific depth and also the distance to be traveled by the carriers to reach the metal contacts. Hence each of these individual contributions get smaller in amplitude and slower as the depth is increased. This effect is a distributed one along all the depth of the structure. Their related responsivity can be plotted as in Figure 2-26 a). Each of them is a typical 20dB/decade slope in theory. The combination of them all however provides a slope which depends on the variation law of the absorption and cutoff frequency as a function of the depth. In the case of a linear variation, a theoretical slope of 10dB/decade is then expected according to [263]. In our case, we can extract a slope of 8dB/decade. Such a slope is very close to the theory and is thus considered as a proof of the substrate contribution on the HPT performances. It is also considered to be related only to the distance of penetration to the sub-collector/substrate junction plane, and can then be transposed all other points from the topological map of the HPT.

This 8dB slope curve will then be exploited to de-embed the intrinsic frequency response of the HPT all over the HPT surface.

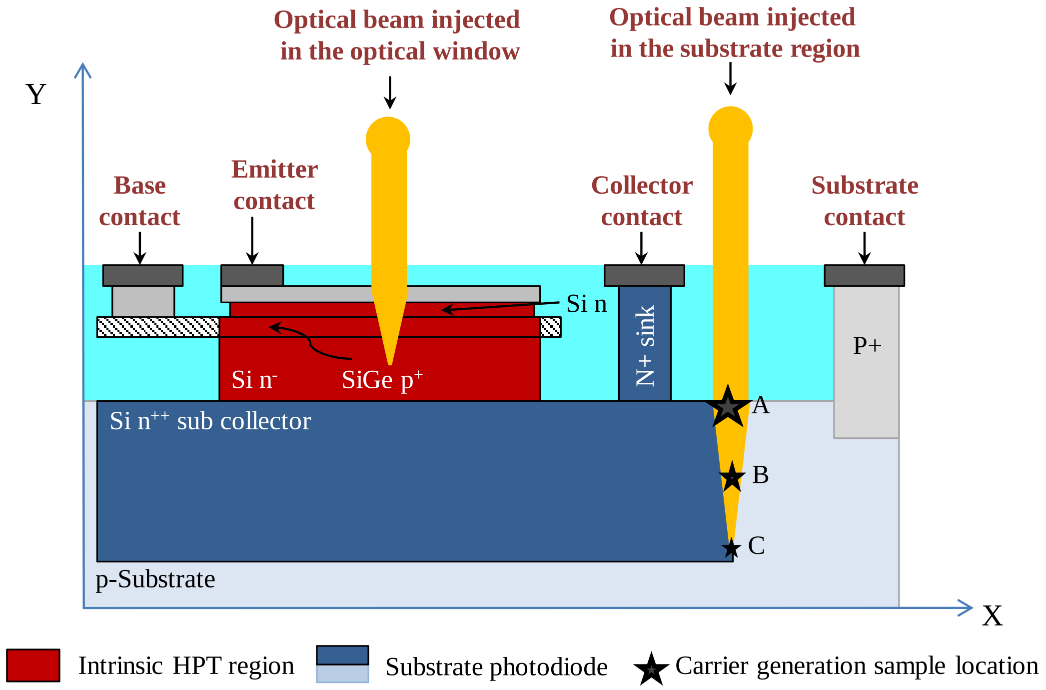

Figure 2-25: The phototransistor structure cross section along X and y plane. The intrinsic and the substrate photodiode regions are indicated, and also the expected light penetration region are shown in the intrinsic and substrate regions.

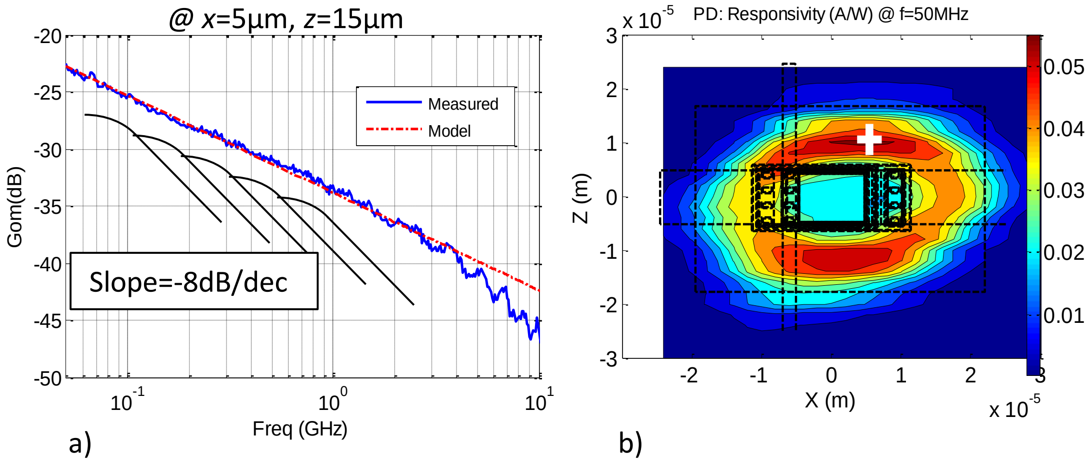

Figure 2-26: Substrate frequency measurement and modeling. a) the transfer function model to fit with the frequency response of the substrate photodiode, b) the topological map of 10x10µm^2 HPT low frequency responsivity in PD mode and the substrate frequency response is measured at x=5µm, y=15µm under Vbe=0Vand Vce=3V dc bias.

There are thus three main steps to extract the intrinsic opto-microwave frequency response of the HPTs.

1. **Intrinsic responsivity of the HPT in PD mode from DC measurement**

We perform the DC SNOM measurement over the surface of the phototransistor and measure the collector and base current. By using the equation (2.28) we compute the intrinsic photocurrent generated (I_{C_ph}) for each position of the optical probe. Then we use the definition of opto-microwave power gain defined in section 2.3 as shown in equation (2.29) to extract the intrinsic dc responsivity, $R_{PD,i,DC}$.

$$I_{C\_PD} = I_{C\_ph} + I_{C\_PD\_dark} + I_{sub} \tag{2.28}$$

$$R_{PD,i,DC}{}^{2} = \left(\frac{I_{C\_ph}}{I_{opt,RF}}\right)^{2} = \left(\frac{I_{C\_PD} - I_{C\_PD\_dark} - I_{sub}}{I_{opt,RF}}\right)^{2} = \left(R_{PD,DC} - R_{sub}\right)^{2} \tag{2.29}$$

With $I_{opt,RF}=\alpha_{cal}P_{opt,RF}$

$$R_{PD,i,DC} = \frac{I_{C\_PD} - I_{C\_PD\_dark}}{I_{opt,RF}} - \frac{I_{sub}}{I_{opt,RF}} = R_{PD,DC} - R_{sub} \tag{2.30}$$

Where $I_{C,PD}$ is the total current measured at the collector contact in PD mode operation, I_{C_ph} is the photocurrent generated in the active area of the HPT in PD mode, $I_{C\_PD\_dark}$ is the dark current measured at the collector contact in PD mode, I_{sub} is the substrate photocurrent, $R_{PD,DC}$ is the complete DC responsivity of the HPT in PD mode, α_{cal} is the coupling factor of the reference diode and $P_{opt,RF}$ is the illuminating optical power expressed in terms of the equivalent current $I_{opt,RF}$.

2. **Extract the low frequency (at 50MHz) responsivity of the substrate**

To extract the substrate responsivity (R_{sub}) at low frequency we assume that the intrinsic dc responsivity ($R_{PD,i,DC}$) is equal to the intrinsic responsivity at low frequency ($R_{PD,i,LF}$) which is true (valid) under voltage bias condition. Hence:

$$R_{PD,i,LF} = \frac{I_{C,ph}}{I_{opt,RF}} \cong \frac{I_{C,ph}}{I_{opt,DC}} = R_{PD,i,DC} \tag{2.31}$$

Thus the substrate responsivity (R_{sub}) at low frequency is deduced from the PD mode intrinsic ($R_{PD,i,LF}$) and low frequency complete ($R_{om,PD}$) responsivity.

$$R_{sub} = R_{om,PD} - R_{PD,i,LF} \tag{2.32}$$

The photodiode mode intrinsic ($R_{PD,i,DC}$), substrate (R_{sub}) and complete ($R_{om,PD}$) responsivities of 10x10µm^2 HPT are presented in Figure 2-27. The $R_{om,PD}$ curve is the slice figure of the PD mode responsivity measured at 50MHz. We observe that the intrinsic responsivity follows the *Erf* function with its peak at $x=y=0$µm and the responsivity of the substrate photodiode is stronger than the intrinsic photodiode. The substrate responsivity is very low in the active region of the HPT, but it is not null due to the penetration of optical light through the substrate.

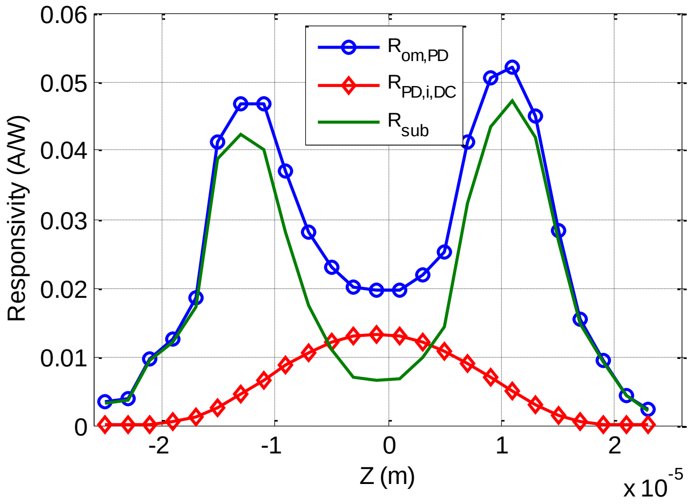

Figure 2-27: The raw, substrate and net responsivities of 10x10µm^2 in PD mode operation (Vbe=0V).

3. Measuring and modeling the substrate frequency response (in substrate regions)

We measure the frequency response of the substrate by pointing the optical probe on the substrate to illuminate the substrate photodiode at x=5µm and z=15µm as shown in Figure 2-26 b). Then the substrate response at low frequency computed by equation (2.32) at the given point is extrapolated to all frequencies by using the transfer function presented in equation(2.33) to fit with the measured substrate frequency response. Thus from this model we can extract the slope of the substrate response. The slope evaluated is then used to extrapolate the low frequency responsivity of the substrate photodiode to all frequencies for each illuminated positions.

$$R_{sub}(f) = \frac{R_{sub}(\mathrm{f}_0)}{\left(1 + j\frac{f}{\mathrm{f}_0}\right)^{\alpha}} \tag{2.33}$$

Where f_0 =50MHz, ∝ is the order of the transfer function. Figure 2-26 a) shows the fitting of our model with the opto-microwave gain of the substrate photodiode. Our model is well fitted with the measurement result for ∝=0.4 which is equivalent to -8dB/decay slope.

To deduce the intrinsic frequency response of the HPT we de-embed the local frequency response of substrate photodiode from the frequency response of the complete HPT which is measured directly at each position of the optical probe in all frequencies ranges by using the following equations for HPT and PD mode respectivly.

$$R_{OM,\mathrm{HPT,i}}(f) = R_{OM,\mathrm{HPT},com}(f) - R_{OM,sub}(f) \tag{2.34}$$

$$R_{OM,\mathrm{PD,i}}(f) = R_{OM,\mathrm{PD},com}(f) - R_{OM,sub}(f) \tag{2.35}$$

Where $R_{OM,HPT,i}$ and $R_{OM,PD,i}$ are the intrinsic responsivities in HPT and PD momde, and $R_{OM,HPT,com}$ and $R_{OM,PD,com}$ are the complete responsivities in HPT and PD mode respectively.

2.5 Extracting techniques of opto-microwave capacitance and transit time terms

In this section we review the extraction techniques of the f_T and f_{Topt}, and then of their related capacitance and transit time terms. Extracting the junction capacitances and transit times of the device are important to observe the impact of light on the HPT internal dynamic parameters. The proposed extraction technique of the opto-microwave capacitance and transit time term will be used in coming chapters to analyze the photo-carriers path flows and their dynamic limitations within HPTs.

2.5.1 Extracting electrical capacitances and transit time

The electrical transition frequency, f_T, is the frequency at which the dynamic current gain (*h21*) of the common-emitter transistor configuration is equal to unity. The h-parameters are calculated from the measured S parameters. An example of the measurement result of the *h21* is presented in Figure 2-28 for a phototransistor of 10x10um² optical window. Frequency extrapolation is required to extract the f_T of the HPT as the VNA used to characterize the HPT runs only up to 40GHz and as extracted f_T from the HPT could be beyond 40GHz, as shown in Figure 2-28.

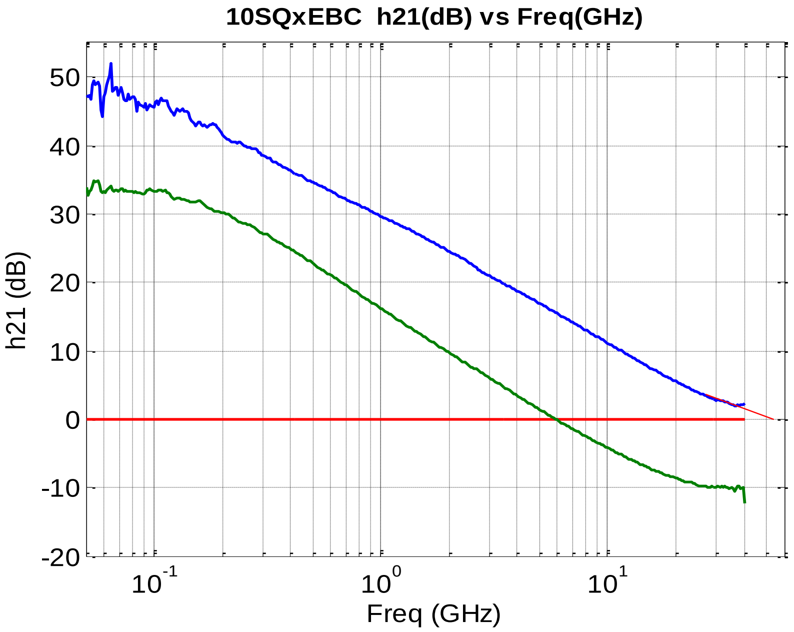

Figure 2-28 : The measured dynamic current gain h21 versus of frequency at two different biasing points.

Figure 2-29 presents results of extraction of transition frequency f_T versus of collector current for 10SQxEBC phototransistors having an active surface area of 100µm².

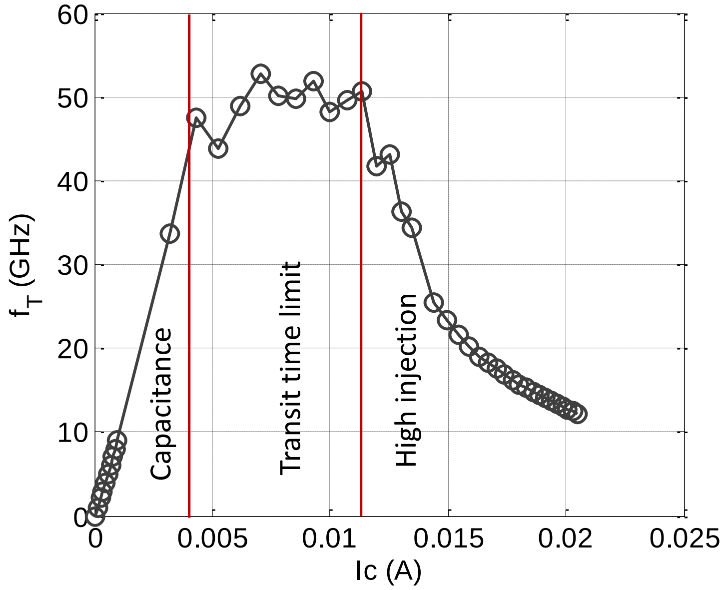

Figure 2-29 : The measured f_T versus of collector current for 10x10 HPT at Vce=3.5V. It also indicates the factors that limit the speed of the HPTs in different regions of the curve.

The transition frequency f_T is fundamentally determined by the collector current I_C. For very low I_C the speed of the transistor is limited by the junction capacitances. With increasing I_C, the intrinsic conductance decreases, and makes eventually the capacitance charging time smaller than the forward transit time. This is the region where f_T reaches its peak and is constant as shown in Figure 2-29. The device speed is then mainly limited by the forward transit time. At high I_C, however, base push-out occurs (Kirk effect) due to the high current injection, and forward transit time itself increases with I_C, leading to f_T roll-off.

Mathematically, the electrical transition frequency (f_T) in bipolar phototransistor can be written in general as [172]:

$$f_T = \frac{1}{2\cdot\pi\cdot\tau_{EC}} = \frac{1}{2\cdot\pi\cdot\left[\frac{k\cdot T}{q\cdot I_C}\cdot\left(C_{BE}+C_{BC}\right)+C_{BC}\cdot\left(R_E+R_C\right)+\tau_b+\tau_e+\tau_{bc}\right]} \qquad (2.36)$$

Where $\tau_F=C_{BC}.(R_E+R_C)+\tau_b+\tau_e+\tau_{bc}$ is the forward transit time, $g_m=\frac{kT}{qI_C}$ is the intrinsic trans-conductance at low injection, C_{BE} and C_{BC} are emitter-base and collector-base depletion capacitances, R_E and R_C are the dynamic emitter and collector resistances, τ_b, τ_e and τbc are base transit time, emitter transit time and base-collector depletion time delay respectively.

To improve f_T in a SiGe HPT, the forward transit time must be decreased by using a combination of vertical profile scaling as well as Ge grading across the base. At the same time, the operating current I_C must be increased in proportion in order to make the intrinsic trans-conductance negligible compared to the forward transit time. That is, the high f_T potential of small forward transit time transistors can only be obtained by using sufficiently high operating current. Figure 2-30 shows the active area vertical stack of the HPTs used to compute the parameters which strongly affect the transition frequency.

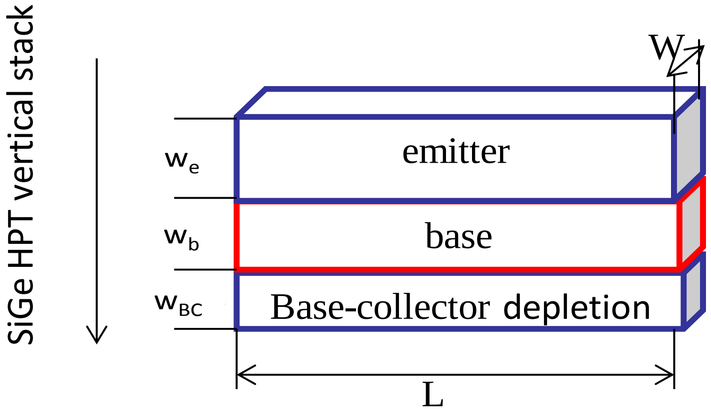

Figure 2-30: The simplified intrinsic vertical stack of the HPT.

In this study, the base is p+ doped with a constant Ge profile. The emitter and collector are n+ and n doped respectively. Thus, having this in mind we drive equations to evaluate the transit time and junction capacitances in the base, emitter and collector as follows.

Base transit time, τ_b : is the time associated with the excess minority carrier charge in the neutral base. It can be expressed by the simplified equation as:

$$\tau_b = \frac{w_b^2}{2D_{nb}} \tag{2.37}$$

Where, D_{nb} is the diffusivity of electron in the base, w_b is neutral base width.

Emitter transit time, τ_e: is the time associated with the excess minority carrier charge in the neutral emitter. The emitter charge storage time can be written as[172] [262]:

$$\tau_e = \frac{1}{\beta_{ac}}\left(\frac{w_e}{s_{pe}} + \frac{w_e^2}{2D_{pe}}\right) \tag{2.38}$$

Where D_{pe} is the hole diffusivity in the emitter, S_{pe} is the hole surface recombination velocity at emitter contact and β_{ac} is the ac current gain of the transistor.

Base-collector depletion time delay τ_{bc}: is the time required for electrons to traverse the base-collector depletion region [172] [262]. Electrons travel across the collector-base depletion region by drift, and hence it can be written as

$$\tau_{bc} = \frac{w_{BC}}{2V_{sat}} \tag{2.39}$$

Where w_{BC} is the base-collector depletion thickness, and V_{sat} is the carrier saturation velocity.

Base-emitter depletion capacitance C_{BE}***:***

$$C_{BE} = \frac{\varepsilon . A_{BE}}{W_{EB,d}} \tag{2.40}$$

Where ε is dielectric constant of the material, A_{BE} is base emitter depletion region surface area and $W_{EB,d}$ is depletion area thickness.

Base-collector depletion capacitance C_{BC}:

$$C_{BC} = \frac{\varepsilon . A_{BC}}{W_{BC,d}} \tag{2.41}$$

Where, A_{BC} is base emitter depletion region surface area and $W_{BC,d}$ is the depletion thickness.

The values of forward transit time and junction capacitances can be easily extracted from a plot of global time delay ($\tau_{tot}=1/2\pi f_T$) versus $1/I_C$, as shown in Figure 2-31. Near the peak of f_T, the global time delay versus $1/I_C$ curve is nearly linear, indicating that the junction capacitance is close to constant for this biasing range at high f_T.

Thus, the C_{EC} junction capacitance can be obtained from the slope:

$$C_{EC} = C_{BE} + C_{BC} \tag{2.42}$$

As we can see in Figure 2-31 the global time delay versus $1/Ic$ has a constant slop after the high injection region. As at infinite collector current the global time delay is equal to the forward transit time, this latter can be extracted. The forward transit time τ_F can be determined from the y-axis intercept at infinite collector current as shown in Figure 2-31.

$$\tau_F = C_{BC} \cdot (R_E + R_C) + \tau_b + \tau_e + \tau_{bc} \tag{2.43}$$

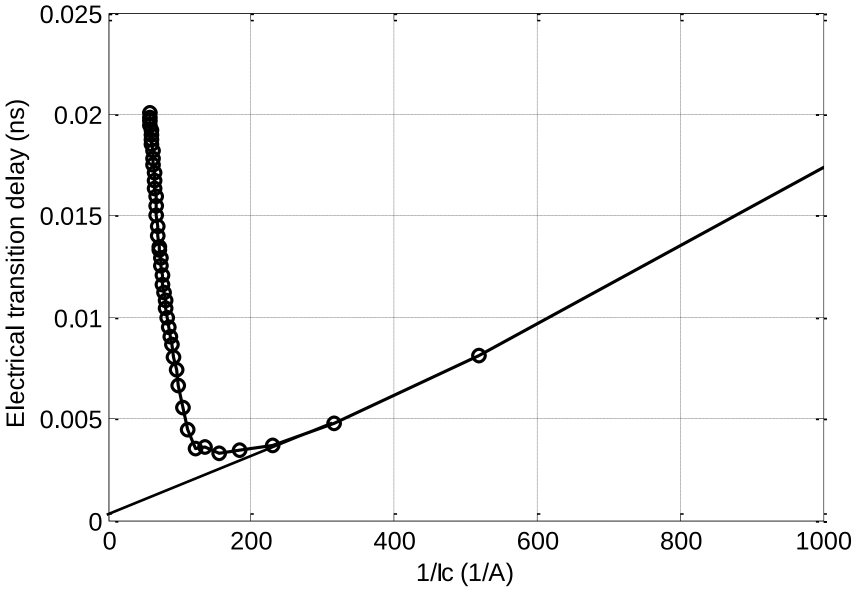

Figure 2-31: Global time delay (electrical transition delay) versus of 1/Ic. From the slope of this curve we can extract the built in capacitances and from the y-intercept we can extract the transit time.

2.5.2 Extracting opto-microwave capacitances and transit time

The optical transition frequency, f_{Topt}, is the frequency for which the responsivity of the HPT in phototransistor mode is equal to the low frequency responsivity in photodiode mode as it is defined in section 2.3.1. Unlike f_T, f_{Topt} is influenced by additional terms related to the photodetection mechanism.

The optical transition frequency, f_{Topt}, is much lower than the electrical transition frequency, f_T. It is explained by the addition of capacitive and transit time terms related to the photodetection mechanism. Other electrical terms remain unchanged. Thus, it is possible to develop an expression for the optical transition frequency f_{Topt} as:

$$f_{Topt}=\frac{1}{2\cdot\pi\cdot\tau_{EC\_opt}}=\frac{1}{2\cdot\pi\left[\frac{k\cdot T}{q\cdot I_C}\cdot\left(C_{EC}+C_{EC\_opt}\right)+\tau_F+\tau_{F\_opt}\right]} \tag{2.44}$$

Where, τ_F is the electrical forward transit time from emitter to collector, C_{EC} is the emitter-base and collector-base electrical junction capacitance (without light effect)

τ_{F_opt} is the optical forward transit time increase from emitter to collector. This term is due to optical illumination effects. It is expressed in terms of base, emitter and collector transit times as:

$$\tau_{F\_opt}=C_{BC\_opt}\cdot\left(R_E+R_C\right)+\tau_{b\_opt}+\tau_{e\_opt}+\tau_{bc\_opt} \tag{2.45}$$

C_{EC_opt} is the emitter-base and collector-base junction capacitance increase due to optical illumination

$$C_{EC\_opt}=C_{BE\_opt}+C_{BC\_opt} \tag{2.46}$$

And C_{EC} and τ_F are the pure electrical terms as described in equations (2.42) and (2.43) respectively. τ_{F_opt} reflects the additional transit time, mainly due to vertical and/or lateral movements of carriers. It is interesting to trace the evolution of transit time τ_{EC_opt} versus $1/I_C$ under illumination. Figure 2-32 compares the opto-microwave (OM) global time delay with the electrical time delay of 10SQxEBC HPTs versus of $1/I_C$

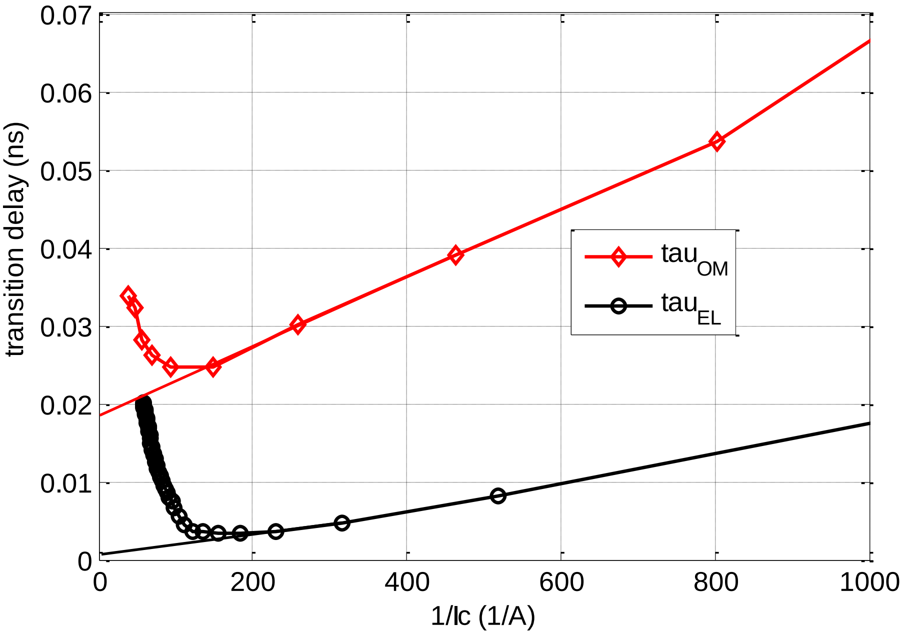

Figure 2-32 : Global opto-microwave and electrical time delays of 10x10(µm)^2 HPT

From this curve we can extract the opto-microwave capacitive and transit time terms. The opto-microwave capacitive value is given by the slope of the asymptote of the curve for high *1/Ic* values. The y-intercept of this line gives the value of opto-microwave transit time. The optical effects associated with the photodetection can be separated from opto-microwave terms as:

Opto-microwave capacitance: $C_{EC\_OM}=C_{EC}+C_{EC\_opt}$ (2.47)

Opto-microwave transit time: $\tau_{EC\_OM}=\tau_F+\tau_{F\_opt}$ (2.48)

Thus, it is possible to subtract the electrical forward transit time τ_F and electrical junction capacitance C_{EC} presented in section 2.5.1 from the measured values of opto-microwave terms expressed in equations (2.47) and

(2.48) respectively and thus, to obtain the optical forward transit time τ_{F_opt} and optical junction capacitance C_{EC_opt} terms.

2.6 Conclusion

In this chapter we presented the tools used to analyze the behavior of SiGe/Si phototransistors. They will be used in the next chapters to perform the HPTs measurements and their post processing.

The phototransistor structures have been described first with a description of the Telefunken GmbH SiGe Bipolar technological process. Opto-microwave gain, optical gain, cutoff frequency and optical transition frequency are important parameters to characterize a phototransistor, and thus have been reminded.

The bench setup to characterize such devices has been explained. De-embedding is important to extract the effect of the bench fixtures like the RF probes and the optical link probing the HPT in order to know exactly the behavior of the phototransistor. The dc photocurrent analysis of a phototransistor both in photodiode and phototransistor mode will help us to understand the structure and behavior of SiGe/Si HPTs. The PD mode is obtained by setting the base-emitter voltage to zero whereas the HPT mode is obtained with a positive base-emitter voltage Vbe.

Extracting the substrate effect on the intrinsic phototransistor response is shown also to be an important topic in order to observe the intrinsic behavior of the SiGe/Si HPTs. A method for the evaluation of its both static and dynamic contribution has been made. The extraction of all individual photocurrent contribution within the intrinsic HPT has been proposed.

For future electrical/opto-microwave modeling of the phototransistor, but also to observe the impact of light on the HPT internal dynamic parameters, extracting the junction capacitances and transit times of the device are important. We also proposed the extraction of the opto-microwave capacitance and transit time term contribution on the optical transition frequency, f_{Topt}, which will be used in further chapters to analyse the photocarriers path flows and their dynamic limitations.

Chapter 3 Experimental study of SiGe HPTs with top illumination

3.1 Introduction

There is a continuous need to verify the ability of integrating phototransistors in newer commercial SiGe process technologies offering faster operating frequencies but also to improve the performances of the HPT without a modification of the technology in terms of vertical stacks of layers. To optimize the speed of the phototransistor, [205] identified the fastest and slowest regions of the structure based on physical simulations. References [249] investigated the performances of phototransistor through opto electric compact circuit modeling. M. D. Rosales et al [245] verified that the proximity of the base, emitter and collector contacts to the optical window has an influence on the dynamic response characteristic of the phototransistor. The existence of substrate photocurrent was demonstrated through modified MEXTRAM model in [250] and they also show that the impulse response is wider when the substrate contact is open. Reference [251] suggests and demonstrates that using the substrate contact we can remove the photo-generated holes in the substrate so that the speed performance of the phototransistor can be enhanced. However, the photo-generated electrons in the substrate still have a great impact on the speed performance of the SiGe HPTs. Reference [250] has demonstrated the impact of the injected optical power on the dc response behavior of the phototransistor. But the impact on opto-microwave behavior of injected optical level and its frequency limitation were still not investigated.

This chapter intends to study further the HPT dynamic behavior. We characterize the HPT technology presented in chapter two in the configuration of top-side illumination.

After this section of introduction, in the second section of this chapter, the electrical static behavior of the phototransistor under dark and illumination conditions is observed through the Ic-Vce characteristics, electrical current gain (β) and the Gummel curve. The dc responsivity of the different optical window size phototransistor is also presented and compared.

The third section deals with the optimization of the dc bias conditions that maximize the opto-microwave behavior of the HPT, with the consideration on the low frequency gain and dynamic behavior of the phototransistor. It starts with the low-frequency opto-microwave gain, and then deals with the comparison on two-terminal (2T-HPT) and three-terminal (3T-HPT) configurations. Finally discuss the opto-microwave 3dB cutoff frequency and optical transition frequency (f_{Topt}) as a function of the biasing.

In the fourth section, we focus on the size dependency of the electrical dynamic behavior of SiGe HPTs, which shows an unusual behavior as compared to HBTs. We thus propose a “2D extension electrical effect” that analyses the two-dimensional and distributed nature of currents within SiGe HPT.

While in second and third sections, the point of illumination was chosen to be fixed, at the center of the optical window, where the optical response is maximized, the fifth section analyses further the spatial dependency on the opto-microwave behavior. The DC current and opto-microwave frequency response are analyzed over the surface of the structure through SNOM investigation under the optimum dc bias conditions.

In sixth section, the impact of the injected optical power level on the dc and opto-microwave performance of the SiGe HPT is presented.

The seventh section focuses on the opto-microwave transit time and junction capacitances of the HPT, deduced from the f_{Topt} current dependency. This analysis is extended as well as a function of the position of the optical beam over the HPT surface to provide further information on the distributed nature of the HPT.

Finally, in section eight, the impact of the optical window size on opto-microwave gain and cutoff frequency is analyzed. The optical window size dependency of the substrate photodiode and 2D carrier distribution effects are also investigated. The conclusion is then provided in the last section.

3.2 HPT Static behavior

The static behavior of the HPT can be observed through the measurement of the output Ic-Vce characteristics, electrical current gain (β) and the Gummel curve under dark and illumination conditions. Under illumination condition, we inject 2.28mW dc optical power which is measured at the tip of the lensed fiber probe.

Output characteristics (Ic-Vce) of a transistor show the collector current (Ic) versus of the collector voltage (Vce) and the base current (Ib). This indicates AC signals can be superimposed on DC bias levels. The typical Ic-Vce output characteristics of the 50SQxEBC HPT are as shown in Figure 3-1. It illustrates how an input base current and collector voltage influence the output collector current. Dark condition is represented in Figure 3-1 a). The output characteristics of the HPT were measured by sweeping the collector voltage Vce from 0V to 4.5V whereas the base current Ib is swept from 10nA-1µA by steps of 0.1µA, from 3µA -20µA by steps of 2.3µA and from 25µA -100µA by steps of 3µA. With 2.5V Vce, the collector current Ic is equal to 950µA with an Ib of 1µA or Ic is equal to 40.5mA with an Ib of 100µA. From the plotted curves we observe that there is a rapid increase of the collector current for the collector voltage greater than 3.5V. This is due to the fact that the phototransistor is operating in the breakdown/avalanche mode.

The effect of illumination with a 2.28mW dc optical beam at 850nm is shown on the Ic-Vce curves in Figure 3-1 b). The high value of Ic is attributed to the generated photocurrent that adds to the initial base current and that is amplified by the transistor action of the HPT. Without illumination, the supplied bias current in the base Ib_{bias} sets the bias point of the HPT. The illumination pushes the bias point of the HPT to Ib = (Ib_{bias} + I_{ph}) and thus modifies the value of the current gain (β). As a result, the measured collector current Ic_{illum} for the HPT will be given by:

$$Ic_{illum} = (I_{ph} + Ib_{bias}) * \beta + I_{ph} \tag{3.1}$$

$$Ic_{illum} = (\beta + 1) I_{ph} + \beta Ib_{bias} \tag{3.2}$$

Under constant base current biasing, illumination of the HPT causes an increase in the Vbe voltage. This is primarily due to the addition of the photocurrent in the base to the initial base bias Ib [235].

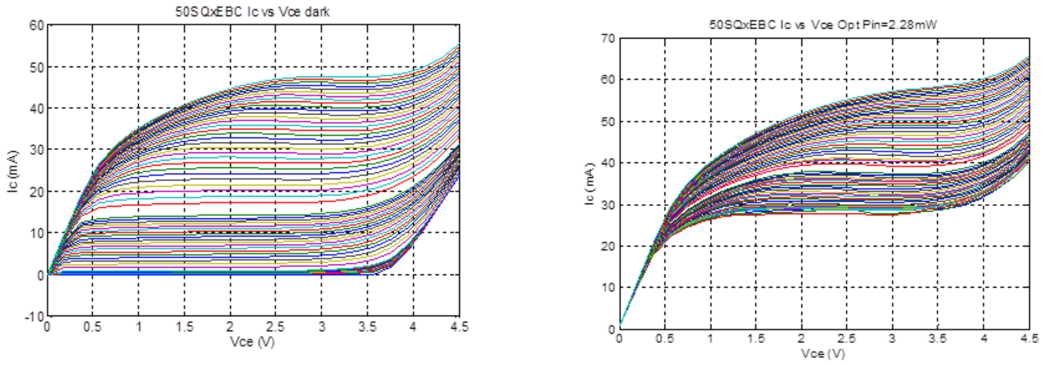

a)

b)

Figure 3-1: Ic-Vce curves of 50SQxEBC HPT for Ib between 10nA and 100µA: a) without optical power illumination b) illuminated by 2.28mW optical power at 850nm

Figure 3-2 shows the superposition of Ic-Vc curves with and without light illumination. In the active region, at Ib=10nA and Vce=2V, Ic is equal to 53µA in dark condition and against Ic_{illum}=31.6mA when light is ON. Thus, the transistor collector current due to the light illumination is around 31mA. This gives a dc responsivity of 50x50µm^2 HPT that reaches up to 13.6A/W at Ib=10nA.

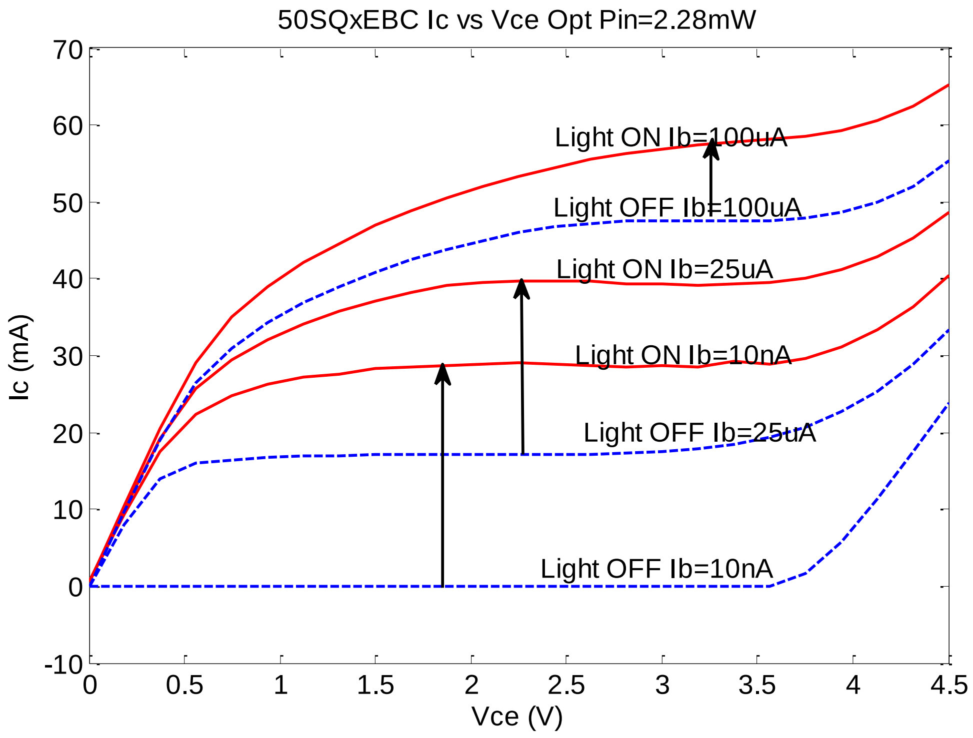

Figure 3-2: The superposition of Ic-Vc curves with and without light illumination. Blue curves (dashed) are in dark condition and red curves (plain) are with illumination.

Figure 3-3 shows the Gummel plot of the 10SQxEBC and 50SQxEBC HPTs with 2.28mW optical beam at 850nm and without (dark). The base voltage is initially provided with 0V, which puts the HPT in a reverse active mode. It is then increased up to 1V where the HPT goes to a forward active mode up to saturation. The collector and base currents are measured as a function of the supplied voltage in the base. In the non-illuminated condition, the measured Ic and Ib clearly show the different regions in the HPT operation: the low current region, the linear region and the high current region. In the low Vbe bias range, the measured dark Ic and Ib saturate in the range of 10^{-9}A. In the high current region, the change in the slope of Ic and Ib is evident.

Without illumination, the 50SQxEBC shows an increase in collector current by a factor of 3.2 compared to the 10SQxEBC as shown in Figure 3-3, it is due to the increase in size of the intrinsic transistor with the optical window size.

At low Vbe bias and under 2.28mW illumination, the base current Ib (flowing out of the base contact) saturates at around 50µA for 10SQxEBC HPT and 91µA for 50SQxEBC HPT. The collector current Ic saturates respectively at around 5mA and 7mA. These currents correspond to the photocurrent generated by the optical absorption, which are far greater than the HPT's transistor dark currents at low base bias level. Under illuminated condition, it is observed that at high base bias (> 0.87V), the effects of the optical absorption are negligible on the biasing level as compared to the dark currents.

The base current is plotted as the absolute value of the measured illuminated base current. The notch shows the reversal in the direction of the base current. The notch moves to higher base emitter voltage for 50SQxEBC HPT, which has higher intrinsic transistor area, indicating that larger size HPT requires higher base emitter voltage to reach its transistor mode operation.

For given HPT size, the difference in the value of Ic and Ib at low Vbe is due to the substrate photocurrent as explained in chapter 2 section 2.4.2.

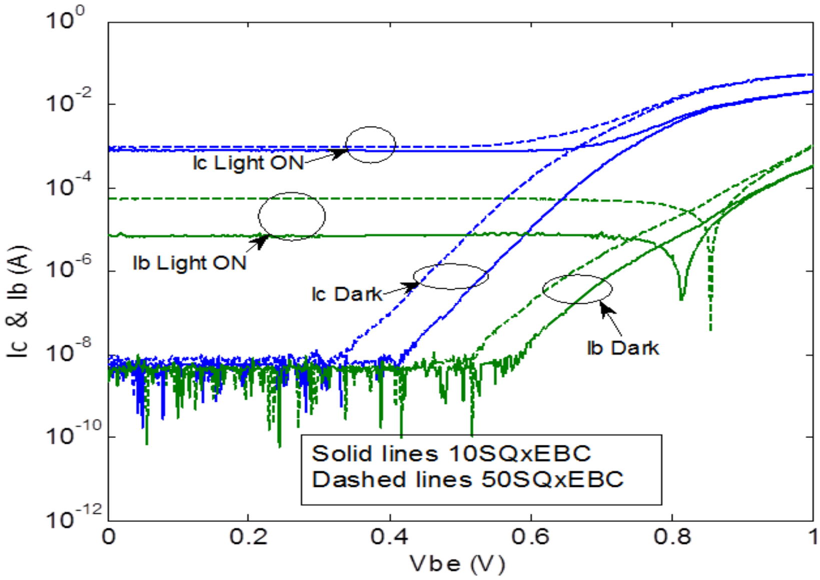

Figure 3-3: The Gummel plot of the 10SQxEBC (10x10µm^2) and 50SQxEBC (50x50µm^2) HPTs with 2.28mW optical beam at 850nm and without (dark).

In summary, at low base-emitter junction bias and high enough optical power, the photocurrent generated in the emitter, base or collector regions swamps the devices transistor action. That is, the effect of electrons injection into the base from the emitter is negligible. By contrast, at high base-emitter bias the transistor action is noticeable and the photocurrent constitutes a small base current injected into the device which is amplified by the transistor operation to provide the device optical gain. The substrate parasitic photodiode proves however to have a deep impact on Ic, especially visible at low Vbe.

Another very important characteristic of a phototransistor that makes it different from a photodiode is its internal current gain (β). Figure 3-4 a) shows the common emitter electrical dc current gain (β) extracted from the Gummel plot in dark conditions versus of the base emitter voltage for different size HPTs respectively. The highest beta is seen in the 50x50µm^2 HPT with a peak value of 1200 at Vbe=0.68V. This is followed by the 10x10µm^2 with a maximal β of 450 at Vbe=0.7V, 5x5µm^2 having β peak of 400 at Vbe=0.75V and finally 3x3µm^2 which has a peak current gain (β) of 260 at Vbe=0.8V.

Figure 3-4 b) shows the common emitter optical dc current gain (β_{opt}) only due to the injection of optical light as versus of the base emitter voltage for 10x10µm^2 and 50x50µm^2 HPTs. The larger optical window size HPT has higher β_{opt} (102 at Vbe=0.898V) than the smaller size HPT (73.1 at Vbe=0.890V).

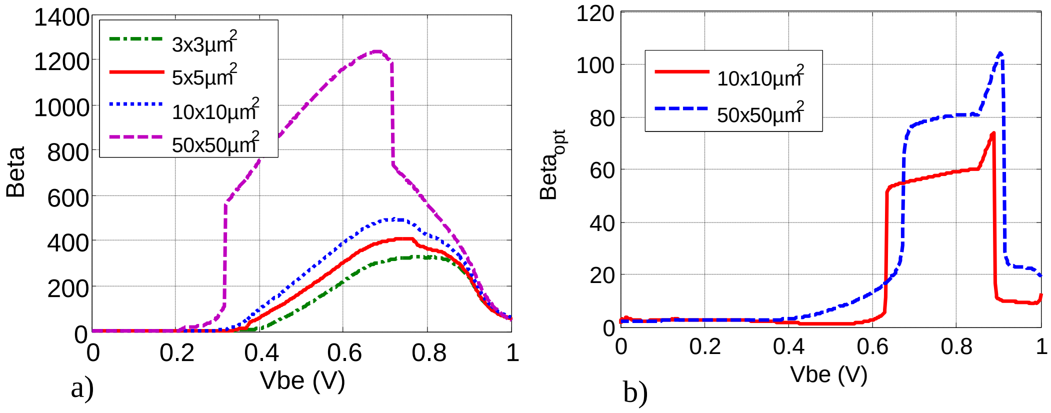

Figure 3-4: a) Common emitter current gain (β) extracted from the Gummel plot versus the base emitter voltage for different size HPTs in dark condition; b) the optical current gain.

The measured collector currents from the illuminated and dark Gummel curves and Ic-Vce measurements are used to extract the DC responsivity of the HPT. For our understanding we were able to extract the complete responsivity, absolute responsivity and intrinsic responsivity of HPT as expressed in equations (3.3) to (3.5) respectively.

Complete responsivity:

$$R\left(\frac{A}{W}\right)=\frac{Ic_{illum}-Ic_{dark}}{P_{in\ opt}} \tag{3.3}$$

Absolute responsivity:

$$R_{abs}\left(\frac{A}{W}\right)=\frac{Ic_{illum}-Ic_{dark}}{\Gamma P_{in\ opt}} \tag{3.4}$$

Intrinsic responsivity:

$$R_{\text{int}}\left(\frac{A}{W}\right)=\frac{Ic_{opt}-I_{sub}}{P_{in\ opt}} \tag{3.5}$$

Where $P_{in,opt}$ is the injected optical power, Ic_{opt} is photocurrent measured at the collector contact, I_{sub} is substrate photocurrent and Γ is the coupling efficiency of the optical beam to the optical window.

Figure 3-5 shows the resulting DC responsivity for the 10x10µm^2 and 50x50µm^2 HPT configuration under 2.28mW optical power illumination versus of the supplied Vbe. The illumination of the HPT under low base emitter voltage bias causes an initial significant increase in the measured dc responsivity due to the photocurrent from the parasitic substrate photodiode. As the base-emitter region becomes forward biased the dc responsivity starts to increase until it reaches a peak value where it starts to descend to lower values as Vbe is increased.

The complete DC responsivity difference between 50x50µm^2 and 10x10µm^2 HPTs under PD mode operation (as shown in Figure 3-5 a) comes mainly from the optical beam coupling efficiency. As it is presented in chapter 2 section 2.4.3, the coupling efficiency of 10x10µm^2 HPT is 32.3% whereas 50x50µm^2 HPT is 100%. Considering these values, we extract the absolute responsivity of both HPTs by using equation(3.4). Thus, as it is shown in Figure 3-5 a), the absolute dc responsivity at low Vbe (PD mode) is the same for 10x10µm^2 and 50x50µm^2 HPTs.

In HPT mode (for Vbe >0.6V), the absolute dc responsivity difference between the two HPTs (ratio of 1.47 at Vbe=0.83V) is mostly due to the electrical dc current gain 1.3 times higher (at Vbe=0.83V) in

50x50µm^2 HPT than in 10x10µm^2 HPT as shown in Figure 3-4. Another explanation comes from an increased base efficiency injection that makes holes flowing out though the base contact more easily within the 10x10µm² HPT (20% of the base injection efficiency) than in the 50x50µm² (17% of the base injection efficiency). The intrinsic responsivity of both HPTs, after removing the substrate response, is also presented in Figure 3-5 b). Here we can also observe the similar influence of coupling efficiency and optical current gain. The DC responsivity peak values under PD and HPT modes along with their optimum bias are summarized in Table 3-1.

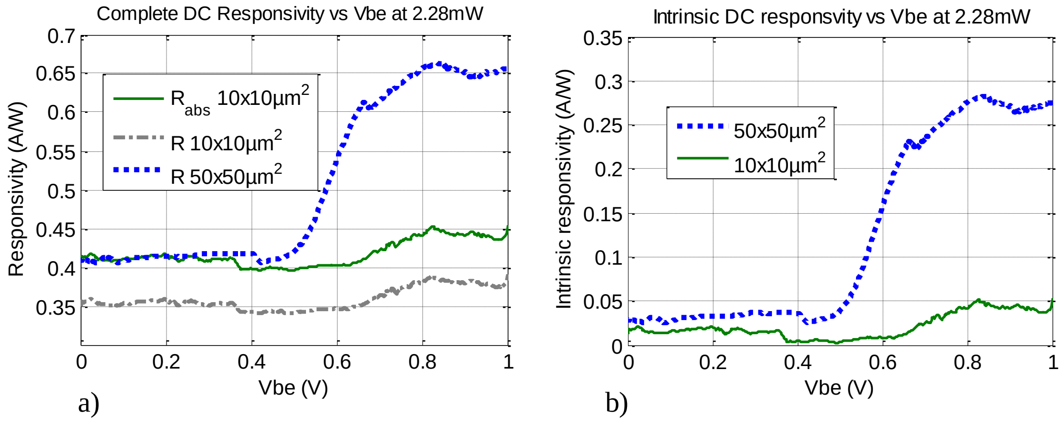

Figure 3-5: DC responsivity extracted from the Gummel plot a) the complete and absolute responsivity, b) the intrinsic responsivity.

Table 3-1: Summary of the dc responsivities in PD and HPT modes along with the optimum Vbe values.

HPT type	**Vbe (V)**	**R$_{HPT}$ (A/W)**	**R$_{PD}$ (A/W)**	**R$_{abs,HPT}$ (A/W)**	**R$_{abs,PD}$ (A/W)**	**R$_{int,HPT}$ (A/W)**	**R$_{int,PD}$ (A/W)**
10x10µm^2	0.826	0.390	0.356	0.450	0.412	0.05	0.020
50x50µm^2	0.834	0.662	0.412	0.662	0.412	0.83	0.033

3.3 HPT optimum biasing

3.3.1 Introduction

Our phototransistor operates under common emitter configuration. However, depending on the level of the dc bias and the base terminal connection, its performance varies. In this section we deal with optimizing the dc biasing conditions and the different connections to the base to maximize alternatively the low frequency gain and dynamic behavior of the phototransistor. We sweep the dc bias at the collector and base and measure the S parameters of the link under opto-microwave and pure electrical conditions. In this study we focus on voltage control biasing condition. Thus, in this section we present the optimum dc biasing conditions on both the collector and base terminal sides that maximize the low frequency gain (such as h_{21}, Gopt, Gom) and the dynamic behavior (such as f_{-3dB} and f_{Topt}) of the phototransistor.

3.3.2 Optimizing the low frequency opto-microwave behavior

This part focuses on the dc biasing conditions to maximize the low-frequency behavior of the HPT.

3.3.2.1 Low frequency opto-microwave gain vs biasing

Here we optimize low frequency opto-microwave gain (Gom) in terms of dc bias. The S-parameters of the link are measured versus of Vbe at different constant voltages Vce. From the link measurement all the setup features are removed using the de-embedding techniques presented in chapter 2 section 2.3.3.

Figure 3-6) shows the opto-microwave responsivity at 50 MHz versus of the base bias voltage Vbe at a fixed Vce of 3V and 1V for 10x10µm^2 and 50x50µm^2 optical window sized HPTs. The responsivity measurements at Vbe=0V-0.55V could be considered as the PD mode biasing of the HPT. In this biasing region, the base-collector junction is reversed biased and the base-emitter junction is not yet forward biased. The responsivity starts increasing fromVbe= 0.6V and reaches its peak at around Vbe=0.857V, it then starts to fall off as the HPTs are in the high injection region. It is also observed that the responsivity enhances as Vce increases from 1V to 3V.

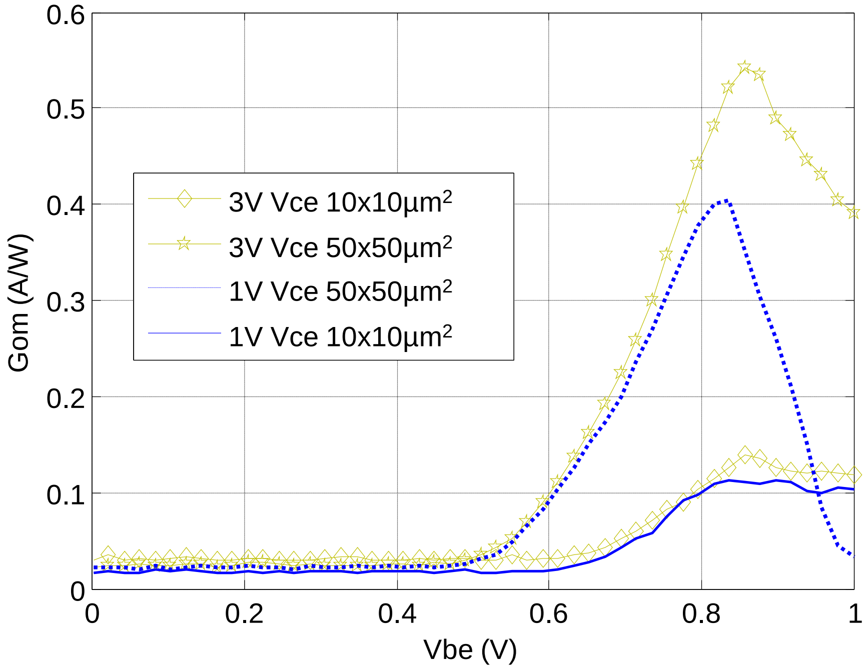

Figure 3-6: Low frequency complete opto microwave responsivity versus base voltage. of 10x10 and 50x50 HPTs at different collector voltages with injected optical power of 2.38mW.

Figure 3-7 shows the complete and intrinsic low frequency opto-microwave gain of 5x5µm^2, 10x10 µm^2 and 50x50 µm^2 sized HPTs versus of the base bias voltage Vbe at a fixed Vce of 3V.In HPT mode operation (Vbe>0.6V), the largest optical window size (50x50µm^2) HPT has the highest complete low frequency opto-microwave gain, and the smallest optical window size HPT (5x5µm^2) has the smallest one due to optical coupling efficiency and internal current gain variations. For 5x5µm^2 HPTs complete Gom curve, the HPT mode cannot be seen. Furthermore, it can be observed that Gom in the PD mode is increased in comparison to higher optical window size HPTs. This may be attributed to the increase of the substrate photodiode impact which shadows the HPT effect at low frequency for small size HPT.

However, the low frequency intrinsic Gom at low Vbe (PD mode) is the same for all size HPTs as the substrate photodiode impact is removed. The gap between the intrinsic and complete Gom, in HPT mode, for smallest size HPT is much higher than the larger size HPTs. This may be related to the influence of the substrate photodiode which is much stronger for smaller size HPTs. This gap for 10x10µm^2 and 50x50µm^2 HPT decreases as Vbe increases. Eventually the complete and intrinsic Gom of 50x50µm^2 becomes equal at high Vbe as shown in Figure 3-7. This indicates that for larger size HPTs the substrate photodiode effect is hidden by the internal optical current gain in active region. For 5x5µm^2 HPTs the intrinsic Gom curve, the HPT mode cannot be seen as it is for complete Gom. This is indicating the intrinsic HPT was not well illuminated by the injected optical beam; rather the beam might be illuminating the substrate region. The will be investigate in the coming sections.

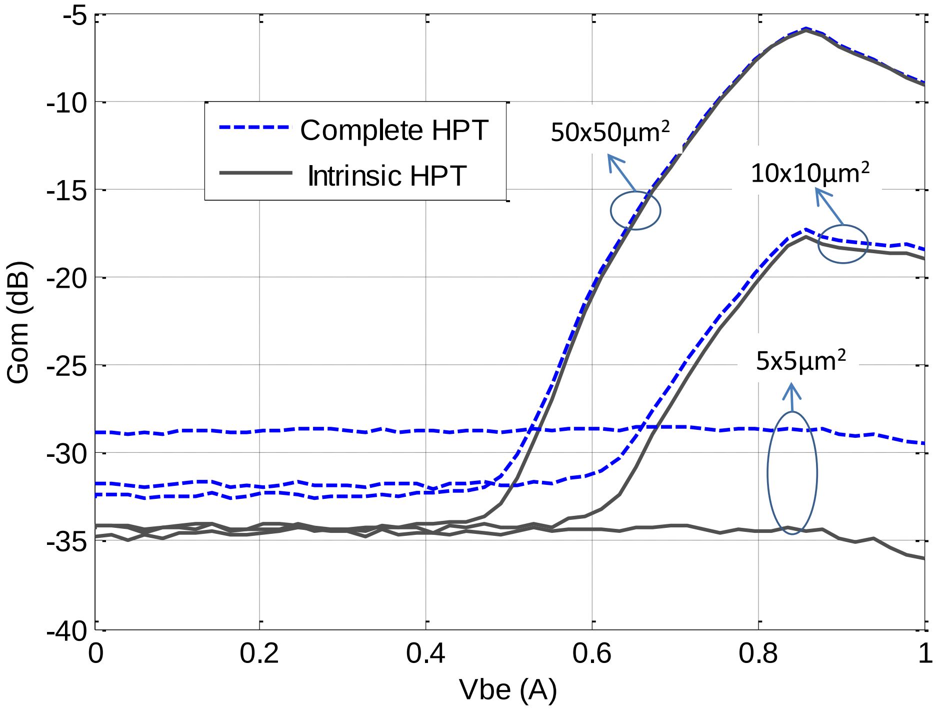

Figure 3-7: Low frequency complete and intrinsic opto microwave gain versus base voltage for 5x5µm^2, 10x10µm^2 and 50x50µm^2 HPTs at 3V collector voltage.

Figure 3-8 shows the measured complete G_{OM} versus of the measured collector current as Vbe is swept from 0V to 1V for different optical window size HPTs. In the 10x10µm^2 optical window size HPT, the peak opto-microwave gain occurs when Vbe is equal to 0.857V at Vce value of 3V. Under this condition, a 10.73 mA collector current is measured. As Vbe is raised above 0.857V, the measured G_{OM} goes lower (Figure 3-8 a) though the measured collector current keeps increasing (Figure 3-8 b). The collector current, which corresponds to the peak of G_{OM}, has a value that increases as the size of the optical window increases. The corresponding Ic for 05xEBC is 5.585mA, for 10SQxEBC is 10.73mA and for 50xEBC is 37.85 mA. These values show the start of the high current operation region of the HPT. If the collector current is above optimal values, then the low frequency gain of the transistor starts the roll off.

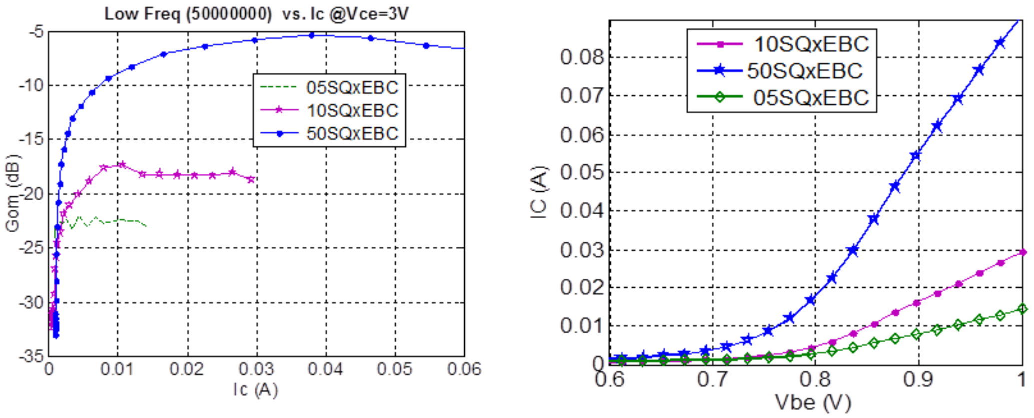

a) b)

Figure 3-8: For various size optical window HPTs a) low frequency opto-microwave gain versus collector current. b) Collector current versus base voltage at Vce=3V

In Figure 3-9 a) the complete G_{OM} is plotted versus of the measured base current Ib as Vb is swept from 0V to 1V for fixed Vce=3V. This shows that the peak G_{OM} could generally be achieved at very small values of Ib under the illuminated condition. It is the lowest possible base current that allows the forward-active mode operation of the HPT. The highest G_{OM} could be achieved in the region of negative Ib as well. The HPT G_{OM} declines as the base current increases further. The optimum Ib to maximize G_{OM} is 9.9μA and it is nearly the same for the three HPTs at Vce=3V and Vbe=0.857V. Figure 3-9 b) shows the base current versus of base voltage for Vce=3V.

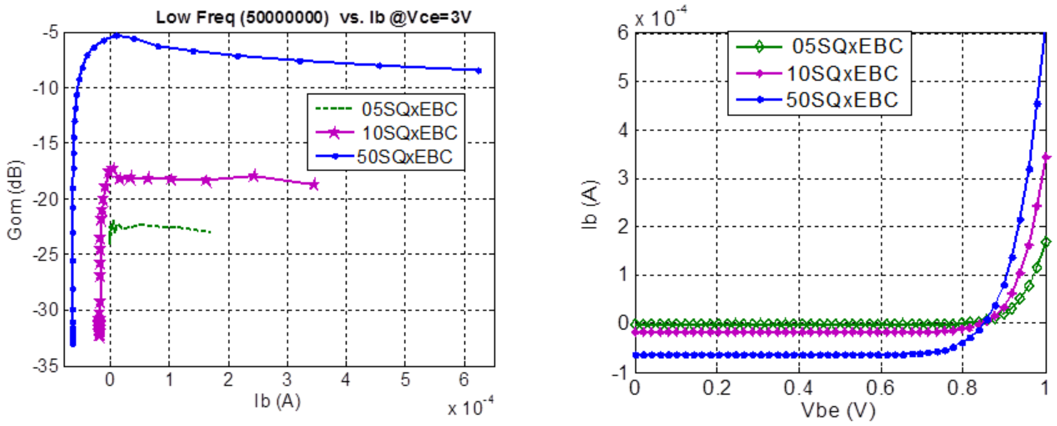

a) b)

Figure 3-9: a) Low frequency complete opto-microwave gain versus base current. b) Base current versus base voltage. For various sized optical window HPTs at Vce=3V

The peak value of the intrinsic and complete low frequency Gom in PD and HPT modes along with their optimum dc bias are presented in Table 3-2. The intrinsic Gom in PD mode has the same value of -34.8dB for all optical window size HPTs. The complete and intrinsic Gom of 50x50μm2 HPT, in HPT mode, have about the same value around of -5.9dB.

Table 3-2: Summary of the peak performance of different size HPTs along with their optimum dc bias.

HPT type	Vce (V)	Vbe(V)	Ic(mA)	$G_{om,PD}$ Complete (Vbe=0V)	$G_{om,PD}$ Intrinsic (Vbe=0V)	$G_{om,HPT}$ Complete	$G_{om,HPT}$ Intrinsic
5x5µm^2	3	0.857	6.50	-28.9	-34.8	-28.69	-34.43
10x10µm^2	3	0.857	10.73	-31.71	-34.8	-17.26	-17.67
50x50µm^2	3	0.857	37.15	-32.35	-34.8	-5.91	-5.98

3.3.2.2 Low frequency current gain vs biasing

Here we optimize low frequency current gain (h_{21}) and low frequency optical current gain (Gopt) in terms of dc bias.

a) Electrical current gain (h_{21})

The electrical low frequency current gain is analyzed in terms of the bias Ib and Vce. The S-parameters of the HPT are measured versus of Ib at different constant voltage Vce and then the current gain (h_{21}) is extracted for S-parameters. The 50MHz low frequency current gain (h_{21}) of the 50SQxEBC HPT is shown in Figure 3-10 a) as a function of Ib. The h_{21} peak occurs at Ib=51.72µA for Vce=4V with a value of 29 dB. The current gain measured at lower Ib and Vce=4V is much higher than the current gain measured under Vce≤3V; this is due to the avalanche gain of the phototransistor.

Figure 3-10b) shows the low frequency current gain of different sized HPTs versus Ib at Vce=3V. 50x50µm2 HPT requires higher base current to achieve its maximum compared to smaller size HPTs thus higher collector current is also measured for this HPT.

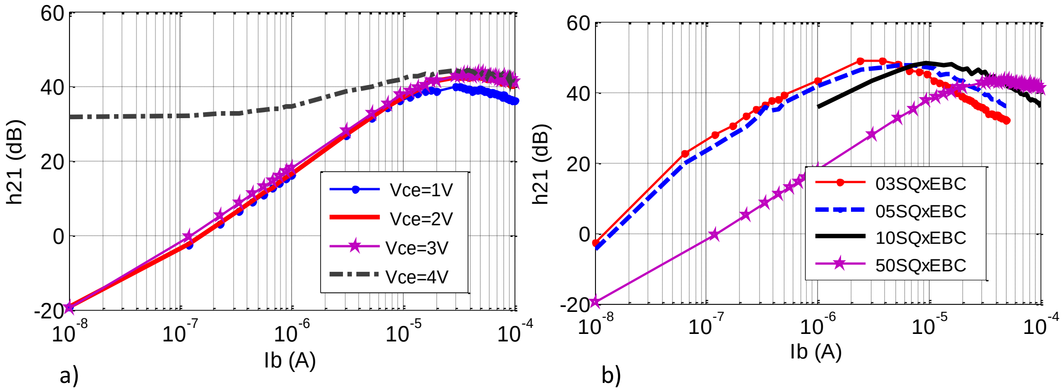

Figure 3-10: a) 50MHz low frequency microwave current gain (h21) of a 50SQxEBC HPT versus base current for different values of collector voltage biasing. b) Low frequency (50MHz) microwave current gain (h21) versus base current for different optical window size HPTs at Vce=3V.

The optimum biasing conditions and the maximum current gain of different size HPT are summarized in Table 3-3. The biasing current and voltage that are presented are selected to reach maximum 50MHz low frequency microwave gain of the HPTs. The low frequency current gain decreases with the optical window size increases. This is due to the fact that at Vce=3V, the smaller optical window size HPT are in avalanche mode.

Table 3-3: Summary of the maximum low frequency (50MHz) electrical current gain of different size HPTs along with the optimum dc bias for the gain.

HPT type	**Vce (V)**	**Ib (µA)**	**Ic(mA)**	**RF max h_{21} at 50MHz (dB)**
03SQxEBC	3	2.42	1.27	48.8
05SQxEBC	3	5.42	3.02	47.7
10SQxEBC	3	9.44	5.50	47.8
50SQxEBC	3	51.72	28.49	43.6

b) Optical current gain (Gopt)

The optical gain is the internal gain of a phototransistor comparing to its photodiode. In other words, Gopt is the difference between the phototransistor opto-microwave gains in HPT mode and in PD mode. Figure 3-11 a) shows the intrinsic and complete low frequency Gopt versus of collector current and base emitter voltage for 10x10µm^2 and 50x50µm^2 HPT at Vce=3V. In terms of Ic, the Gopt reaches its peak for 10x10µm^2 HPT at low collector current compared to 50x50µm^2 HPT (its peak appears at higher collector current) as shown in Figure 3-11 a). At high Ic the Gopt is compressed as the HPT reaches its maximum current injection point.

The optical gain is zero dB until Vbe=0.55V (in PD mode region) and starts increasing for Vbe=0.6V (in HPT mode region) and eventually reaches its peak at Vbe=0.857V in both structures as shown in Figure 3-11 b). The Gopt starts collapses as the Vbe keeps increasing beyond 0.857V due to high current injection again.

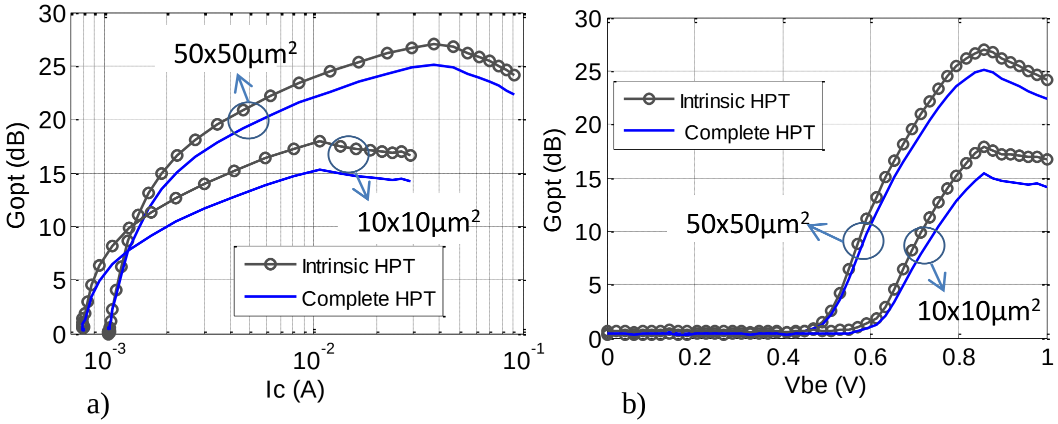

Figure 3-11 Low frequency intrinsic and complete Gopt at Vce=3V a) versus Ic; b) versus Vbe.

The maximum complete and intrinsic optical gain of 10x10µm2 and 50x50µm2 HPT are presented in Table 3-4. The peak Gopt appears at Vbe=0.857V for both HPTs. However, as the measured Gopt value is different for the two HPTs, the maximum collector current measured for 10x10µm2 HPT is smaller than the maximum collector current of 50x50µm2. This is due to the fact that larger device has a capacity to handle larger power (current) than small size device.

Table 3-4: The low frequency complete and intrinsic Gopt along with their optimum bias.

HPT type	**Vce (V)**	**Vbe(V)**	**Ic(mA)**	**Gopt Complete HPT at 50MHz (dB)**	**Gopt Intrinsic HPT at 50MHz (dB)**
10x10µm^2	3	0.857	10.73	15.36	17.93
50x50µm^2	3	0.857	37.15	25.15	27.03

3.3.3 2T and 3T HPT configurations

We show the impact of the base terminal connection (2T and 3T configuration) on the opto-microwave behavior under top illumination condition.

As it is defined in [174] and [203], phototransistors have 3 terminals (these are the base, collector and emitter) in addition to the optical access terminal call the optical window. Based on how we inject the dc polarization; we can operate a phototransistor into 2 main configurations as three terminal (3T) and two terminal (2T) configurations.

- **3T configuration**

In this configuration the RF modulated signal is injected through the optical window, the output of the opto-microwave signal is captured and Vce is supplied through the collector-emitter contact. On the base-emitter contact a dc bias is supplied through T-bias as shown in Figure 3-12 where the RF input of the T-bias is locked by 50Ω. The experimental result of such configuration is shown in Figure 3-14 both in HPT (3T-Vbe=0.857V) and PD (3T-Vbe=0V) modes.

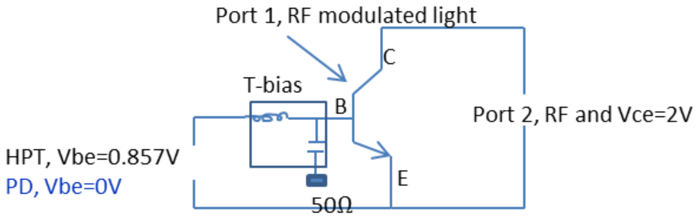

Figure 3-12: 3T configuration

- **2T configuration**

Similarly to the 3T configuration the RF modulated optical signal is injected on the optical window and the output is measured on the collector-emitter contact. Vce is also injected through the collector-emitter contact. The difference with the pervious configuration is on the base-emitter contact where three different connections are possible as shown in Figure 3-13.

a) ***Case one (2T-50Ω on RF and DC):*** Figure 3-13 a) shows a 2T configuration where both the dc and RF terminals of the T- bias are locked by 50Ω. It has similar configuration as 3T in PD mode configuration, as B1500 on the dc bias provides 50Ω load.

b) ***Case two (2T-50Ω on RF only):*** The second type of connection in 2T configuration is shown in Figure 3-13 b), where the dc input of the T-bias is left open and the RF port is loaded by 50Ω.

c) ***Case three (2T-DC contact UP from the base):*** In 3rd connection of 2T configuration, no T-bias is connected on the base emitter pad, rather the base-emitter terminal left open as shown in Figure 3-13 c). The base terminal is unprobed either DC or RF probes.

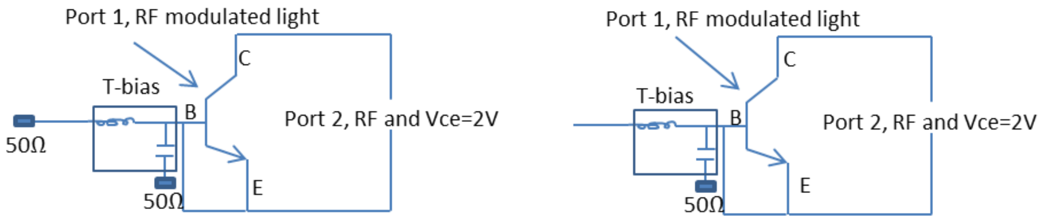

a) 2T-50Ω on RF and DC

b) 2T- 50Ω on RF only

c) 2T- DC contact UP from the base

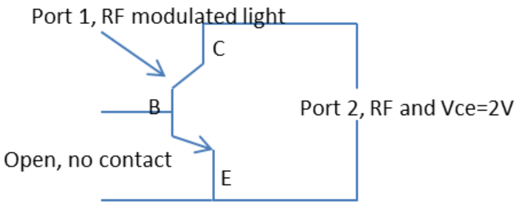

Figure 3-13: Different 2T configurations

Figure 3-14 shows the opto-microwave gain versus of frequency for different configuration and connection of 10x10µm^2 HPT. Form this curve we draw the following observations:

- The 2T configuration when the DC contact is left UP from the base contact (2T-DC contact UP from the base or case three) has very high responsivity at low frequency. For this configuration we can achieve a positive opto-microwave gain of more than +12dB at 50MHz. However, its cutoff frequency is quite small compared to other configurations. This high opto-microwave gain compared to 3T configuration could be due to high current gain under this configuration as the photo-generated holes are blocked on the base-emitter junction (as there is no way to flow out through the base contact) so that they can collect more electrons from the emitter region through the transistor action.
- The 3T configuration in HPT mode (3T-Vbe=0.857V) and 2T configuration when the DC port of the T-bias is left open (2T-50Ω FR Only or case two) have the same frequency response behavior. This could be explaining from the physical nature of the phototransistor: when we operate our transistor in 3T under CV condition, there is a possibility of the flow of holes out of the base contact rather than collecting more electrons from the emitter region, whereas in 2T configuration when the dc connection on the base contact is left open, all the photo-generated holes are kept near to base-emitter junction and then they collect electrons from the emitter region due to transistor action.
- The 3T PD mode (3T-Vbe=0V) configuration and 2T configuration when both T bias ports are loaded by 50Ω (2T-50Ω RF and DC) have the same frequency response behavior.
- For high frequency application, such as greater than 2GHz, 3T under HPT mode, 2T when the base contact is floating and 2T when the DC connection on T bias is floating (2T-50Ω FR Only) have equal frequency responses.

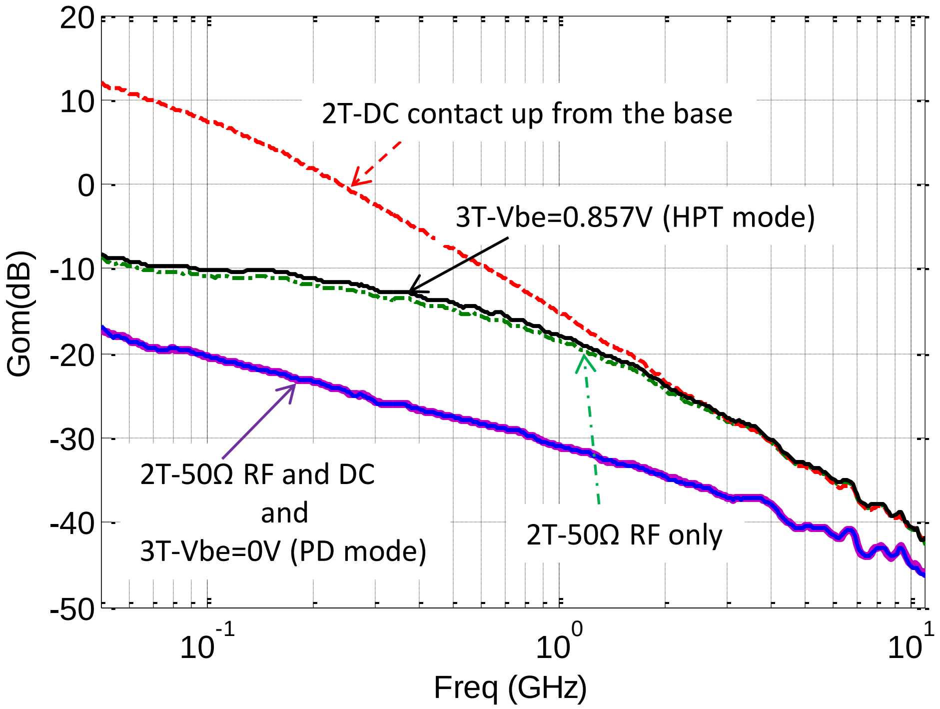

Figure 3-14: Opto-microwave gain versus frequency 10x10µm^2 SiGe HPT under 2-terminal and 3-terminal configuration.

The low frequency opto-microwave gain of the phototransistor in different configuration is summarized in Table 3-5. From this we conclude that the 2T-DC contact up from the base configuration has maximum (+12dB) low frequency Gom.

Table 3-5: The low frequency Gom for different HPT configurations

Terminal configuration	**Vce (V)**	**Vbe(V)**	**Low frequency Gom (dB)**
3T-Vbe=0.857V (HPT mode)	2	0.857	-8.28
2T-50Ω RF only	2	-	-8.43
2T-DC contact up from the base	2	-	+12.00
2T-50Ω RF and DC	2	-	-16.79
3T-Vbe=0V (PD mode)	2	0	-16.79

3.3.4 Optimizing the dynamic opto-microwave behavior

The dynamic behavior of the phototransistor is analyzed through the optical transition frequency f_{Topt}, opto-microwave cutoff frequency f_{-3dB}, and cutoff frequency–responsivity product. This part will focus on the optimization of the dc biasing conditions to maximize the dynamic behavior of the HPT.

3.3.4.1 Optical cutoff frequency

The opto-microwave cutoff frequency is the -3dB cutoff frequency of the opto-microwave gain, G_{OM}. It is measured in using the 50 MHz gain value as a reference, which is the lowest possible frequency of our VNA. This means that the f_{3dB} values are significant above typically 150MHz, and limited by the VNA below. The f_{3dB} curve of 10SQxEBC HPT is shown in Figure 3-15as a function of the DC biasing conditions (Vce and Vbe). The cutoff frequency decreases with increasing Vce from 2V to 3.5V, rises to a peak for Vbe=0.857V and Vce=2V (in the HPT mode region).

The cutoff frequency and low frequency gain (Gom) maxima appear at the same base-emitter bias (Vbe =0.857V) point (see Figure 3-9 and Figure 3-15). However, their maxima are obtained at different emitter-collector biasing (Vce=2V to maximize f_{-3dB} and Vce>3V to maximize the low frequency gain). From this analysis we understand that the low frequency Gom increases whereas f_{-3dB} decreases as Vce increases. This is attributed to the start of the avalanche effect that contributes to the Gom and degrades the cutoff frequency.

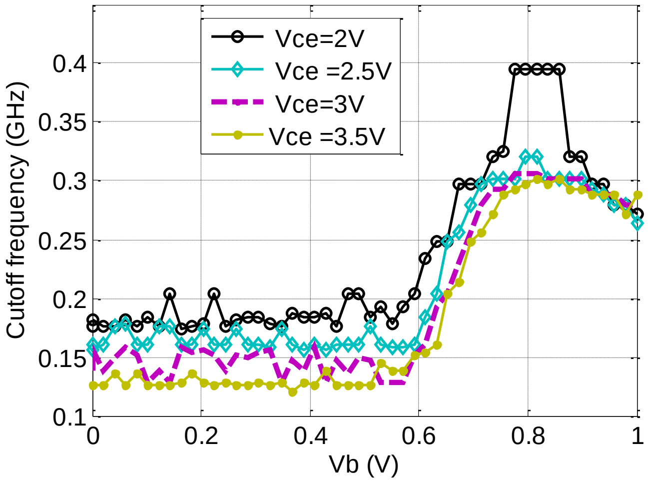

Figure 3-15: Opto-microwave cutoff frequency of 10SQxEBC versus dc biasing.

Figure 3-16 shows the cutoff frequency of different optical window size HPTs as a function of the base voltage at Vce=2V. In the PD mode operation the 5x5µm^2 HPT has a cutoff frequency of 130MHz, the 10x10µm^2 HPT of 176MHz and the 50x50 µm^2 one of 400 MHz. The cutoff frequency in the HPT mode operation (Vbe=0.857V) at the peak of G_{OM} is as follows: 151.5MHz, 395.1 MHz, and 79.55 MHz for increasing optical window size. Usually, the HPT mode operation has a highest cutoff frequency at a given optical window size compared with their respective PD mode cutoff frequency. However for the 50x50 µm^2 HPT the inverse is observed.

The explanation could be as follows: For our measurement we used a lensed fiber having optical beam Full Width Half Maximum (FWHM) of 28µm diameter. It is wider than the optical window size of 10x10µm^2 and 5x5µm^2 HPTs. Thus, when illuminating the device, most of the optical power passes through the light sensitive substrate and creates slow substrate photocurrents. In PD mode operation substrate photocurrent dominates the photocurrent generated in the active area of the devices. As a result the PD mode frequency responses of the smaller optical window sized HPTs have lower cutoff frequency. In HPT mode operation of those smaller HPTs, the substrate current is highly dominated by the photocurrent generated in the active region. And hence the cutoff frequency rises for Vbe>0.65V. However, for the 50x50µm^2 HPT, as the whole optical beam is coupled, there is a reduced substrate photocurrent effect (only from the bottom side). As a result its PD mode f_{-3dB} is higher than its HPT mode f_{-3dB}. Its cutoff frequency dramatically decreases in HPT mode operation because of the rising of the base resistance and the junction capacitances of the larger HPT.

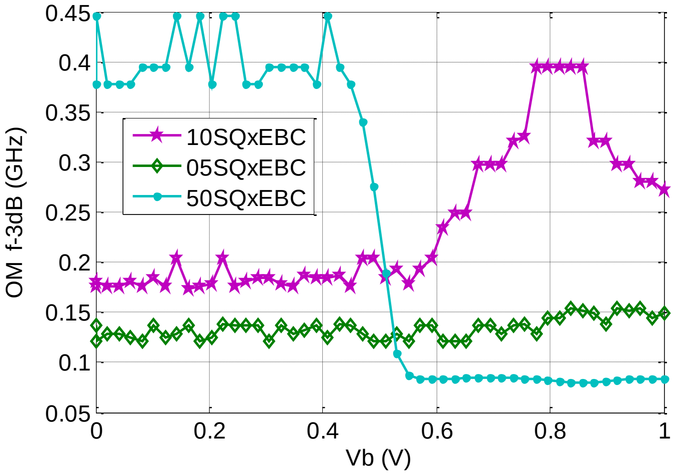

Figure 3-16: Cutoff frequency of different optical window sized HPTs versus base voltage at Vce=2V.

Figure 3-17 shows the low frequency opto-microwave responsivity-bandwidth product of the different size HPTs. Gom*f$_{-3dB}$ product increases with Vbe as it switches from PD mode to HPT mode. In HPT mode, 10x10µm^2 and 50x50µm^2 HPTs have the same peak Gom*f$_{-3dB}$ product, because its high Gom compensates the difference of a very low cutoff frequency. The 5x5µm² HPT has a flat gain bandwidth product. This tends to indicate that the HPT is overwhelmed with its substrate contribution. We hardly see a small increase in the HPT mode. Also some further 2D effect, decreasing its cutoff frequency may additional explain this limitation (this will be discussed in section 3.4). We summarize the peak opto-microwave response in Table 3-6.

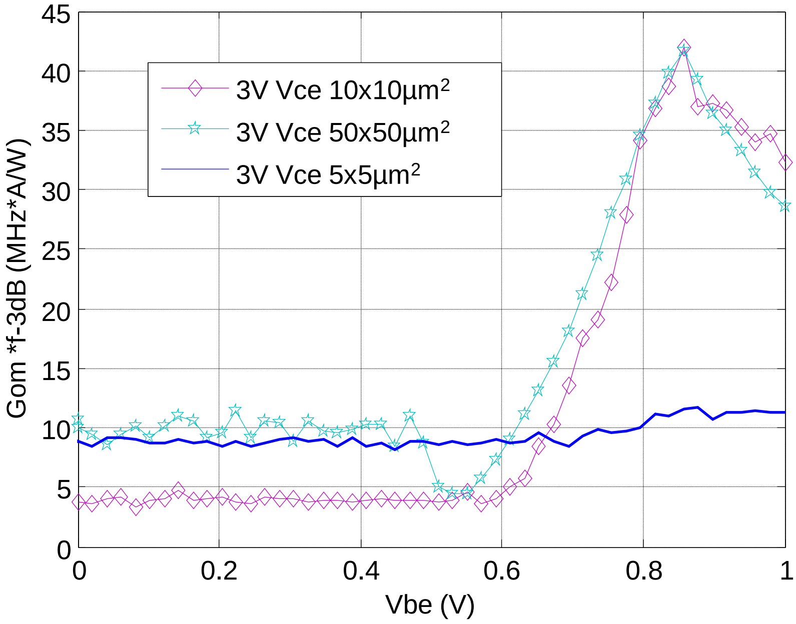

Figure 3-17: Low frequency Gom to f$_{-3dB}$ product versus Vbe for different optical window size HPTs at Vce=3V.

Table 3-6: Summary of the performance of different optical window size HPTs at their optimum dc bias.

HPT type	**$f_{-3dB,HPT}$(MHz)** **at Vce=2V and Vbe=0.857V**	**$f_{-3dB,PD}$(MHz) at Vce=2V and Vbe=0V**	**$G_{om,HPT}$*$f_{-3dB,HPT}$ (MHz*A/W) at Vce=3V and Vce=3V**
05SQxEBC	153.8	136	11.5
10SQxEBC	400	181	41.9
50SQxEBC	79.6	400	41.7

3.3.4.2 Optical transition frequency (f_{Topt}) vs dc bias

As it is defined in chapter 2 section 2.3.1, the optical transition frequency, f_{Topt}, is a frequency at which the optical gain of the phototransistor is equal to one (where the transistor stops amplifying). In this section we optimize the dc biasing points of the HPT that maximizes the f_{Topt}. We also present and compare the intrinsic and complete HPT optical transition frequencies.

a) Complete optical transition frequency ($f_{Topt,comp}$)

Figure 3-18 a) shows the extraction results of optical transition frequencies f_{Topt} for phototransistors having 10x10 and 50x50µm^2 optical window size versus of the collector current. From these curves and electrical transition frequency (f_T) vs I_C curve presented in Figure 3-21, we can directly compare the evolution of f_T and f_{Topt} under the same biasing condition (let say Vce=3.5V). That means we can compare the transition frequency measured when the RF power is injected through the base (f_T) and when the RF power is injected through the optical window by modulating the optical power (f_{Topt}). Compared to the electrical transition frequency, for non-optimum position of the optical probe, the optical transition frequency is dramatically reduces to 2.2GHz from 50GHz for 10x10µm^2 under the same biasing condition (see Figure 3-21 and Figure 3-18 a). This is due to the presences of additional capacitance and transit time related to the injected optical power.

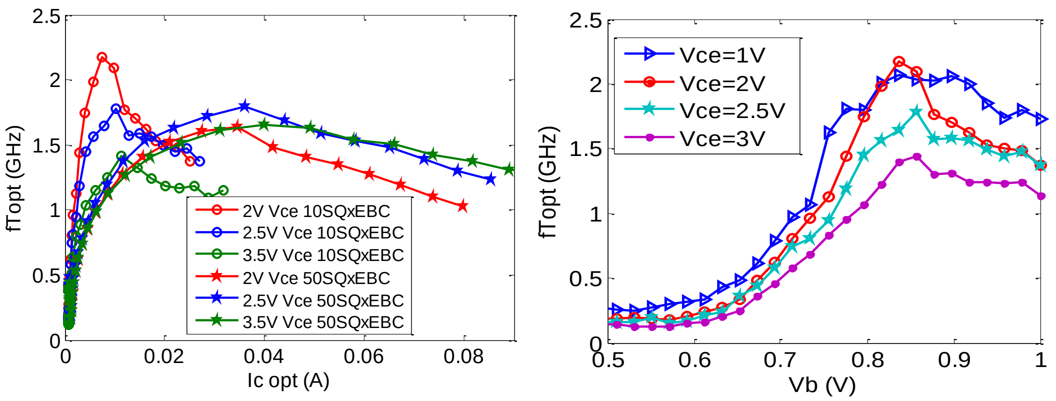

a) b)

Figure 3-18: Optical transition frequency at non-optimum position of the optical probe with different Vce: a) versus collector current of 10x10µm^2 and 50x50µm^2 HPTs b) versus Vbe of 10x10µm^2 HPT.

For the HPT having 10x10µm^2 active surface area, the optical transition frequency is getting smaller as Vce increases. It can be explained as when Vce increases, the base collector depletion area increases, which in turn increases the junction capacitance of the phototransistor. It is not the case for 50SQxEBC under the same biasing condition as it can handle high power. The maximum value of f_{Topt} of 50x50µm^2 HPT is 1.56GHz at Vce=2.5V and Ic =0.036A as presented in Figure 3-18 a).

We also optimize the optical transition frequency, $f_{Topt,}$ in terms of Vbe and Vce. The preliminary results of f_{Topt} of 10x10µm^2 HPT versus of the base voltage at various Vce are extracted and shown in Figure 3-18 b). For this optical probe position, a maximum f_{Topt} of 2.2GHz is obtained at Vbe=0.857V and Vce=2V.

b) Intrinsic optical transition frequency ($f_{Topt,int}$)

The complete and intrinsic opto-microwave gains versus frequency at non optimum optical probe position are plotted in Figure 3-19 for both photodiode (Vbe=0V) and phototransistor (Vbe=0.857V) modes at Vce=2V. The frequency response of the substrate photodiode at the same location of the optical probe is modeled and plotted in the same figure. From this we can extract the complete and intrinsic optical transition frequencies as it is indicated in the figure.

As we can observe in Figure 3-19, the impact of the substrate photodiode is observed at low frequency in HPT mode of operation and this impact is not visible at high frequency (f>200MHz) as the substrate response is dominated by the internal transistor action. However, in PD mode, the influence of the substrate photodiode is observed at all frequencies up to 10GHz. Hence, we conclude that the substrate effect is more visible for SiGe/Si photodiode than for SiGe/Si phototransistor.

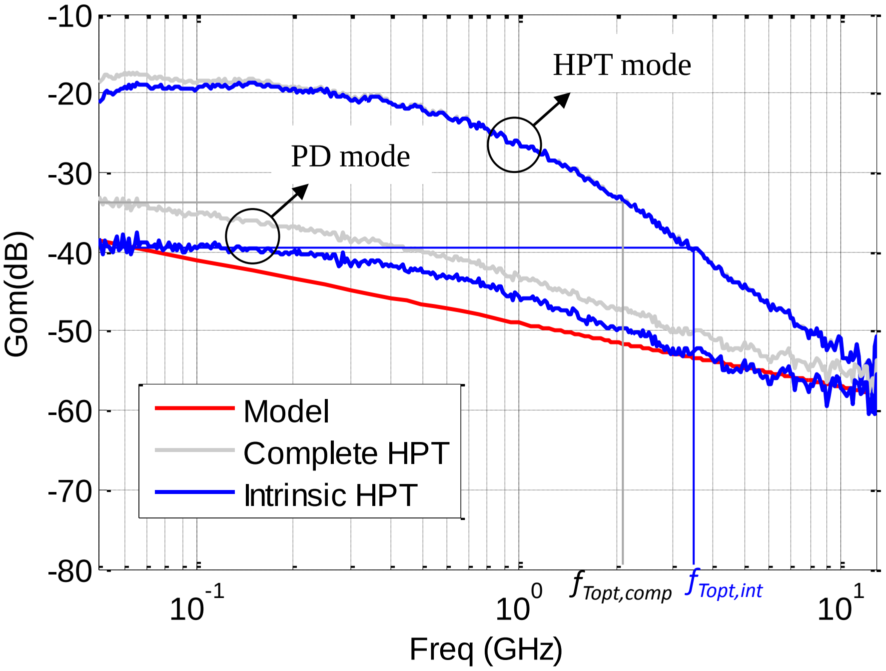

Figure 3-19: The complete and intrinsic Gom versus frequency for 10x10µm2 HPT in PD and HPT modes at Vce=2V.

As we observe in Figure 3-19, the substrate photodiode contributes to the low frequency gain and thus lower the 3dB cutoff frequency. However it contributes to the overall detection and is still contributing even up to 10GHz. Figure 3-20 shows the complete and intrinsic optical transition frequency curve versus the collector current Ic of 10x10µm^2 and 50x50µm^2 HPTs at Vce=2V. After removing the substrate response, the optical transition frequency is improved from 2.17GHz to 3.5GHz for 10x10µm^2 and from 1.8GHz to 3GHz for 50x50µm^2 HPT. The intrinsic optical transition frequency of 50x50µm^2 HPT is smaller than the intrinsic optical frequency of 10x10µm^2 HPT. This is due to the higher junction capacitances and base resistances in 50x50µm^2 HPT as the surface area is larger. Table 3-7 provides the peak values of the intrinsic and complete optical transition frequencies of 10x10µm^2 and 50x50µm^2 HPTs with their corresponding dc bias points.

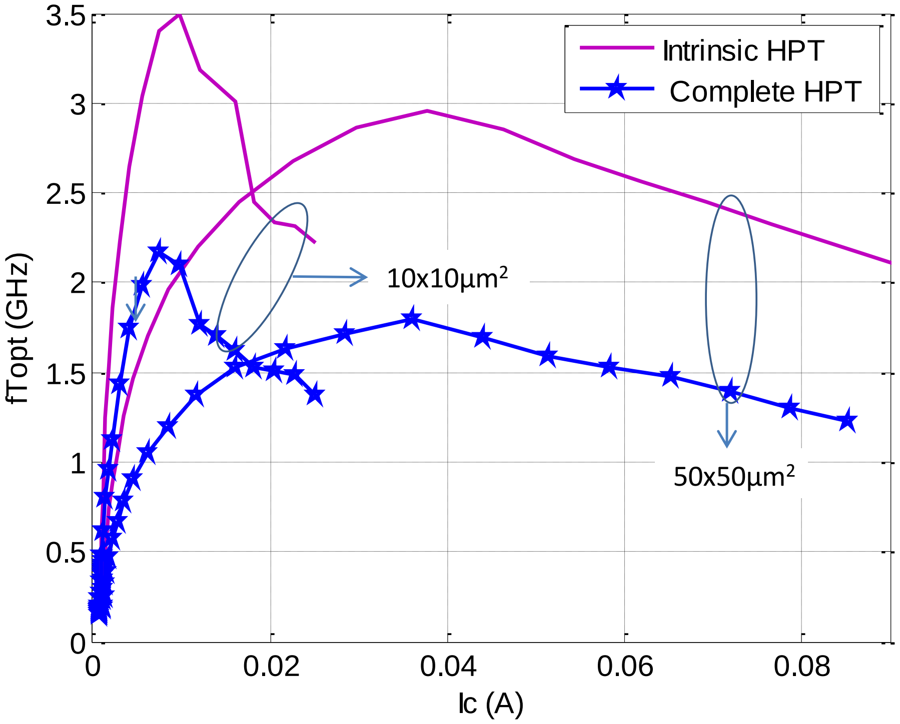

Figure 3-20: The complete and intrinsic optical transition frequency versus collector current for 10x10µm^2 and 50x50µm^2 HPTs at Vce=2V.

Table 3-7 : The peak values of intrinsic and complete HPT optical transition frequencies along with their optimum dc bias.

HPT type	**Vce (V)**	**Vbe(V)**	**Ic(mA)**	**f_{Topt} Complete HPT (GHz)**	**f_{Topt} Intrinsic HPT (GHz)**
10x10µm^2	2	0.857	7.5	2.17	3.5
50x10µm^2	3	0.857	36.0	1.8	3.0

3.3.5 Conclusion on dc bias

According to this study we conclude that at Vbe=0.857V and Vce=3V the low frequency behaviors (Gopt, Gom and h21) are maximized. However, the dynamic behaviors (f_{Topt}, f_{-3dB}) are optimized at the same Vbe and Vce=2V for smaller size HPTs. Thus we will use Vbe=0.857V (under HPT mode) and Vce=3V or 2V for further opto-microwave experimental studies such as the localization of photocurrent sources in the structure and 2D dependence of dynamic behavior in the following section.

We have observed the impact of the base terminal contact on the low frequency behaviors. We understand that the substrate photodiode degrades the dynamic behavior and contributes to the low frequency behavior in SiGe/Si HPTs with a great impact in the PD mode operation. In this 1st study we also understand that 10x10µm^2 HPT have better performance in terms of frequency, even though it has lower responsivity compared to 50x50µm^2.

3.4 Two dimensional Electrical Extension effects

3.4.1 Introduction

In this section, we analyze the electrical frequency limitations from the HPT, and its deviation from the standard HBT behavior.

The electrical transition frequency f_T versus I_C characteristic is shown in Figure 3-21 for a SiGe HPT with different optical window sizes. Figure 3-21 can be explained as follows: From a technological point of view all the four HPTs have the same vertical stacks. The only difference is the section size of the extended emitter, base and collector (optical window size). As a result their electrical characteristics (the transition frequency) mainly differ from their surface area.

As expected the larger devices (50x50µm^2) can handle high current. But, in such a large HPT the transition frequency is mainly limited by the capacitance of the device as its surface area is too large. In our device we obtain the maximum f_T of 28.5GHz for a 50x50µm^2 HPT. As the 10x10µm^2 HPT has a smaller surface area compared to the 50x50µm^2 HPT, its f_T is much larger and reaches up to 50GHz. These values have to be compared to the 50GHz value of pure HBT from the technology.

However, we observe an unusual behavior for very small size HPTs (like 3x3µm^2 and 5x5µm^2) compared to larger size HPTs. Theoretically such smaller size HPTs may have similar or even higher f_T as the junction capacitance gets smaller. But the 3x3µm^2 HPT has the lowest f_T (26.5GHz) while the 10x10µm^2 HPT appears to be optimum with f_T as high as 50GHz.

Phenomena that limit the f_T at lower dimensions of HPT have then to be investigated. Increasing the size to 10µm appears beneficial and optimum as it reached the optimum value of pure HBT, but increasing further limits again the f_T. This is more intuitive considering the increasing in capacitances and access resistances of such large 50x50µm² HPT.

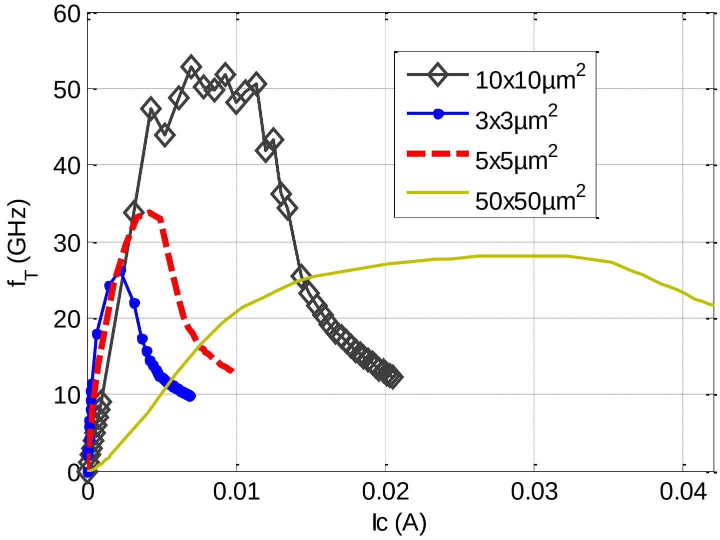

Figure 3-21: A typical f_T versus I_C characteristic for SiGe HPT of different optical windows size at Vce=3.5V.

This unusual frequency behavior of the HPTs could be due to the 2D dependency of carrier movement. From the design point of view the optical window size W is varying from 3µm, 5µm, 10µm and 50µm. We believe that the total optical window size W (see Figure 3-22) may not act electrically as an active transistor. We believe that the area under the emitter contact may be the only active area of the transistor with however a partial spreading of the electrical active region in its vicinity into the optical window. The active region below the emitter is fixed to l= 1.5µm for the four HPTs. Hence the effective active area of the transistor could be modulated in size due to the dc supply bias. That means that due to the dc bias the effective active region of the transistor could be extended into the optical window as shown in Figure 3-22. The extension of the electrical region, Δ, could be also dependent on the optical window size. The properties of the carrier flow could be modified for each HPTs size and thus the frequency behavior modified.

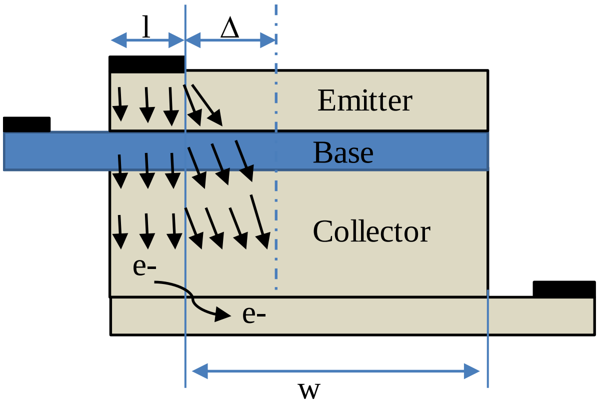

Figure 3-22: The simplified schematic picture of the transistor under study along with the vertical and lateral carrier flow.

In order to validate and analyze further such a mechanism, we propose further experimental investigation supported through some theoretical models. In the first part we present the extraction of junction capacitances and transit times. We then analyze the experimental results, related to the size of the transistor, to draw a hypothesis about the variation. The theoretical model to explain the 2D dependency of the transit time and capacitance is presented in the second part. We then compare the electrical transition frequency curves versus the current density, where the collector current density is deduced from the current to surface ratio with the surface computed according to the active part of various models. Finally, the maximum transition frequency, fmax, and the 2D dependency of the base resistance and base-collector junction capacitance related to the dc bias are presented.

3.4.2 Experimental hypothesis

The values of the forward transit time and junction capacitances can be easily extracted from a plot of the global time delay ($\tau_{tot} = 1/2\pi f_T$) versus 1/I_C, as explained in chapter 2. Figure 3-23 a) represents the global time delay of a 5x5µm^2 HPT at different Vce. It also shows the way to extend the slope and to obtain y-intercept.

Figure 3-23 b) shows the global time delay at Vce=3.5V for different sized HPTs. At low I_C the global time delay versus 1/I_C curve is nearly linear. As it is explained in chapter 2 section 2.7.1 the junction capacitance can be obtained from the slope. As we can see in Figure 3-23 c) representing the first derivative of the global time delay versus 1/Ic, the slope is constant after the high injection region, meaning that the capacitance is not varying with I_C, for all types of HPTs except 50x50µm^2. This exception will be investigated further.

The forward transit time τ_F can be determined from the y-axis intercept at infinite collector current (see chapter 2 section 2.5.1) as shown in Figure 3-23 a).

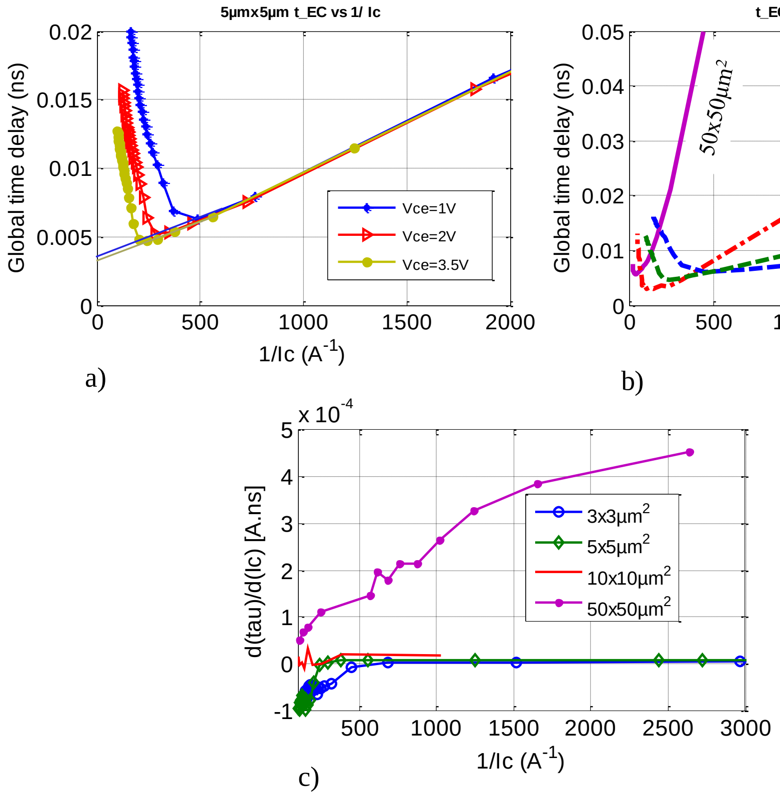

a) b)

c)

Figure 3-23: Global time delay versus 1/Ic a) 5x5μm^2 HPT at different Vce to show how to extract the junction capacitance and transit time, b) Different size HPTs (3x3μm^2,5x5μm^2, 10x10μm^2 and 50x50μm^2) at Vce=3.5V and c) The first derivative of global time delay with respect to 1/I_C.

The extracted values of the junction capacitance and transit time of 3x3μm^2, 5x5μm^2, and 10x10μm^2 and 50x50μm^2 optical window sized HPTs are presented in Table 3-8. As expected the transit time and the junction capacitance of 50x50μm^2 HPT are larger than for the three other structures as its base-emitter and base-collector junction surface areas are larger. The transit time of 3x3μm^2 was expected to be the smallest, mostly due to its capacitance and resistance contributions as $\tau_F = C_{BC}\,(R_E + R_C) + \tau_b + \tau_e + \tau_{bc}$. But it has a higher transit time than the 10x10μm^2 and 5x5μm^2 HPTs. This could be due to the variation of the electrical field in each transistor that modifies the electrical extension region, Δ, of the active area of the transistor, and may create either larger capacitances or may increase the path length of carriers, mostly increasing the base-collector transit time. This fact is analyzed in the following section with the help of theoretical models.

Table 3-8: Capacitance and forward transit time extracted from figure 2.26 b) for different sized HPTs (3x3μm^2, 5x5μm^2, 10x10μm^2 and 50x50μm^2 HPTs)

Device size (μm^2)	**Transit time (ps)**	**Slope (A.s)**	**Capacitance (pF)**
50x50	5.5	1.95E-13	7.5540
10x10	1.5	2.06E-14	0.7979
5x5	3	7.25E-15	0.2805
3x3	5.4	2.80E-15	0.1083

3.4.3 Transit time extrapolation model

In this sub section the impact of the optical window size on the transit time is investigated and explained with the help of theoretical models. We focus our analysis on how the size of the optical window modifies the electrical extension region.

Figure 3-24 shows the emitter area top view along with the emitter contact and the electrical extension region of 3x3µm^2, 5x5µm^2 and 10x10µm^2. The size of the emitter contact, l, is the same for all transistors. Due to the presence of the electrical extension region Δ, the carrier movement experiences two phenomena as shown in Figure 3-22.

- In the vertical flow region (the region under the emitter contact) the carriers move vertically. Therefore the forward transit time is only due to the pure vertical flow carriers.
- In the extension region, Δ, the carriers flow both vertically and laterally. Thus, the forward transit time is extracted from a 2D lateral and vertical movement of carriers.

However, does the electrical extension region, Δ, depend on the optical window size, W, at the same dc supply bias?

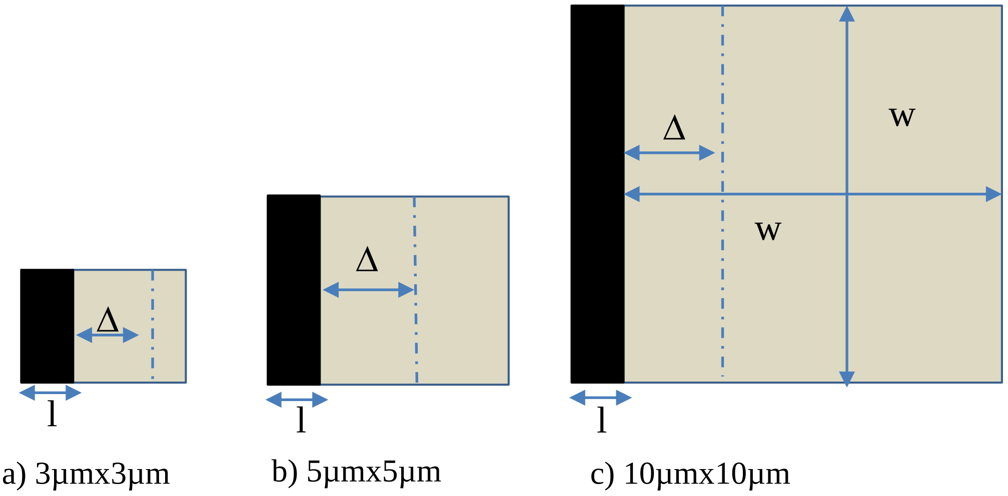

Figure 3-24: The schematic of the total surface area and active surface area of the transistor.

To answer the above question we consider the following three models that we will then analyze using the experimental results presented in Figure 3-26:

Model one: In this model we assume the electrical extension region to be independent on the optical window size, W (Δ=constant**)**.

For this assumption the section ratio, SR, can be determined from the ratio between the regions of the phototransistor where only a vertical flow of carriers exists (l width) and where both a vertical and a lateral flow of carriers (Δ width).

Thus SR can be written as:

$$SR = \frac{\mathrm{W}.l}{\mathrm{W}.(\mathrm{l}+\Delta)} = \frac{1}{(1+\Delta/l)} \tag{3.6}$$

This indicates that the section ratio does not depend on the optical window size. As a consequence, the overall current is a constant share of the purely vertical current contribution and the 2D current contribution. The electrical transit time should not vary with the opening surface.

Model two: In this case we assume that the electrical extension region, Δ, is dependent on the optical window size, W. The dependency of Δ on W, at the same dc supply, is due to the lateral variation of the built in electric field due to the voltage difference between the sub-collector at the collector contact and the base voltage beneath the emitter contact. It appears indeed that neither the base nor the collector is an equipotential from physical simulations of the potential within the cross-section of the HPT from [260] as shown in Figure 3-25. As the electrical field increases, it may lead to an increase of lateral path and thus of the transit time when W reduces. In this case the transit time is expected to vary with the optical window.

It has to be noted that our SiGe HPT has actually only one emitter contact, as opposed to [260], which lies on the left hand side of the HPT, at the opposite of the collector contact. This may then exacerbate further the lateral electrical field and voltage inhomogeneity in the base and collector regions.

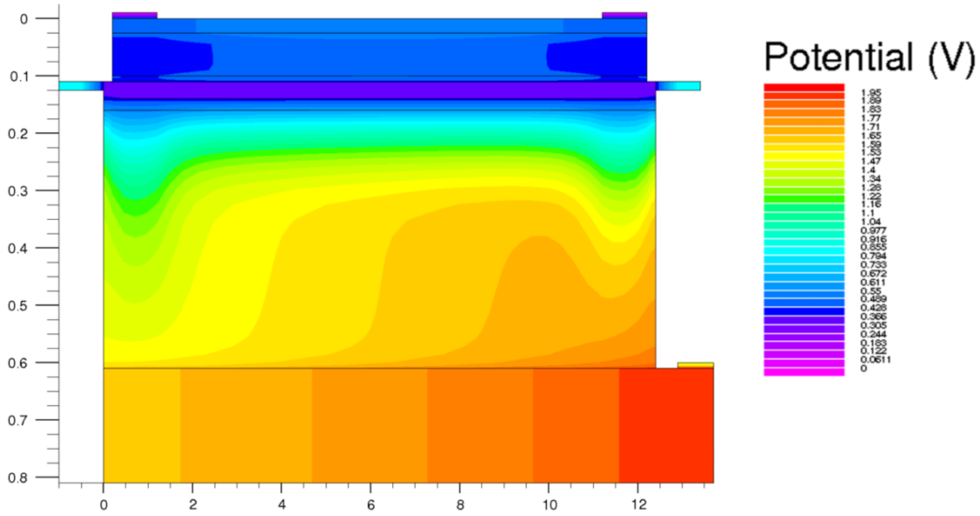

Figure 3-25: The potential distribution over the HPT structure simulation result [260]

Model three: In the last case we assume that the lateral flow of carriers occurs in all regions of the transistor (i.e Δ=W) under the same dc bias condition. Under this assumption the transit time increases directly with the optical window size as the lateral distance increases.

Experimental observation: In order to observe in which one of the above three situations is our transistor working, we experimentally extract the transit time of various size HPT (3µm, 5µm, 10µm and 50µm). The result is presented in Figure 3-26. It shows that the transit time decreases as the optical window size increases from 3µm, 5µm to 10µm. This proves that the electrical extension region, Δ, depends on the optical window size, W. This is because the lateral electrical field is higher with lower dimension under the same dc biasing condition. Thus the lateral flow of carriers may dominate over the vertical one when the optical window size is smaller. This finally increases the forward transit time of the smaller transistor as shown in Figure 3-26. This fits with the assumption of model two.

The transit time of W=50µm optical window size transistor is however much larger. This may be due to the fact that the collector surface and sub-collector dimension gets so large that the $R_C.C_{BC}$ term of the transit time becomes predominant. The capacitance increases with the width of the window and is proportional to l.(l+Δ). On the other side the resistance is controlled by the length from the collector contact to the vertical point below the emitter active region. This length is then approximately the optical window size. The width of this resistance is also defined by the width of this optical window. Thus, as the length and width are almost equal (when considering Δ small or negligible for the 50x50µm² HPT), the resistance keeps constant. In overall, the $R_C.C_{BC}$ product then increases.

This then keeps consistent with model 2 and consolidates this approach.

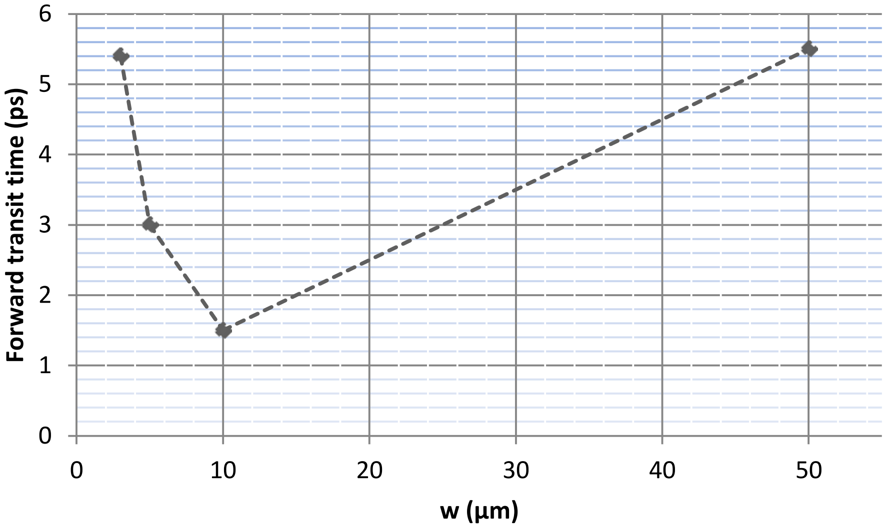

Figure 3-26: Experimentally measured forward transit time versus the optical widow size at Vbe=0.823V and Vce=3.5V

3.4.4 Geometrical dependence of the capacitance

In this section we present the geometrical dependence of the capacitance related to the electrical extension region Δ. The capacitance is extracted from the f_T curve versus I_C at low collector currents. The result is given in Figure 3-27 which shows that the device capacitance increases with the optical window size W, as expected.

The junction capacitance increases with the size of the HPT by assuming that the total surface area of (l+W).W determines the capacitance of the HPT. However, as the emitter contact is smaller than the total emitter size, the definition of the capacitance might be far different from this. Thus, we are interested in observing closely this phenomenon by comparing experimental results with a number of mathematical models. Here we define three models as shown in Figure 3-28 (Model 1, Model 2 and Model 3) that have the purpose to consider either a 2D electrical extension effect (Δ) or not, according to extreme cases.

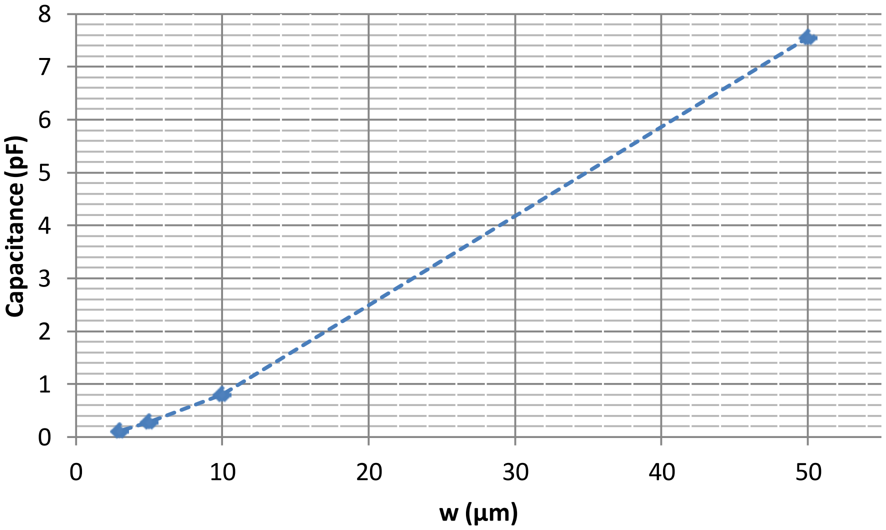

Figure 3-27: Experimentally measured junction capacitances versus the optical window size.

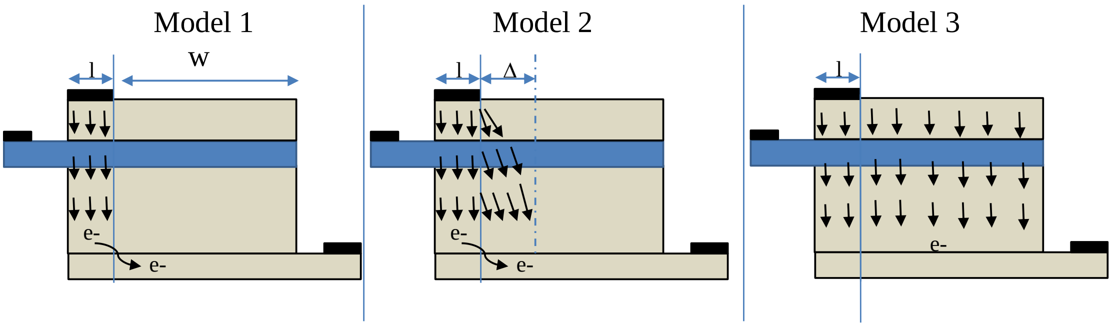

Figure 3-28: The possible behavior of the transistor under dc bias.

Model 1: In this model we assume that the flow of carriers is only vertically under the emitter contact. Hence the capacitance of the transistor can be determined by the surface area under the emitter contact. This represents a case where there is no electrical extension Δ. Mathematically this can be modelled as shown in equation(3.7):

$$C = \frac{\varepsilon . l . w}{w_{SCR}} \tag{3.7}$$

Where w_{SCR} is the junction space charge region width and ε is the dielectric permittivity.

Model 2: In this model we assume that the flow of carriers is vertical under the emitter contact, l, and both vertical and lateral under electrical extension region, Δ. Hence the surface area of the active region of the transistor is increased by Δ. As a result the capacitance can be determined by the surface area under the emitter contact and electrical extension region. In this model the electrical extension region, Δ, depends on the optical window size. Mathematically the capacitance can be expressed as:

$$C = \frac{\varepsilon .(l + \Delta). \mathrm{W}}{\tilde{w}_{SCR}} \tag{3.8}$$

Where $\tilde{w}_{SCR}$ is an average value of the space charge width of the base-emitter and base-collector all over the transistor.

Model 3: In third model we assume that the flow of carriers is distributed through all regions of the transistor, l+W. This represents a case where there is no restriction of the carrier path beneath the emitter metal contact only, and thus no concept of electrical extension Δ. In other words it would be a case where the high doping of the polysilicon of the emitter and the high doping of the base are providing sufficiently low resistances to create a homogenous voltage and current distribution across the HPT. Hence the capacitance of the transistor can be determined through the whole surface area of the transistor. Mathematically this can be model as:

$$C = \frac{\varepsilon .(l + W). \mathrm{W}}{w_{SCR}} \tag{3.9}$$

We consider l=1.5µm from the design, and we assume that εr= 11.7, this is to say that silicon is the dominant component of the HPT. We assume the smallest envisageable space charge region width is of w_{SCR}=10nm thus providing the maximum boundary to the capacitance. Figure 3-29 shows the curves of the three models expressed in terms of ratio of the capacitance to the optical window size (C/W) versus the optical window size, W. Model 1 and Model 3 show the two extremes of the possible operation of the transistor. That means for model l, the C/W ratio is constant whereas for model 3 it linearly increases with W. Model 2 is an intermediate model, which lies between model 3 and model 1. Comparing measurements data in Figure 3-29 and the model trends, it appears that the HPT is rather following a model 2 shape. This is then an additional verification of the validity of this model proving that Δ varies with W. From this we understand that the junction capacitance is modified by the electrical extension region Δ.

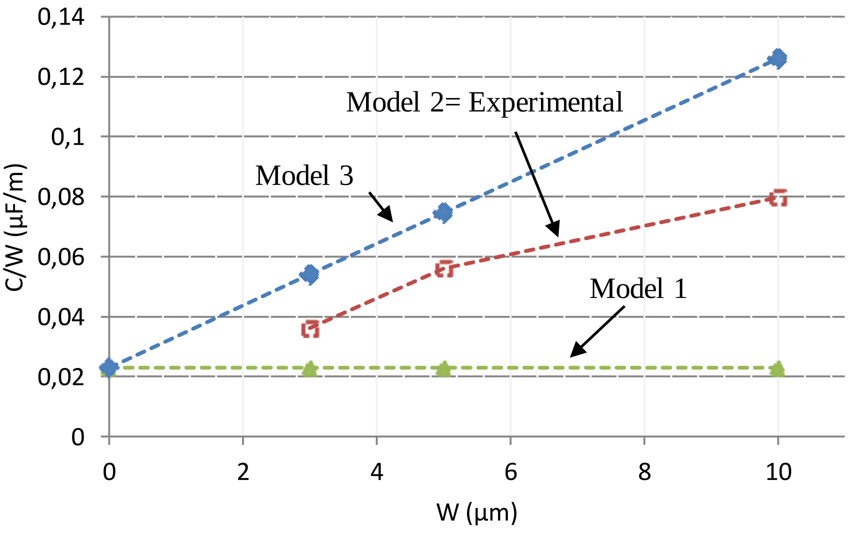

Figure 3-29: C/W versus optical window size curve for the three models, and experimental data for Vce=3.5V and Vbe=0.823V.

3.4.5 Transition frequency, fT, vs current density

To validate the above models we plot the electrical transition frequency versus the collector current density as shown in Figure 3-30. The current density is computed by considering the effective active area of the intrinsic transistor from the above three models. Hence we compute the current density for each model as shown in Table 3-9

Table 3-9: Current density computation for different models

Model	**Collector current density (Jc)**
Model 1	$I_C / \mathrm{W}.l$
Model 2	$I_C / \mathrm{W}.(l+\Delta)$, thus $\Delta = f(\mathrm{W}) = I_C / w.J_C - l$
Model 3	$I_C / \mathrm{W}.(l+W)$

From this result we can observe that the peak of f_T appears at a different collector current density for models 1 and 3 as shown in Figure 3-30 a) and b) respectively depending on the transistor size. This comes from the fact that the high injection degradation starts appearing at some threshold current density which varies with the size of the transistor. However, one may consider that the injection level is mostly controlled by the doping levels (which are the same for all HPTs) and hence the f_T curve in high injection region should follow the same decreasing for all HPTs; so having a convergence of the f_T curve at high current density. We therefore define the Δ dimension in model 2 to be adjusted so that all HPTs have their f_T curves following the same decrease in high injection as presented in Figure 3-30 c). According to model 2, the electrical extension region (Δ) is expected to decrease while the optical window size (W) increases. According to the result from the Figure 3-26, we can even assume that the electrical extension region (Δ) of 50µm HPT is negligible, which means Δ=0. This is our reference point to be able to define values for Δ as a function of the HPTs size. The values of Δ that are then extracted are plotted as a function of W in Figure 3-31.

As a result of this optimization, we can observe that the peaks of the f_T are then well aligned for the four HPTs as shown in Figure 3-30 c). We can also observe that while the slope of f_T at low Jc are not equal for models 1 and 3, they have nearly similar slopes for model 2. This means the capacitance per unit of active surface are similar for all phototransistor, which is consistent in the fact they have exactly the same vertical stack.

From this analysis we then confirm the validity of our proposed model of 2D electrical extension effect. By extracting such an average and effective Δ width of such an extension, we can unify the behavior of all HPTs as a function of their size.

The active region of the transistor is neither only under the emitter contact nor the whole emitter (l+w), it is rather determined by the emitter contact size and the electrical extension region, Δ. This electrical extension region depends on the electric field distribution in the transistor and the size of the optical window, and is increased when the voltage gradient gets higher between the base contact and the collector, thus, at a given Vcb value, when the size of the HPT decreases, which is a confirmed trend as observed by the result of Figure 3-31.

According to this extraction of the Δ value, we observe that for HPT of 3µm in size of optical window, and then 1.5µm of emitter contact and 0.7µm of regions around the emitter contact which are shadowed by the metal layer above, thus 5.2µm in width in total, the electrical extension comes to be as high as 3µm.

This explains that the electrical field in such a structure is highly transverse and justify then why this structure comes to be the slowest test structure as compared to the 5x5µm² and 10x10µm² optical window sizes HPTs. A clear design rules could then be deduced to improve their speed: perspective would be: - to get a symmetric contact of the collector, or even circular shape, that will make the electrical field more vertical; - to get simultaneously a symmetrical contact of the base and emitters; - eventually to fragment the HPT in smaller individual HPTs, as the electrical extension may reach a limit in its increase. This limits is however not visible from the curve yet.

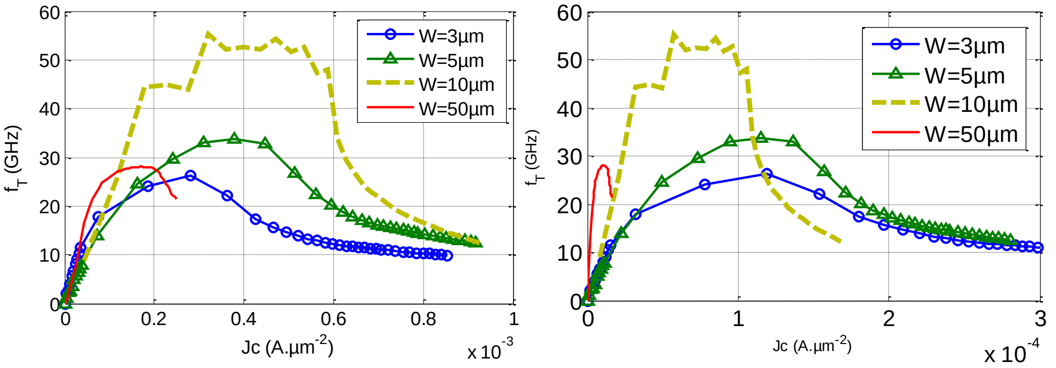

a) Model 1

b) Model 3

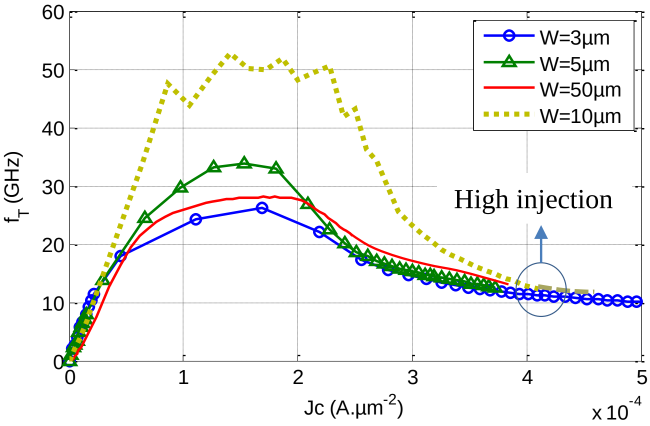

c) Model 2

Figure 3-30: Electrical transition frequency versus current density.

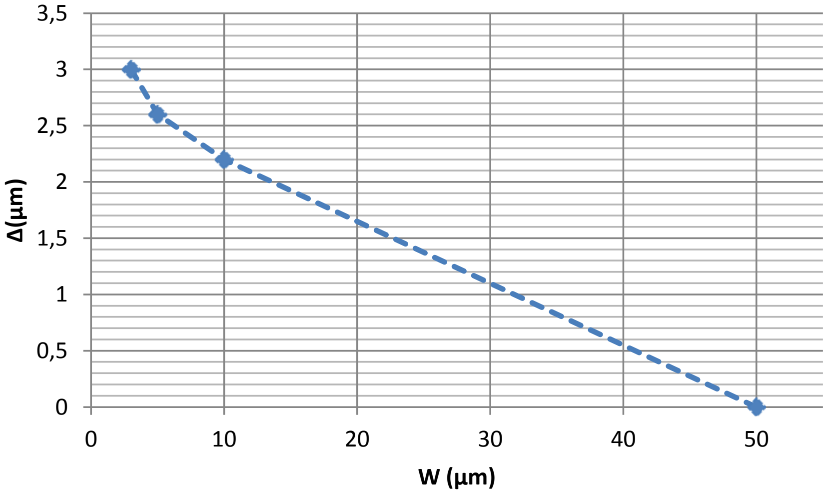

Figure 3-31: Electrical extension region, Δ, versus w

3.4.6 Maximum Oscillation frequency-f_{max} and $C_{BC}.R_B$ model

In this part we present the maximum oscillation frequency of different size phototransistors to observe its behavior versus the size of the phototransistor and to provide another verification of our theoretical model. Its size dependency is investigated through experimental results. The product of the collector-base junction capacitance and base resistance is extracted experimentally. It is then analyzed with respect to the dc bias and compared with the theoretical model previously proposed.

a. Maximum oscillation frequency f_{max}

f_{max} is defined as the frequency at which the power gain of a bipolar transistor drops to unity. An expression for f_{max} of the transistor is:

$$f_{\max} = \sqrt{\frac{f_T}{8\pi C_{BC} R_B}} \tag{3.10}$$

Where $R_B = \rho \frac{L}{t_B.\mathrm{w}}$ is the neutral base resistance, C_{BC} is the base-collector junction capacitance, ρ is the resistivity, L is the base length under the active region and t_B is the base thickness.

This equation shows that the f_{max} of a bipolar transistor is determined not only by the f_T but also by the collector-base capacitance C_{BC} and the base resistance R_B. These two parameters have great influence on the electrical performance of the HPT.

Figure 3-32 shows the extraction results of the maximum oscillation frequency f_{max} as a function of the current, for phototransistors having different optical window sizes.

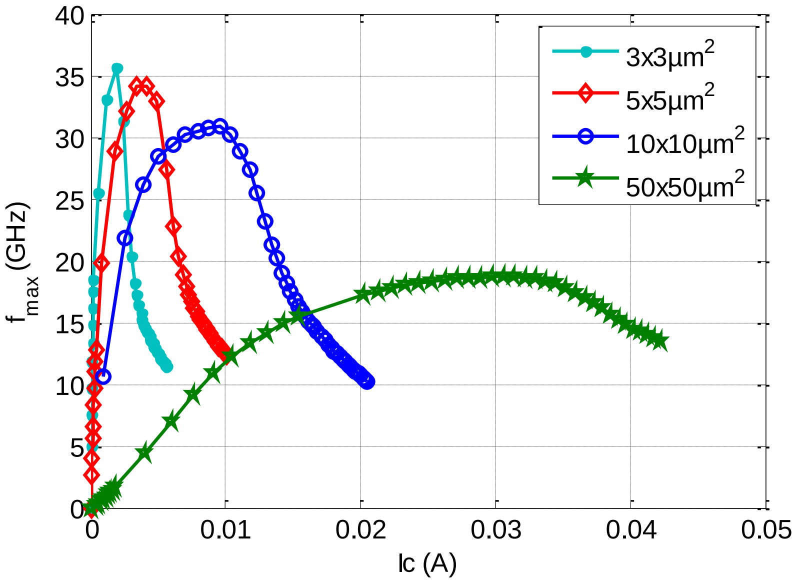

Figure 3-32: The maximum oscillation frequency versus collector current at Vce=3.5V for different size HPTs.

The maximum frequency of oscillation increases with the collector current until it achieves the phenomenon of “roll-off” as for f_T curves. Smaller optical window size HPTs (3x3µm^2) thus have fastest f_{max} (35GHz) performance despite a lower f_T. This indicates that when decreasing the optical window size of the HPT, the $C_{BC}.R_B$ product decreases. The base collector junction capacitance decreases indeed. The base resistance (without considering the 2D extension electrical effect) increases with the decrease in the optical window size W. As the $C_{BC}.R_B$ product increases with the length of the extended base, the maximum oscillation frequency lowers when the HPT sizes increases. The required I_C also increases, according to the f_T curve. HPT with 50x50µm^2 has f_{max}=17.5GHz at I_C=25mA, which is half of f_{max} of 3x3µm^2 HPT (35GHz) with required collector current 10 times higher.

These values have to be compared to the 80GHz value of pure HBT from the technology. The values are much smaller, due to the large width of the optical window.

b. $C_{BC}.R_B$ model

We analyzed the product of the base resistance and the base-collector junction capacitance by comparing the experimental result with the theoretical model. The base resistance of the transistor can be expressed as:

$$R_B = \frac{\rho.L}{S} = \frac{\rho.(l+\Delta)}{\mathrm{W}.\mathrm{t}_B} = \frac{\rho}{\mathrm{W}.\mathrm{t}_B}(l + f(\mathrm{W})) \tag{3.11}$$

An expression for base-collector junction capacitance is:

$$C_{BC} = \frac{\varepsilon.S}{W_{BC}} = \frac{\varepsilon.\mathrm{W}.\left(l+\Delta\right)}{W_{BC}} = \frac{\varepsilon.\mathrm{W}}{W_{BC}}(l + f(\mathrm{W})) \tag{3.12}$$

Where W_{BC} is the space charge region between the base and collector regions. From the above equations we can observe that when the electrical extension region, Δ, increases, the base resistance and base-collector junction capacitance also increase.

Base resistance and base-collector junction capacitance product is then deduced from equations (3.11) and (3.12). This results in:

$$R_B.C_{BC} = \frac{\rho}{\mathrm{W}.\mathrm{t}_B}(l + f(\mathrm{W})).\frac{\varepsilon.\mathrm{W}}{W_{BC}}(l + f(\mathrm{W})) = \frac{\rho.\varepsilon}{W_{BC}.\mathrm{t}_B}(l + f(\mathrm{W}))^2 \tag{3.13}$$

Thus:

$$R_B.C_{BC} = \frac{\rho.\varepsilon}{W_{BC}.\mathrm{t}_B}(l^2 + 2.l.f(\mathrm{W}) + (f(\mathrm{W}))^2) \tag{3.14}$$

From equation (3.14) we observe the $R_B.C_{BC}$ is a quadratic function of the electrical extension region, Δ=f (W) and it is inversely proportional to the product of the base thickness, t_B, and base-collector junction depletion region, W_{BC}.

From equation (3.10), the $R_B.C_{BC}$ can be extracted from fT and fmax measurements. It is plotted in Figure 3-33 a) as a function of $V_{be.}$

It is also plotted in Figure 3-33 b) as a function of Δ (thus W indirectly), with the value of Δ as extracted in Figure 3-31 at Vce=3.5V. For all optical window sizes, $R_B.C_{BC}$ decreases as Vbe increases in the range below 0.85V and then starts to increase as Vbe further increases beyond 0.85V.

From this Figure 3-33, we can then deduce the flowing observations:

Influence of Vbe at constant W:

- ***At lower Vbe (Vbe<0.75V for 3µm, 5µm and 10µm HPTs, Vbe<0.8V for 50µm HPT):*** R_B is expected to be independent on Vbe.

  At low Vbe, the base-collector potential Vbc gets higher. As a result the space charge region between the base and collector (W_{BC}) increases when Vbe decreases. Thus according to equation(3.12), the base-collector junction capacitance C_{BC} is expected to decrease. $R_B.C_{BC}$ would then decrease when Vbe decreases. However, according to Figure 3-33, $R_B.C_{BC}$ increases when Vbe decreases.

  Only an increase in Δ may explain such an increase in $R_B.C_{BC}$, according to (3.14). R_B and C_{BC} increase simultaneously with Δ. From the development seen in previous subsections, considering that a low Vbe induces a large Vbc, we create a larger electrical field which thus indeed enhances the lateral extension width.

  This experimental results are then in line with our electrical extension effect as well.

- ***At higher Vbe (for Vbe> 0.85V):*** $R_B.C_{BC}$ increases with Vbe according to Figure 3-33. Here according to the previous considerations, the lateral electrical field in the base-collector may get smaller and the Δ width as well. This increase in $R_B.C_{BC}$ may then mainly related to the decrease of W_{BC} (C_{BC} increases) as Vbe increases in this region.

  According to [262] the base resistance is bias dependent and decrease with increasing base current for standard HBT (for a full emitter contact structure) assuming the base current flow is strictly one direction. Adapting this HBT physical model to the HPT structure by considering bidirectional base current flow (which is the case in our HPT) and the effect of optical window size or Δ could make our model more realistic. This is a perspective of this work.

Influence of W at constant Vbe:

- According to Figure 3-31, the electrical extension region, Δ, decreases as the optical window size W increases. Thus according to equation(3.14), $R_B.C_{BC}$ should increase as Δ increases (W decreases). However, it is not the case according to Figure 3-33 b). This indicates that equations (3.11) and (3.12) must be revised to be more realistic. One could take into account models as developed in [262] (that relates the bias with the base resistance and junction capacitances) and to adapt them to the HPT case by considering the effect of Δ or W. This is a perspective of our work.

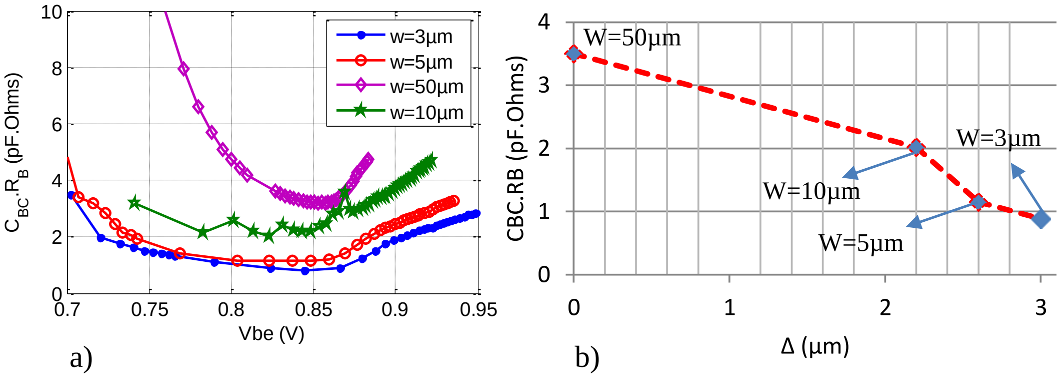

Figure 3-33: $C_{BC}R_B$ model extraction at Vce=3.5V a) versus Vbe and optical window size,w, b) versus electrical extension region, Δ, at Vbe=0.823V.

3.5 Localization of the photocurrent sources and OM behavior in the HPT Structure

3.5.1 Introduction

For further understanding we perform DC-and Opto-Microwave (OM) Scanning Near-field Optical Microscopy (SNOM) analysis to investigate the physical behavior of SiGe HPT. We analyze the impact of the vertical stacks and lateral dimensions of the structure under study on its performance. The photocurrent and opto-microwave behavior is studied by scanning the illumination spot over the surface of the HPT.

The bench setup described in chapter 2 section 2.3.2 is used to perform the opto-microwave and DC mappings over the structure of SiGe/Si HPTs. In this setup a 12GHz 850nm VCSEL is directly modulated and illuminates the HPT through a lensed MMF scanning over the surface of the HPT by a well-controlled step. For each position, the S-parameters of the optical link are measured with the help of the VNA over a 50MHz to 20GHz frequency range. For each position the DC currents and voltages are also measured at the collector and base contacts with the help of the B1500. The DC currents and S-parameters are measured in both photodiode and phototransistor modes of operation. The phototransistor mode is obtained by setting collector emitter voltage of 3V or 2V and base emitter voltage of 0.857V. The photodiode mode is obtained by setting collector emitter voltage of 3V or 2V and base emitter voltage of 0V. These biasing conditions are the optimum biasing conditions investigated in the previous sections. A 2µm step is used to cover a 60µmx60µm surface above the HPT. To extract the actual behavior of the HPT the calibration and de-embedding techniques described in section 2.4.3 are used.

Figure 3-34 a) shows the microscope picture of the 10x10µm^2 phototransistor (over which the topological mapping is performed) where the ground (top and bottom) and signal (left and right) lines are clearly visible. The base contact is taken from the left side, collector contact is taken from the right side and the emitter contact is connected at its top and bottom side to the ground. The layout is accordingly sketched in Figure 3-34 b) which defines the optical probe coordinates with its origin given at the center of the optical window. The 5x5µm^2 and 50x50µm^2 HPTs have similar structure as in Figure 3 except the optical window size difference. We perform the experimental mapping on 5x5µm^2, 10x10µm^2 and 50x50µm^2 HPTs at two different bias conditions (photodiode and phototransistor mode) at each position of the optical probe.

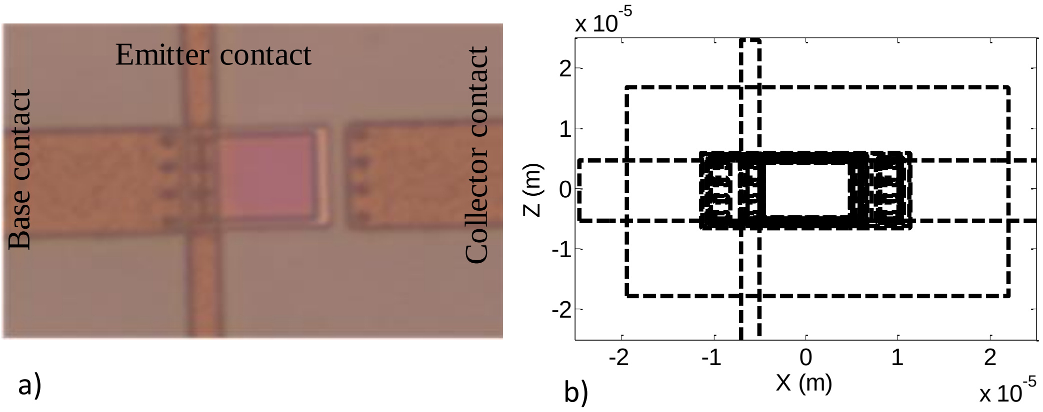

Figure 3-34: a) Top view of the 10x10µm^2 phototransistor. b) The layout of the HPT with optical window at the center of the optical probe position coordinate system. X and Z are given in meter.

In this section we observe the distribution of photocurrent and dynamic behavior of the phototransistor when displacing the optical probe over the surface of the structure. The substrate photocurrent source is localized and its impact on the opto-microwave gain and frequency behavior is presented. The intrinsic behavior of the phototransistor is analyzed by de-embedding the dc and local frequency response of the substrate photodiode.

3.5.2 Localization of the photocurrent source in the HPT structure

The mathematical equations presented in chapter 2 section 2.5 based on the physics of SiGe HPT allow to compute the different photocurrents at each position of the optical probe. This part will focus on the localization of the dc photocurrent sources over the structure of the HPT. The substrate photodiode is located in the structure by computing the substrate photocurrent. The complete and intrinsic dc responsivity are also deduced and presented. For such study we focus on 10x10µm^2 HPT.

The primary photocurrent generated, defined in chapter 2, in the HPT is computed using equation (2.16) in section 2.4.2 from the PD mode base current. Its map versus the optical probe position is shown in Figure 3-35 a). It is really symmetrical with respect to X and Z axes. From this result we observe that the maximum photocurrent generated in the HPT is -30µA when the optical probe is pointed at the center of the active area (X=0µm and Z=0µm). In this photocurrent there is no transistor effect as it is measured in the PD mode operation. The photocurrent measured at the base in HPT mode operation is shown in Figure 3-35 b). It is also well centered to the active area. The maximum photocurrent measured on the base is -11µA at X=0µm and Z=0µm.

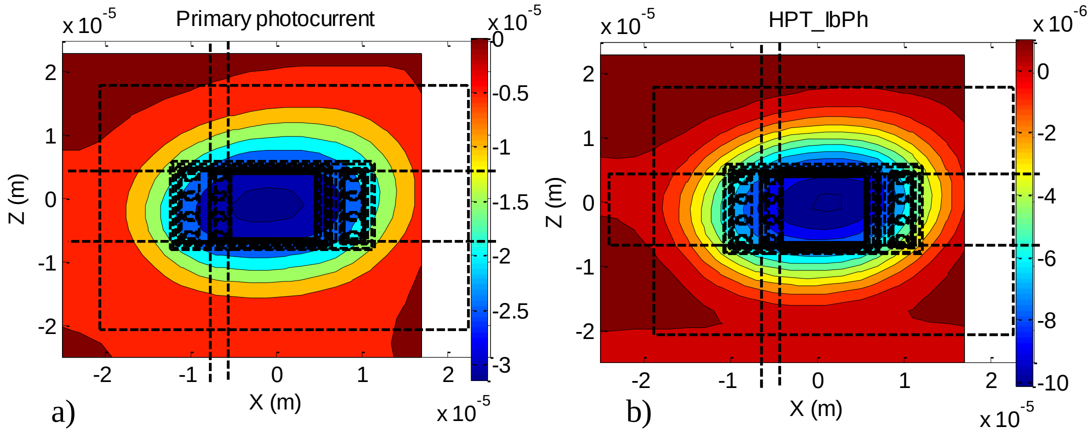

Figure 3-35: a) Primary photocurrent distribution over the 10x10µm² HPT structure; b) The photocurrent measured at the base under Vce=3V and Vbe=0.857V.

Most part of the primary photo-generated holes is flowing towards the emitter contact. Figure 3-36 a) shows parts of primary photo-generated carriers (holes) flowing from the base to the emitter ($I_{be\text{-}ph}$) that enables the phototransistor effect. Figure 3-37 shows the slice figures of the primary photocurrent (I_{prim}), the photocurrent activating the transistor effect ($I_{be\text{-}ph}$), the base photocurrent ($I_{b\text{-}ph}$) and the base photo-detection efficiency (γ) of the transistor. Due to the transistor effect, electrons are injected from the emitter to the base to compensate or neutralize accumulated holes at the base-emitter junction. A maximum of 25µA photocurrent is flowing to the emitter for amplification. The efficiency of the base is plotted in Figure 3-36 b) which is the ratio of the photocurrent measured at the base contact to the primary photocurrent. At z=x=0, 20% of the primary photocurrent reaches the base contact, thus 80% of it is used for the phototransistor action. Base efficiency is getting larger when the optical beam moves closer to the edge of the optical window, reaching up to near 100%. This means that on a design point of view, a phototransistor with a good proximity of base contacts will have less phototransistor action, but will have a higher photocurrent injected toward the base contact. Then matching the base terminal to reinject the photo-detected signal into the structure (HPT base matching, see [235], [200]) will be important.

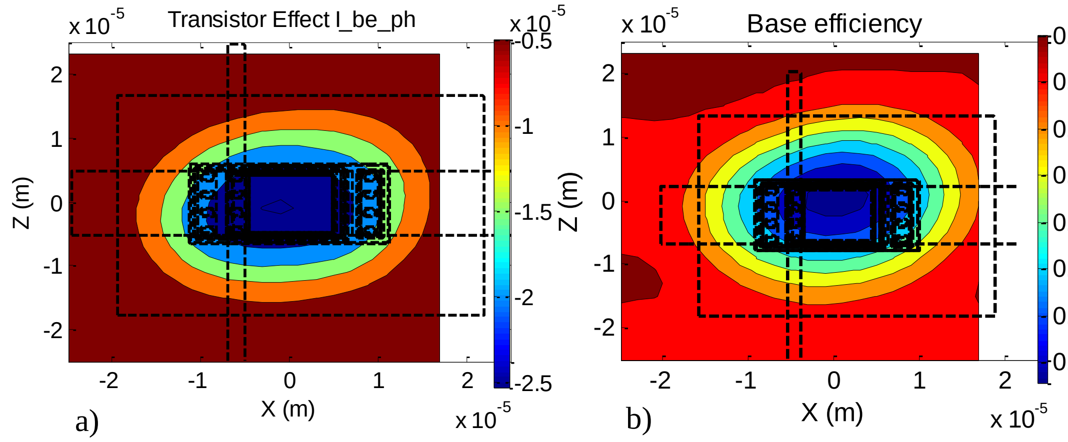

Figure 3-36: a) Transistor effect photocurrent map; b) Base efficiency map under Vce=3V and Vbe=0.857V of the 10x10µm² HPT.

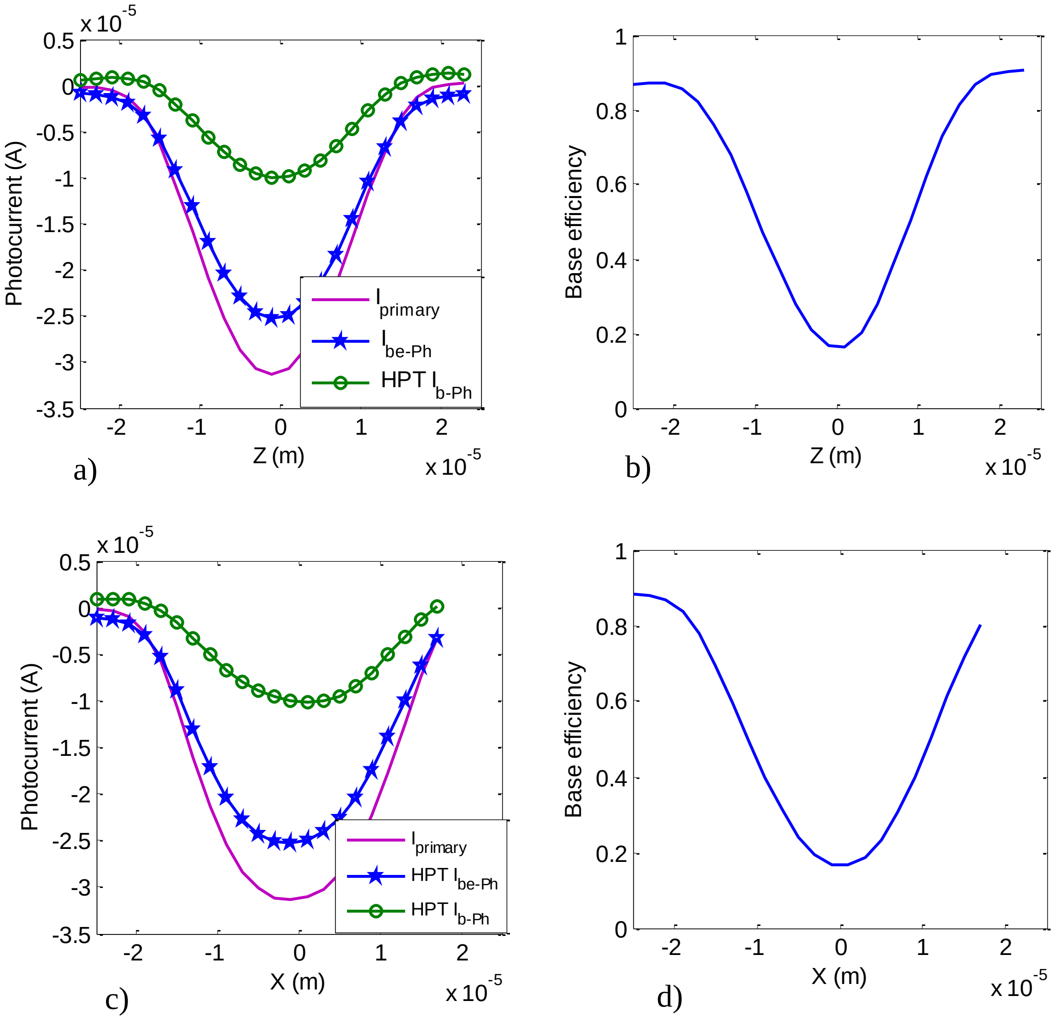

Figure 3-37: The 10x10µm² HPT slice curve of a) Primary, transistor effect and base photocurrent at X=0m. b) Base efficiency at X=0m. c) Primary, transistor effect and base photocurrent at Z=0m. d) Base efficiency

The complete collector current topological mapping is presented in Figure 3-38 in HPT (a) and PD (b) mode. Its mapping is not symmetrical along both X and Z axes. In HPT mode the Ic peak is located at

X=0µm and Z=0µm with a value of 11.1mA. This peak comes from the contribution of the dark and photo-generated collector currents in the transistor and also from the underneath substrate photodiode. Both dark and photo-generated currents are amplified by the transistor effect. There are also secondary peaks around X=5µm and Z=±15µm. And there are also two small peaks around X= -17µm and Z=±15µm. Those peaks are due to the illumination of the substrate photodiode.

However, in the PD mode the collector current secondary peaks are higher than the primary one (at the center of the active area) as shown in Figure 3-38 b). Those peaks are exactly at the same position under the HPT mode. They are induced by the parasitic photocurrent in the extrinsic substrate.

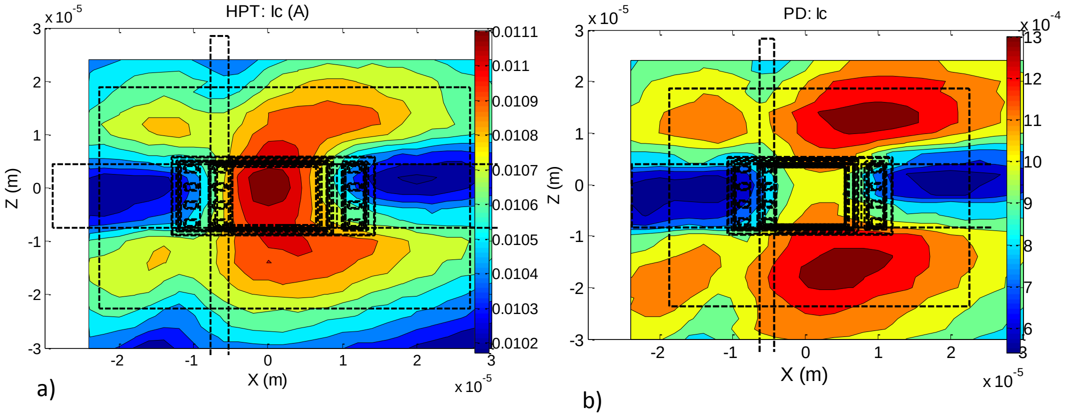

Figure 3-38: Collector current versus optical probe position of the 10x10µm² HPT in a) HPT mode under Vce=3V and Vbe=0.857V, b) PD mode under Vce=3V and Vbe=0V

The substrate photocurrent is deduced by using equation (2.18) in chapter 2. The topological map of the substrate photocurrent versus the probe position is given in Figure 3-39 a). There are indeed two main peaks outside the active area close to the base and collector contacts.

The slice curve of the substrate photocurrent is shown in Figure 3-39 b) at X=0µm. The two peaks appear on the side at about Z=±15µm, and correspond to substrate photocurrent. The substrate photocurrent has a low value at the center of the optical window. Indeed rhe light is partially absorbed by the intrinsic HPT before it reaches the substrate photodiode underneath.

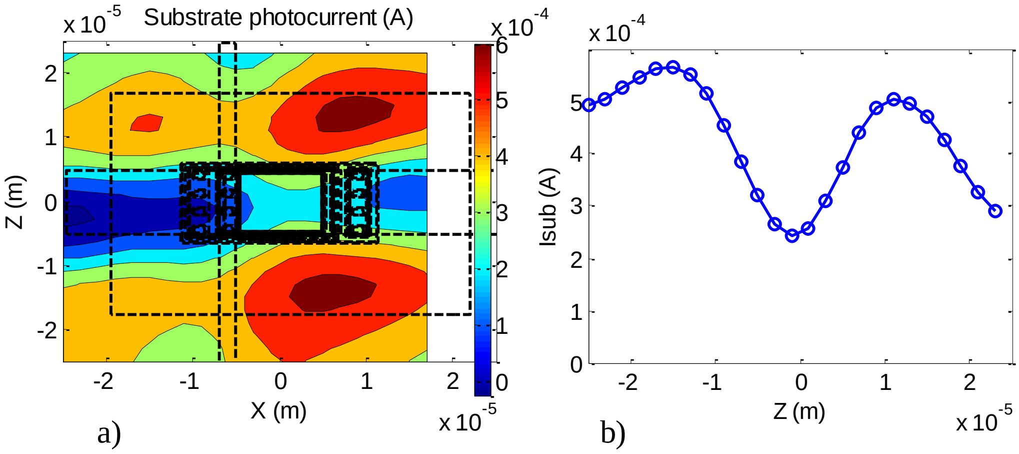

Figure 3-39: Substrate photocurrent of the 10x10µm² HPT under Vce=3V and Vbe=0.857V a) topological map; b) slice curve at X=0µm.

The peak location of the substrate photocurrent can be explained from the vertical and lateral structure of the HPT. Figure 3-40 shows the simplified stack of SiGe HPT structure along with the substrate contact. We use the substrate contact in order to minimize the frequency limitation of the substrate effect (to discharge the photo-generated holes carriers from the substrate). When the optical probe moves over the structure, the optical beam passes through different stacks depending on the position of the probe. The two peaks of the substrate photocurrent (on the top and bottom of the optical window as shown in Figure 3-39) are due to the illumination of the photodiode created by the n++ sub collector and p type Si substrate. We call it extrinsic substrate photodiode effect, which is an extrinsic contribution to the HPT photocurrents. We have a maximum substrate photocurrent of 600µA at X=0.5µm and Z=±15µm. When the optical probe is pointing at the center of the active area of the HPT, the substrate photodiode contribution is smaller. We reach a photocurrent value of 250µA at X=0µm and Z=0µm. This means that when the light is injected through the active area of the transistor (X=0µm and Z=0µm), more than half of the light is absorbed in the in the intrinsic region of the HPT.

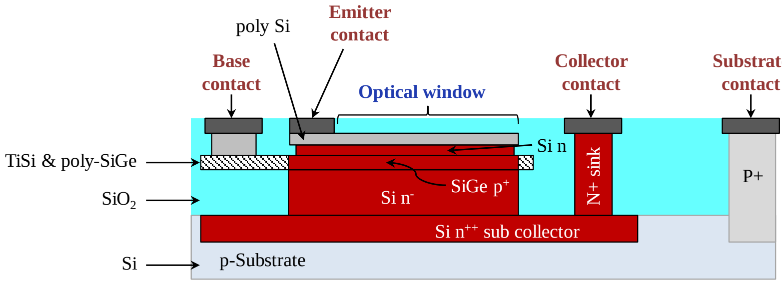

Figure 3-40: Phototransistor structure under study.

Figure 3-41 shows the topological map of the pure photocurrent (i.e. with dark contribution removed) measured at the collector in PD (a) and HPT (b) modes. Where Icph and Icopt are the photocurrent measured at the collector contact in PD and HPT mode after the substrate photocurrent is removed as it is presented in section 2.4.2. As we can see from the figure, in both modes, collector photocurrents are well centered to the device and they are symmetrical to both axes.

In PD mode operation, Ic_ph=27µA is measured at X=0µm and Z=0µm which is equivalent to the primary photocurrent. Whereas in HPT mode Ic_opt=0.4mA is measured at X=0µm and Z=0µm as shown in the cross section Figure 3-41 d). Here we clearly observe that the improvement on the collector photocurrent in the HPT mode is due to the transistor effect. The photocurrent amplification factor (β_{opt}) versus the optical probe position is plotted in Figure 3-42. We measure a value of β_{opt} of 40 at X=0µm and Z=0µm, where the base efficiency is at its lower value as well, and gets higher up to 100 at the edge of the phototransistor, which is still lower than the electrical transistor gain of 390. The difference can be explained by the fact that photo-generated carriers are amplified in another region than the electrical currents. As shown in section 3.4, the electrical currents and thus the transistor amplification mainly occur at the vertical of the emitter contact. Here we can assume that holes accumulate at the base-emitter junction further away from it, thus degrading the amplification rate, i.e. the optical current gain β_{opt}. Then, indeed β_{opt} is increasing when the lensed fiber illuminates a less the center and more the edge side. Illuminating only the edge is not possible within this 10µm scan range as the spot size is very large. We can also consider that illuminating the edge of the optical window is still on the side of the electrical active area and not strictly below, inducing some lateral path of carriers, and thus inducing an equivalent size of emitter and base which differs from the effective electrical ones.

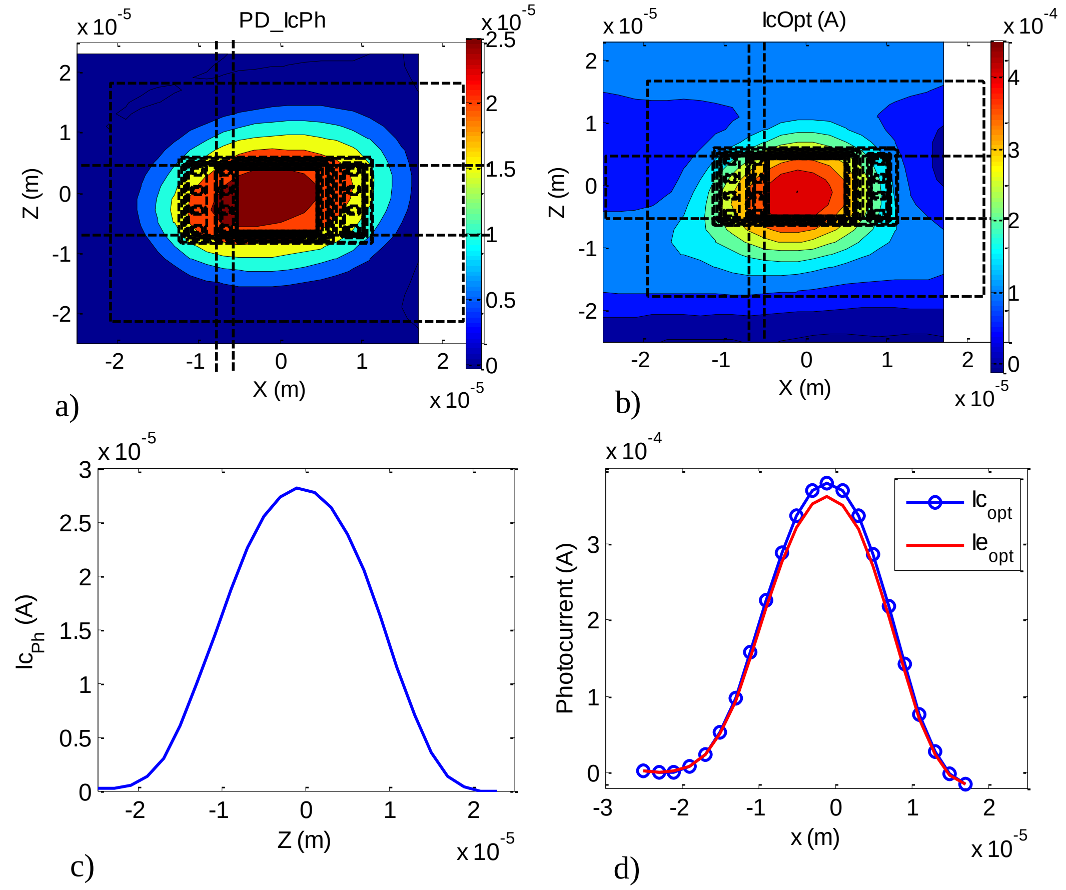

Figure 3-41: Photocurrent measured at the collector of the 10x10µm² HPT in a) PD Mode, b) HPT mode. The slice curves of the collector photocurrent c) PD mode, d) HPT mode.

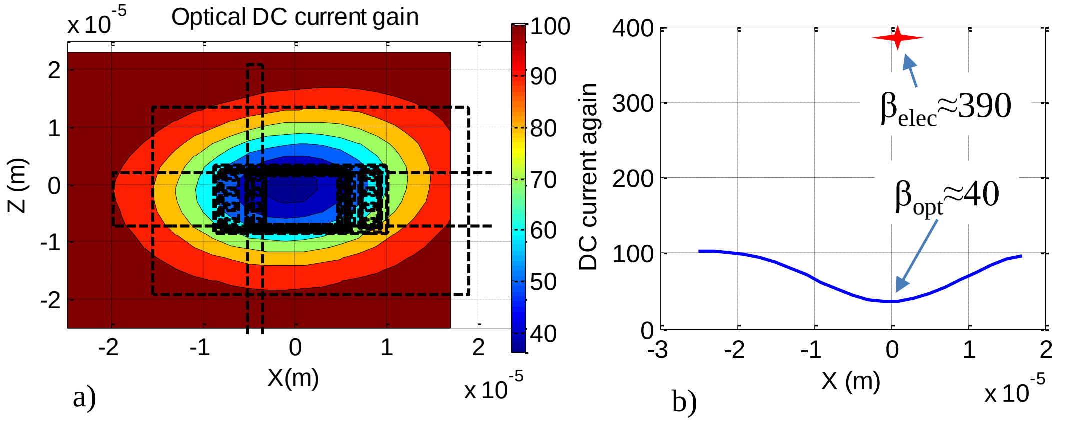

Figure 3-42: a) The topological map of photocurrent amplification factor; b) The slice of the photocurrent amplification factor at Z=0µm of the 10x10µm² HPT.

Figure 3-43 shows the topological map of the complete DC responsivity of the 10x10µm^2 HPT in phototransistor (a) and photodiode (b) modes respectively. We clearly observe the influence of the substrate photocurrent at the peaks of the responsivity in PD mode operation. It has the same shape as the substrate photocurrent shown in Figure 3-43 a). In the PD mode operation a maximum responsivity of 0.3A/W at X=5µm and Z=±15µm is measured whereas when we illuminate the active area of the HPT (X=0µm, Z=0µm), the responsivity is 0.2A/W. This difference is due to the presence of high sensitivity photodiode formed by the sub collector and p type silicon substrate. In the phototransistor mode, the peak of the complete DC responsivity occurs at the center of the active area because of the amplification of the photocurrent in the active region is dominating over the substrate photodiode.

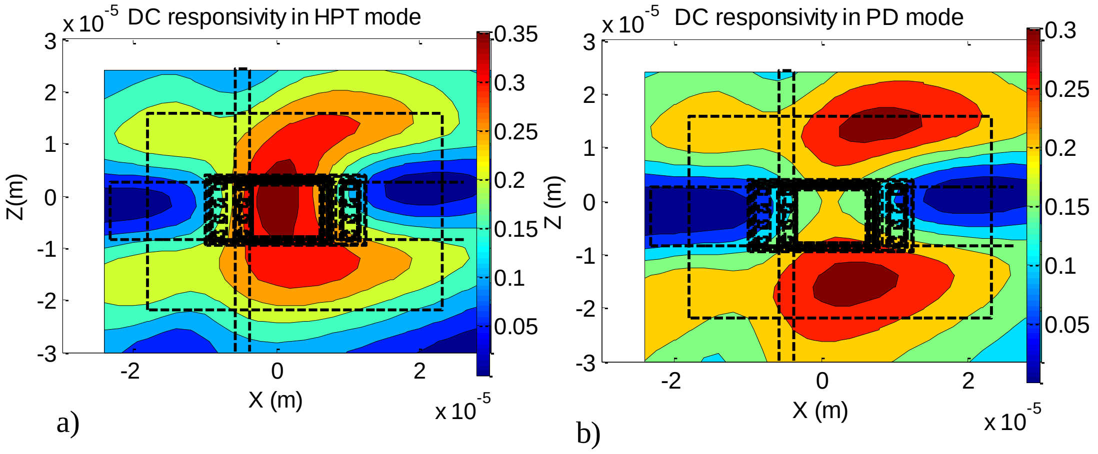

Figure 3-43: DC responsivity of the 10x10µm^2 HPT in a) HPT mode and b) PD mode

Figure 3-44 shows the slice curves of the complete and intrinsic DC responsivity in PD and HPT modes of 10x10µm^2 HPT. In the same figure the slice curve of substrate dc responsivity is also presented. As we observe from the curves, the complete responsivities are highly influenced by the substrate photodiode. The shapes of the complete responsivity are irregular and indicate a high response outside the optical window. However, after removing the substrate response, the intrinsic responsivity peak appears in the optical window in both modes and the curves follow the erf model with the given size of the intrinsic HPT.

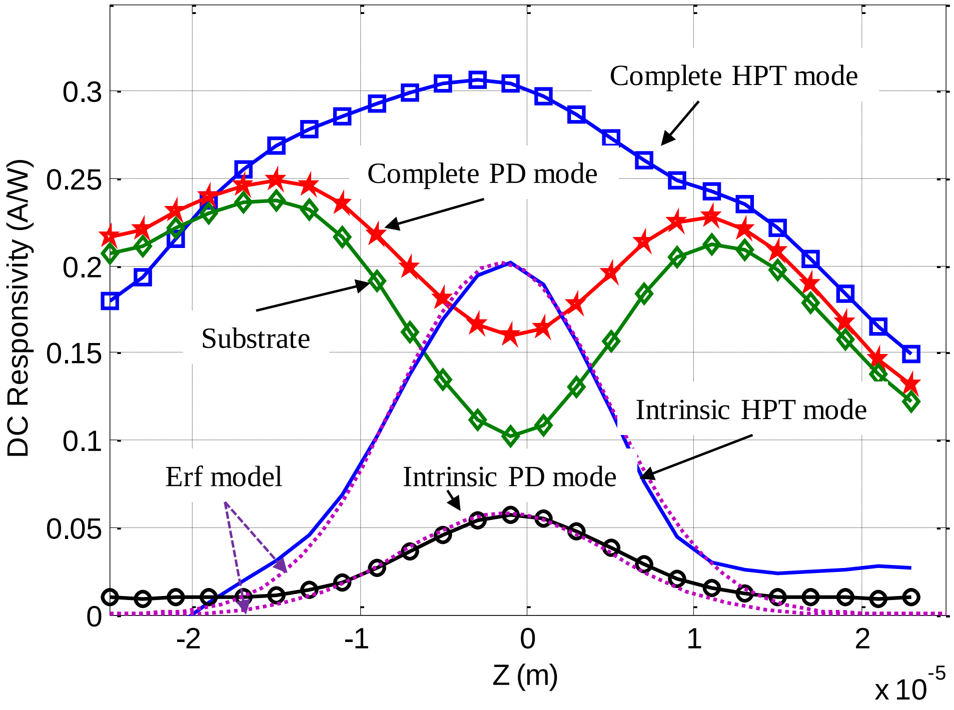

Figure 3-44: The slice curve of the complete, intrinsic and substrate DC responsivities at X=0m in HPT and PD mode of the 10x10µm^2 HPT.

3.5.3 Localization of the Opto-microwave behavior in the HPT structure

Figure 3-45 shows the complete and intrinsic opto-microwave gain versus frequency in PD and HPT modes at center of the optical window (X=0um, Z=0um). The model of substrate photodiode frequency response at X=Z=0µm is also presented in the same figure. The complete and intrinsic Gom are equal in the whole frequency range in HPT mode operation. This indicates that the frequency response of the substrate photodiode is hidden by the internal transistor amplification effect. However, in PD mode, the substrate photodiode contributes to its opto-microwave gain and reduces its dynamic behavior.

In general, from such a curve, we can extract both complete and intrinsic cutoff frequencies optical transition frequency, optical gain and low frequency Gom. Thus, in this section we focus on the localization of the frequency behavior of the HPT over the surface of the structure through OM SNOM investigation. The effect of the substrate photodiode on the OM gain and dynamic behavior of the HPT is studied.

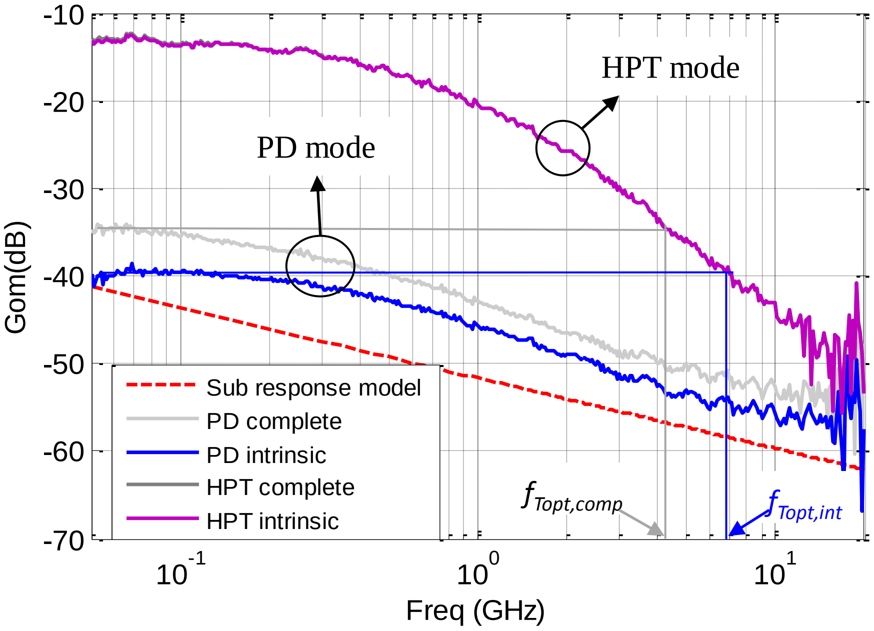

Figure 3-45: Complete and intrinsic opto microwave gain in PD and HPT modes at X=0µm, Z=0µm and the substrate frequency response model of the 10x10µm² HPT.

3.5.3.1 Low frequency behavior

In this part we are going to present the low frequency Gom and optical gain topological map of the HPT. The contribution of the substrate photodiode is also detailed.

a) Low frequency Opto-microwave gain (Gom)

The complete opto-microwave responsivity at 50MHz (low frequency of the VNA) of the HPT in transistor and photodiode modes versus optical probe position is presented in Figure 3-46 a) and b) respectively. A similar behavior as DC responsivity is observed on the opto-microwave response. A low frequency complete responsivity of 0.26A/W (resp. 0.241A/W) is measured when Vce=3V (resp. 2V) at the center of the optical window as shown in Figure 3-46 c). Taking into account the 32.3% fiber to HPT coupling efficiency, this corresponds to a 0.805A/W absolute responsivity. In PD mode, high responsivity value is observed in the substrate at x=10µm and z=14µm, at x=2µm and z=-16µm.

The measured opto-microwave gain in HPT mode at 50MHz under 50Ω (i.e. responsivity) is well fitted with an *Erf* function for -5µm < *x* < 5µm as shown in the cross-section presented in Figure 3-46 c). The responsivity is not well fitted with the model outside the optical window. As we observe in Figure 3-46 c), the experimental result has higher value outside the optical window compared to the *Erf* model curve. This indicates that the opto-microwave gain, in HPT mode, is actually affected by the substrate photodiode according to the location of the illumination.

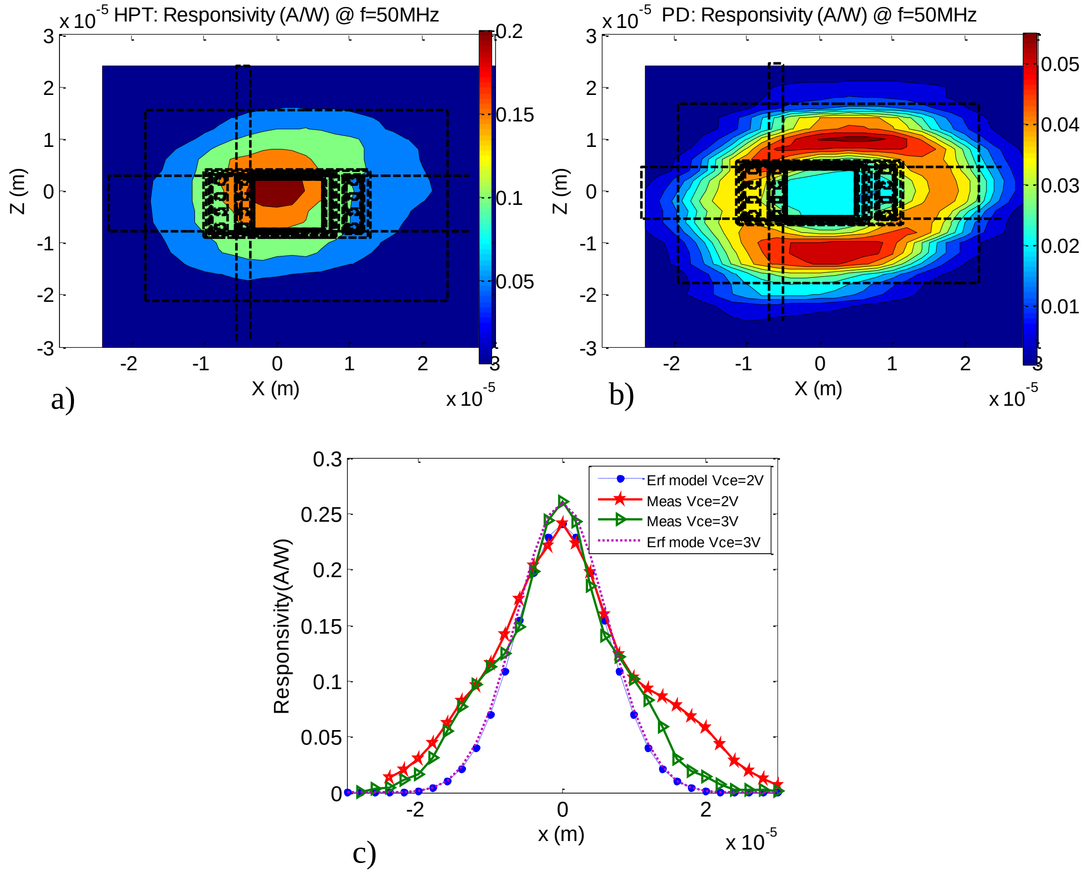

a) b) c)

Figure 3-46: Low frequency opto-microwave responsivity of the 10x10µm² HPT in a) HPT mode, b) PD mode under Vce=3V and Vbe=0.857V/0V respectively and c) The HPT mode responsivity slice plot at X=0m and its fitting with Erf model under Vce=2V or 3V and Vbe=0.857V.

The complete and intrinsic low frequency opto-microwave gain slice curves of 10x10µm^2 HPT are shown in Figure 3-47 at X=0µm in PD and HPT modes. The low frequency Gom of the substrate photodiode is also presented in the same figure. The complete and intrinsic Gom peak in HPT mode of operation appears at X=0 and Z=0; whereas in the PD mode operation the complete Gom peak appears at x=±15µm and Z=±15µm, where the peaks of substrate photocurrent appear. This provides a 2D donut shape in the PD mode. The intrinsic HPT is indeed hiding the underneath substrate photodiode when X=0µm; Z=0µm.. This donut shape should be thought carefully when one is optimizing the coupling of an HPT.

At the peak of detection in HPT mode, the complete and intrinsic Gom have equal value. They are dominated by the transistor action, and the substrate contribution is negligible. However it comes to be again present when the optical spot is deviating from the center.

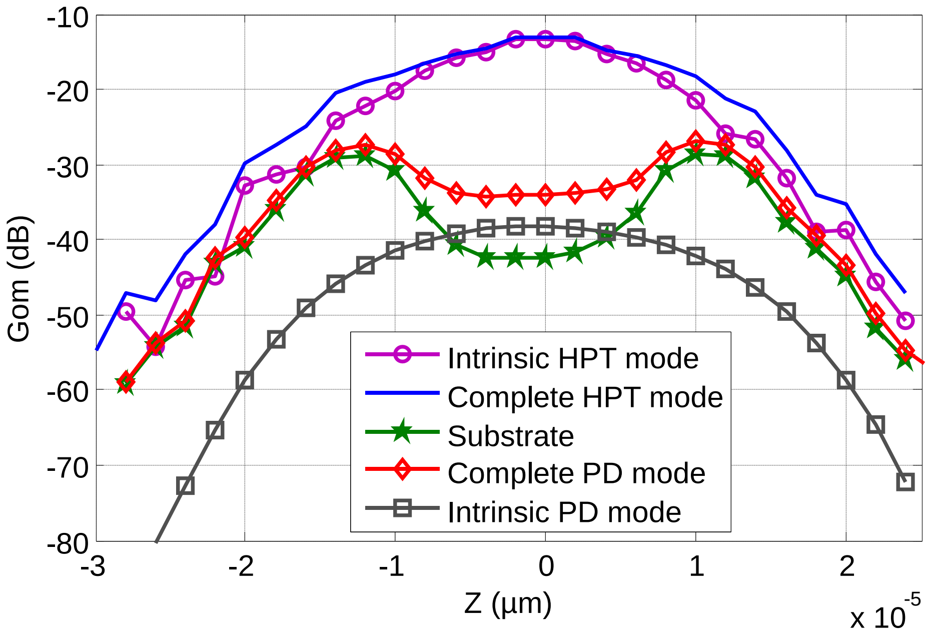

Figure 3-47: The slice curves of complete and intrinsic low frequency opto-microwave gain in PD and HPT modes of the 10x10µm² HPT at X=0m.

b) Optical gain (Gopt)

As defined in chapter 2 section 2.3.1 another way to characterize the phototransistor is the optical gain, G_{opt}. It is the difference between the HPT mode G_{OM} versus frequency and the PD mode G_{OM} at low frequency. The opto-microwave gain at the peak position (X=0, Z=0) is plotted in Figure 3-45 for both photodiode and phototransistor modes. We reach up to a 20dB complete optical gain at 50MHz at the peak of detection.

Figure 3-48 shows the comparison between the complete and intrinsic optical gain (G_{opt}) as well as the electrical current gain (h_{21}) of the 10x10µm^2 HPT at Vce=3V and Vbe=0.857V. At these biasing conditions the electrical current gain appears to be the upper limit of the optical gain at all frequencies. At 50MHz, the electrical current gain is 36dB and the complete and intrinsic optical gain is 20dB and 24.5dB respectively. The low frequency intrinsic optical gain is 11.5dB lower than the electrical current gain. The gap between Gopt and h_{21} for the intrinsic HPT however reduces at the frequency of 400-800MHz. This may be due to an internal matching effect of the base of the phototransistor. The photocurrents flowing in direction of the base contact are reflected back internally to the base-emitter junction so as to fully amplify the primary photocurrent.

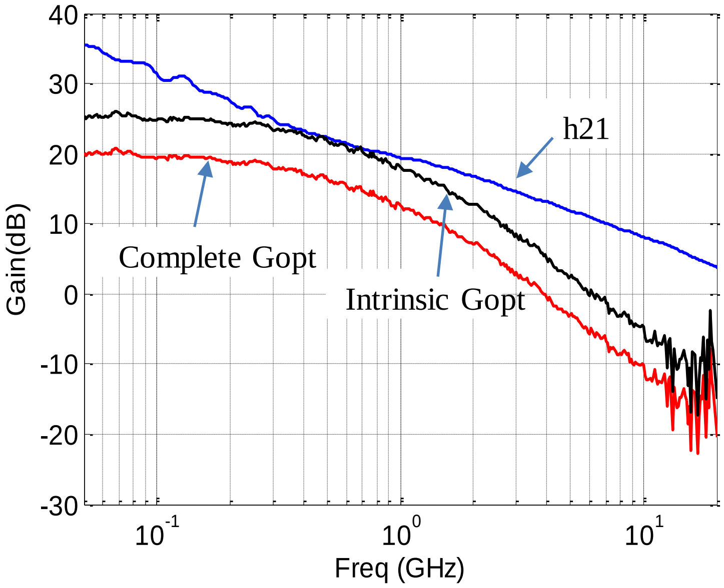

Figure 3-48: Optical gain (complete and intrinsic) and Electrical current gain at the peak position (X=0µm and Z=0µm) of the 10x10µm² HPT.

The optical gain over the surface of the HPT is shown in Figure 3-49. The complete Gopt has a symmetrical topological shape on both X and Z axes and is well centered to the optical window. Optical gain is highly modified by the substrate photodiode and optical coupling ratio. Figure 3-49 b) shows the complete and intrinsic optical gain slice curve along Z axis. The optical gain increases from about 19dB to 24.5dB when the substrate influence is removed. Compared to the complete Gopt, the intrinsic Gopt is almost flat in the optical window (Z=±5µm).

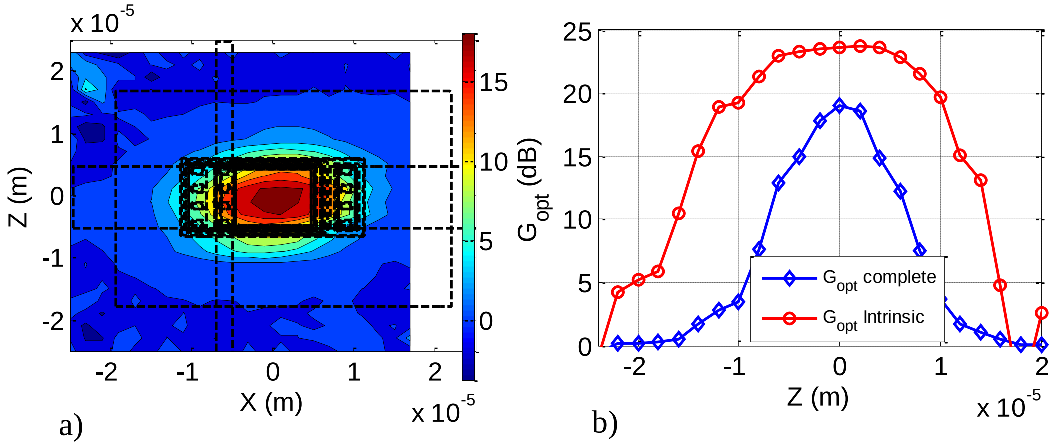

Figure 3-49: Optical gain (Gopt) a) The complete HPT topological mapping. b) The complete and intrinsic slice curves at X=0m of the 10x10µm² HPT.

3.5.3.2 Dynamic Behavior

The dynamic behavior of the phototransistor over the surface of the structure is analyzed through the measurement of the optical transition frequency (f_{Topt}) and the cutoff frequency ($f_{-3dB,OM}$) of the phototransistor in PD and HPT modes.

a) Cutoff frequency (f_{-3dB})

Figure 3-50 presents the topological and slice plots of the -3dB cutoff frequency of 10x10µm^2 optical window HPT in PD mode and HPT mode of operation. The cutoff frequency is usually small in phototransistor mode as the HPT has a -20dB/dec slope response (related to its internal amplification processes). Thus, theoretically it is assumed that the complete HPT cutoff frequency is higher in the photodiode mode. However, the experimental result shown in Figure 3-50 indicates that the HPT mode complete cutoff frequency is much higher than the PD mode complete cutoff frequency. This is due to the substrate photodiode which dominates over the base-collector intrinsic photodiode in PD mode operation. In HPT mode, however, the substrate photodiode is hidden by the transistor effect.

Thus the substrate photodiode effect is predominating in PD mode operation and controls its dynamic behavior, while in HPT mode the intrinsic HPT is dominating.

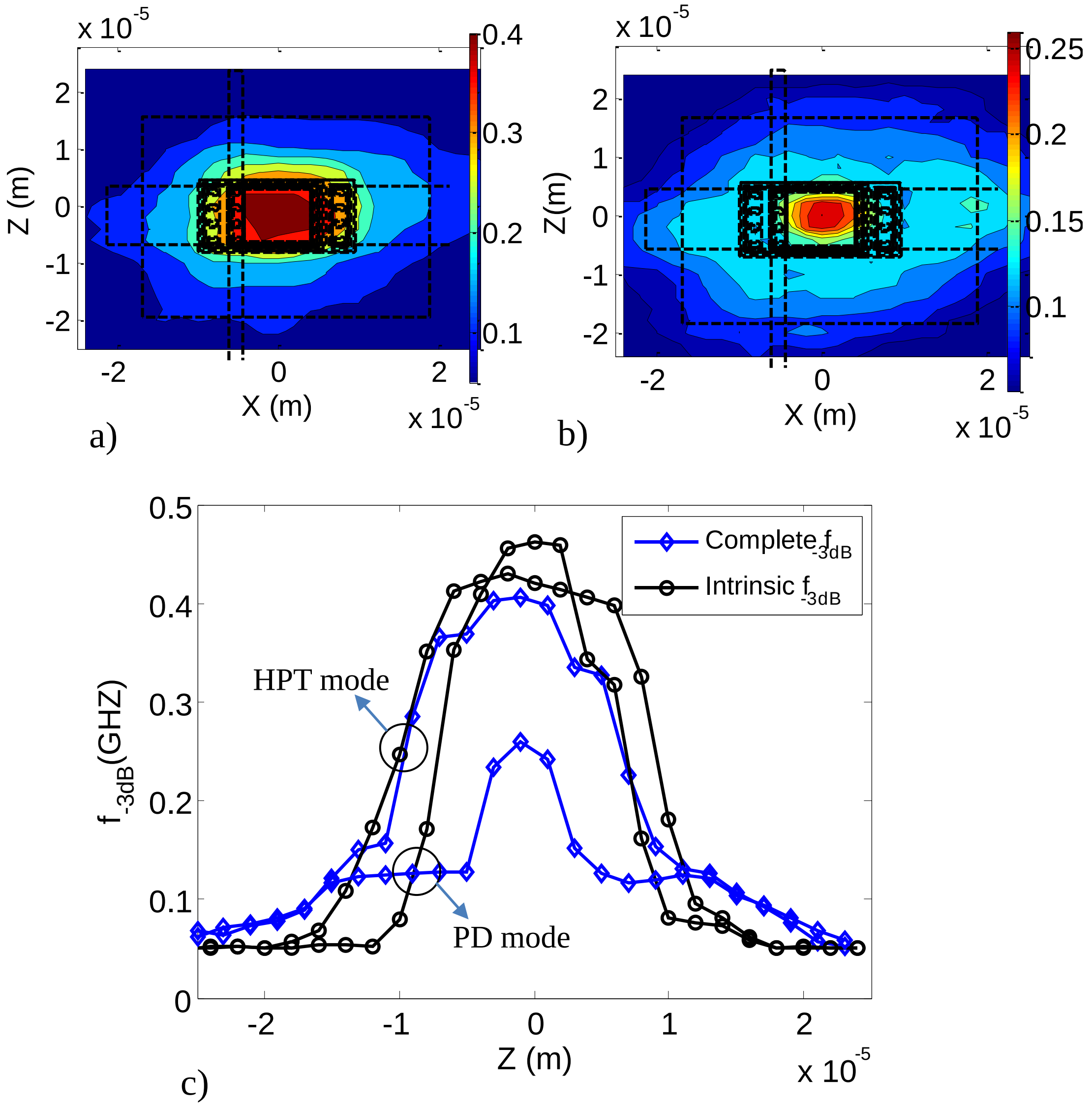

Figure 3-50: Opto microwave -3dB frequency a) The complete HPT topological map in HPT mode, b)The complete HPT topological map in PD mode and c) the complete and intrinsic slice curves at X=0 in PD and HPT modes, of the 10x10µm² HPT.

We reach complete cutoff frequency up to 420MHz in HPT mode and 260MHz in PD mode operation at x=z=0µm. It increases from 260MHz to 463MHz in PD mode after removing the influence of the substrate and it is flat in the optical window as shown in Figure 3-50 c). In HPT mode, a slight increase also happens as well a flattening of its value over the optical window. Finally, the intrinsic cutoff frequency in PD mode is larger than the intrinsic cutoff frequency in HPT mode. This confirms the consistency of the experimental result with theory.

The cutoff frequency outside the optical window is mainly due to the substrate effect. It has very small value which is equal in both modes. When we measure the cutoff frequency far from the optical window (metal contact), the distance traveled by the photo-generated carriers into the substrate is longer than the one close to the optical window.

After removing the substrate response in both modes the cutoff frequency outside the optical window becomes null as it goes below the limit of the measurement bench of the VNA (≈50MHz).

b. Optical transition frequency (f_{Topt})

Figure 3-51 presents the optical transition frequency versus the fiber position. The f_{Topt} curve is symmetrical with respect to the X and Z axes and has a peak at the center of the optical window.

A maximum complete f_{Topt} of 4.12GHz is measured at the peak position under Vce=2V and Vbe=0.857V. According to Figure 3-51 b), the f_{Topt} curve versus the fiber position follows the Erf function variation. At both extremities, its value is very low and could be attributed mostly to substrate detection noise. It is also not flat across the active window of the HPT. This indicates that f_{Topt} is affected by the coupling efficiency into the HPT and the substrate photodiode. If there wouldn't be a substrate photodiode effect, the f_{Topt} would be flat over the optical window.

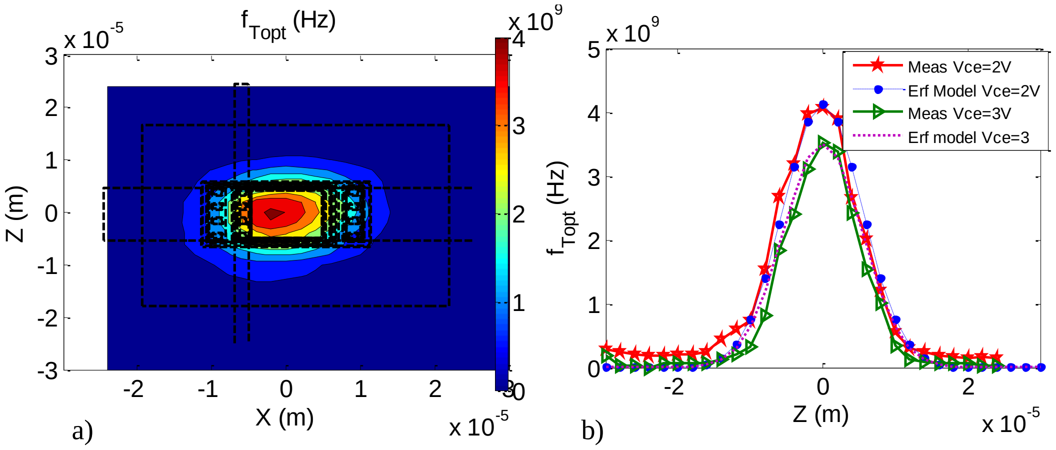

Figure 3-51: a) Optical transition frequency (f_{Topt}) versus optical probe position, b) The slice view of the f_{Topt} at X=0m and its fitting with Erf model under Vce=2V or 3V and Vbe=0.857V, of the 10x10µm² HPT.

The slice figure of the f_{Topt} for 10x10µm^2 HPT at x=0µm and z=0µm before and after removing the substrate photodiode effect is shown in Figure 3-52 a) and b) respectively for Vce=2V and Vbe=0.857V. The intrinsic f_{Topt} has a flat shape in the optical window along Z axis (Figure 3-52 b) as it mostly depends on the vertical stack parameters, and it drops faster to zero outside the optical window. Along the x axis, the intrinsic f_{Topt} is not flat and its peak is shifted from the center of the optical window to the edge of the optical window as shown in figure Figure 3-52 a). This may be explained by the tilted angle of the lensed fiber along this direction, which may affect the distribution of photo-carriers within this direction, and then the related transit times. The f_{Topt} then improves from 3.41GHz to 6GHz when the intrinsic response is de-embedded. This gives access to the intrinsic HPT performance and physics.

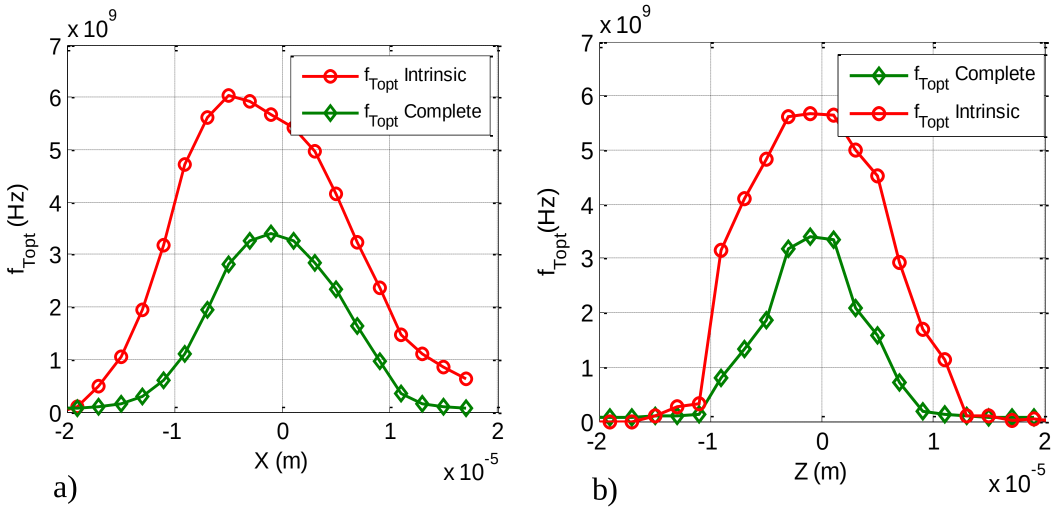

Figure 3-52: The raw and extracted f_{Topt} *a) at z=0µm, b) at x=0µm of the 10x10µm² HPT.*

3.6 Dependency on the injected optical power level

3.6.1 Introduction

The opto-microwave performance of the phototransistor could be changed related to the injected optical power intensity. This could be due to many factors such as self-biasing effect and variation of modes of the injected optical power versus current biasing of the multimode VCSEL source (this could change the beam width).

Thus, in this section we observe the effect of the injected optical power level on the performance of SiGe HPTs. For this study we focus on 10x10µm^2 SiGe/Si HPT and we choose three optical power levels (Popt=0.83mW, 1.14mW and 2.38mW measured at the peak of the optical probe). DC and OM SNOM are performed in PD and HPT modes for the three power levels. To observe this effect we start from the dc characters by fitting Ib with the erf model and go through the injected power level dependency of opto-microwave responsivity and frequency behavior.

3.6.2 Injected optical power level impact on DC characteristics

We start this study by analyzing the behavior of the optical beam through the fitting of *Ib* in PD mode with the *erf* model as shown Figure 3-53. Figure 3-53 a) shows the erf fitting with the experimentally measured base current in PD mode. According to the development in section 2.4.3, the beam is evaluated to get a beam width of 28µm. This model fits well with our measurements for Popt=2.38mW and we can extract a 32.3% coupling rate, but it doesn't fit when we reduce the optical power to Popt=0.83mW and 1.14mW as shown in Figure 3-53 a). Thus, we need to adjust the Erf fit with Ib measured at Popt=0.83mW and 1.14mW. As a result for these two optical power levels we extract a coupling efficiency of 26.1% and an optical beam width of 34.8µm as shown in Figure 3-53 b).

This variation of beam width indicates that there is change in the modes of the VCSEL source at different dc biasings.

In Figure 3-53 we can also observe that the photocurrent flowing out to the base contact increases along with the injected optical power (it is higher for high optical power). This could be explained by self-biasing effect of the injected optical power. That means at high optical power level a large number of electron hole pairs could be generated in the base-collector region and then the holes are collected at the base contact.

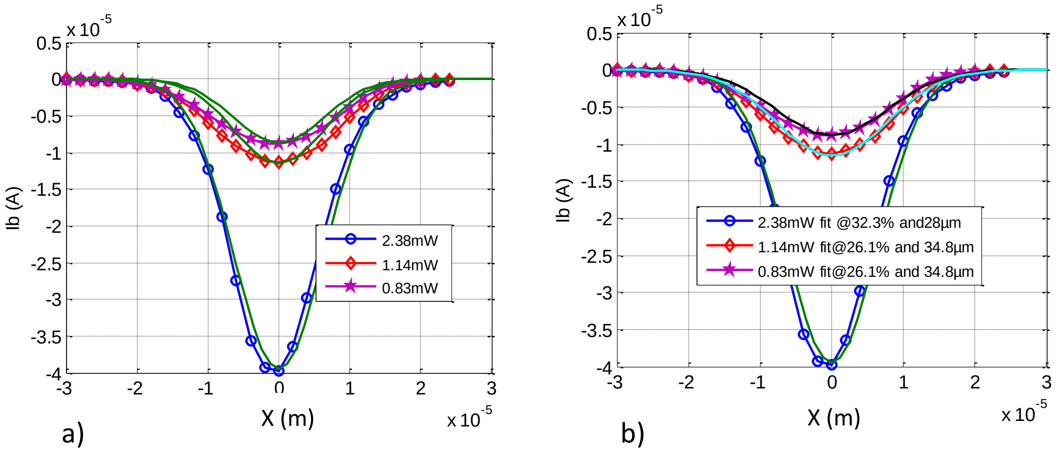

Figure 3-53: Base current in PD mode fitting with erf model (curves without marks) for different injected optical power levels of the 10x10µm² HPT. a) The fitting targeting the model developed in section 2.4.3 for Popt=2.38mW which has 32.3% coupling efficiency and 28µm diameter beam width. b) The fitting made for each power level individually.

Figure 3-54 a) shows the base current in HPT mode for the three injected optical power. At high injected optical power, larger amount of electrons and holes are generated and hence we measure more base current for an injected optical power of 2.38mW than other.

Figure 3-54 b) shows the intrinsic photocurrent measured at the collector contact in PD mode operation at different optical power levels. When the optical probe is pointing at the center of the optical window, Icph increases from 27.5µA to 32.5µm as the injected optical power increases from 0.83mW to 1.14mW and then it decreases to 28µA for Popt=2.38mW. Icph decrease at 2.38mW could be related to the current saturation at high optical power.

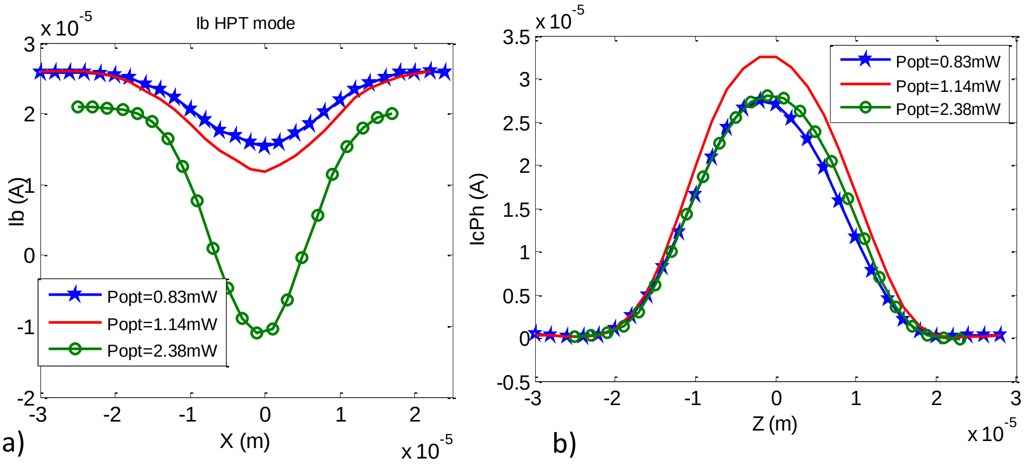

Figure 3-54: a) Base current measured in HPT mode at Popt=1.14mW and 2.38mW. b) The intrinsic photocurrent of the HPT measured in PD mode at different input optical powers of the 10x10µm² HPT.

We present the slice figure of the photocurrent amplification gain, β_{opt}, and of the base efficiency at z=0µm in Figure 3-55 a) and b) respectively. β_{opt} increases from 36 to 48 and then to 55 when the injected optical power level decreases from 2.38mW to 1.14mW and then to 0.83mW respectively.

The base efficiency also increases as the injected optical power level decreases: At the center of the optical window about 20%, 26% and 46% of the photo-generated holes are moving out from the base region to the base contact for an injected optical power of 2.38mW, 1.14mW and 0.83mW respectively.

Somehow the phototransistor effect (β_{opt}) is even less activated when the power is higher in the middle of the optical window, and in parallel fewer holes contribute to this effect, escaping through the base contact.

The optical dc current gain (β_{opt}) and base efficiency variation with the injected optical power level can be explained by the following reasons:

a) Self-biasing effect that is mostly believed to be the case. At high optical power, the hole density in the base increases and reduces further the resistance. Then holes resistance to reach the base contact lowers and the base efficiency increases. In parallel, the current gain decreases because the voltage induced self-biasing across this resistance inside the optical window gets lower: the transistor effect is less activated.

b) High injection phenomenons due to a high optical power within the HPT, eventually. Absorption rate are in the range of 10^{3}cm^{-1}. Thus the generation rate is in the range of 10^{19}cm^{-3}.s^{-1}. Accumulated into the base, this may create some equivalent modification of the base doping. This effect would be more pregnant at the center of the optical window where the time for accumulation is large (less base efficiency).

c) Due to injected optical beam width variation, that could explain a less concentrated effect of the self-biasing effect for example.

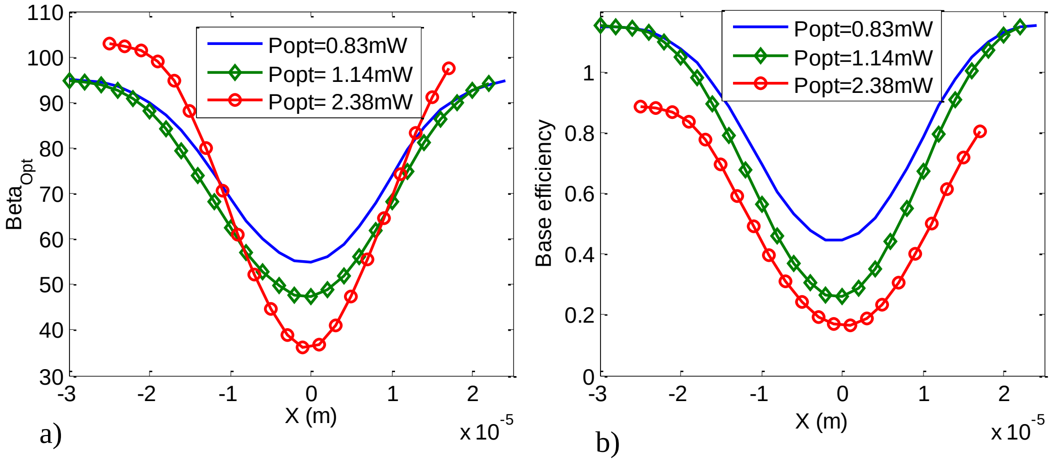

Figure 3-55: a) Photocurrent amplification, β_{opt} at different Popt. b) Base efficiency at different P_{opt}.

The intrinsic responsivity ($R_{PD,i}$) of the phototransistor in PD mode operation and the responsivity of the substrate photodiode at different optical power levels are presented in Figure 3-56 a) and b) respectively. The intrinsic responsivity is much less when Popt is high at 2.38mW. A small decrease is also observed but with similar values for the lower values of Popt.

The substrate responsivity has peaks outside the optical window which are related to the illumination of the substrate photodiode. The substrate response at the center of the optical window has nearly equal value for all injected optical level. However, outside the active area, the substrate responsivity is also less for the power of 2.38mW. This is meanly related to the increase of the optical beam width when the optical power is lower. As we presented in Figure 3-53 the beam width for smaller optical power injection is larger than for higher optical power and thus, the coupling efficiency is less for smaller Popt. This reduced coupling efficiency results in large portion of optical power injected into the substrate and thus the effective substrate responsivity increases.

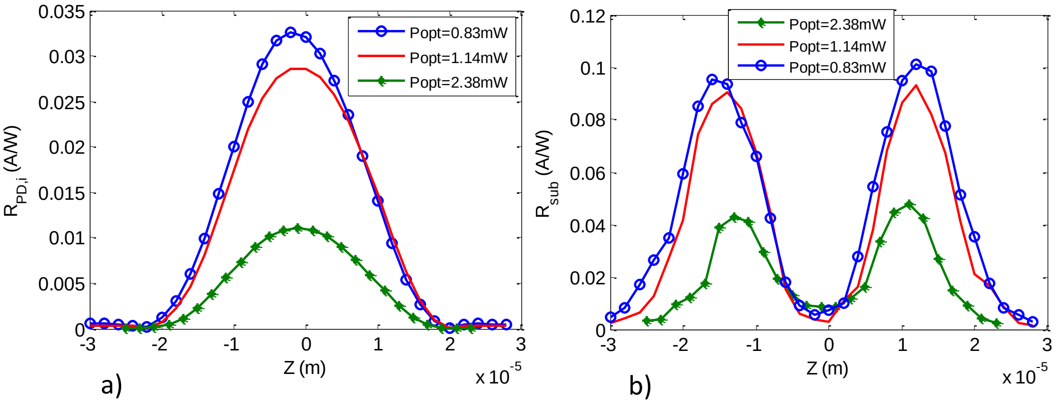

Figure 3-56: Slice curves at x=0µm and different injected optical power levels a) DC intrinsic responsivity. b) Low frequency (50MHz) substrate responsivity.

3.6.3 Injected optical power level impact on opto-microwave frequency response

We measure the S-parameters in PD mode (Vce=2V, Vbe=0V) and HPT mode (Vce=2V, Vbe=0.857V) by varying the injected optical power level (0.83mW, 1.14mW and 2.38mW). Then, we extract the opto-microwave responsivity and the frequency response behavior of the phototransistor after removing the test bench effect through the de-embedding techniques presented in section 2.3.3.

Figure 3-57 shows the opto-microwave gain versus frequency of 10x10µm^2 optical window size HPTs for different injected optical power levels at x=0µm and z=0µm both in PD and HPT mode operation. The opto-microwave gain increases as the injected optical power decreases for both modes. We could explain this variation accordingly:

1. The Gom difference in PD mode is due to the influence of the substrate photodiode response which depends on the level of injected optical power as presented above. The Gom has a lower cutoff frequency for 0.83mW and 1.14mW optical powers than 2.38mW, which verifies the influence of the slow substrate photodiode on the frequency response.
2. The Gom has nearly equal relative frequency response in HPT mode. This indicates that the impact of the substrate photodiode is less visible. However, the Gom is higher for small optical powers. This is due to the fact that the optical gain at low injected optical power level is higher than at 2.38mW as shown in Figure 3-55 a).

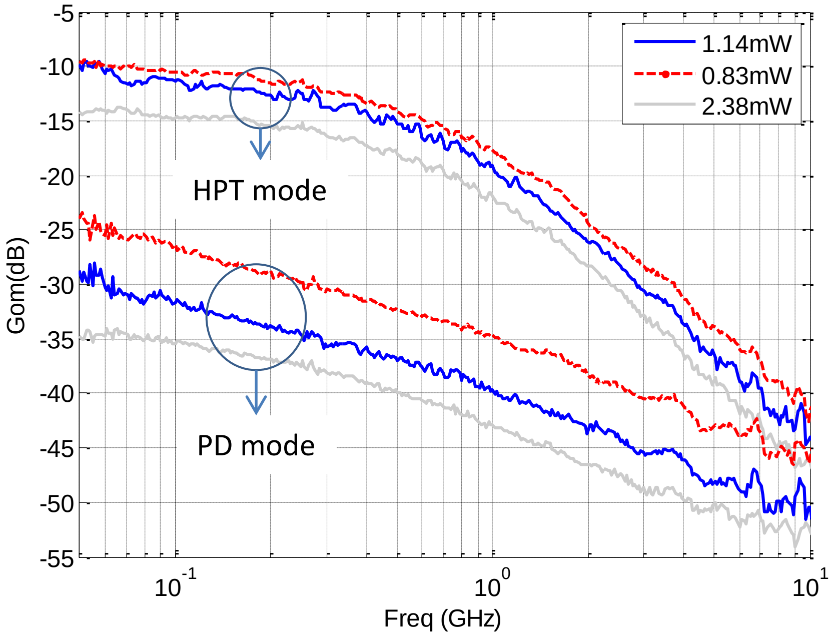

Figure 3-57: Opto-microwave gain versus frequency in PD (Vce=2V, Vbe=0V) and HPT (Vce=2V, Vbe=0.857V) modes at x=0µm and z=0µm by varying the injecting optical power level of the 10x10µm² HPT.

We present the slice figure of the low frequency (at 50MHz) opto-microwave gain at x=0µm both in HPT and PD modes at different optical power levels in Figure 3-58. The Gom decreases from -10dB to -14dB as the injected optical power increases from 0.83mW to 2.38mW in HPT mode.

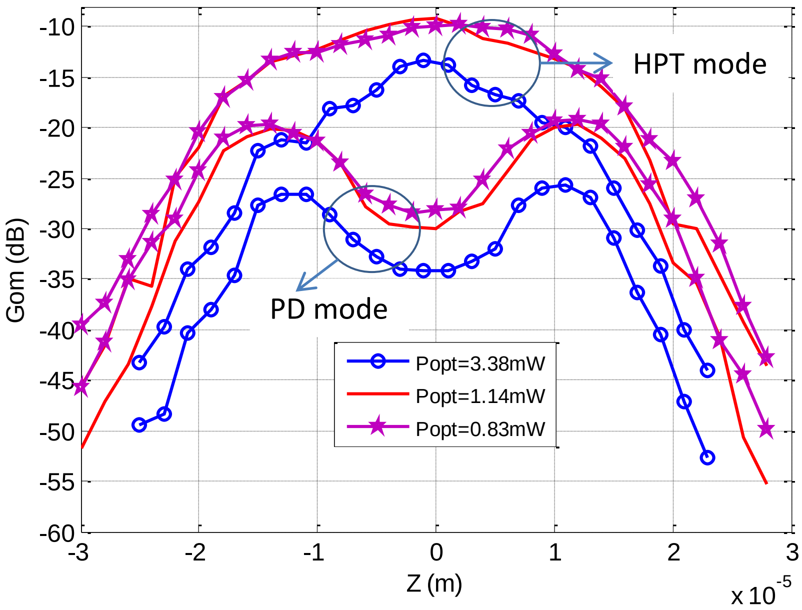

Figure 3-58: The slice figure of low frequency Gom in PD and HPT mode at x=0µm and different injected optical power levels on the 10x10µm² HPT.

The complete and intrinsic optical transition frequencies are presented in Figure 3-59 at different optical power levels and z=0µm. The complete f_{Topt} is directly extracted from the measured S-parameters, whereas the intrinsic f_{Topt} is obtained after the substrate response removal. The complete f_{Topt} increases as the injected optical power increases from 0.83mW to 2.38mW. It is mainly due to the substrate effect. Indeed, after correcting the substrate photodiode response f_{Topt} has nearly the same value for all injected powers. The f_{Topt} for Popt=2.38mW is a bit smaller than others and has a tilted shape along the X axis over the optical window as shown in previous sections. This may be due to the tilted optical beam with a more focused beam spot which makes the angle getting more impact. The peak value reduction is also explained by a reduced optical gain at 2.38mW. We are able to extract an intrinsic optical transition frequency of 6.5GHz for an injected optical power of 0.83mW and 1.14mW.

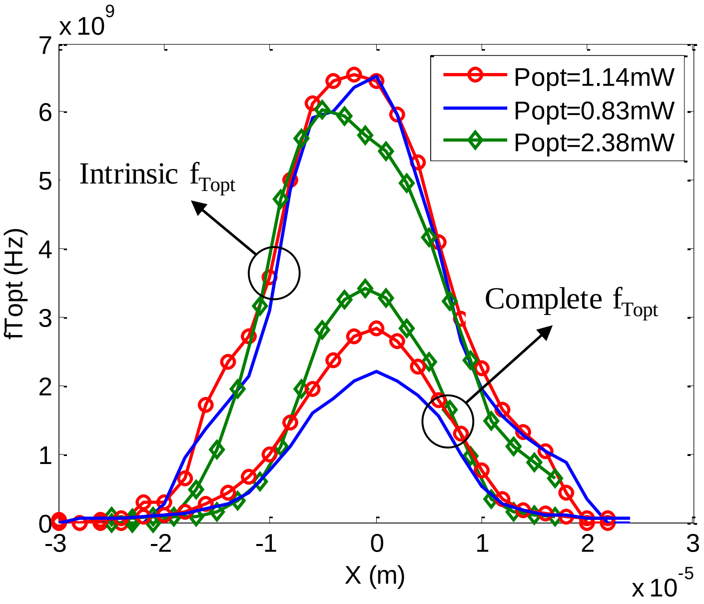

Figure 3-59: The influence of the injected optical power level on the optical transition frequency for the 10x10µm² HPT.

Another very important parameter to characterize the dynamic behavior of a phototransistor is the cutoff frequency. Figure 3-60 shows the slice figure at x=0µm of the cutoff frequency for injected optical power of 0.83mW, 1.14mW and 2.38mW in HPT mode. We observe 400MHz, 395MHz and 390MHz cutoff frequency at the peak detection for 2.38mW, 1.14mW and 0.83mW respectively. In HPT mode the cutoff frequencies for the three optical power levels are nearly equal when the optical probe is pointing at the center of the optical window (there is only 5MHz difference between the power levels). This small difference is due to the substrate photodiode effect at different optical power levels. The slope of Gom versus frequency as shown in Figure 3-57 is nearly equal in HPT mode operation as well.

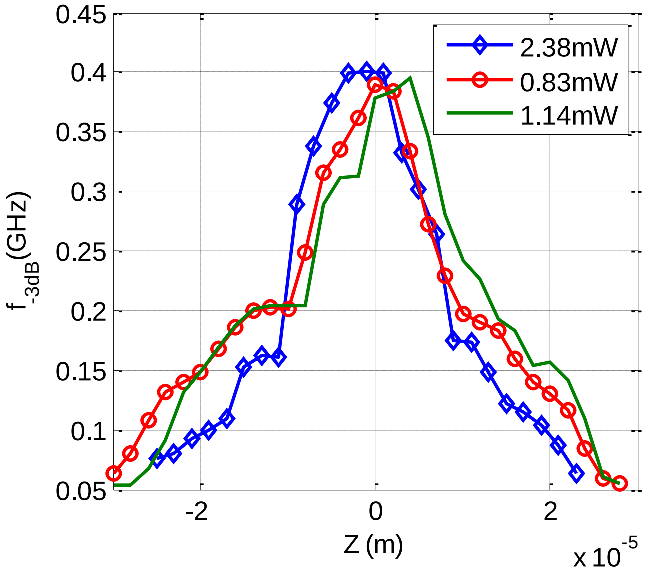

Figure 3-60: The slice curve of cutoff frequency at x=0µm and at different injected optical powers in HPT mode of the 10x10µm² HPT.

From this section we conclude that the level of the injected optical power affects the dc and opto-microwave behaviors of SiGe/Si HPTs. The effect could be related mostly to self-biasing effect and to the modification of the VCSEL optical power beam shape injected into the structure, improving diffusion current into the base and modifying the substrate contribution rate..

3.7 Current dependence of $f_{Topt,}$ and transit time and capacitance evaluation

3.7.1 Introduction

Observing the current dependency of the optical transition frequency is quite important to understand the behavior of a phototransistor. In section 3.30 we have presented the current dependency of f_{Topt} in order to optimize the dc biasing conditions at non optimum position of the optical probe. In this section we present the f_{Topt} vs collector current at the peak detection of the HPT (X=Z=0µm). The opto-microwave capacitance and transition time delay induced contributions to f_{Topt} are extracted and then compared with the equivalent electrical junction capacitance and transit time terms presented in section 3.4.

To do so, we perform opto-microwave experiment by sweeping Vbe from 0V to 1V and fixing Vce=2V at the peak detection of the phototransistor (X=0µm and Z=0µm). Actually to perform such experiment we did a scan over the surface of the HPT to cover 12µmx4µm surface area with 2µm step by sweeping Vbe at each location of the optical probe (It took a day to characterize a single HPT at a single injected optical power). We performed this experiment over a single HPT three times at three injected optical power level and then we extract from the Ib curve the peak response, which then defines the X=Z=0µm reference position.

3.7.2 Current dependency of optical transition frequency f_{Topt}

Figure 3-61 shows the complete and intrinsic optical transition frequencies versus collector current (I_C) at different injected optical power levels. To validate this result we can compare with the f_{Topt} topological map result presented in Figure 3-59, section 3.6.3 (they have the same peak f_{Topt}). As we can observe, the intrinsic f_{Topt} has the same maximum values for injected optical power of 0.83mW, 1.14mW and 2.38mW and their maximum appears at $I_C \approx 9$mA. However, the complete f_{Topt} has different maximum values.

In f_{Topt} versus Ic curve we have three mean regions (at low I_C, medium I_C and high I_C).

Capacitance limiting region: for I_C lower than 6mA, f_{Topt} increases with the collector current as the base emitter junction depletion region increase and thus the junction capacitance reduces by the dc supply.

The intrinsic f_{Topt} curves have almost the same slope at low Ic for different injected optical power level. The complete f_{Topt} curves have different slopes at low Ic for various injected optical power levels. This is due to the existence of additional capacitance in the substrate photodiode which depends on the level of injected optical power. For an injected optical power of 2.38mW the complete f_{Topt} slope is steeper than the slope at lower optical power level. The first reason could be the better coupling efficiency of the optical beam at 2.38mW (it has 32.3% coupling, whereas others have 26.5% coupling efficiency). The second reason could be the fact that its high level optical power could help the substrate photodiode depletion region to increase locally and thus reduces the capacitance value (self-biasing effect). Even though the optical beams at 0.83mW and 1.14mW have the same coupling coefficient, the f_{Topt} slope at 1.14mW is steeper than at 0.83mW. This can prove the second reason has great impact on f_{Topt} behavior at low Ic.

Transit time limit region: This is the region where the peak of f_{Topt} is reached that is between IC=6mA and 12mA as shown in Figure 3-61. The frequency behavior in this region is mainly limited by the carrier time to reach the metal contacts. The complete f_{Topt} peak increases as the injected optical power increases. This can be explained by the presence of numerous slow carriers from the substrate when we illuminate by 0.83mW and 1.14mW as they have lower coupling coefficient than with 2.38mW injected optical power beam. As the substrate effect is removed the intrinsic f_{Topt} peaks have the same level at all injected optical powers.

High current injection limiting region /Kirk effect: For I_C greater than about 12mA, f_{Topt} drops quickly for all the injected optical power levels. This is owing to the injection of a large number of carriers in the device which limits the speed of the HPTs.

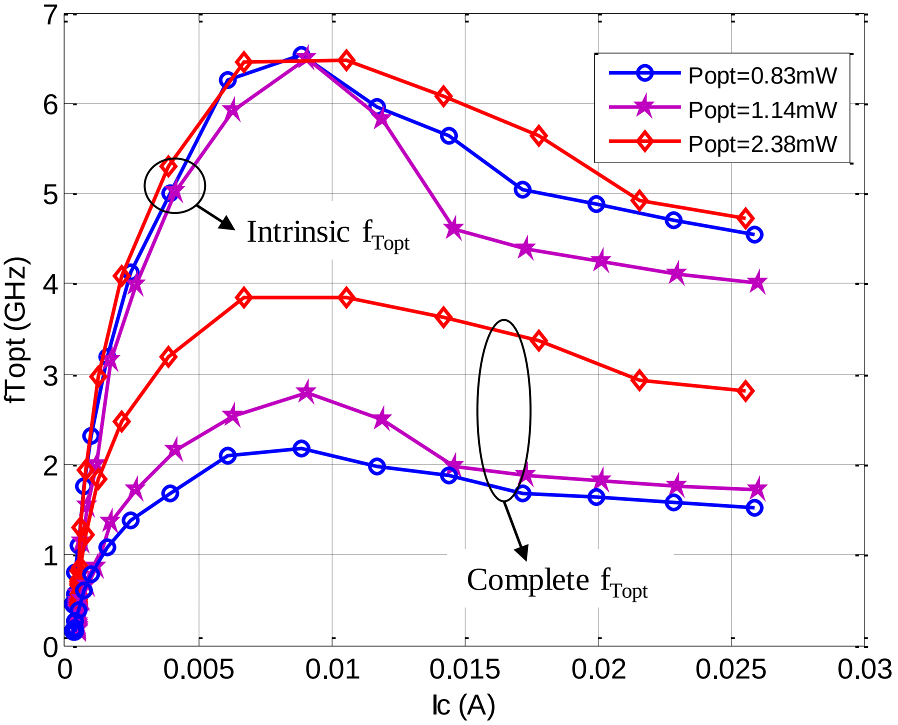

Figure 3-61: Optical transition frequency of the 10x10µm² HPT versus collector current at various injected optical power levels before and after the substrate photodiode effect is corrected.

3.7.3 Transit time and junction capacitance evaluation

As defined in chapter 2 section 2.5, the opto-microwave transition time delay is the time required by the photo-generated carriers to reach any of the contacts. Mathematically, it is related to the optical transition frequency as proposed in chapter 2 equation(2.44). Compared to photodiodes, phototransistors could have higher junction capacitance due to the presence of additional np junction between the emitter and the base. Thus, the source of a capacitive behavior of a phototransistor comes from the emitter-base and collector-base junctions.

Figure 3-62 shows the complete and intrinsic optical transition delay versus 1/IC at different optical power levels measured at the peak detection region of the HPT (X=Z=0µm). Before the substrate effect is removed, the slope and y-intercept of the optical transition time curves have very large difference at different optical power levels, whereas after correction this difference decreases and the extracted value become almost equal. Thus, the substrate photodiode changes the y-intercept and the slope of the complete delay depending on the level of the injected optical power.

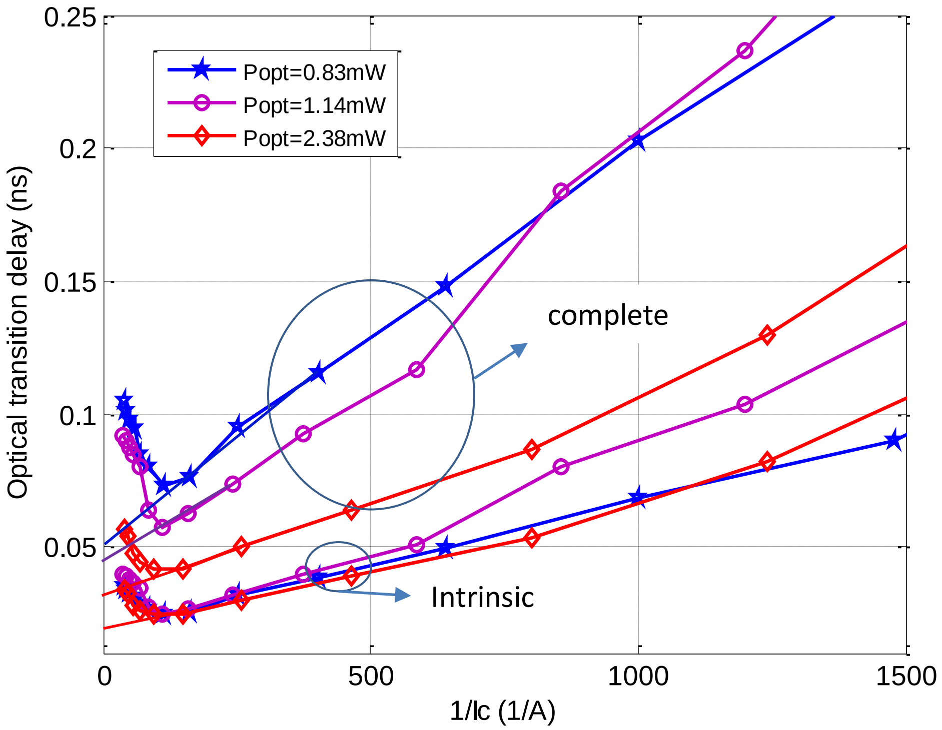

Figure 3-62: Global optical transition delay of the 10x10µm² HPT versus 1/IC at different optical power levels before and after substrate effect corrected.

As it is explained in details in section 2.5, the capacitance and the transit terms of the phototransistor can be extracted from the slope and y-intercept of the transition delay curve.

These values are given in Table 3-10 for a 10x10µm^2 HPT at different injected optical power levels. We compare the intrinsic and complete capacitances and transit times. We have also compared these values with the electrical capacitance and transit time presented in section 3.4.

In general, the complete junction capacitance and transit time terms are higher than the intrinsic ones. The opto-microwave capacitances and transit times are much larger than the electrical equivalent values due to the increase of junction capacitance and transit time experienced by the photo-generated carriers.

A larger value of capacitance and transit time means that photo-generated carriers experience a longer path along the phototransistor than in the electrical transistor. Indeed the electrical transistor lies only in the vertical region of the emitter plus a given electrical extension as seen in section 3.4, while the phototransistor effect is distributed along the whole device with additional lateral path of photo-carriers which are imposed in order to reach the electrical contacts.

As well capacitance terms are larger, related to the given surface of the optical window and variation of the space-charge-region width along the lateral position.

Thus, we deduce the complete and intrinsic “optical” capacitance and transit time by removing the electrical parameters from the opto-microwave extracted ones as described in chapter 2 section 2.5.2. These values give us the additional junction capacitances and transit time that describes the added path length and added equivalent surface supported by photo-generated carriers compared to the electrical ones.

The complete HPT opto-microwave capacitance and transit time increase with the injected optical power decrease.

Table 3-10: The capacitance and transit time terms at various injected optical power levels (P_{in}) before and after the substrate effect is corrected for 10x10µm^2 HPT.

P_{in} (mW)	**Electrical**		**Complete HPT**				**Intrinsic HPT**			
			Opto-microwave		*Optical*		*Opto-microwave*		*Optical*	
	C_{EC} (pF)	τ_F (ps)	C_{EC_OM} (pF)	τ_{F_OM} (ps)	C_{EC_opt} (pF)	τ_{F_opt} (ps)	C_{EC_OM} (pF)	τ_{F_OM} (ps)	C_{EC_opt} (pF)	τ_{F_opt} (ps)
2.38	0.798	1.5	2.657	31.2	1.859	29.7	1.7	18.7	0.902	17.2
1.14	0.798	1.5	4.480	44.4	3.682	42.9	2.0	20.8	1.202	19.3
0.83	0.798	1.5	5.350	53.6	4.552	52.1	1.8	19.6	1.002	18.1

We observe that the "optical terms" for the intrinsic device increase with the optical power decrease, and then decrease. We can consider that the increase is due to the increase in photo-carriers density, which has an impact on the diffusion/drift of photo-generated holes to reach the base region of amplification and on the extension of the equivalent capacitance for the electrons injected from the emitter by the phototransistor effect.

"Optical" capacitance terms are more than half of the full contribution. This means that the equivalent capacitance has either a double surface or a reduced base-collector space-charge-region width (or both). Transit time "optical" terms are however much larger than the electrical ones. Considering that the vertical stack is unchanged, this may be attributed to a lateral path required for holes to be amplified or injected electrons from the emitter to reach the photo-generated holes in the base.

To complete this analysis, we perform an analysis of the capacitances and opto-microwave transit times over surface of the HPT. Figure 3-63 a) and b) respectively shows the slice curves of the complete and intrinsic opto-microwave junction capacitances and transit time at Z=0, 2 and -2µm.

The complete HPT capacitance and transit time increase when we move aside from the center of the active region (X=Z=0). This is explained by the fact that the substrate effect starts dominating over the intrinsic HPT.

The intrinsic capacitance and transit time are smaller compared to their complete one and still important variations over the optical window of the HPT. We observe an increase by a factor more than 2 when the optical beam is closer to the collector electrical contact toward X=10µm, i.e farther from the emitter and base ones, and by a factor more than 1.5 when the optical beam is closer to the base contact toward X=-10µm, ie farther from the collector ones.

The optimum value of these "optical" terms is then somehow at the medium distance of both of them. This may validate the approach of a required lateral path for photo-generated carriers which dominate over the vertical ones. A measurement using a finer beam width would help to improve further such an analysis to be compared with physical simulations as conducted in [260]. This is a perspective of this work which is ongoing.

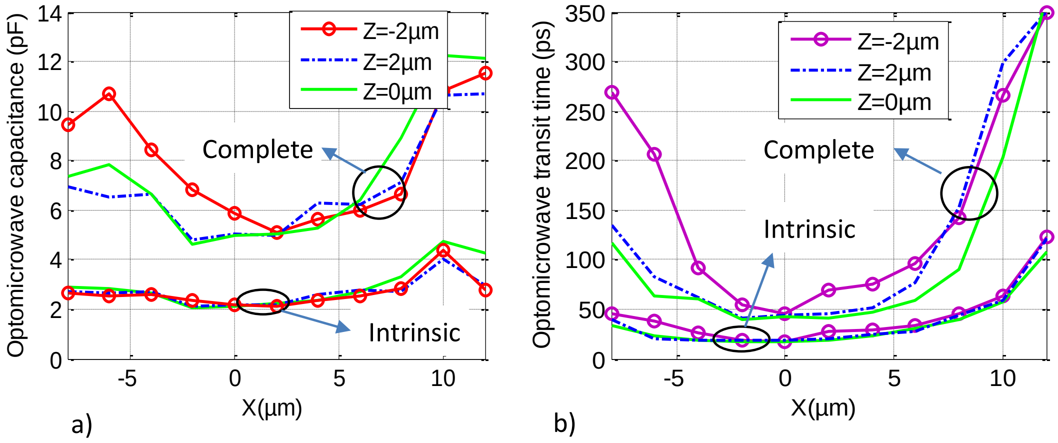

Figure 3-63: The complete and intrinsic a) opto-microwave capacitance b) opto-microwave transit time of the 10x10µm² HPT.

3.8 Selection rules for HPT size and geometry

In this section we demonstrate the size dependency of SiGe/Si HPTs through the complete opto-microwave behavior at 2.38mW injected optical power. The impact of the optical window size on opto-microwave gain and cutoff frequency in both photodiode and phototransistor mode operation is analyzed. The optical window size dependency of the substrate photodiode impact is also investigated.

Figure 3-64 shows the opto-microwave gain slice curve of the three HPTs, having the optical window size of 5x5µm^2, 10x10µm^2 and 50x50µm^2, at 50MHz in HPT and PD modes. In HPT mode configuration the Gom of 50x50µm^2 is higher by 8.3dB than the Gom of 10x10µm^2 HPT and by 15.2dB than the Gom of 5x5µm^2. This is mostly due to higher electrical current gain (β) of 50x50µm^2 HPT as presented in Table 3-11 and its 100% coupling efficiency.

However, in PD mode operation the Gom of the 50x50µm^2 and 10x10µm^2 HPTs is lower than for the Gom of 5x5µm^2 at the center of the optical window. This is demonstrated to be due to the fact that when 28µm diameter optical beam is pointing at the center (*x*=0µm and *y*=0µm) to illuminate over the 5x5µm^2 HPT, a larger portion of the light is illuminating the substrate photodiode. In PD mode operation, the substrate photodiode is more sensitive than the base-collector diode as shown in Figure 3-46 b). Thus, in PD mode, because of the substrate photodiode and coupling efficiency, the opto-microwave gain of 5x5µm^2 HPT is higher than the Gom of 10x10µm^2 and 50x50µm^2 HPTs; Gom of 10x10µm^2 HPT is higher than of 50x50µm^2 HPT.

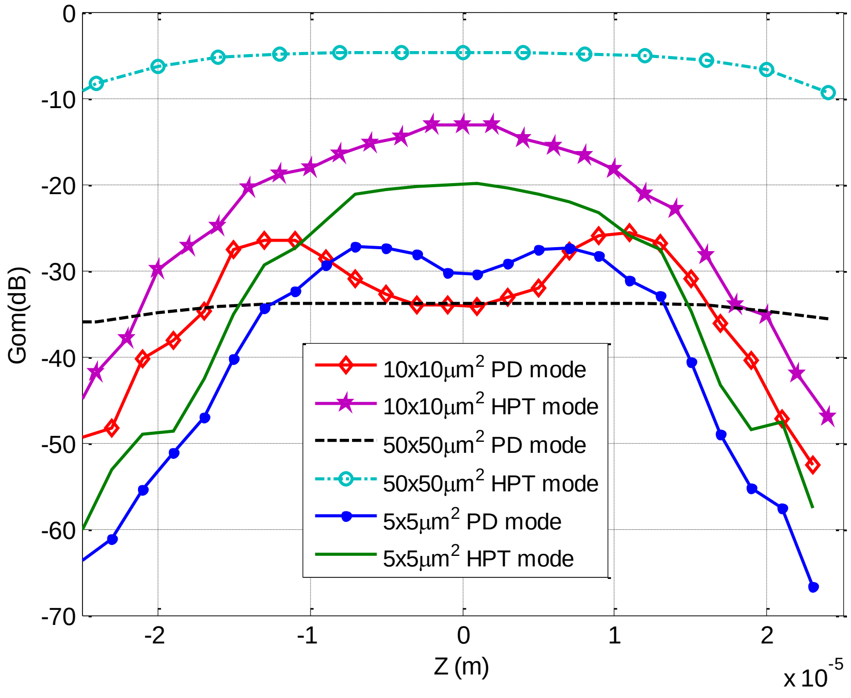

Figure 3-64: The slice curve of the low frequency opto-microwave gain of 50x50µm^2, 10x10µm^2 and 5x5µm^2 optical window size HPTs at X=0m in HPT (Vbe=0.857V) and PD (Vbe=0V) modes of operation for Vce=3V.

Table 3-11: The electrical current gain and low frequency opto-microwave responsivity of the three different size HPTs at x=0µm and y=0µm

HPT window (µm²)	*β at Vbe=0.857V*	*Gom HPT mode at 50MHz (dB)*	*Gom PD mode at 50MHz (dB)*
50x50	438	-4.8	-33.8
10x10	390	-13.1	-33.8
5x5	332	-20.0	-30.3

The low frequency opto-microwave gain slice curve by considering the coupling efficiency of 16.5%, 32.3% and 100% for 5x5µm², 10x10µm² and 50x50µm² HPTs respectively, is presented in Figure 3-65. At the peak detection all sized HPTs have nearly -4dB opto-microwave gain, which is equivalent to the responsivity of 0.67A/W.

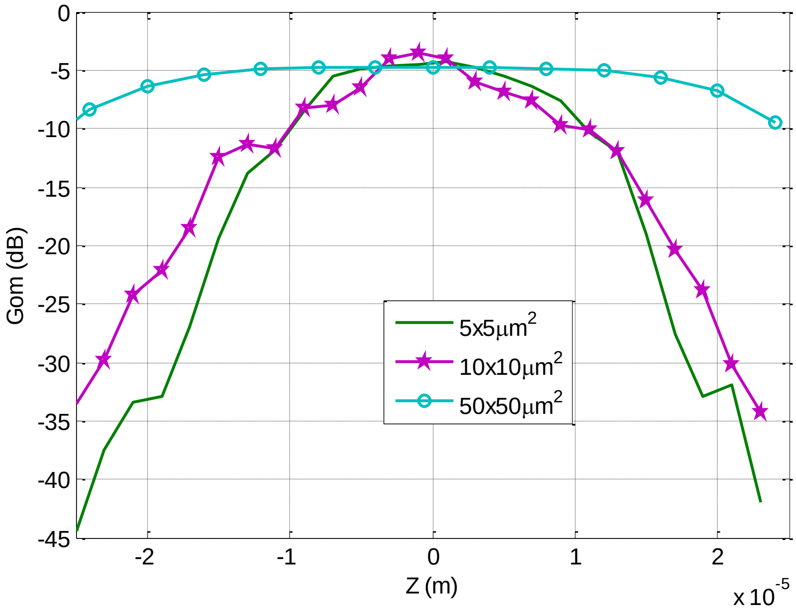

Figure 3-65: Absolute opto-microwave gain of 5x5µm², 10x10µm², 50x50µm² HPTs in phototransistor mode.

Figure 3-66 shows the slice plots of cutoff frequency for 10x10µm², 5x5µm² and 50x50µm²optical window size HPTs at *x*=0 both in PD and HPT modes. The cutoff frequency curves can be decomposed into three different regions (A, B and C) as shown in Figure 3-66 a). Region A represents an extracted cutoff frequency close to the low frequency limitation of the Vector Network Analyzer (VNA) we used (namely 50MHz). Thus, the cutoff frequencies presented in this region are not reliable. The cutoff frequency in region B is mainly related to the substrate response. In this region the cutoff frequency gets smaller and becomes equal in both modes which indicate that the cutoff frequency in this region is extracted from the substrate photodiode. In region C we have high cutoff frequency corresponding to the frequency response of the phototransistor.

Theoretically, the cutoff frequency of smaller surface area transistors is higher than the one of larger surface area transistors due to the RC limit. This theory is consistent if we compare 50x50µm² HPT with the other two in HPT mode. The cutoff frequency of 50x50µm² is less than 80MHz which is much closer to the VNA's low frequency limitation; this cutoff frequency is much smaller than with 5x5µm² and 10x10µm² HPTs. However, when we compare the -3dB cutoff frequency of 5x5µm² and 10x10µm², the theory is no more valid (the cutoff frequency of 5x5µm² HPT is smaller than of

10x10µm^2 HPT). This is due fact that substrate photocurrent and 2D effect in smallest size HPT are much stronger compared with larger optical window size HPT. The excess substrate current is related to the weak coupling efficiency of 5x5µm^2 HPT and has a higher response to the optical beam but lower cutoff frequency. As it is presented in section 3.4, 2D effect in smaller optical window size HPT is stronger as the lateral electrical field is higher with lower dimension under the same dc biasing condition. Thus the lateral flow of carriers dominates over the vertical one when the optical window size is smaller and hence the cutoff frequency degraded.

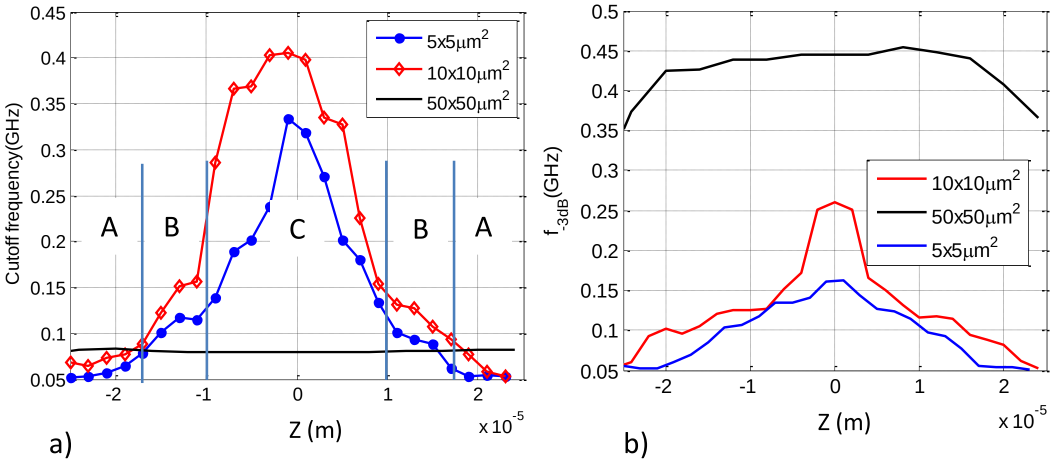

Figure 3-66: Opto-microwave -3dB cutoff frequency of 10x10µm^2 and 5x5µm^2 optical window size HPT at X=0m in a) HPT mode (Vbe=0.857V and Vce=3V), b) PD mode (Vbe=0V and Vce=3V).

Figure 3-66 b) presents the 3dB cutoff frequency in PD mode. The cutoff frequency is usually smaller in phototransistor mode than PD mode due to the large capacitance found in the forward biased base-emitter junction. However, the experimental result shown in Figure 3-66 indicates that the HPT mode cutoff frequency is much higher than PD mode cutoff frequency for 5x5µm^2 and 10x10µm^2. This is once again the influence of the substrate as their coupling efficiency is poor. The substrate photodiode dominates indeed over the intrinsic diode, in PD mode operation. In HPT mode, the substrate photodiode is however dominated by the transistor effect.

However, for 50x50µm^2 HPT as it has 100% coupling efficiency, and the intrinsic HPT is shadowing the underneath substrate photodiode, the substrate effect is not visible. As a result the cutoff frequency in PD mode (≈450MHz) is much higher than its cutoff frequency in HPT mode (≈80MHz) as shown in Figure 3-66. This is consistent with the theory.

We reach up to a complete HPT f_{-3dB} of 420MHz in HPT mode and 260MHz in PD mode operation for 10x10µm^2 HPT, whereas for 5x5µm2 HPT we measure an f_{-3dB} of 350MHz in HPT mode and 160MHz in PD mode.

In general, as we know in photodiode technology there is a trade-off between responsivity/efficiency and cutoff frequency related to the size of the optical window. The responsivity increases with size and the cutoff frequency decreases as the size increases. However, in SiGe/Si phototransistor or photodiode there are additional parameter for the trade-off which are the substrate photodiode and the 2D electrical extension effect. As we have presented in this chapter the impact of the substrate photodiode as well as 2D electrical extension region are larger in smaller size HPTs. The substrate photodiode contributes to the low frequency response but also reduces the apparent cutoff frequency for smaller HPTs. As well depending on the desired function to be realized within the HPT, one may note that the intrinsic HPT responsivity is reduced by the coupling coefficient. So in our study we believe that 10x10µm^2 HPT is a well optimized structure to be implemented in RoF systems.

Due to the presence of the substrate photodiode, the physical behavior of the phototransistor or photodiode deviates from its intrinsic behavior. Hence, we suggest redesigning the HPT structures in order to avoid or minimize the impact of the substrate. This could be achieved:

- Through lateral illuminated structure or
- By properly designing the optical window with a proper metallization.
- By using either smaller optical beam optical source with SMF at 850nm or use MMF with a proper optical coupling structure to characterize the HPTs.

One could also take the advantage of the substrate photodiode to enhance the low frequency responsivity at low frequency applications.

The 2D electrical effect is also modifies the internal dynamic behavior of the HPT. Hence a proper design rules could then be deduced:

- To get a symmetric contact of the collector, base and emitters that will make the electrical field more vertical.
- To fragment the HPT in smaller individual HPTs, as the electrical extension may reach a limit in its increase.

3.9 Conclusion

This chapter presented the different experimental results in the study, optimization and operation of top illuminated SiGe HPTs. We have shown the performance of an HPT both in static and opto-microwave measurements. We have also studied the influence of the HPT physical structure through the localization of the DC and OM behavior over the surface of the device. The substrate photocurrent distribution over the surface of the HPT is deduced from the experimental results and its effect on responsivity and speed of the HPT is extensively studied. An extraction method was then developed to isolate the substrate effect and then measure the intrinsic behavior of the HPT. The influences of various optical window sizes on the performance of the HPT both electrically and for the opto-microwave response are studied. The injected optical power level effect on the performance of SiGe HPT is also presented.

DC characterization of the HPT involves measuring the output Ic-Vce characteristics of the HPT, electrical current gain (β) and the Gummel measurements. The effect of illumination with optical beam at 850nm on the Ic-Vce curves of the HPT is presented. The dc optical current gain is isolated and compared with the electrical behavior.

From the microwave behavioral study we observe that the speed of 3x3µm^2 HPT (26.5GHz) is smaller than of 10x10µm^2 HPT (50GHz). This is due to the 2D electrical extension effect as it is demonstrated through various mathematical models. A proper design rules is then proposed to get a symmetric contacts on the collector, base and emitters so that the electrical field will be more vertical; and also to fragment the HPT in smaller individual HPTs as the electrical extension may reach a limit in its increase.

The opto-microwave gain, the optical transition frequency and opto-microwave cutoff frequency of different size SiGe HPT structures are studied and analyzed at different biasing points. This allows finding an optimum bias point that maximizes the frequency responsivity (Vbe=0.857V, Vce=3V) and speed (Vbe=0.857V, Vce=2V) of the HPT.

We have carried out OM SNOM and DC SNOM analyses as they are crucial to understand the behavior and physical structure of SiGe HPTs. OM SNOM analysis allowed the extraction of an opto-microwave response and the dynamic behavior over the surface of the device at each position of the optical illumination. DC SNOM analysis allowed the extraction of the photocurrent distribution over the structure of the HPTs. This also allowed the extraction of substrate photocurrent over each optical probe position and hence the substrate source is isolated.

From SNOM analysis we have studied the effects of the substrate photocurrent on the responsivity and speed of the SiGe HPT. Both DC and opto-microwave responsivities of the HPT are highly affected by the substrate photodiode. The extrinsic substrate photodiode is much stronger than the intrinsic one. The substrate effect is much visible in PD mode operation than in HPT mode as it is hidden by the transistor effect.

We reach complete cutoff frequency of 420MHz in HPT mode, 260MHz in PD mode and complete optical transition frequency of 4.2GHz for 10x10µm^2 HPT. An extraction method was then applied to isolate the substrate effect and then measure the intrinsic behavior of the HPT. An intrinsic cutoff frequency of 463MHz in PD mode and an intrinsic optical transition frequency of 6.5GHz are then deduced. The intrinsic cutoff frequency is also slight increases in HPT mode.

An alternative to get rid of the substrate contribution could be through a proper design of the optical window with proper metal diaphragms around it. Indeed, the substrate photodiode would be hidden either by metal contacts or by upper layers of the intrinsic HPT, or through the use of a lateral illumination of the HPT. Alternatively taking advantage of the substrate could be envisaged leading to combined HPT+PD structure.

We have also demonstrated the performance of SiGe/Si HPT is highly affected by the level of the injected optical power. This could be related to self-biasing or to variation in the optical source modes at different biasing levels that changes the beam width. The latter effect modifies the coupling efficiency so that the influence of the substrate photodiode is changed for each optical power level.

The optical transition frequency (f_{Topt}=6.5GHz for 10x10µm2 HPT) is much lower than the electrical transition frequency (f_T=50GHz for 10x10µm2 HPT). It is explained by the addition of capacitive and transit time terms related to the photodetection mechanism. The transit time and junction capacitances of the SiGe HPT are extracted experimentally (in electrical, opto-microwave and optical point of view). The opto-microwave capacitance and transit time terms are increased by more than a factor of 3.5 and 21 respectively when compared with their electrical equivalent values. This is due to the increase of junction capacitance and transit time experienced by the photogenerated carriers. We also observed that the complete HPT opto-microwave capacitance and transit time increases with decreasing the injected optical power level. These parameters could be used for further modeling of the SiGe HPT.

Chapter 4 Millimeter Wave and optical Interconnections on Silicon

4.1 Introduction

High speed communication and remote sensing are moving at a rapid pace toward millimeter-wave and optical frequencies in order to achieve extremely high data-rates, enhanced detection capabilities or superior image resolution. The integration of millimeter wave circuits with digital and baseband frequency analog circuits as well as interconnecting optical components using silicon technology is of great interest. Although complete monolithic integration strongly facilitates packaging and offers compactness, the integration of several functionalities into a single chip is not straight-forward and is strongly driven by the system requirements and the aimed costs. There are two approaches to develop integrated microwave-photonics (IMWP) circuits on Silicon platform that could vary based on the technological availabilities and the targeted applications.

Hybrid IMWP circuits:

This approach targets the realization of IMWP circuits by combining VCSELs, high speed detectors and antenna units together with Silicon-based optical and electrical interconnections for RoF applications. In this approach each optical element is developed separately using its optimal substrate, the various elements are then combined on a common Silicon substrate. This Silicon substrate is designed to include passive optical waveguides and electrical interconnections where the active components will be placed in etched cavity such as in Figure 4-1 is the approach that we propose to follow.

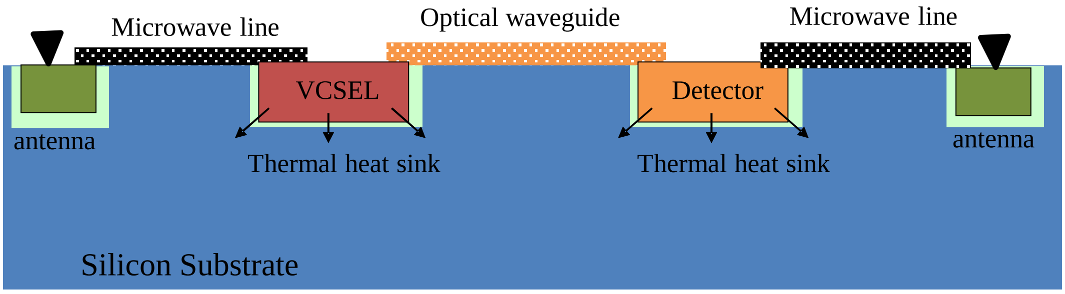

Figure 4-1: The schematic of hybrid integrated microwave photonic circuit.

Since the emission spectrum of the VCSEL lies mainly within the absorption band of silicon (450- 850 nm), it implies that optical waveguide cannot be Silicon based. Standard low resistivity Silicon substrate is also lossy and provides high signal attenuation in the millimeter frequency band. Thus, technologies for circuit interconnections and passive elements on low resistivity CMOS grade silicon still need to be further developed in order to overcome the high signal losses at millimeter and optical frequencies.

High resistivity silicon (HRS) substrates (>1000Ω.cm) are available, but at higher cost and their use deviates from the standard CMOS fabrication process. Micro-machined microstrip waveguide using polyimide as a dielectric interface layer has been investigated [47] [48]. However it has limitations due to the difficulty to achieve a large layer thickness, poor aspect ratio between the layer width and thickness, high curing temperature, and low transparency making subsequent optical alignment difficult. Polymer based electrical interconnections overcome these limitations and are also used for optical interconnections at the board level. The use of polymers such as SU-8, Parylene and BCB is expected to be very efficient to achieve inter-chip interconnections through micro-meter size waveguide, and to be furthermore compatible with the use of lithographic process to design electrical interconnections.

Monolithic IMWP circuits:

The second approach combines on a single chip monolithic optical sources, waveguides and detectors. It is therefore required to have CMOS-compatible Si light emitting sources, detectors, optical waveguides and electrical interconnections. This integration will have the benefit of low cost multi functionality and reduced size of opto- microwave integrated circuits. The targeted applications can be biomedical analysis, microfluidic or Datacom. Detectors and LEDs based on SiGe BiCMOS technology are demonstrated in chapter 3 and 5 respectively. A major stumbling block, however, is the development of low loss and low cost opto-electric interconnections (millimeter wave transmission lines and optical waveguides) in CMOS technology.

In general, this thesis aims at improving the integration of opto-electronic circuits by providing information on the design aspect of individual components that could be implemented into either one or both approaches described above.

Thus, this chapter focuses on the development of interconnecting devices such as: millimeter transmission lines and optical waveguides that are compatible with those approaches.

For the first approach, we investigate a novel method of fabricating transmission line structures in the millimeter frequency range (60GHz) on low resistivity CMOS grade silicon substrates using polymers (SU8 negative resist, BCB and Parylene) as a dielectric interface layer and as optical waveguide (optical interconnections). We investigate the mixed integration of millimeter-waves transmission lines and of optical waveguides simultaneously.

Based on the simulation results through HFSS, we develop the schematic patterns/layout of the transmission lines and optical waveguides using CADENCE software. The validity of the design is then demonstrated through experiment results as presented in the last section.

For the second approach, we design optical waveguides by taking advantage of different oxide layers in SiGe BiCMOS technology. This enables us to develop a full optical link which will then be validated experimentally in chapter 5.

4.2 Planar transmission lines

4.2.1 Introduction

Connections between components are necessary in a circuit design. Typically a metal interconnect is used for these connections. Planar transmission lines, as opposed to waveguides, are commonly used in RF circuits due to the ease of manufacturing, their low cost, their well understood electrical behavior, the availability of Electronic design automation (EDA) tools for design and their small space requirements, among other design benefits. The chief characteristic of planar transmission lines is that the lines are generally routed in two dimensions. Typically, planar transmission lines are metal lines routed on a substrate material such as a printed circuit board, a microwave monolithic integrated circuit (MMIC), etc. A ground plane (continuous metal sheet used as a circuit reference) is commonly located close to transmission lines, either on the opposite side of the substrate (i.e. microstrip), on both sides of the line, or above the substrate.

The performance of transmission lines is highly affected by the losses along the line (attenuation) and circuit matching impedance (characteristics impedance). Planar circuit transmission lines suffer from losses that reduce the signal energy passed through the line. The line losses have various origins that can be ranked in three categories: losses in the conductor (metal), losses in the dielectric, radiation losses. These losses are dependent on the type of line used.

Metal/conductor losses: In RF lines the resistance of the conductors is never equal to zero. Whenever current flows through one of these conductors, some energy is dissipated in the form of heat. This heat loss is a power loss. Another type of conductor loss is due to skin effect. When DC current flows through a conductor, the movement of electrons through the conductor cross section is uniform; the situation is somewhat different when AC is applied. At high frequency AC current tends to avoid travel through the center of a solid conductor, limiting itself to conduction near the surface. This limits the cross-sectional conductor area available to carry alternating current flow. Since resistance is inversely proportional to the cross-sectional area, it increases as the frequency is increased. Also, since power loss increases as resistance increases, power losses increase with frequency because of skin effect.

Dielectric Losses: Result from the heating effect in the dielectric material between the conductors. The heat produced is dissipated into the surrounding medium. When there is no potential difference between two conductors, the atoms in the dielectric material between them are normal and the orbits of the electrons are circular. When there is a potential difference between two conductors, the orbits of the electrons change. The excessive negative charge on one conductor repels electrons on the dielectric toward the positive conductor and thus distorts the orbits of the electrons. A change in the path of electrons requires more energy, introducing a power loss.

Radiation or Induction Losses: Radiation or induction losses are similar as both are caused by the fields surrounding the conductors. Induction losses occur when the electromagnetic field around a conductor cuts any nearby metallic object and a current is induced in that object. As a result, power is dissipated in the object and is lost. Radiation losses occur because some magnetic lines of force about a conductor do not return to the conductor when the cycle alternates. These lines of force are projected into space as radiation, resulting in power losses.

In our model we consider all types of losses and the targeted characteristic impedance is 50Ω. To model our transmission lines we use the commercial electromagnetic simulation software HFSS (High Frequency Structure Simulator). The propagation characteristics of Coplanar, Micro strip and Grounded coplanar lines on low resistive silicon (20Ω.cm) substrate and polymers (SU8, BCB, and Parylene) in 50GHz to 70GHz frequency range are studied. From this model the appropriate dimensions of the lines are determined in order to achieve minimum attenuation and 50Ω characteristic impedance.

4.2.2 Transmission lines modeling using HFSS

High Frequency Structure Simulator (HFSS) is a three-dimensional electromagnetic simulation software based on the finite elements method. This software allows the calculation of the electromagnetic behavior of a structure, and it has post-processing tools for a more detailed analysis of attenuation, propagation constant, characteristic impedance, and the S-parameters of the line.

This work is devoted to model transmission lines of low loss in the millimeter frequency range (60GHz). There are three different methods of extracting the propagation attenuation of lines using HFSS [257].

- The first method (denoted gamma-HFSS) considers the real part of the propagation constant obtained by taking into account only the port surface excitation, irrespective of the actual line length. This is a 2D calculation and it is very fast.
- The second method (rated power) uses the difference between the Poynting vector flows through two surfaces (of identical dimensions) perpendicular to the propagation direction of the traveling wave.
- The third method (denoted extraction) consists of extracting losses from the S_{ij} parameters of two identical lines of different lengths by de-embedding method. The S_{ij} parameters are calculated by HFSS.

Table 4-1 from [257] compares the three methods of losses extraction using HFSS for a microstrip line on glass and on high resistive silicon substrate at 60 GHz. The presented results permit to conclude that the three methods give similar results. Thus, we prefer to use the 1st method to extract the attenuation due to its simplicity.

Table 4-1: Comparison of different methods of calculating losses by using HFSS for a microstrip line on glass and high resistive silicon at 60 GHz. Glass thickness = thickness of silicon = 100µm, metallization width = 100µm and t = 1µm [257]

Method	**Microstrip line on**	
	Glass substrate at 60GHz	**Silicon substrate at 60GHz**
Poynting vector	0.0534 dB/mm	0.0899 dB/mm
Extraction	0.0539 dB/mm	0.0899 dB/mm
Gamma-HFSS	0.0538 dB/mm	0.0894 dB/mm

In this section we study the Coplanar, Microstrip and Grounded coplanar lines from 50 to 70GHz. Low resistive silicon is used as substrate and the metallization is deposited over polymer (SU8, Parlyne or BCB). These lines are in vacuum.

In our simulations we consider materials with the following specifications. The thickness of the substrate is 550µm and the polymer thickness and the line dimensions will be precisely modeled through HFSS simulator.

- The silicon substrate thickness = 550 µm, of resistivity 20Ω.cm, of permittivity ε_r =11.7.
- Gold for metallization having thickness of 1.2µm.
- Different types of polymers (SU8, BCB and Parylene); their properties as specified in table 3.2
- Glass thickness 500µm, tanδ=0.0005, ε_r=4. The glass wafer is put below the silicon one in order to minimize the chuck effect during the measurements using the probe station; it is also considered in simulations for a better match with measurement conditions.
- Stainless steel used as metal chuck with thickness 10µm.

Table 4-2: The electrical properties of polymers (SU8, BCB and Parylene N) used in our model

Polymer	ε_r	tanσ or ρ	Frequency(GHz)	optical above 650nm	Reference
SU8	3.25	0.027	30	Transparent	[52]
BCB	2.5	0.002	60	Transparent	[252]
Parylene-N	2.35	0.0006	60	Transparent	[253] [254]
LR Silicon	11.7	20Ω.cm		absorb	Substrate what we have

The target line dimension and polymer thickness should provide the minimum losses and 50Ω characteristics impedance. We have also taken into consideration the pitch width of GSG probe as an additional constraint to be able to do on wafer measurement. In our laboratory we have 150µm pitch RF probes for 60GHz characterization.

In the following sections we present the simulation results of Coplanar, Microstrip and Grounded Coplanar lines by using SU8, BCB and Parylene-N as dielectric layer over low resistive silicon substrate.

4.2.3 Coplanar Line

a. Structure presentation

We study here the coplanar line on low resistive silicon substrate with the metallization deposited on polymer layer (as shown in Figure 4-3). The optimal metal strip width (s) and slot width (W) will be determined through HFSS simulations. We also fix the polymer thickness based on the possibilities of our technological fabrication process; we will see this thickness has a great impact on the line characteristics. Our main target is to minimize the line loss and to achieve 50Ω characteristics impedance at 60GHz. In our model we have taken into consideration the metal chuck effect during on wafer measurement and also the mechanism to minimize this effect by adding a glass wafer as shown in Figure 4-3 . We put 500µm thick glass wafer under LR silicon wafer during on wafer measurement to avoid the chuck effect on the measurement results.

To characterize the coplanar line, we made several simulations in the frequency band 50 to 70 GHz; we focused on the band 57 - 64 GHz allocated for radio services.

Several modes can propagate in a coplanar line, whose excitation depends on the line excitation system. We meanly distinguish the coplanar and the coupled slot line propagation modes as shown in Figure 4-2. In the following we always consider the coplanar mode corresponding to the classical use of coplanar waveguides: the signal propagates along the metal strip whereas the two metallic planes besides are connected to the ground as shown on Figure 4-3.

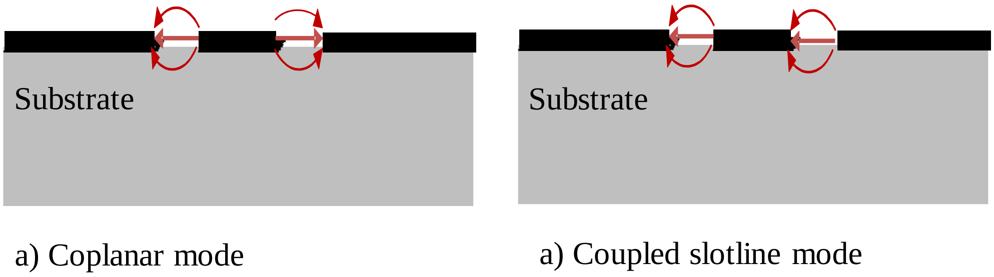

a) Coplanar mode

a) Coupled slotline mode

Figure 4-2: coplanar line wave propagation modes.

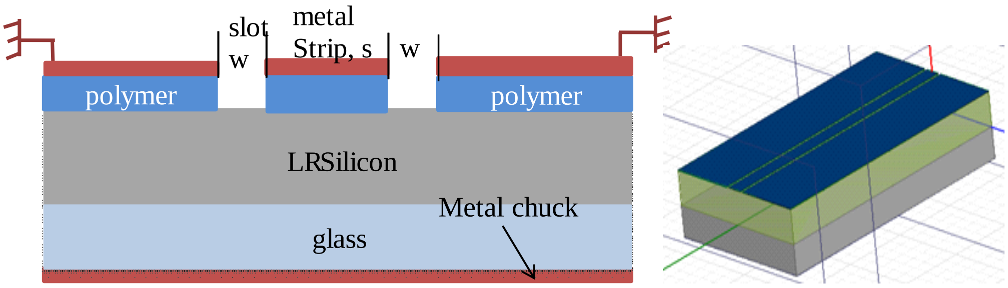

a) Vertical stack of the line along with measurement bench setup effect and protection

b) Picture taken from HFSS simulator

Figure 4-3: CPW transmission line structural schematic

b. Study of the characteristics of the line

The target is to model and design low loss coplanar lines on low resistive silicon substrate having characteristic impedance of 50 Ohm at 60GHz. In this sub-section we present the simulation results of coplanar lines with and without a polymer layer between the metal and the substrate. The influences of the polymer thickness, the metal strip width and the slot width on the characteristic impedance and on the attenuation of the line are presented. We then present the final simulation results for the optimal line dimensions and polymer thickness.

i. Coplanar line with/without polymer layer and metal strip width effect

A 4mm long coplanar line with a central conductor (s) width varying from 114µm to 250µm and a slot gap (w) varying from 13µm to 58µm over 550µm thick low resistive silicon substrate has been simulated at 60GHz. The simulation results are presented in Table 4-3 with 20µm thick SU8 and without SU8 layer between the metal and substrate. As the substrate is low resistive silicon, the lines fabricated without polymer layer have very high losses. In this case, one obtains losses of 2.15dB/mm at 60GHz with line dimensions leading to 50Ω characteristic impedance (metal strip width of 114µm and slot width of 10µm). These losses are strongly reduced just by introducing 20µm SU8 layer between the metal and the silicon substrate: losses of 0.77dB/mm are obtained at the same frequency and for the same characteristic impedance. Table 4-3 also shows how the attenuation of the line varies with metal strip (s) and slot width (w). Large strip width and air gap imply high loss. To achieve 50Ω characteristics impedance we need to play with the metal strip and air gap widths. The characteristics impedance decreases as the metal strip width (s) increases and it increases as the slot width (w) increases. Thus, to get 50Ω line both or one of these parameters could be manipulated depending on our design requirements (such as the characterization GSG probe pitch width).

Table 4-3: Comparison of the attenuation at 60GHz of coplanar lines with 20µm thick SU8 interface over LR Si substrate and coplanar lines directly on low resistive Si substrate; all these lines have a 50Ω characteristics impedance

SU8 h (µm)	Metal width (s) (µm)	Slot width (w) (µm)	α (dB/mm)
20	250	58	1.10
	200	41	0.99
	150	22	0.86
	114	13	0.77
0	250	45	2.29
	200	41	2.28
	150	10	2.15
	114	10	2.15

ii. Polymer thickness effect on the line characteristics

For this study a 4mm long coplanar line with a 150µm wide central conductor (s) and a 22µm wide slot gap (w) is considered. The thickness of the bulk silicon substrate is 550µm and the SU8 thickness varies from 10µm to 30µm with a step of 5µm.

Table 4-4 shows the characteristic impedance and attenuation of coplanar lines estimated by HFSS at 60GHz for different SU8 thicknesses. The characteristic impedance and propagation loss of the line highly depend on the thickness of the SU8 layer. As the SU8 thickness increases the characteristic impedance also increases. Thus, the SU8 thickness is one parameter to be considered in order to achieve the appropriate line impedance. It is also clearly shown in Table 4-4 that as the SU8 thickness increases the attenuation of the line decreases. Thus, to reduce the line losses, it is recommended to deposit thick SU8 layer over low resistive silicon substrate. However, the deposition of very thick polymer layers requires very complicated technological process due to the mechanical properties of polymers (limitations of large thickness achievability and aspect ratio between the layer width and thickness). As a result we choose 16µm polymer thickness for further studies of coplanar line in the following sections.

Table 4-4: Characteristic impedance for different SU8 thicknesses, for s=150µm w=22µm at 60GHz.

SU8 thickness (µm)	Attenuation (dB/mm)	Characteristics impedance (Ohm)
10	1.06	43
15	0.94	47.3
20	0.87	49.67
25	0.80	52.6
30	0.75	53

c. Optimal line dimensions and line characteristics

The parameters that characterize the transmission line on low resistive silicon such as the characteristic impedance, attenuation and propagation constant of the line versus frequency are presented. These values are necessary for the dimensioning of passive devices. 16µm thick polymer is used as a dielectric layer between the low resistive silicon substrate and the conductors. We are targeting 45Ω, 50Ω and 55Ω characteristic impedances to evaluate the effect of fabrication uncertainties and quantify the ones resulting in ±5Ω difference from 50Ω impedance matching. And thus, the width of the metal strip varies for fixed air gap accordingly as shown in

Table 4-5. When we use BCB or Parylene as a dielectric layer, the dimensions of the line (metal strip and slot width) leading to one fixed impedance are the same.

Table 4-5: Line dimensions to obtain coplanar lines of 45Ω, 50Ω,and 55Ω characteristic impedance at 60GHz frequency over 16µm polymer used to elevate the metal over the low resistive silicon substrate.

Polymer type	**Metal strip width, s (µm)**	**Probing slot width, w (µm)**	**Target characteristics impedance (Ω)**
SU8	140	13	45
	114	13	50
	80	13	55
BCB or Parylene	162	13	45
	120	13	50
	90	13	55

We studied the behavior of the lines in the frequency range from 50GHz to 70 GHz for the three different polymer layers; we only present here the results for the lines of characteristic impedance 50Ω at 60 GHz. Thus, the strip width is fixed at 114µm withSU8 or 120µm with BCB/Parylene for the same slot width of 13µm as shown in Table 4-5. Then we perform a simulation in the required frequency range.

Figure 4-4 shows the characteristic impedance versus frequency for SU8, BCB and Parylene layers. The characteristic impedance is almost equal in the three configurations and it slightly decreases with frequency.

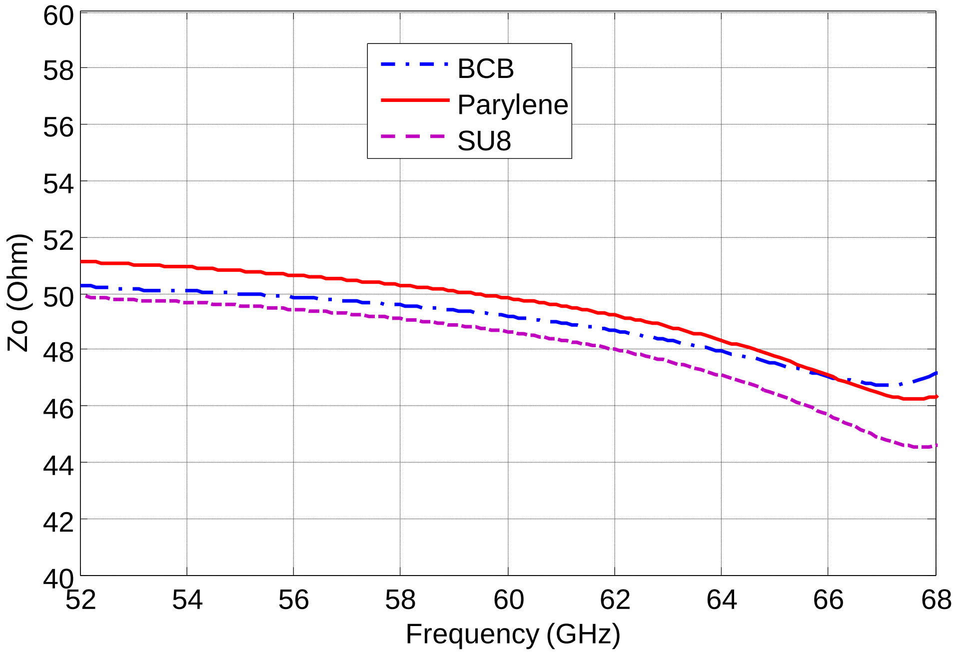

Figure 4-4: The simulated result of the characteristic impedance of coplanar line versus frequency when 16µm polymer layer covers the silicon substrate. The metal strip width is of 114µm and air gap width of 13µm with SU8 against 120µm metal strip width and 13µm slot width with BCB and parylene.

Figure 4-5 and Figure 4-6 show the real and imaginary parts of the propagation constant indeed the attenuation constant α (dB/mm) and the phase constant β (rad/m), for a coplanar line with a central conductor width of 114µm for SU8 and 120µm for BCB or Parylene layers, a thickness of metallization of 1.2µm and a substrate thickness of 550µm. Figure 4-5 details the magnitude of losses in the line related to each polymer layer. Using SU8 as dielectric interface results in the highest losses compared to BCB and Parylene as SU8 has a higher tangent loss for the frequency range of 52GHz to 70GHz. We obtain 0.64dB/mm, 0.66dB/mm and 0.724dB/mm attenuation for Parylene, BCB and SU8 respectively at 60GHz. Figure 4-6 shows the imaginary part of the propagation constant versus frequency; it varies linearly up to 67 GHz.

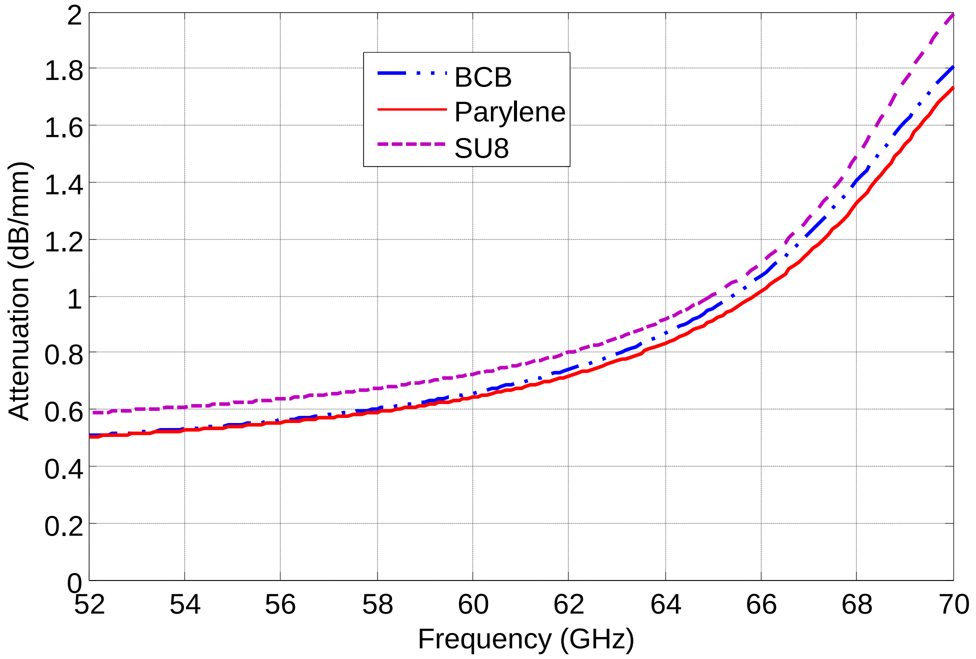

Figure 4-5: The simulated result of the attenuation of coplanar line versus frequency with 16µm polymerlayers and line dimensions for 50Ω characteristic impedance.

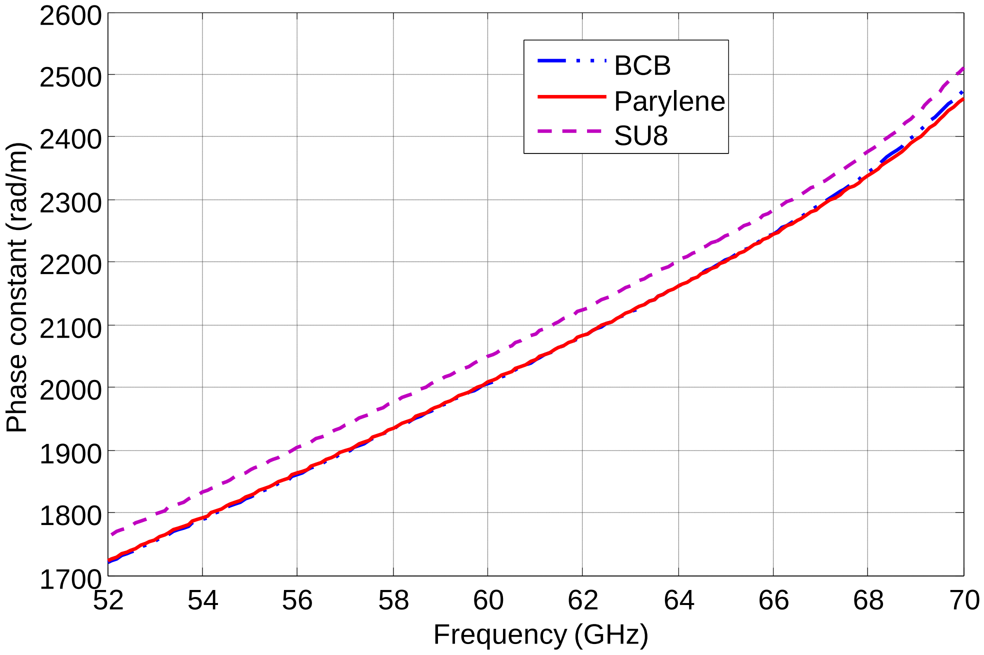

Figure 4-6: The imaginary part of the propagation constant of coplanar line versus frequency with 16µm polymer layer and line dimensions for 50Ω characteristic impedance extracted from the HFSS simulator.

Both transverse and longitudinal electric field distributions of a coplanar line are shown in Figure 4-7 when SU8 is used as dielectric layer between metal and low resistive silicon substrate. The electric field is presented by its magnitude and as a vector. The electric field is confined in the slots between the strip line and the two ground metallic planes situated on both sides of the strip (See Figure 4-2). Since the polymer layer is thin, we can observe in Figure 4-7 a) and b) that at 60GHz a part of the RF signal propagates through the silicon substrate. As a consequence, the losses in coplanar line are high compared to micro strip and grounded coplanar lines on polymer layer. At 50GHz (Figure 4-7 c) and d)) the field confinement in SU8 is better: it is coherent with the lower losses (see Figure 4-5).

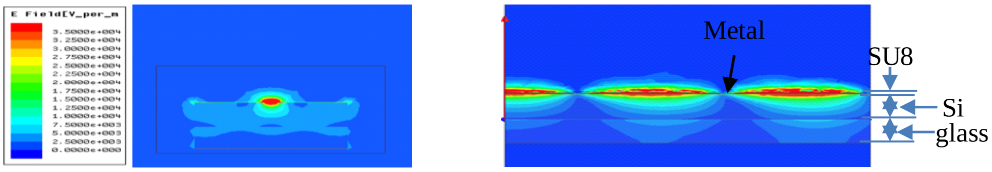

a) Transversal E-field at f=60GHz coplanar mode d) Longitudinal E-field at f=60GHz coplanar mode

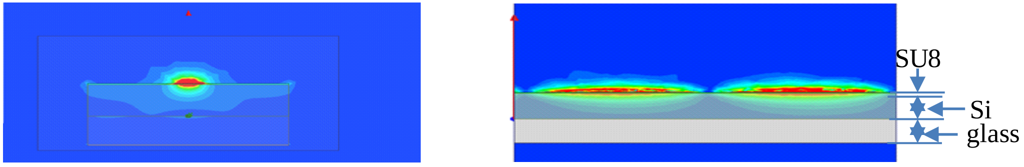

c) Transversal E-field at f=50GHz coplanar mode d) Longitudinal E-field at f=50GHz coplanar mode

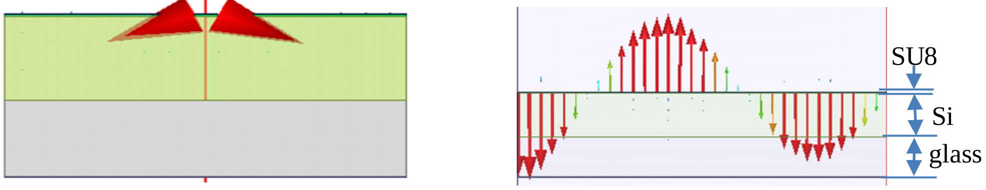

e) Transversal E-field vector at f=60GHz coplanar mode f) Longitudinal E-field vector at f=60GHz coplanar mode

Figure 4-7: Electric field amplitude (V / m) and vector in the transverse and longitudinal planes of the coplanar line on low resistive silicon substrate with a SU8 layer. The line dimensions are s=114µm, w=13µm h_{SU8}*=16µm*

The simulation results of coplanar line over 16µm thick polymer layer at 60GHz and to achieve characteristic impedances of 45Ω, 50Ω and 55Ω are summarized in Table 4-6. To reach this goal we fix the slot width at 13µm and vary the metal strip width. To get higher characteristic impedance the metal strip width has to be smaller. Eventually, the line loss decreases from 0.81dB/mm to 0.70dB/mm while the metal strip width decreases from 140µm to 80µm.

Table 4-6: Summary of the estimated dimensions of the coplanar line obtained using HFSS simulations. Different polymer types are used and several targeted characteristic impedances at 60GHz are considered. The line losses are also evaluated at 60GHz using HFSS simulator.

Polymer type	**Metal strip width, s (µm)**	**Probing slot width, w (µm)**	**Target characteristics impedance (Ω)**	**Attenuation (dB/mm)**
SU8	140	13	45.5	0.81
	100	13	49.5	0.72
	80	13	54.8	0.70
BCB	162	13	45.5	0.74
	120	13	49.8	0.65
	90	13	55.2	0.62
Parylene	162	13	45.6	0.70
	120	13	50.5	0.63
	90	13	55.3	0.60

4.2.4 Micro-strip line

a) Structure explanation

In this section we are interested in the modeling of the micro-strip line consisting of a metallic ribbon and ground plane separated by polymer (see Figure 4-8). Low resistivity silicon substrate is used as mechanical support as it is cheap and widely used for CMOS technology. Its high losses in high frequency band won't be a problem in this configuration as it is hidden by the ground plane. We use a polymer layer between the ground metal and metal strip; and thus the effect of low resistive silicon substrate is avoided as the electric field is confined above the ground plane. We study here the electrical characteristics of the line between 50 and 70 GHz for different polymers (SU8, BCB and Parylene), and compare the obtained electrical characteristics. Our main goal is to obtain a micro strip line having 50Ω characteristic impedance and low loss.

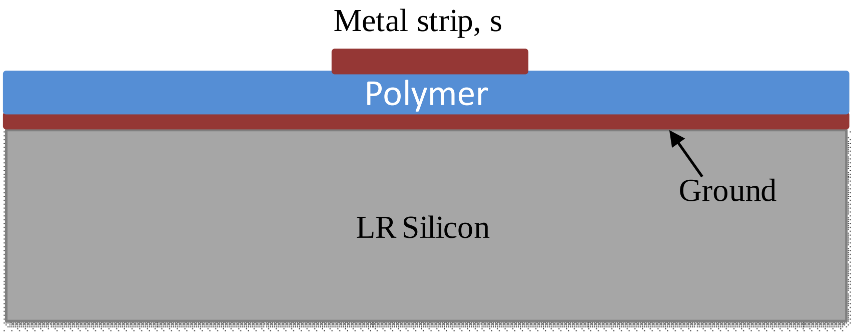

a) Side view of Micro strip line structure at the center of the line

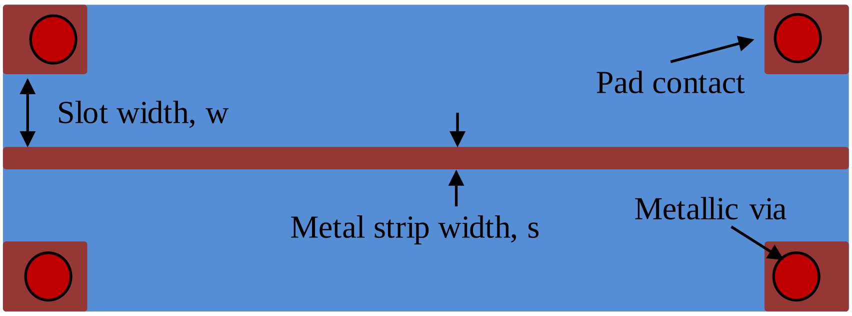

b) Top view of Micro strip line structure

Figure 4-8: Side view and top view of micro strip line structure. Metallic vias permit to connect the ground of the measurement setup to the microstrip line ground plane is shown in b).

Several simulations have been performed in the 50-70 GHz frequency band. For this study, we took the silicon substrate thickness of 550µm, resistivity of 20Ω.cm and permittivity of 11.7. The line is 4mm long and 1.2µm thick gold metallization. The electrical characteristics of the polymers used in this simulation are shown in Table 4-2.

First of all we focused on the influence of the polymer thickness (by using SU8 only) on the propagation of electromagnetic waves with a metal strip width of 51µm and a length of 4 mm. Then for 16µm polymer thickness, we will fix the metal strip width according to the polymer type to reach 50Ω characteristic impedance in the studied frequency band.

b) The effect of Polymer thickness on micro-strip line characteristics

We study here the effect of SU8 thickness on the characteristics of micro-strip lines, for a silicon substrate thickness of 550µm, a metal strip and ground metal thickness of 1.2µm and metal strip width of 51µm.The SU8 thickness varies from 10µm to 30µm with 5µm step.

We find a characteristic impedance of 32Ω for SU8 thickness of 10µm and 57.6Ω for SU8 thickness of 30µm as shown in Figure 4-9. The characteristics impedance increases with SU8 thickness. Thus, to achieve 50Ω characteristics impedance with low SU8 thickness, the metal strip width needs to be thinner than with a thicker SU8 layer as the impedance decreases with metal strip width increase.

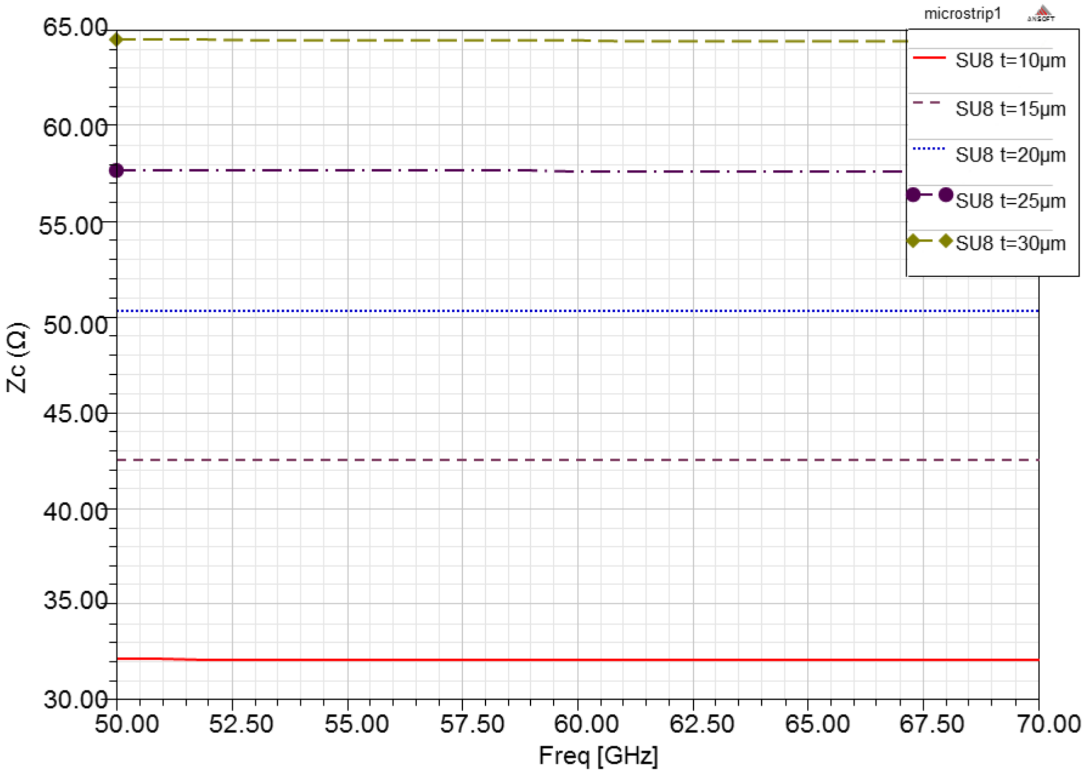

Figure 4-9: Micro-strip line characteristic impedance versus frequency for variable SU8 thickness and metal strip width s=51µm as it is deduced from the simulation

As it is shown in Figure 4-10 the attenuation decreases as the polymer thickness increases from 10µm to 30µm. It was expected as, when the polymer thickness is high enough, the micro-strip mode electric field is confined properly between the two metals, and the radiation in the air is reduced (reduced radiation loss). Besides, the attenuation slightly increases with frequency.

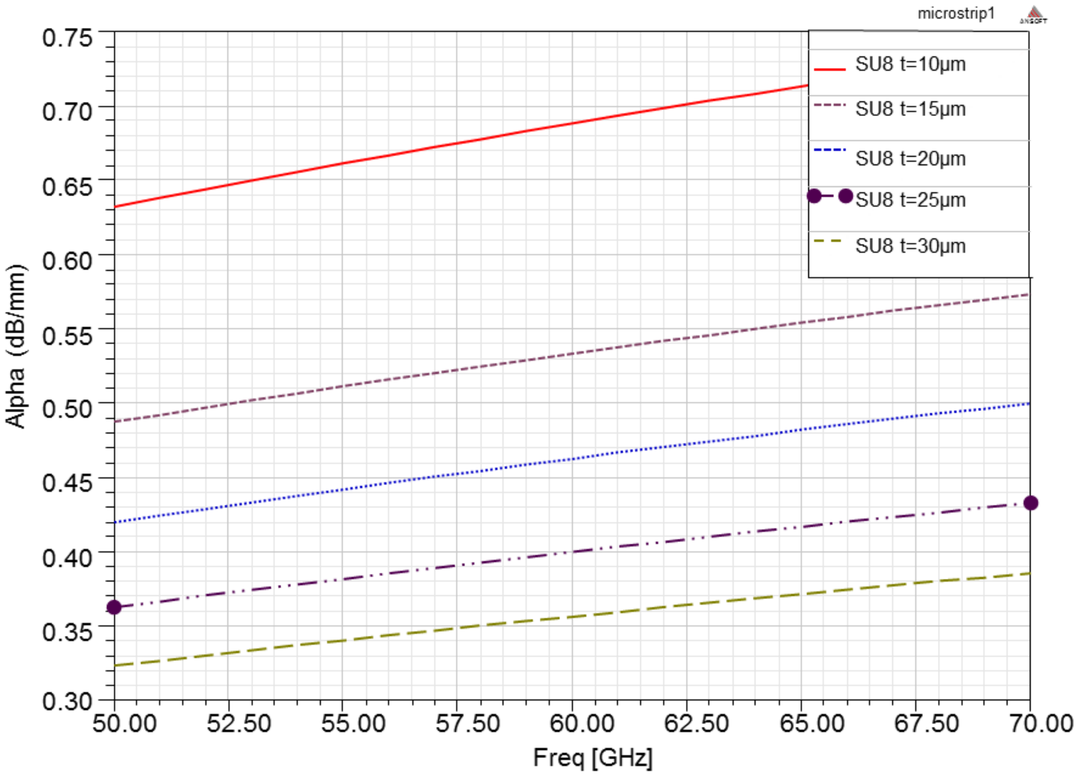

Figure 4-10: Micro-strip line attenuation versus frequency for variable SU8 thickness and metal strip width s=51µm obtained from simulation result

c) Optimal line dimensions and characteristics

The parameters that characterize the micro-strip line such as the characteristic impedance, attenuation and propagation constant versus frequency (from 50 to 70 GHz) are presented for different layers. These values are necessary for the dimensioning of passive devices. Since there is a limitation of technological fabrication process to obtain thick polymer layer, we choose a 16µm thick polymer layer to be deposited as metal to substrate interface. To achieve 45Ω, 50Ω and 55Ω characteristic impedance the dimension of the metal strip width varies. We target three different characteristic impedances to search of matching flexibility and to take simulator and fabrication imperfections into account. The dimension of the strip also varies with the type of polymer used as shown in Table 4-7.

Table 4-7: Line dimensions computed through HFSS simulator to achieve 45, 50 and 55 characteristic impedance at 60GHz for different polymers used to isolate the micro-strip line from silicon substrate

Polymer type	**Metal strip width, s (µm)**	**Probing slot width, w (µm)**	**Target characteristics impedance (Ω)**
SU8	48	20	45
	41	20	50
	35	20	55
BCB and Parylene	56	20	45
	48	20	50
	44	20	55

To study the behavior of the line in the frequency range of 50GHz to 70 GHz for the three polymers; we fix the strip width at 41µm with SU8 or 48µm with BCB/Parylene to obtain a characteristic impedance of 50Ω.

Figure 4-11 shows the characteristic impedance versus frequency with SU8, BCB and Parylene. As expected, the characteristic impedance is close to 50Ω in the three cases.

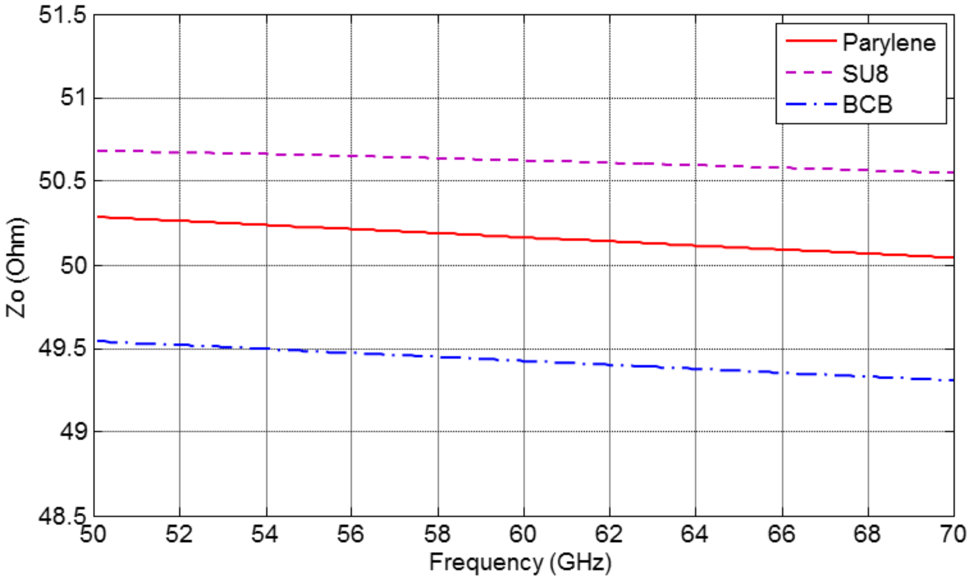

Figure 4-11: The simulated result of the characteristic impedance of micro-strip line versus frequency for different dielectric layers. The metal strip width is of 41µm for SU8 and 48 for BCB or Parylene layers; the slot width is of 20µm.

Figure 4-12 and Figure 4-13 show the propagation constant related to the attenuation α (dB/mm) and the phase constant β (rad/m), for a metal strip width of 41µm with SU8 and 48µm with BCB or Parylene, the thickness of metallization is of 1.2µm and a silicon thickness of 550µm. Figure 4-12 details the magnitude of losses related to the each chosen polymer. Using SU8 as dielectric layer leads to higher loss than with BCB and Parylene as it has a higher tangent loss in the 50GHz-70GHz frequency range. We obtain 0.151dB/mm, 0.153dB/mm and 0.325dB/mm attenuation for Parylene, BCB and SU8 respectively at 60GHz. Figure 4-13 shows the propagation constant imaginary part (phase constant) versus frequency. It is linear over 50GHz to 70GHz frequency range for all polymers.

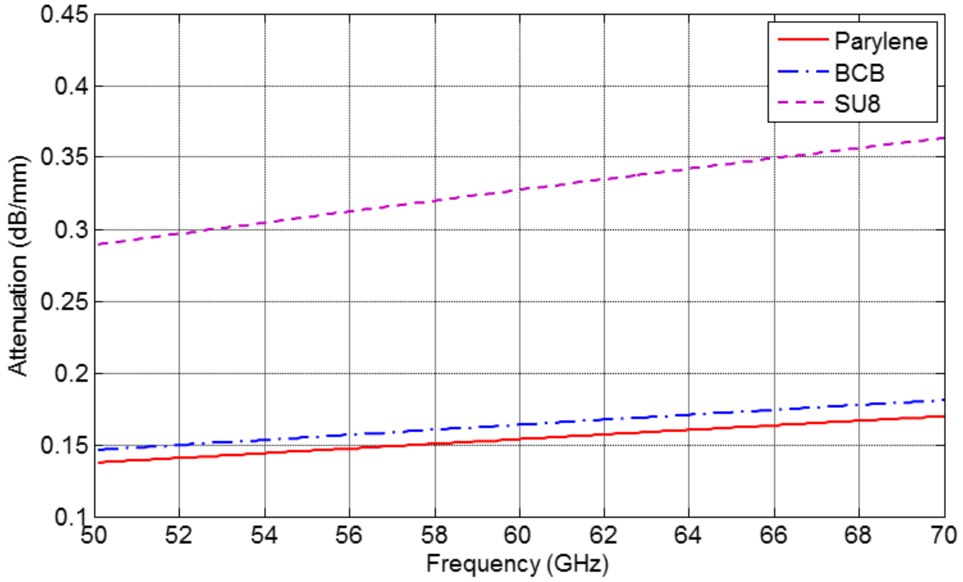

Figure 4-12: The simulated result of the attenuation of micro strip-line versus frequency for different dielectric layers. The metal strip width is of 41µm for SU8 and 48µm for BCB or Parylene and the slot width of 20µm.

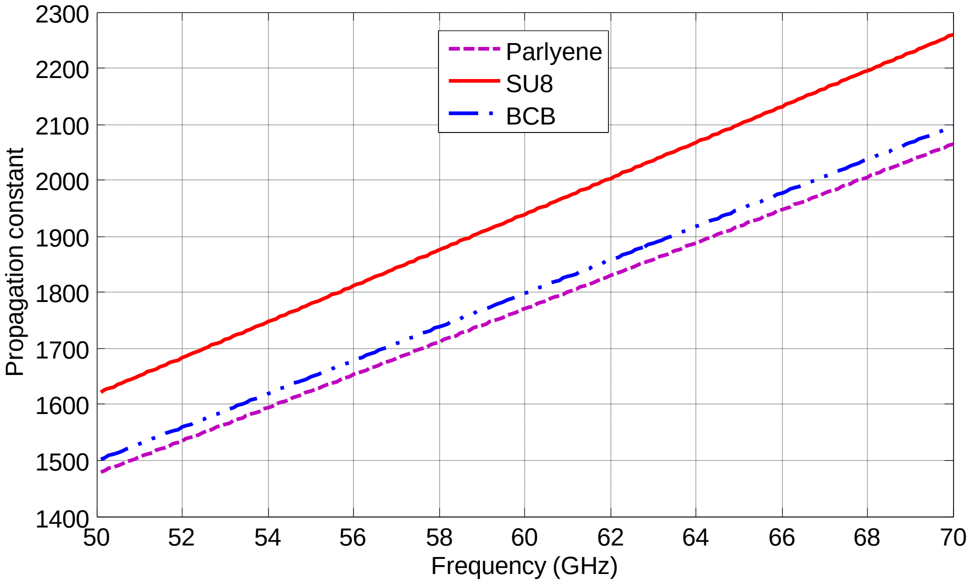

Figure 4-13: The simulated result of the phase constant of micro-strip line versus frequency for different dielectric layers. The metal strip width is of 41µm for SU8 and 48µm for BCB or Parylene and the slot width of 20µm.

Both transverse and longitudinal electric field distribution of microstrip line are shown in Figure 4-14 when SU8 is used as dielectric layer. We observe that the electric field is well confined between the strip line and the ground metal. As there is no energy propagating through the low resistive silicon, the attenuation is kept small. The good field propagation is noticed for example at 60GHz and 70GHz in Figure 4-14 a) and c) respectively as the electric field distribution remains quite similar along the line.

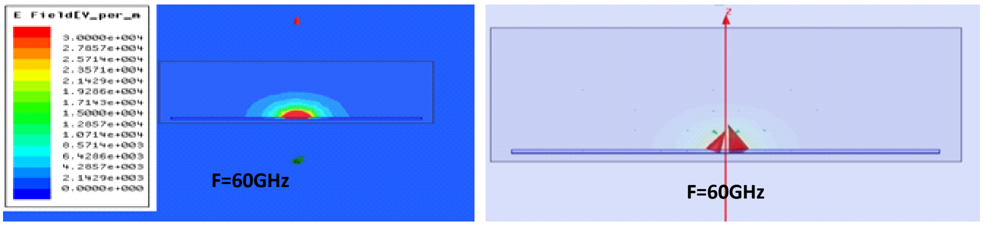

a) Electric field amplitude in the transverse plane at 60GHz **b) Electric field vector in the transverse plane at 60GHz**

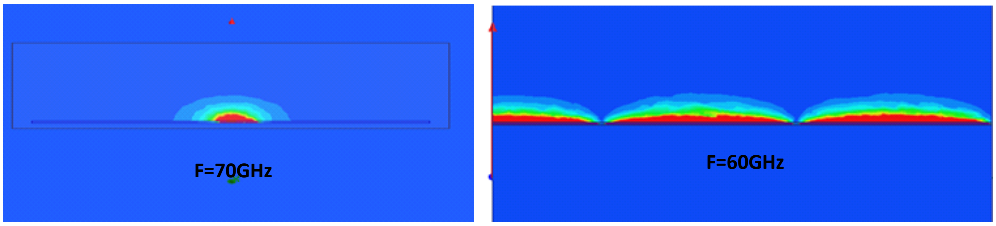

c) Electric field amplitude in the transverse plane at 70GHz **d) Electric field amplitude in the longitudinal plane at 60GHz**

Figure 4-14: Electric field amplitude (V / m) and vector in the transverse and longitudinal planes of the micro-strip line with SU8 layer for strip width of 41µm.

In Table 4-8 we summarize the simulation results at 60GHz for 16µm thick polymer and micro-strip lines of characteristics impedance 45Ω, 50Ω and 55Ω. To achieve these different characteristic impedances we modify the metal strip width from 48µm to 41µm as shown in Table 4-8. The corresponding attenuations are also presented in the same table. We observe higher attenuations and smaller strip widths are obtained with SU8, whereas similar results are obtained with BCB and Parylene

Table 4-8: Summary of dimension estimations using HFSS simulator of micro-strip line with different polymers and for several targeted characteristic impedances at 60GHz. The propagation attenuation is also evaluated using HFSS simulator at 60GHz.

Polymer type	**Metal strip width, s (µm)**	**Probing slot width, w (µm)**	**Target characteristics impedance (Ω)**	**Attenuation (dB/mm)**
SU8	48	20	45.5	0.31
	41	20	50.7	0.33
	35	20	55.5	0.37
BCB	56	20	45.1	0.15
	48	20	49.8	0.153
	44	20	55.8	0.16
Parylene	56	20	45.5	0.15
	48	20	50.2	0.15
	44	20	55.2	0.155

4.2.5 Grounded Coplanar Line

a) **Structure explanation**

In this section we study the grounded coplanar line. As the coplanar waveguide, it consists of a metal strip along which the signal propagates and the two metallic planes besides connected to the ground. The difference with the coplanar waveguide leads in the presence of a ground plane hiding the low resistive silicon substrate, so that the signal can propagate within the polymer deposited above this inferior ground plane as shown in Figure 4-15. We aim to use this line for high frequency applications. In this case, the propagation takes place in the polymer and in the air, so the propagation medium can be considered as inhomogeneous. We will use low resistivity silicon substrate as mechanical support as it is cheap and widely used for CMOS technology. We use a polymer layer between the ground metal and metal strip; and thus the effect of low resistive silicon substrate is avoid as the electric field is confined within the two slots around the metal strip. The polymer is removed in the slot in order to minimize the propagation attenuation. We study here the electrical characteristics of the line between 50 and 70 GHz for different polymers (SU8, BCB and Parylene), and compare the electrical characteristics in each configuration. Our main goal is to obtain a grounded coplanar line having 50Ω characteristics impedance and low loss.

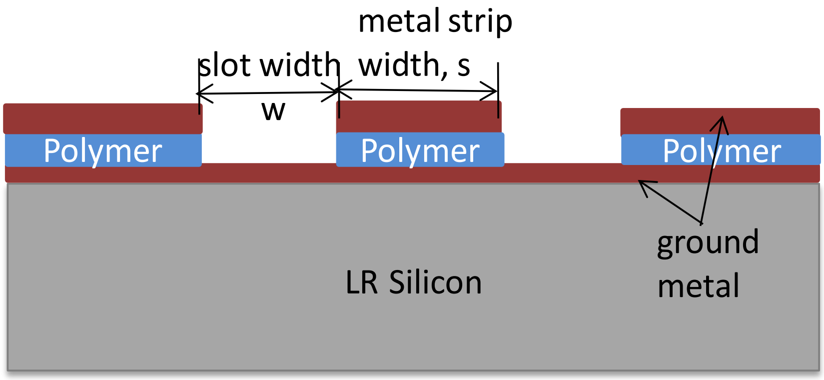

Figure 4-15: Cross sectional view of grounded coplanar line structure

To characterize such transmission line, we performed several simulations in the 50-70 GHz frequency band, looking more specifically at its behavior around 60 GHz. In this study, we consider a silicon substrate thickness of 550µm, resistivity of 20Ω.cm and permittivity of 11.7. The line is 4mm long and gold thickness is of 1.2µm. Metal dimensions will be chosen according to the polymer layer and the target characteristic impedance. The electrical characteristics of the polymers used in simulations are shown in Table 4-2.

We saw that the thickness of the polymer deposited between the upper and the lower metallic layers has similar effect as already observed with the micro-strip line.

b) Optimal line dimensions and characteristics of grounded coplanar lines

The characteristic impedance, attenuation and phase constant of grounded coplanar line versus frequency (from 50 to 70 GHz) are presented when SU8, BCB and Parylene are used as dielectric layers. These values are necessary for the line dimensioning. Due to the technological fabrication process limitations, we choose 16µm thick polymer rather than a thicker polymer layer. For matching flexibility with different circuit interconnections and taking fabrication errors into account; we targeted 45Ω, 50Ω and 55Ω characteristic impedances. Thus, the dimensions of the metal strip and air gap widths vary accordingly. These dimensions also vary with the polymer used as shown in Table 4-9.

Table 4-9: Grounded coplanar line dimensions determined using HFSS simulations to get characteristic impedances of 45Ω, 50Ω, 55Ω at 60GHz for different polymer layers.

Polymer type	Metal strip width, s (µm)	Probing slot width, w (µm)	Target characteristics impedance (Ω)
SU8	90	30	45
	80	30	50
	72	30	55
BCB and Parylene	100	30	45
	88	30	50
	79	30	55

To study the behavior of the line between 50GHz and 70 GHz, we fix the strip width at 80µm with SU8 or 88µm with BCB/Parylene. We take a slot width of 30µm. For these specifications the characteristics impedance is of 50Ω.

Figure 4-16 shows the characteristics impedance versus frequency for SU8, BCB and Parylene. The characteristic impedance is almost constant from 50GHz to 70GHz and it is a slightly higher with Parylene layer.

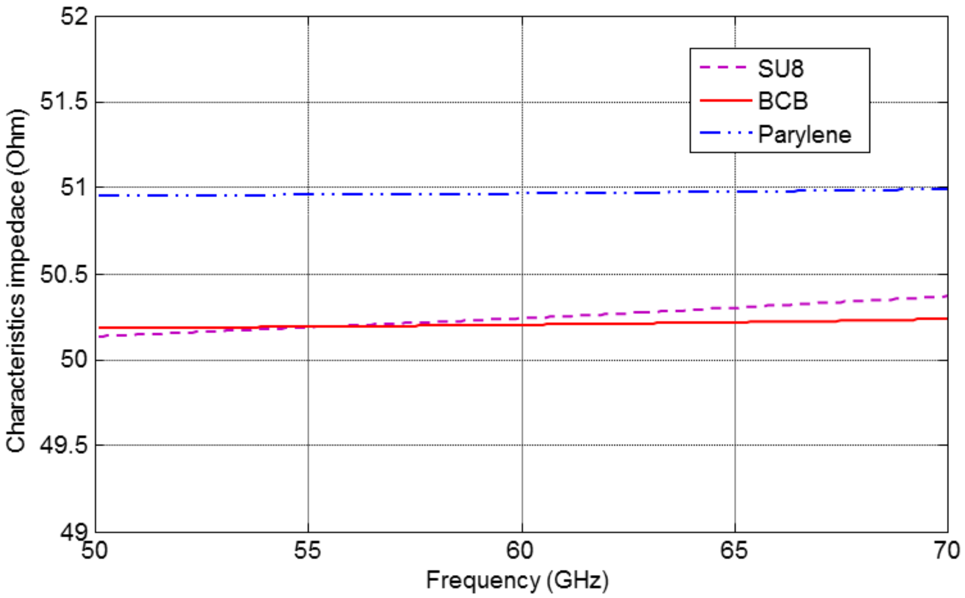

Figure 4-16: Characteristic impedance vs frequency for different polymers as it is extracted from HFSS simulator

Figure 4-17 and Figure 4-18 show the propagation constant real and imaginary parts, namely the attenuation α (dB/mm) and the phase constant β (rad/m), for a metal strip width of 80µm with SU8 and 88µm with BCB or

Parylene, a metallization thickness of 1.2µm and a substrate thickness of 550µm. Figure 4-16 details the magnitude of losses for each chosen polymer. With SU8 the grounded coplanar line has higher losses than with BCB and Parylene due to the higher tangent loss of BCB in the studied frequency range. We obtain attenuation of 0.135dB/mm, 0.15dB/mm and 0.31dB/mm for Parylene, BCB and SU8 respectively at 60GHz. The signal loss slightly increases with frequency regardless of the polymer type. The slop of the attenuation curve with BCB and Parylene are equal and it is smaller than with SU8. This indicates that the use of BCB and Parylene as a dielectric layer in Grounded coplanar line highly minimizes the losses in the 50-70GHz frequency band compared to SU8.

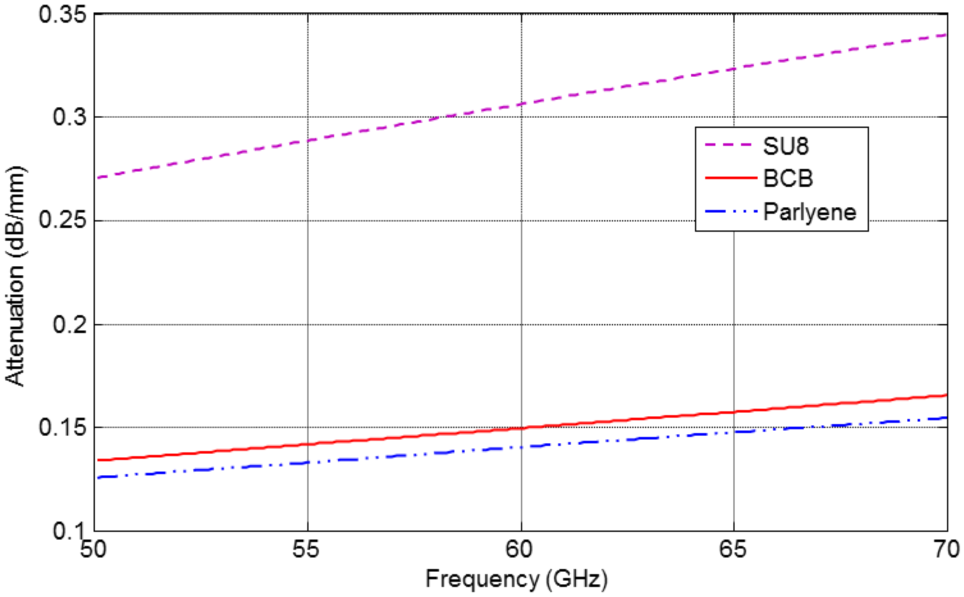

Figure 4-17: The simulated result of the attenuation of grounded coplanar line versus frequency for different dielectric layers. The metal strip width is of 80µm for SU8 and 88µm for BCB or Parylene, whereas the slot width is of 30µm.

Figure 4-17 shows the imaginary part of the propagation constant versus frequency. It is linear over 50GHz to 70GHz frequency range.

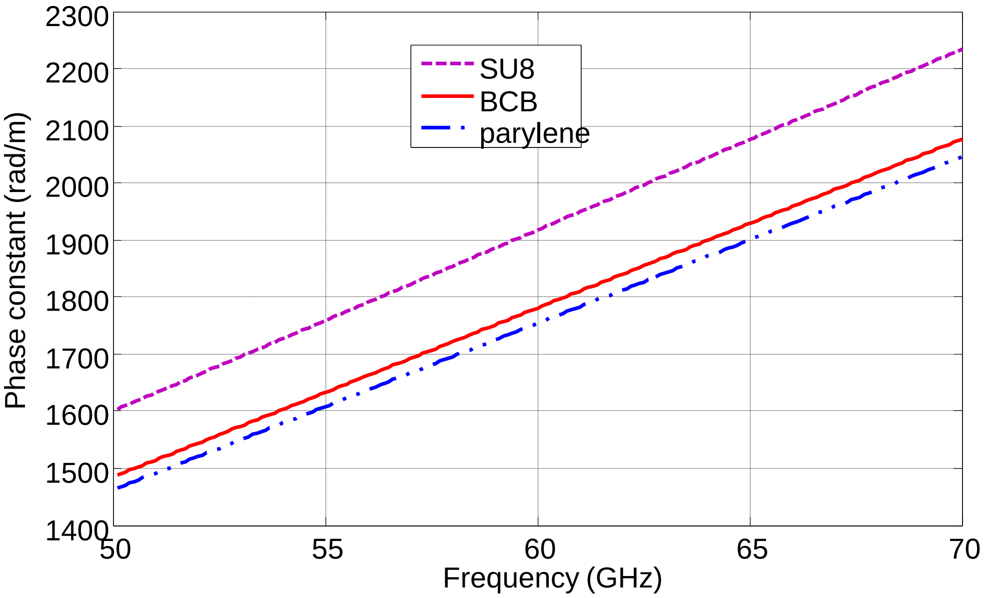

Figure 4-18: The simulation result of the phase constant versus frequency for different dielectric layers. The metal strip width is of 80µm for SU8 and 88µm for BCB or Parylene, and the slot width is of 30µm.

Figure 4-19 shows the distribution of the transverse electric field amplitude of grounded coplanar line with an SU8 layer. We observe that the electric field is well confined in the polymer around the strip as well as in the air around it. As there is no field propagation through the low resistive silicon, the loss is kept small. The E-field distributions at all frequencies in the simulated frequency range show a good propagation along the line.

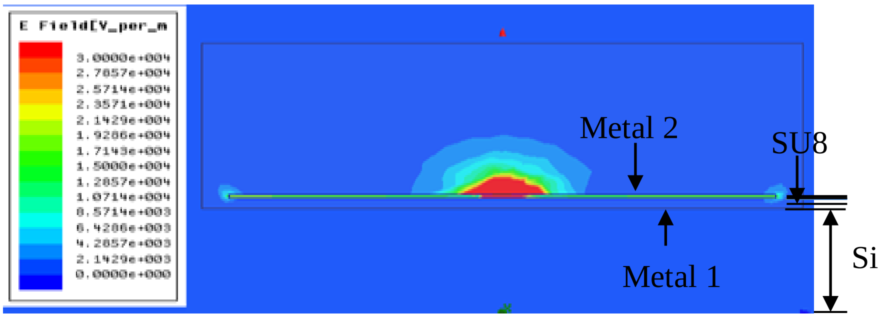

Figure 4-19: Electric field amplitude (V / m) in the transverse plane of the grounded coplanar line on low resistive silicon substrate with SU8 layer and a strip width of 80µm.

As explained before, we search to simulate transmission lines of characteristic impedance 50Ω. However, due to fabrication process and simulation imperfection the characteristic impedance could deviate from the target. Thus we designed grounded coplanar lines of 45Ω, 50Ω and 55Ω characteristic impedances by varying the metal strip width for a fixed slot width of 30µm as presented in Table 4-10 for the three different polymers and at 60GHz. As for the micro-strip line, we observe the attenuation is higher with SU8 layer and the line width is smaller.

Table 4-10: Summary of dimensions of grounded coplanar line estimated using HFSS simulator for different polymer layers and several targeted characteristic impedances at 60GHz. The losses in the line also evaluated via HFSS simulator at 60GHz are presented.

Polymer type	**Metal strip width, s (µm)**	**Slot width, w (µm)**	**Target characteristics impedance (Ω)**	**Attenuation (dB/mm)**
SU8	90	30	45.1	0.31
	80	30	50.2	0.31
	72	30	55.2	0.31
BCB	100	30	44.5	0.15
	88	30	50.2	0.15
	79	30	54.6	0.15
Parylene	100	30	45.4	0.14
	88	30	50.6	0.14
	79	30	55.5	0.15

4.3 Optical Waveguide

The optical waveguide is the fundamental element that interconnects various devices of an optical integrated circuit, just as the previously presented lines do in an electrical integrated circuit. However, whereas in these lines one single propagation mode appears in the considered use conditions, several distinct optical modes can propagate in an optical waveguide. A mode, in this sense, is a spatial distribution of optical energy associated to propagation characteristics. In this section, simulation results of optical waveguides are presented. First we present the simulation results of polymer based optical waveguides and then of optical waveguides based on different oxide layers of SiGe BiCMOS technology.

4.3.1 Polymer based optical waveguide

Polymer materials are used for optical interconnections at the board level. Using polymers such as SU-8 and BCB is foreseen to be very efficient for inter-chip interconnections with micro-meter size waveguides, while being furthermore compatible with lithographic interconnections for electrical interfaces. SU8 and BCB exhibit optical attenuation in 1dB/cm range in the near-IR region [79] [80]. Proven to be good candidates for optical waveguides within a chip, they offer the promise of an excellent convergence with the lithographic interconnections for electronics. The processing properties of photoresists enable the design of 3D shapes. Combined with wafer-level packaging, these waveguides demonstrate very good passive coupling capabilities. Polymer waveguides could couple to on-chip embedded waveguides that could be based on III-V, Si3N4, Si02 or SOI.

Thus, in this thesis we model an optical waveguide based on SU8 and parylene. We simulate optical waveguide of 5µm long with a rectangular SU8 core of 2µmx3µm as sketched in Figure 4-20. SU8 is associated with Parylene or BCB to design the clad of the waveguide, SU8 having the higher optical index. The core of SU8 has the higher optical index (1.5843) and is taken away from silicon substrate of high refractive index by using a layer of parylene that has a lower refractive index (of 1.5); the structure is laterally surrounded by air. Optical propagation is guided within the core of higher refractive index due to Snell’s law of refraction and total internal reflection.

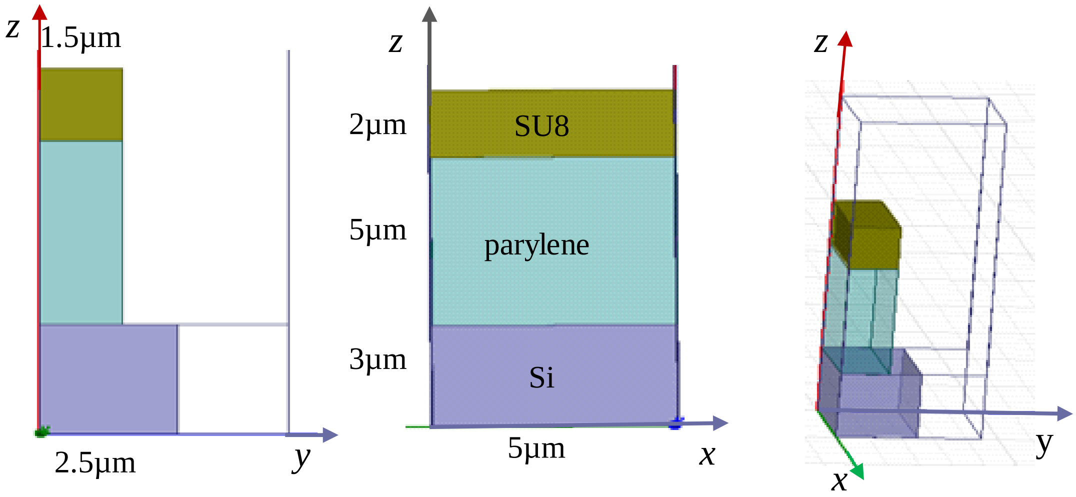

Figure 4-20: Simulated structure of optical waveguide over low resistive silicon substrate. Due to symmetry properties in regard to xOz plane, only the half of the structure is simulated

Table 4-11: Electrical properties of SU8 and Parylene at very high frequency.

Material	Relative permittivity	Tangent loss	Wavelength (nm)	References
SU8	2.51	0.00036	1000	[255]
Parylene	2.25	0.0006	900	[256]
LR Si (20Ω.cm)	11.7	-	-	-

Using the electrical properties shown in Table 4-11 we simulate the structure at very high frequency (150THz to 206THz) which corresponds to the optical waveguides of interest. The simulation results of this structure are shown in Figure 4-21 and Figure 4-22. Figure 4-21 shows the propagation attenuation versus wavelength. Low loss characteristics of 0.46dB.mm^{-1} are predicted in the 850nm to 1000nm wavelength range.

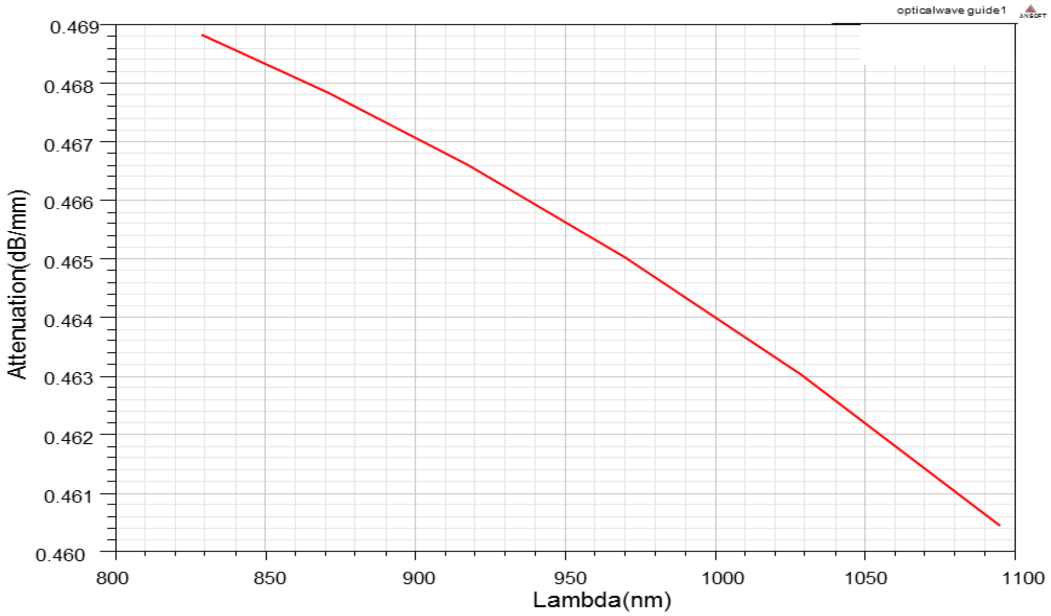

Figure 4-21: The attenuation of optical signal over the 5µm length of optical waveguide versus wavelength as it is deduced from HFSS simulator.

The predicted transverse and longitudinal field profile of optical modes are shown in Figure 4-22. For such a planar waveguide structure up to 4 modes can propagate with a very low optical attenuation.

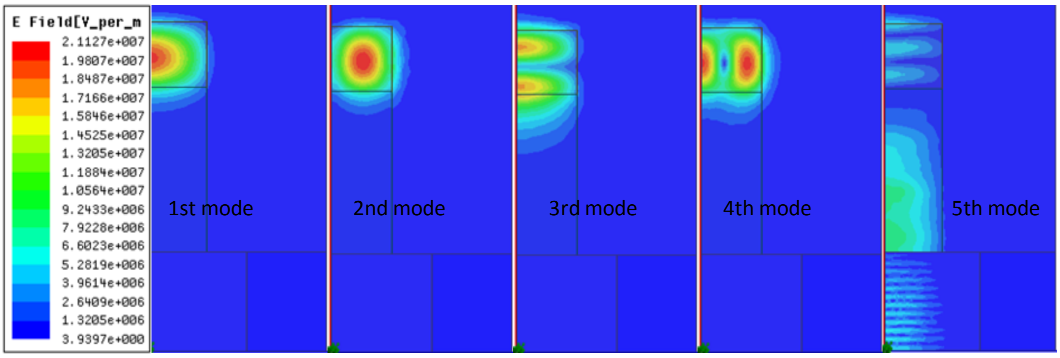

a) Transversal view of electric field distribution

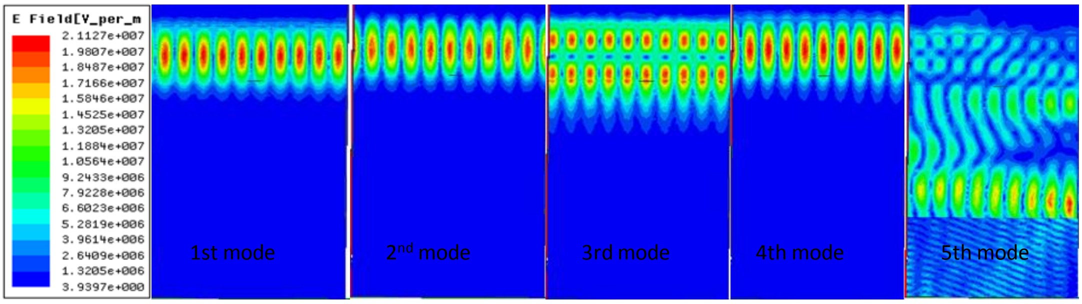

b) Longitudinal view of electric field distribution

Figure 4-22: Transverse electric field profile at the excitation port and longitudinal electric field of polymer base optical wave guide at 950nm wavelength.

4.3.2 SiN and SiO_2 based optical waveguide for on-chip interconnections

We established a partnership with the team of Pr. Snyman in the University of South-Africa (UNISA) and formerly in the Tshwane University of Technology (TUT). We present here the results of this collaboration in designing optical waveguides directly integrated in the Telefunken SiGe Technology.

We have taken advantage of different oxide layers of the technology to develop the waveguides. The designed waveguide will be implemented in a full on-chip optical links presented in chapter 5. The development of an efficient Silicon based waveguide at submicron wavelengths presents major challenges, particularly due to higher absorption and scattering effects at short wavelengths. We have hence extensively studied three different waveguide structures. Kingsley Ogudo made the simulations, while Pr. Snyman and Dr. Polleux made the layouts. My contribution was on the characterization.

1. Simulations of the optical waveguide Design 1 (OWGD1)

The first design test structure is shown in Figure 4-23a) and b). The waveguide structure is placed in a TetraEthylOrthosilicate (TEOS1) plasma deposited layer. A channel crevice is etched in the TEOS1 layer (n = 1.46) and then filled with a second TEOS layer (TEOS2). This layer is then densified by a thermal process, increasing its refractive index to about 1.48. A V-shaped cross-section (shown Figure 4-23 b) as defined by built-in processing procedures was chosen in order to ensure the highest radiation coupling of the optical source, which is of submicron dimension and presents a spherical radiation shape, and which is positioned slightly subsurface of the surface of the optical source columnar structure. This technology is well suited to obtain single mode waveguides which are transparent from 450nm to 850nm wavelengths and Figure 4-23 shows such a design. The typical layers thickness as offered by Telefunken process procedures was used during our design. The side delimitation of the waveguide is facilitated by reactive ion etching or by plasma etching of all the oxides down to the silicon substrate interface. This minimizes the lateral parasitic capacitive couplings with the surrounding oxide layers which might arise due to the RF modulation at the optical source.

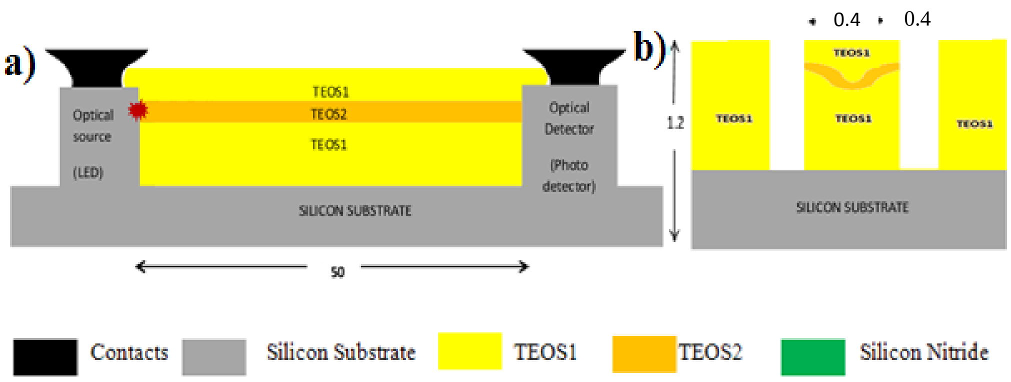

Figure 4-23: Waveguide structure for design 1 (a) Side view section (b) Cross-sectional view. All dimensions are in micro meters

For the first design test structure (OWGD1) shown in Figure 4-23, we simulated the optical waveguide structure designed with the TEOS1 and TEOS2 areas, where TEOS2 has a higher optical index due to densification strategy used to increase the optical index from 1.46 to 1.48. The core of high refractive index (1.48) is surrounded by silicon oxide of refractive index 1.46, thus optical waves are guided within the core of higher refractive index due to Snell's law of refraction and total internal reflection.

R-Soft simulation results of this structure are shown in Figure 4-24 at 750nm wavelength. Figure 4-24 shows very low loss propagation and weak influence of higher order modes as the field distribution is very closed to the one of the first optical mode. Figure 4-24 a) displays E-field amplitude versus x and z as a 2D color-coded contour map, and Figure 4-24 b) is a 3D contour graph that displays electric field amplitude versus x and z in 3D contour graph with color coding to indicate amplitude value.

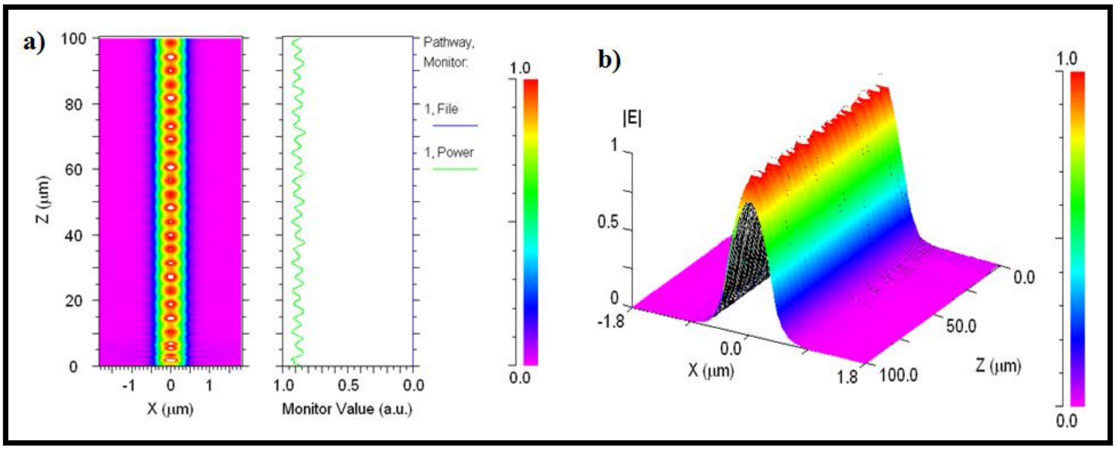

Figure 4-24: Waveguide simulation (a) Contour Map (XZ), (b) height-coded E-field amplitude

2. Simulations of optical waveguide Design 2 (OWGD2)

Figure 4-25 shows a schematic of the second design, where vertical slots are predefined by a poly silicon window obtained using Telefunken technological process. This leads to a 45 degree hollow in the Tetraethyl orthosilicate1 (TEOS1) oxide before positioning the silicon nitride layer. The etched crevice of 0.4 micron in the first TEOS layer is filled up with a silicon nitride layer, followed by further CVD deposited TEOS oxide over-layer. Hence a high refractive index core of n = 2.4 is formed by silicon nitride with a surrounding index of n = 1.46.

By tailor made designing the dimensions of the various layers in the waveguide, a V-shaped waveguide profile is achieved. This enables vertical lowering of the higher index core of the waveguide into the silicon layers, which facilitates a good vertical alignment of the core of the waveguide with the light emission spot of the optical source.

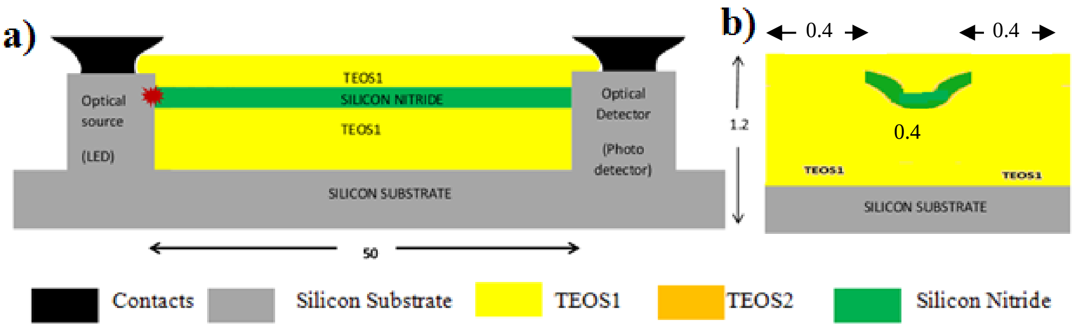

Figure 4-25: Waveguide structure for design 2 (a) Side view section (b) Cross-sectional view. All dimensions are in micrometers

Figure 4-26 shows the simulation results for the optical test structure 2 (OWGD2) as described in Figure 4-25 by taking the material properties and dimensions into account at optical wavelength of 750nm. The simulation results of this silicon nitride waveguide structure show a quite broad field distribution and high multimode content with some optical energy losses at the beginning of the waveguide near the optical source position as demonstrated in Figure 4-26 b).

Despite the initial optical coupling loss, the simulation results show a good optical propagation through the waveguide. Multi-mode propagation have the advantage of allowing both a large acceptance angle for coupling of the optical radiation from the silicon LED into the waveguide as well as for emission of light out of the waveguide at the end of the waveguide, and they can also accommodate high curvatures and bends in the waveguides.

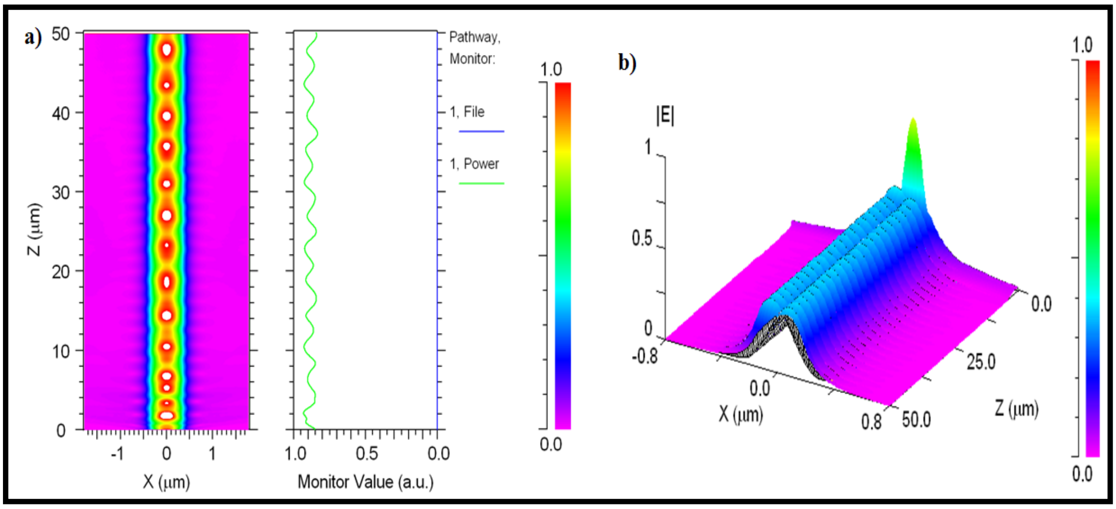

Figure 4-26: Waveguide simulation for design 2 (a) Contour Map (XZ), (b) height-coded E-field amplitude

3. Simulations of optical waveguide Design 3 (OWGD3)

Figure 4-27 shows the waveguide structure side view and cross section view of our third design. In this design the lateral width of the silicon nitride layer is reduced to about 0.2 micron in order to form a narrow higher index core, in order to reduce multi-mode propagation and the resulting propagation dispersion. We use the capacitor definition technique of the process. One mask permits the nitride deposition of 850nm thickness. No poly-silicon or metal over-layers are defined in the layouts; only a thin nitride layer is embedded in the surrounding layers of TEOS oxide. Since the refractive index of Si nitride is generally of the order of 2.4 at 650-850nm wavelengths, various multimode (wider core) and single mode (narrower core) waveguides can be obtained.

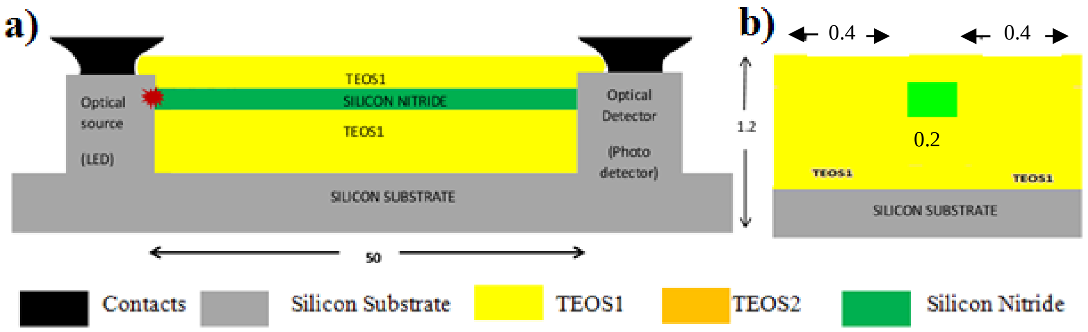

Figure 4-27: Waveguide structure for design 3 (a) Side view section (b) Cross-sectional view. All dimensions are in micrometers

We simulated the narrower silicon nitride core waveguide design 3 (OWGD3) as in Figure 4-27 at optical wavelength of 750nm. From the simulation results presented in Figure 4-28, OWGD3 yields narrower single mode propagation, with low losses and very low multimode content. Although it is more difficult to couple light into the waveguide in single mode operation, we see the loss along the waveguide is lower in single mode propagation. This will enable high modulation bandwidth to be achieved in this kind of narrower core waveguide.

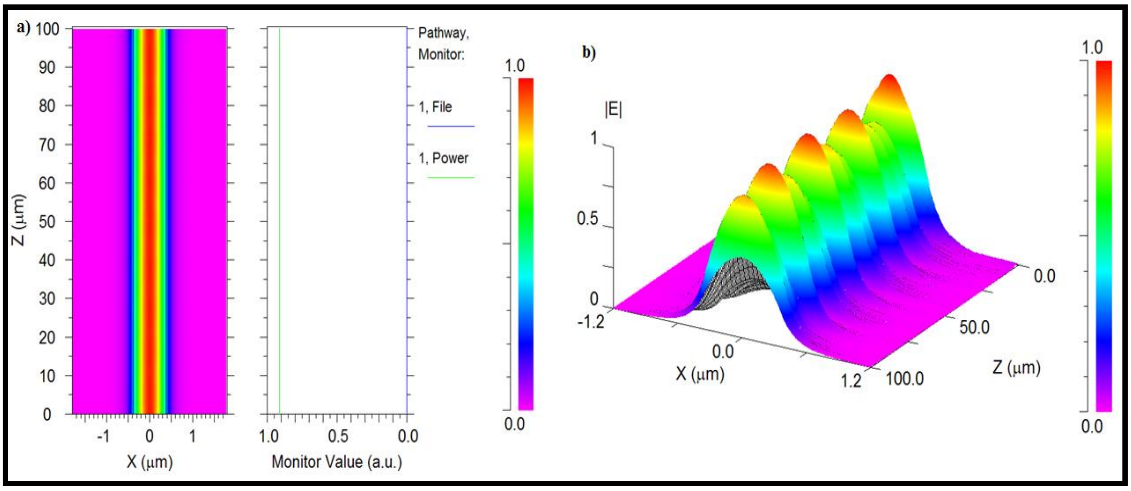

Figure 4-28: Waveguide simulation for design 3 (a) Contour Map (XZ), (b) height-coded E-field amplitude

Figure 4-29 shows the predicted distribution of transverse field amplitude for a 0.2 micron diameter nitride core waveguide embedded in a silicon oxide surrounding matrix. Low loss characteristics of 0.65dBcm^{-1} are predicted, taking the material properties into account.

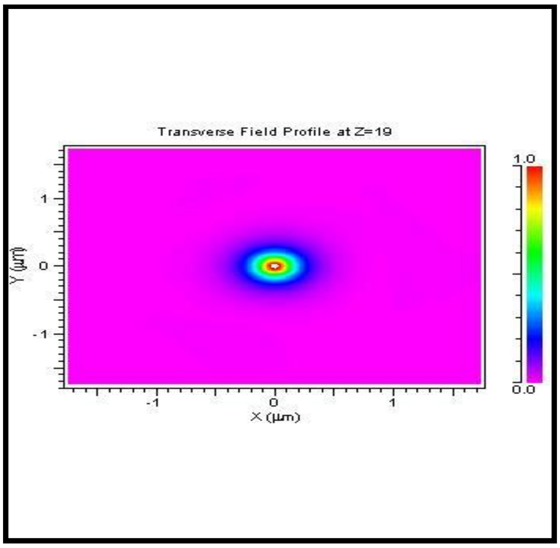

Figure 4-29: Transverse field profile for a silicon nitride based waveguide with a silicon nitride core of 0.2 micron diameter embedded in a 1 micron diameter silicon oxide cladding.

These analyses show that both silicon nitride and TEOS offer good possibilities for low loss light transmission in the wavelength range of 650nm to 850nm. The experimental results by A. Gorin [258] on thin film planar silicon nitride waveguide show the variation of the attenuation versus wavelengths; with high losses of 4.3dB.cm^{-1} at 530nm against losses of only about 1dB.cm^{-1} at 650nm and 0.1dB.cm^{-1} at 750nm. This suggest that compromises could be made with respect to the choice of operating wavelength, anticipated waveguide losses and detection efficiency while using CMOS technology. At shorter wavelengths both silicon nitride and TEOS reveal higher absorption coefficients with good efficiency of silicon detectors for small detection volumes, while longer wavelengths reveal lower transmission losses but with lower detection efficiency of silicon detectors per unit silicon volume.

Especially the transparency of silicon-nitride based waveguides on 750nm-850nm range, offers remarkable possibilities with regard to the integration of optical communication, data transfer and photonic systems directly into CMOS integrated circuitry. In particular, this technology is very attractive for the anticipated low levels of technological complexity compared to the incorporation of III-V or hybrid III-V with silicon technologies.

4.4 Combination of optical and electrical waveguides

A combined on-chip or inter-chip integration of photonics and microwave-photonics interconnections towards performance improvement together with a clear target of cost reduction, reliability and simplicity is one of the challenge and target of microwave photonic researchers.

For this purpose, we model and present in this section the integration, almost “imbrication”, of optical and electrical interconnections on low resistive silicon substrate and polymer technologies. We simulate grounded coplanar and coplanar transmission lines by incorporating an optical waveguide between the line and the ground contact (in the slot) using HFSS. The influence of the optical waveguide on the microwave transmission line characteristics is examined.

4.4.1 Grounded coplanar line with optical waveguide

In this section we present a grounded coplanar line associated with an optical waveguide. The optical waveguide is placed in the air gap between the metal strip and ground metal as shown in Figure 4-30. This interconnection structure consists of a ribbon metal conductor, two ground planes on each side of this line separated by an air gap, grounded metallic plane deposited on low resistive silicon substrate over which a polymer is deposited and the high index SU8 layer forming the optical waveguide core in the slot. The Parylene or BCB layer is 16µm thick and the SU8 layer 2µm thick. The use of these polymer layers permits first to avoid the effect of low resistive silicon substrate on the electric field propagation then to form the 2µmx2µm high index SU8 core of the optical waveguide.

Such imbrication of the optical waveguide within the microwave transmission line is somehow important for edge- and velocity matched photodetectors and modulators, where the RF access and optical access have to be collinear, but also to optimize and reduce the number of access connection to the chip, providing a greater ease in the chip-to-chip alignment, and to increase the density of interconnections (coplanar RF lines are large compared to the optical ones).

We study here the electrical characteristics of the transmission line between 50 and 70 GHz, and compare the obtained results with the electrical characteristics of the grounded coplanar line without optical waveguide.

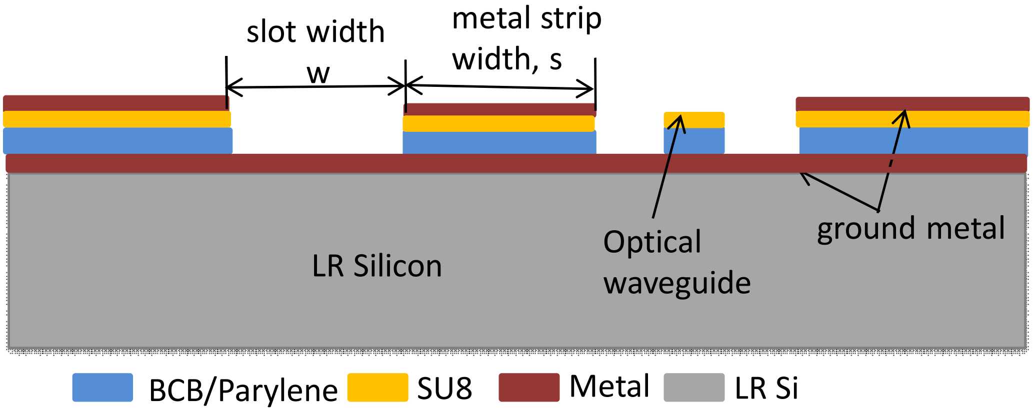

Figure 4-30: Cross section view of grounded coplanar line with optical waveguide structure

In this study; we fix the metal strip width at 100µm and slot width at 30µm. The targeted characteristics impedance is 50Ω. When simulating the coplanar waveguide without optical waveguide on BCB and Parylene, 2µm SU8 layer is removed on BCB or Parylene and thus the polymer layer thickness was 16µm.

Figure 4-31 and Figure 4-32 show the attenuation of the line with BCB and Parylene layers respectively with and without the optical waveguide. The attenuation in both structures, with and without the optical waveguide, is nearly equal. That means that the optical waveguide introduced in the slot of the grounded coplanar line doesn’t affect the electrical behavior of the line.

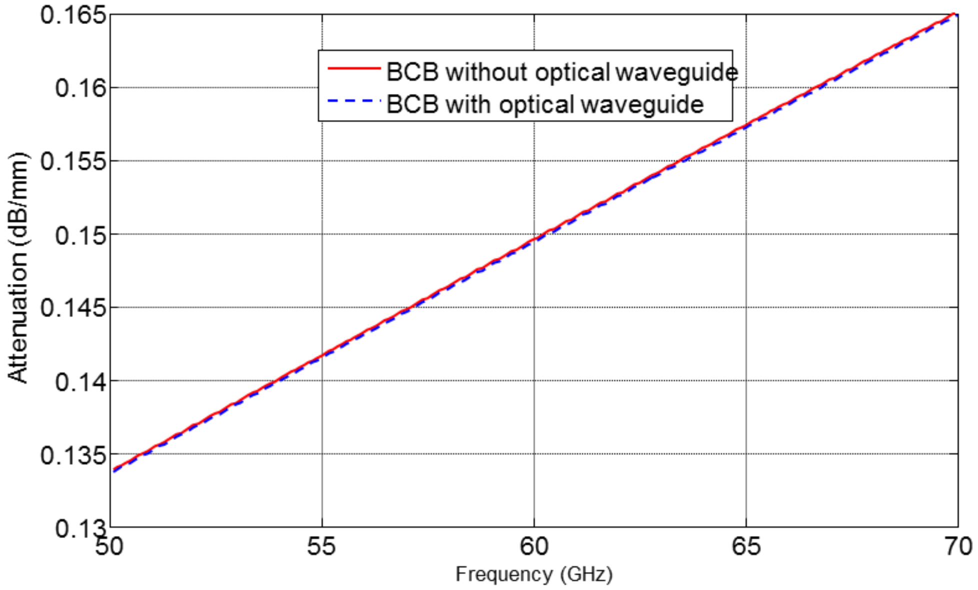

Figure 4-31: The simulation result of grounded coplanar line with and without optical waveguide over BCB polymer (the optical waveguide is 2µm SU8) attenuation versus frequency

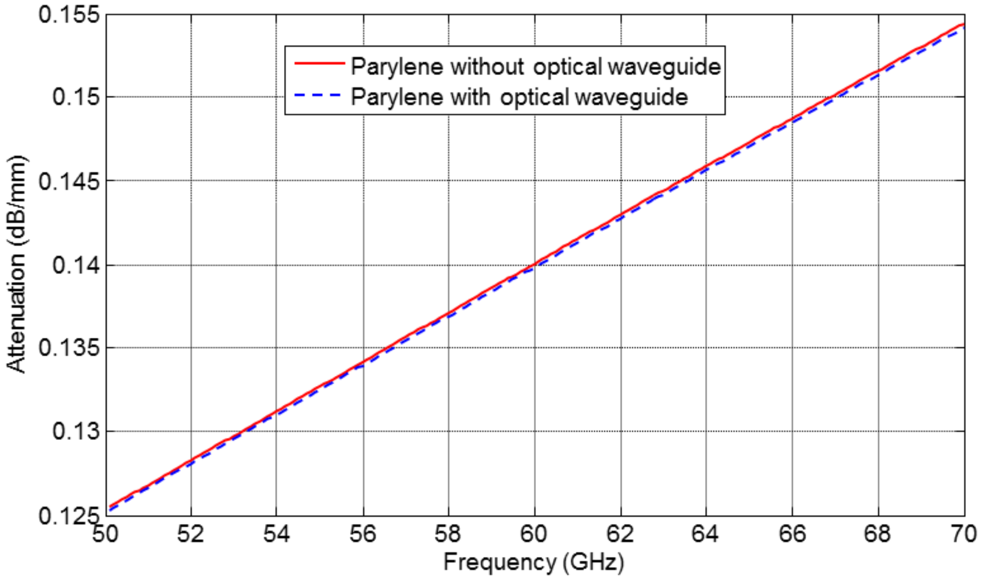

Figure 4-32: The simulation result of grounded coplanar line with and without optical waveguide over Parylene polymer (the optical waveguide is 2µm SU8) attenuation versus frequency

Figure 4-33 and Figure 4-34 show the characteristic impedance versus frequency for BCB and Parylene layers. The characteristic impedance in both cases is the same. There is a small difference; this could be attributed to the deposition of 2µm thick SU8 over 16µm BCB or Parylene.

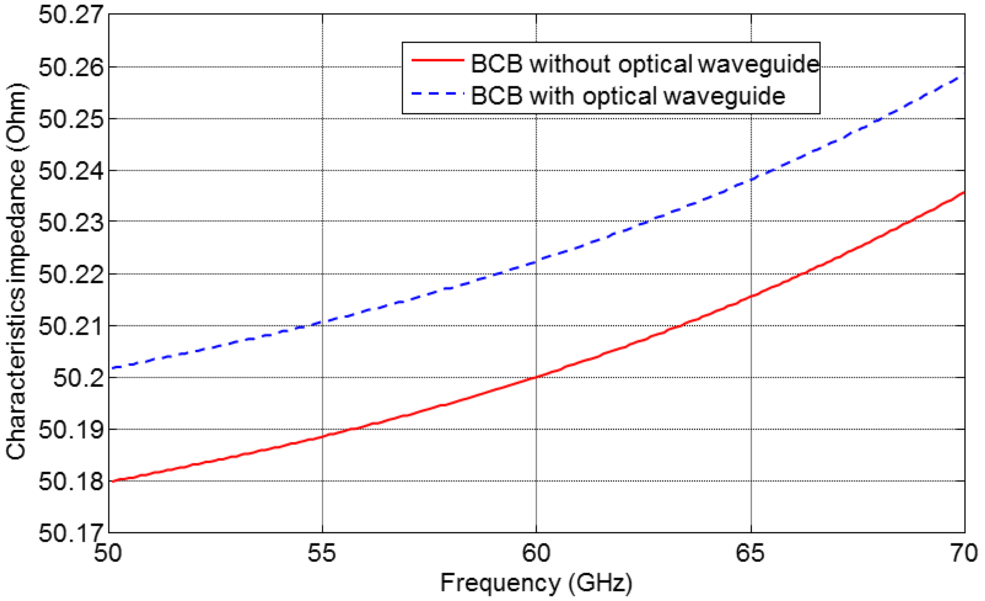

Figure 4-33: Characteristic impedance vs frequency with and without optical waveguide over BCB polymer (the optical waveguide is 2µm SU8)

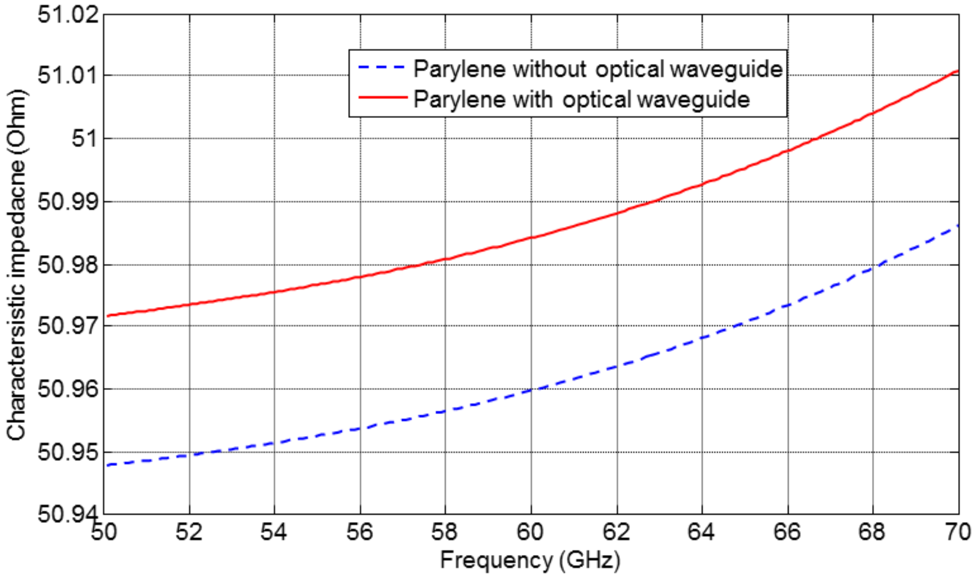

Figure 4-34: Characteristic impedance vs frequency with and without optical waveguide over parylene polymer (the optical waveguide is 2µm SU8).

4.4.2 Coplanar line with Optical waveguide

We now study the coplanar line with optical waveguide on low resistive silicon substrate where the metallization and SU8 based optical waveguide are elevated using a polymer such as BCB or Parylene (see Figure 4-35). We aim to minimize the propagation attenuation, to achieve 50Ω characteristic impedance and to observe the effect of the optical waveguide on the line characteristics from 50GHz to 70GHz. A glass wafer of 500µm thickness is added under LR silicon as will be performed during on wafer measurements to avoid the influence of the setup metallic chuck on the extracted line characteristics.

The 16µm thick Parylene or BCB layer deposited on silicon is covered by a 2µm thick SU8 layer forming the optical waveguide core. In the case of simulations without optical waveguide, the SU8 layer is removed and the thickness of Parylene or BCB layer becomes 16µm. Parylene or BCB layer permits to minimize the effect of low resistive silicon on the attenuation of the coplanar waveguide as well as of the optical waveguide. The main focus is to study the electrical behavior of the coplanar line between 50 and 70 GHz, and compare the result with the electrical behavior of the coplanar line without optical waveguide. Optical propagation is guided within the core of higher refractive index SU8.

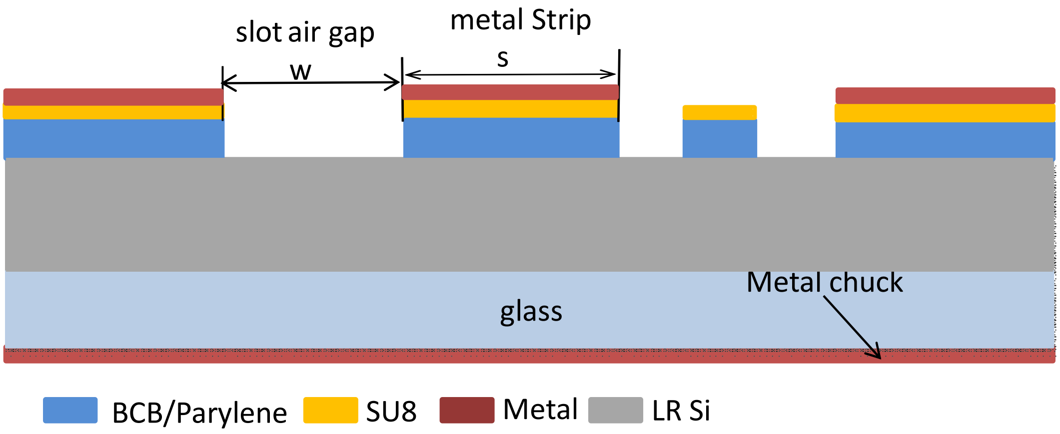

Figure 4-35: Cross section of coplanar line with optical waveguide

The study of the optical waveguide influence on the line electrical behavior is only performed with Parylene layer; with a strip width fixed at 200µm and slot width of 30µm. The targeted characteristic impedance is 50Ω in 50GHz-70GHz frequency range.

Figure 4-36 shows the resulting attenuation over the required frequency band as computed using HFSS with and without optical waveguide. The attenuation in both structures is nearly equal. That means the optical waveguide introduced in the slot of the coplanar line doesn't affect the electrical behavior of the line.

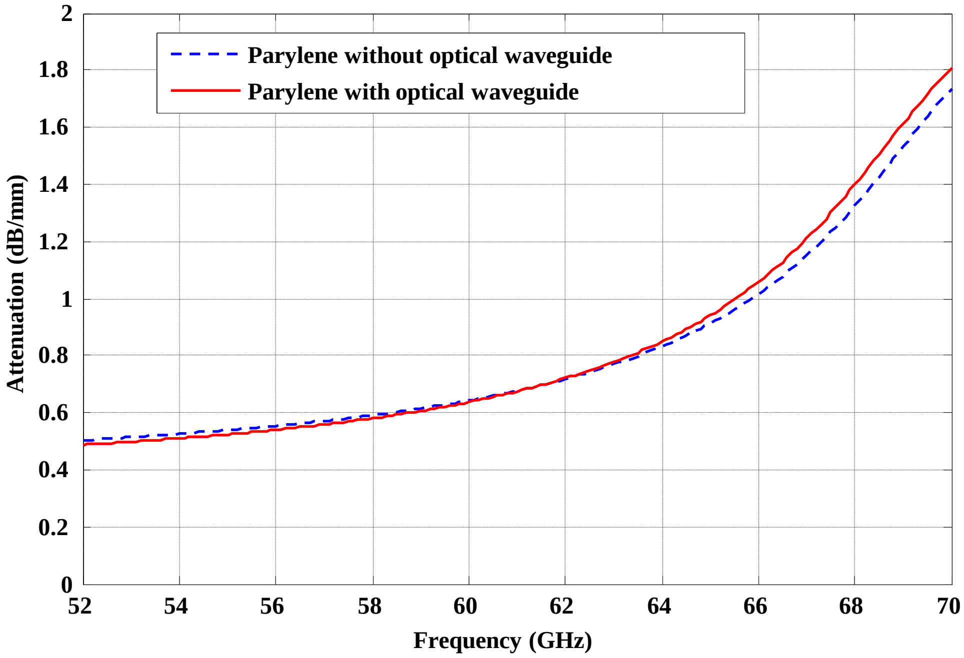

Figure 4-36: The simulation result of coplanar line with and without optical waveguide over Parylene polymer (the optical waveguide is 2µm SU8) attenuation versus frequency

Figure 4-37 shows the characteristics impedance versus frequency with a Parylene layer. The characteristic impedance in both cases is nearly the same.

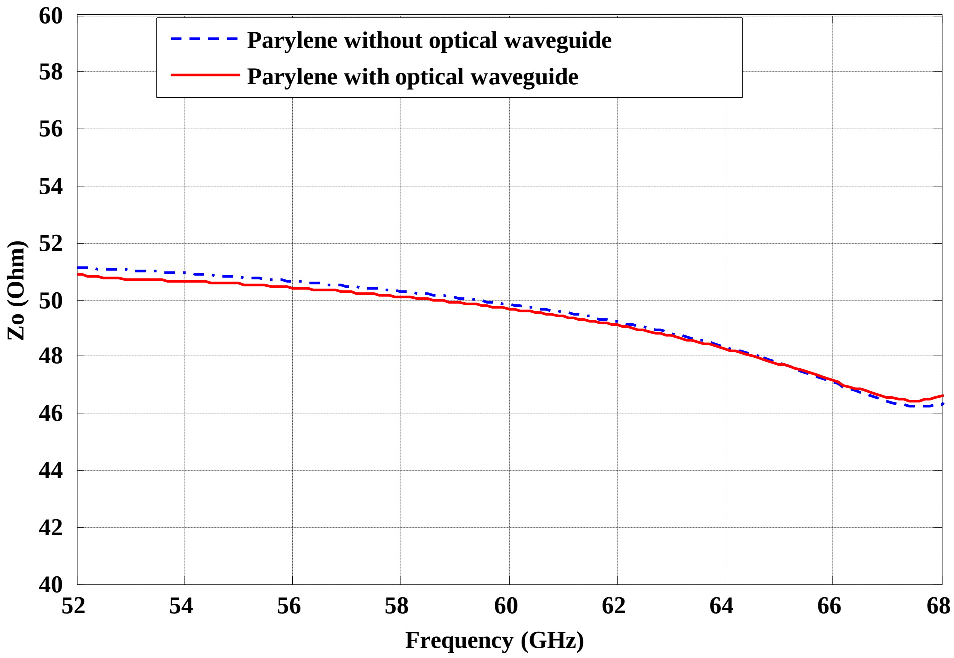

Figure 4-37: Characteristic impedance vs frequency with and without optical waveguide over parylene polymer (the optical waveguide is 2µm SU8)

4.4.3 Transmission line interconnections

Usually opto-microwave devices are fabricated on silicon substrate (without any polymer layer), hence a transition might be required for interconnections with a transmission line realized on polymer in intra or inter chip interconnecting systems. Thus we design an interconnection via as shown in Figure 4-38. Coplanar lines directly on low resistive silicon substrate and on SU8 dielectric interface are interconnected through a hole digged through the polymer. The lengths of each section of the lines are as shown in Figure 4-38. The excitation port are at x=0mm for the input and at x=3mm for the output. The metal strip and slot width of the coplanar line on Silicon and on SU8 dielectric interface are as presented in Table *4-12*. We design these line dimensions to achieve characteristic impedance of 50Ω.

Table 4-12: The line dimensions of the structure under simulation

Line on silicon		Line on SU8	
s(µm)	**w(µm)**	**s(µm)**	**w(µm)**
40	25	115	25

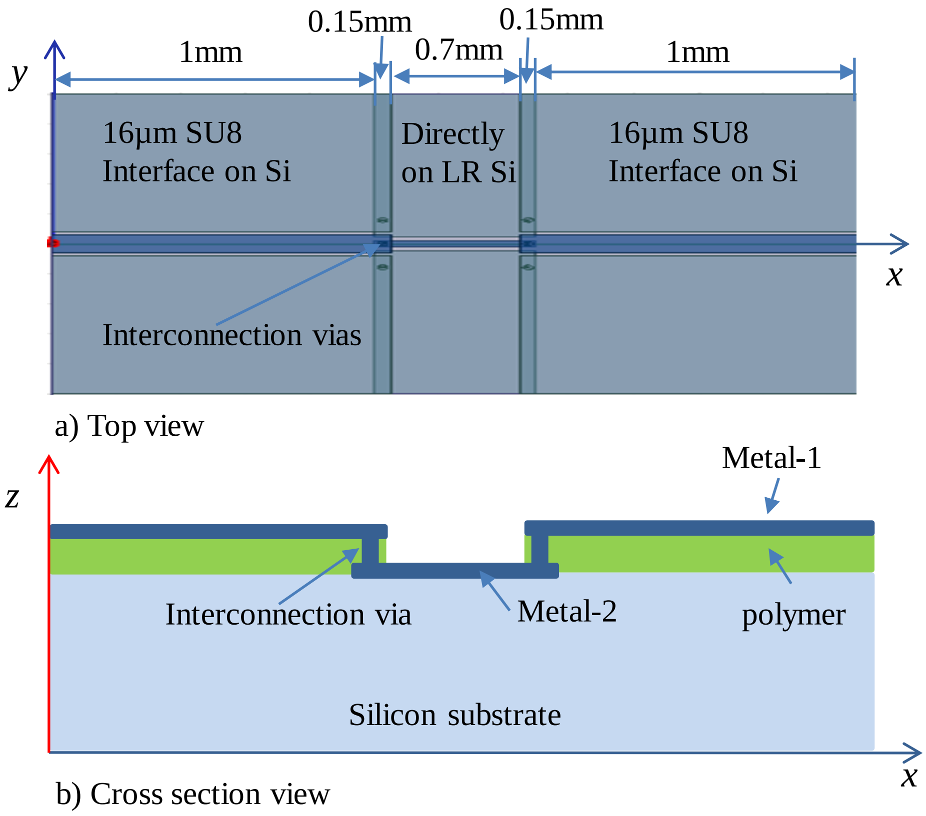

Figure 4-38: Top and cross sectional view of via interconnection of coplanar lines on Low silicon and SU8.

The simulation results are presented in terms of the transmission parameter (S_{21}) and characteristic impedance as shown in Figure 4-39 and Figure 4-40 respectively. We compare three different structures such as via interconnected lines (the one described above), the coplanar line printed directly on low resistive silicon and the coplanar line printed on SU8 as a dielectric interface between low resistive silicon and the metallization. In the three cases the total length of the structure is 3mm and we use the line specifications mentioned in Table 4-12.

Due to the presence of the SU8 dielectric interface, the transmission loss for the line realized on SU8 is lower than for the other two cases. The via interconnected line has a transmission loss between the two structures as shown in Figure 4-39 as it is deposited partly on Silicon and partly on SU8 dielectric interface. A line directly on low resistive silicon has very high transmission loss due to the absorption of signals in the silicon substrate.

The transmission loss for via interconnected structure slightly decreases as the frequency increases beyond 60GHz. This is due to the variation the characteristic impedance when the line is realized directly on Si and using SU8. The characteristics impedance difference decreases at high frequency, as shown in Figure 4-40, hence the impedances of the two sections in via interconnected structure become too well match at high frequency. However, at low frequency the impedance variation is higher and thus increases the transmission loss due to impedance mismatching.

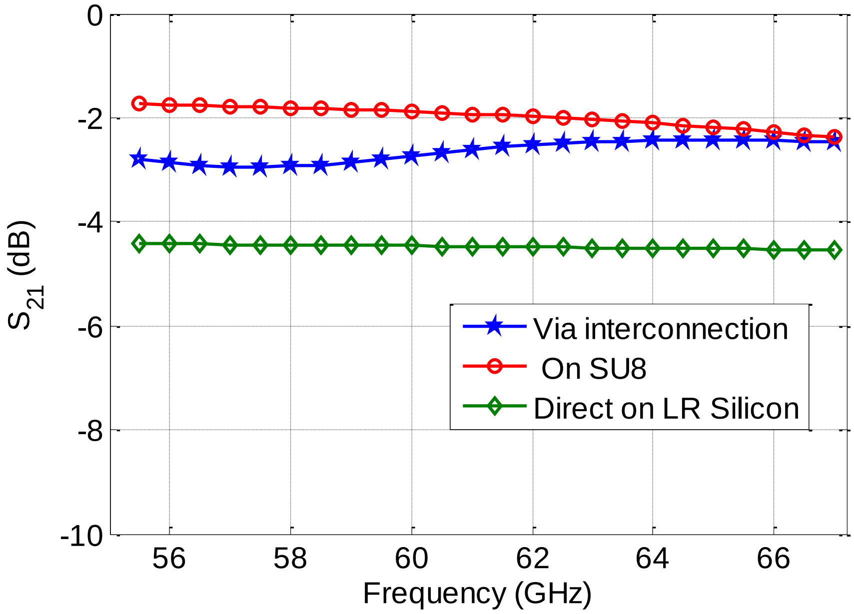

Figure 4-39: The simulation result of the forward transmission (S21) from x=0mm to x=3mm versus frequency when the line is printed directly on low resistive silicone, fully on SU8 dielectric interface above the Si substrate and a line partly directly on Silicon and partly on SU8 interconnected through Vias.

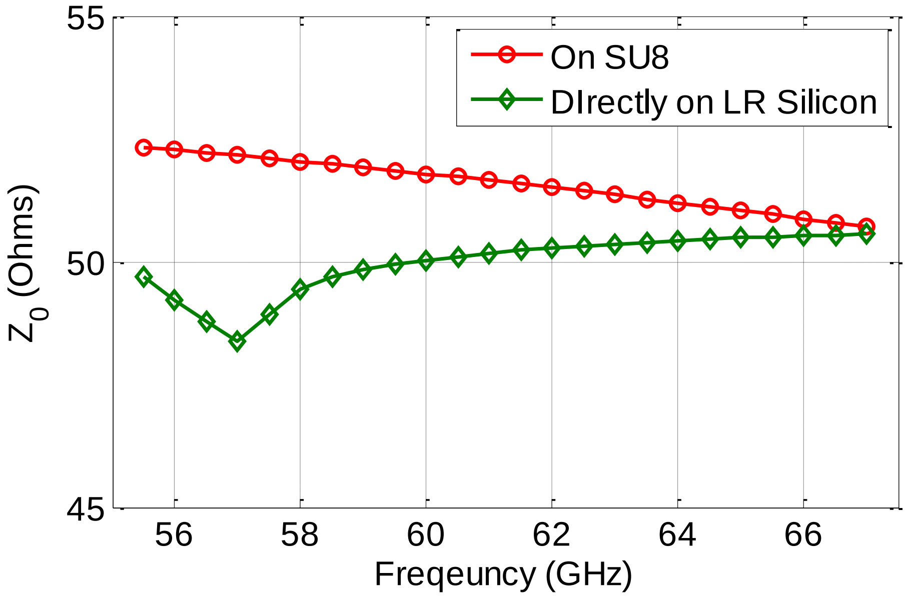

Figure 4-40: The simulation result of the characteristic impedance at various frequencies when the line is simulated directly on low resistive silicon substrate and on SU8 dielectric interface above the substrate

4.5 Experimental validation of Planar Transmission line

Based on transmission line dimensions optimized through electromagnetic simulations using HFSS software and polymer optical waveguide dimensions determined through optical simulations using CADENCE software, we have drawn the schematic patterns/layout of Coplanar, Microstrip and Grounded coplanar transmission lines along with polymer based optical waveguides. Each type of line is designed with several different lengths so that the line characteristics can easily be extracted from the measurement results.

The mask is divided into several cells as shown in Figure 4-41 where in each cell all the structures are based on a same type of transmission line (either coplanar waveguide, microstrip line or grounded coplanar waveguide). For example C-1 stands for *cell one* and only comprises coplanar lines on SU8; C-4 stands *cell four* and contains coplanar lines on BCB, and C-5 stands for *cell five* and is reserved for grounded coplanar lines on BCB or Parylene and so on as detailed in Table 4-13. The same area is used for lines on BCB and Parylene as simulations have led to the same estimated dimensions associated to the same characteristic impedance; so BCB and parylene can be deposited alternatively. We have also designed the patterns of grounded coplanar lines and coplanar lines with an optical waveguide; these structures are located in cells from C-8 to C-12. We have also inserted patterns with via transitions (C-VT) to test the interconnection/transition between transmission lines on polymer and transmission lines directly on low resistive silicon. Table 4-13 details for each cell the technology used. Cells C-9, C-10 and C-11 aim to test the optical waveguide by providing an optical fiber alignment at the two ends of the optical guide by deep reactive ion etching (DRIE). These cells are also important to study the coupling between optical and microwave signals (to observe experimentally the effect of optical signal on the microwave one). Optical waveguides of different sizes, namely (5µm width, 2µm thick) and (10µm width, 2µm thick), and having different lengths are designed.

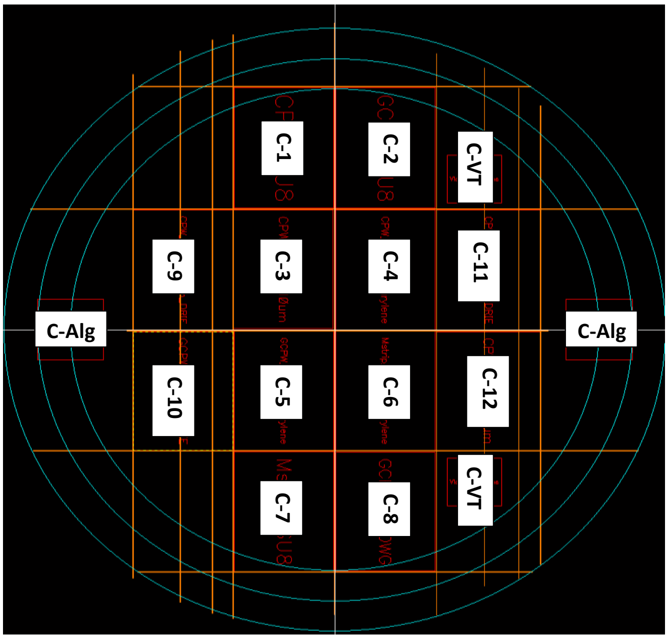

Figure 4-41: Schematic view of the mask used to fabricate the transmission lines

Table 4-13: Cell numbering and their description.

Cell number	**Cell name**
C-VT	Via transition test structure
C-Alg	alignment mask
C-1	Coplanar line over SU8
C-2	Grounded coplanar line over SU8
C-3	Coplanar line with 10µm wide optical waveguide
C-4	Coplanar line on BCB or Parylene N
C-5	Grounded coplanar line on BCB or Parylene N
C-6	Microstrip line on BCB or Parylene N
C-7	Microstrip line on SU8
C-8	Grounded coplanar line with 10µm wide optical waveguide
C-9	Coplanar line with 10µm wide optical waveguide plus optical fiber alignment (need mask 5, see Table 4-14)
C-10	Grounded coplanar line with 5µm and 10µm wide optical waveguides plus optical fiber alignment (needs mask 5, see Table 4-14)
C-11	Coplanar line with 5µm wide optical waveguide plus optical fiber alignment (need mask 5, see Table 4-14)
C-12	Coplanar line with 5µm wide optical waveguide

Where: **-C** stands for Cell: in each cell we have the same type of transmission line

VT stands for via transition

Alg stands for alignment

Figure 4-42 shows the mask with patterns of various types of transmission lines and different layers of the mask to be used during fabrication. Depending on the technology and the structure that we want to fabricate, we need up to five masks as it is shown in Figure 4-42 and Table 4-14. Mask1 (L3) is used to print the ground metal that is deposited on the substrate. Where the patterns are available (dark), the ground metal will be printed. Mask 2 (L6) is used to create via through the polymer in order to have an interconnection between the top layer ground contact (Metal 2) of microstrip and grounded coplanar line with underneath ground metal (Metal 1) deposited on substrate. Mask 3 (L2) is used during metal 2 depositions to print the signal line and the top ground layer contacts. We use Mask 4 (L4) to fabricate the optical waveguides and Mask 5 (L5) is used to etch silicon substrate so that we can create a cavity to align the optical fiber during on wafer characterization. Table 4-14 shows each mask along with the design layers and their purpose, basic processes and tells about the geometry and mask relationships.

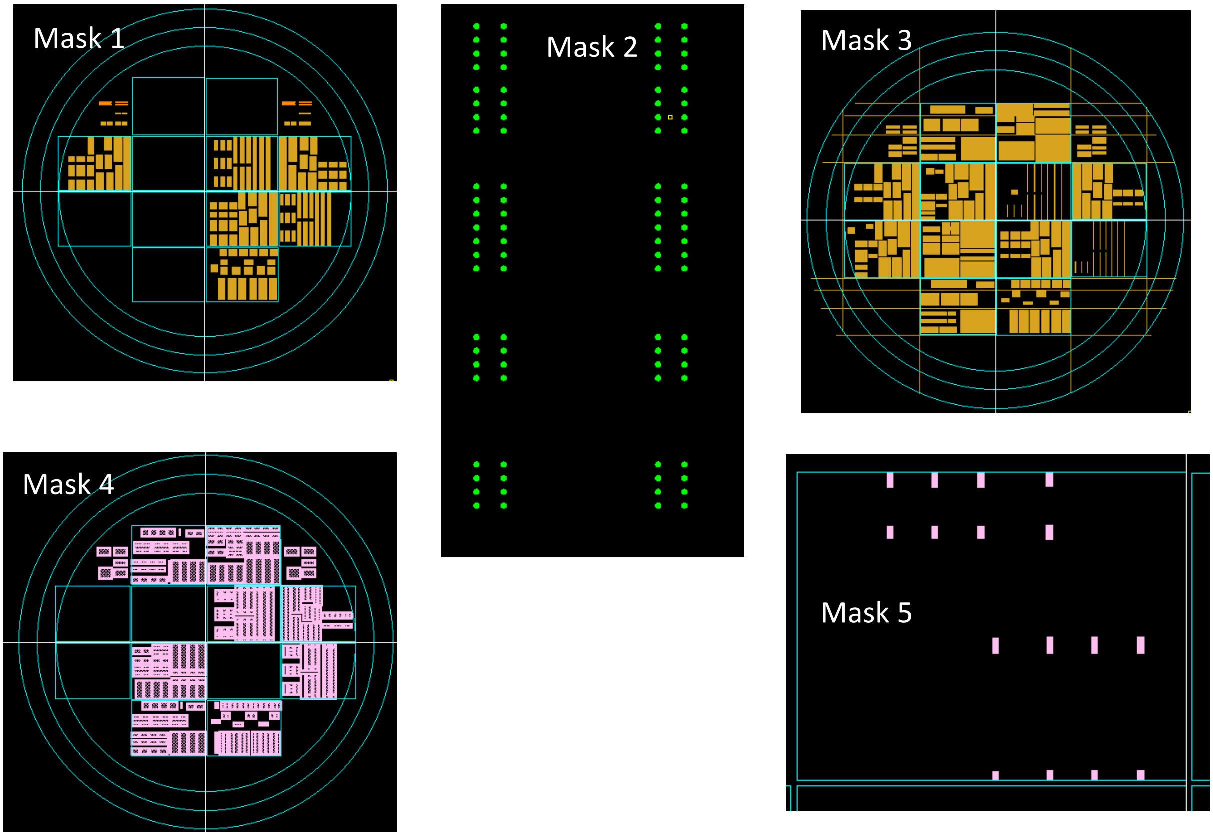

Figure 4-42: The designed five maskes to fabricate the whole patterns.

Table 4-14: The descriptions of each mask or layer along with their basic process and purpose.

Mask Number	Layer	Mask Name	Purpose	Basic process	Metal and polymer remove where mask is	Geometry dark where pattern is (polarity)
mask 1	L3	Metal_1	to print the ground metal	photolithography (+) etch and protect	clear	dark
mask 2	L6	Via	via opening	photolithography (-)	dark	dark
mask 3	L2	Metal_2	Metallization	etch and protected	clear	dark
mask 4	L4	OPT-WG	optical waveguide	SiO2 deposition and PFR photolithography, etching and protection	clear	dark
mask 5	L5	DRIE	u-groove opening	etch and protect	dark	clear

Even though it is possible to fabricate transmission lines on low resistive silicon substrate using polymer as a dielectric interface between the substrate and the metal as it is presented in [39], we weren’t able to fabricate our lines with a polymer layer using the proposed fabrication processes in ESIEE clean room. We encountered difficulties to etch the polymer. RIE would be necessary to perform this process but it is difficult as it is very long in time and heat up the whole structure a lot. The process development was then stopped here.

Therefore, we only targeted to fabricate a coplanar line on 16µm thick SU8 as a first test, and kept our masks for a future fabrication using an optimized fabrication process. We keep the SU8 in the air gap (it is not removed as initially foreseen). The fabricated line photography (a) and microscopic picture (b) are shown in Figure 4-43. As we can observe on the Figure 4-43 b), there are small metal residues within the line slot gap. This could degrade the performance of the line. We also observe rugosities on the metal layer that will probably increase the line propagation losses.

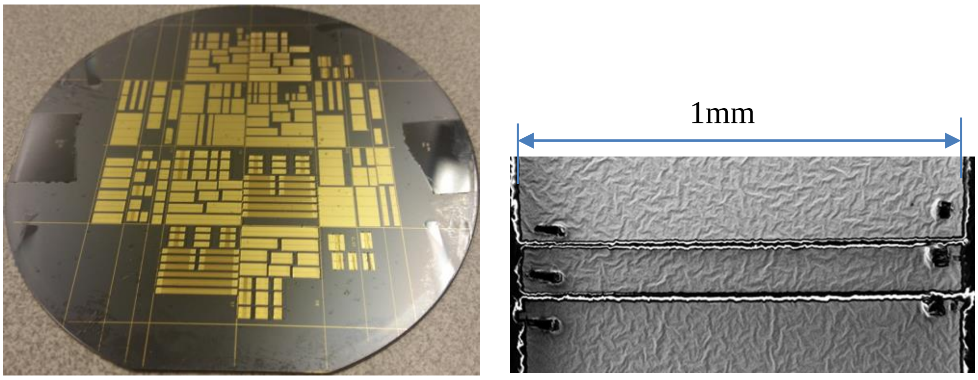

a) b)

Figure 4-43: The fabricated transmission lines on low resistive silicon and 16µm SU8 as a dielectric interface between the substrate and the metallization. a) The photography of fabricated transmission lines on full wafer. b) The microscopic picture of a coplanar line having a length of 1mm.

We characterize a coplanar line by using a vector network analyzer that operates up to 65GHz. We follow the LRM (Line-Reflection-Match) calibration method to calibrate the bench used for this characterization.

From the measurement of two coplanar lines having the same geometrical properties (strip width of 108µm and slot width of 19µm) except their lengths of 5mm and 1mm, we extract the line attenuation and phase constant by using the technique presented in [257]. The line dimensions are measured after the fabrication of the line. According to our design, the strip width was 114µm and slot width was 13µm. The variation could be due to the over etching of the metal that reduces the strip width by 6µm and increases each slot width by 3µm.

The measured line attenuation versus frequency along with the equivalent simulation curve are presented in Figure 4-44. The post simulated curve is obtained by simulating the coplanar line having a metal strip width of 108µm and air gap of 19µm. We keep the SU8 in the air gap as in the fabricated line and this layer is 16µm thick. The simulation fits well with the measurement. A variation of less than 0.2dB is observed.

It is shown on the experimental results a loss of less than 1.2dB/mm up to 65GHz. This result is quite good given the roughness of the metal that was achieved. This validates our transmission design.

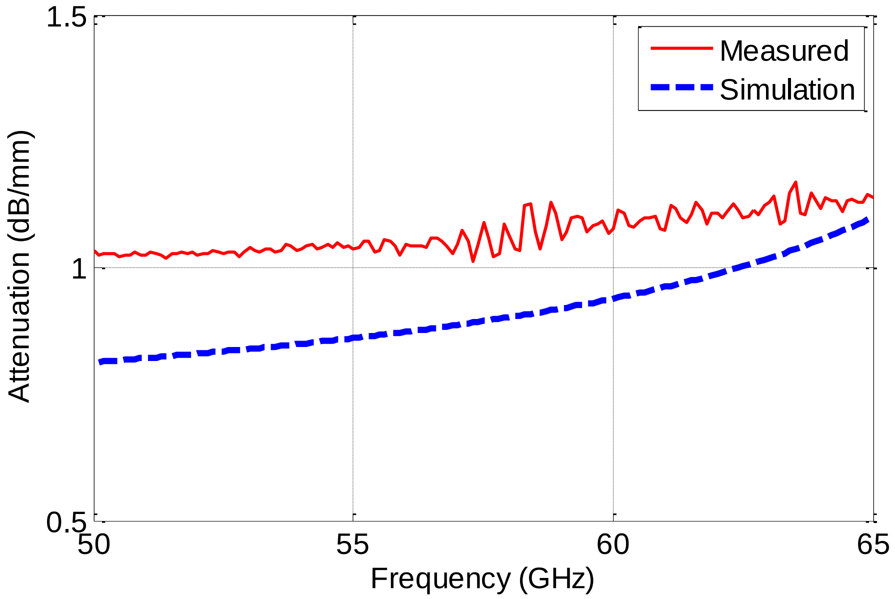

Figure 4-44: The attenuation experimental result and simulation result of coplanar line fabricated on low resistive silicon substrate by using 16µm SU8 as a dielectric interface. The line strip is of 108µm and the slot width of 19µm.

The experimental phase constant variation versus frequency along with the equivalent simulation curve is presented in Figure 4-45. The post simulated curves are obtained by simulating the coplanar line having a metal strip width of 108µm, air gap of 19µm and SU8 thickness of 16µm. As we can observe from Figure 4-45, the measurement phase constant is linear and close to fit with the simulation one.

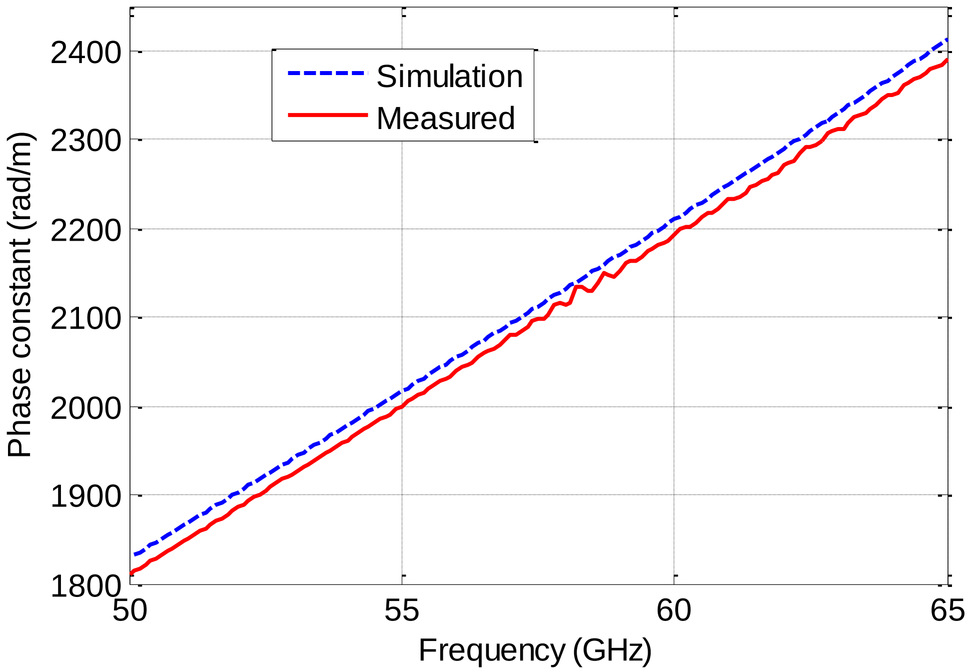

Figure 4-45: The measured and simulation phase constant of the fabricated coplanar line having a strip width of 108µm a slot width of 19µm and with a SU8 thickness of 16µm.

4.6 Conclusion

The following major conclusions can be derived from the work presented in this chapter:

We have successfully designed low loss microwave transmission lines on low resistive silicon substrate by using polymer layers between the line and the substrate. Coplanar, microstrip and grounded coplanar lines based on SU8, BCB and Parylene in the mm wave frequency range are investigated and designed. Grounded coplanar and microstrip lines have less attenuation compared to coplanar line as the grounded metal avoids the propagation of electric field within the silicon substrate. The targeted characteristic impedance for all types of line is 50Ω. The first experimental result indeed indicates that our design using HFSS is suited. Less than 1.2dB/mm attenuation in the millimeter-wave frequency range is measured for a coplanar waveguide structure.

We have also successfully designed polymer based optical waveguides that have been included with mm microwave transmission lines. The interconnection of mm-wave lines on silicon and polymer are demonstrated through HFSS simulation. They provide an input for the future integration of mm and optical signals in a single chip or through interconnections between chips.

Silicon based optical waveguide are also designed to be directly integrated into the SiGe Telefunken Technology. Their design takes advantage on the oxide layers existing in this SiGe technology. The major advantages of using such optical waveguides associated to the choice of 0.75µm-0.85µm operating wavelength range are the ease of integrating the optical source, waveguides and optical detectors in a same chip, this integration implying ease of design and processing procedures.

Chapter 5 Edge illuminated SiGe HPT and On Chip Microwave Photonic Links on Silicon

5.1 Introduction

For next generation Micro Optical Electro-Mechanical sensors (MOEMS), lab on chip technologies, optical communications and data transfers as well bio sensor applications, BiCMOS based Integrated Microwave Photonic (IMWP) systems are the most viable solution [11]. IMWP also offers new functionalities that would not be possible using electronic based approach [11] [261]: microwave photonics systems deal with the generation, processing and distribution of microwave and millimeter signals by optical beams by benefiting from low loss, large bandwidth and immunity from electromagnetic interference. Other functionalities are tunable and reconfigurable filter, optoelectronic oscillators, arbitrary waveform generation and so on [261]. Furthermore, the use of IMWP greatly reduces the system complexity and offers major advantage of integrating all the technological processes into mainstream silicon fabrication technology. With little adaptation, it could be made compatible with standard silicon BiCMOS fabrication technology, the most promising of the current silicon technology.

While in the literature such IMWP circuits are realized at 1.55µm (using III-V lasers on Silicon and Ge detectors for example), we investigate in this chapter the possibility to use pure Si and SiGe materials to provide both the optical detector and emitter, through the use of shorter wavelength. While the previous approach is considered to be BiCMOS compatible, our approach is expected to be fully BiCMOS integrated. For instance the demonstration is made on bipolar Telefunken Technology.

The applications of our approach are not only related to the communication field, but could embrace much larger field such as the optical sensing domain for biochemical applications or others.

Key constituents of such a system are an effective BiCMOS compatible optical source, optical waveguide and an effective optical coupling from the source to the waveguide and to the optical photodetectors such as our SiGe HPT. These all seem to be highly viable in regard to the present analyses and proposed technology process.

In the previous chapter, in addition to polymer based optical waveguides, we proposed and analyzed the transmission characteristics of the Si_3N_4 and TEOS optical waveguides which can be implemented directly in the Telefunken GmbH SiGe HBT technological process. The simulation results of such optical waveguide were showing losses less than 0.65dB/cm at 750nm.

This chapter starts with section two where we demonstrate the first edge illuminated SiGe HPTs. It has been fabricated using the 80 GHz SiGe2RF Telefunken GmbH SiGe Bipolar technological processes which is crucial to be implemented for ultra-low-cost silicon based IMWP systems. Its performance in terms of DC, opto-microwave cutoff frequency and gain are presented. In order to avoid complex optical packaging systems, we focus to the potential, yet lossy, use of a direct coupling via a simple lensed multimode 850nm fiber.

The third section focuses on the development of Si or SiGe LEDs within our SiGe technology. Design approaches are presented as well as an understanding of the emission process and experimental validation of their optical emission.

Finally, we present on-chip full optical link developed in co-operation between ESYCOM and the team of Pr. Snyman in South-Africa. Such a full optical link utilizes a BiCMOS Si Avalanche LEDs [112] [238] [239] as the optical source, the Si_3N_4 /TEOS optical waveguides which were discussed in Chapter 4 and our SiGe edge HPT, used in photodiode mode.

The designed full optical link operates in the 650-850nm wavelength range. The experimental results of the link performance in terms of DC and RF behavior are presented.

5.2 Edge illuminated SiGe HPT

5.2.1 Introduction

Vertically illuminated photodetectors or HPTs are known for their ease of light coupling but suffer from a tradeoff between conversion efficiency and frequency performance, the latter being limited by the transit time [196] [199]. Edge-coupled devices overcome this problem as the optical signal enters through the side of the device and propagates orthogonally to the bias field. This gives the freedom to design longer devices to ensure a high proportion of the optical signal to be absorbed while maintaining a narrow absorption region to keep transit times low [196] [197] [199]. Edge coupled HPTs based on InP-InGaAs technology have been intensively studied since 1993 [196] [199].

In this section we present the first edge illuminated SiGe phototransistor based on the available commercial SiGe/Si technology for low cost detector or mixer in Radio-over-Fiber applications and/or on-chip or inter chip optical packaging applications. Its technology and structure are described. Its DC behavior based on Ic-Vce curve, Gummel plot and DC current gain is presented. The DC biasing values are optimized to maximize either its cutoff frequency and or its low frequency responsivity. Then, we perform an opto-microwave SNOM (edge mapping) measurement of the edge-phototransistor in order to observe the fastest and the highest sensitive areas of the structure.

5.2.2 Description of the structure

The SiGe/Si HPT structure was implemented according to the geometry presented in Chapter 2. The basic HPT structure is designed by extending the emitter, base and collector layers of the reference HBT. In the case of our edge SiGe HPT, it is increased from 0.8x1.4µm^2 to 4.5x5µm^2 for better coupling with the optical fiber as shown in Figure 5-1 b).

The final HPT is then 4.5µm wide (corresponding to the width through which light is horizontally coupled) and 5µm long (maximum absorption length of light) as shown in Figure 5-1 b). The Si$_{1-x}$Ge base layer sandwiched between the collector and emitter, both made of Silicon, is expected to play the role of an evanescent optical waveguide that detects light, at least partly given the optical beam size that will be injected in our multimode fiber injection. The base profile is a 40-80nm thin abrupt SiGe layer with Ge content in the range of 20-25% and high p doping in the range of 10^{19}cm^{-3}. The collector is typically 300-400nm thick with low doping.

The emitter metal contact is designed on a reduced surface of the emitter to avoid additional optical losses by metal absorption of the light throughout the longitudinal direction, and to reduce the electrical parasitic capacitances. The optical access at the edge requires the HPT to be diced using a smooth shallow dicing blade close to the active area of the devices as shown in Figure 5-1 a), giving a slickly polished surface state. We dice 80µm down to the substrate to have a smooth surface at the optical beam input and then dice fully in depth and farther from the surface using a microscopic saw. The full and smooth dicing was processed at the Universté Paris Sud – IEF laboratory with the help of Pr. Vivien.

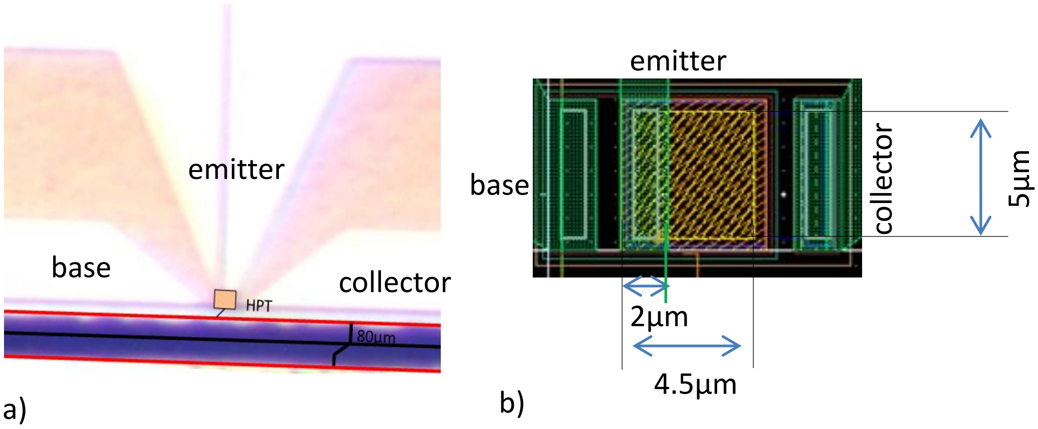

Figure 5-1: a) Microscopic picture of the edge SiGe HPT, b) Layout of structure along with its dimensions.

5.2.3 Light propagation behavior in SiGe/Si HPT structure

In this sub section we demonstrate on a theoretical basis the behavior of light propagation into a SiGe/Si phototransistor by using HFSS simulator. Figure 5-2 shows the vertical stacks of the SiGe/Si HPT structure under study. We simulate a 5µm long edge illuminated phototransistor under an 850nm wavelength illumination.

The SiGe base of the HPT is modeled with a high refractive index of 3.57. The surrounding Si layers are modeled with a lower refractive index of 3.42. We define a 1x1µm square excitation port at the input and output of the structure aligned to the SiGe base. We use the material properties as given in Table 5-1 to perform the simulations.

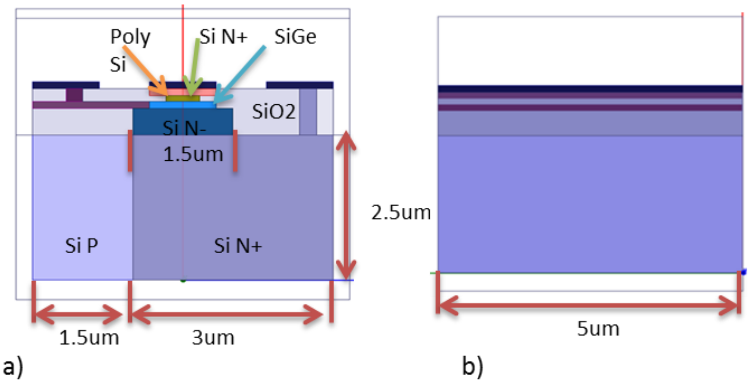

Figure 5-2: Basic simplified structure of SiGe/Si HPT used for simulation.

Table 5-1: Properties of the materials used in HFSS simulator.

	Material	**Purpose**	**Thickness (nm)**	**Relative permittivity**	**Conductivity (S/m)**
1	Contact metal	metallization	100	1	5.80E+07
2	poly Si	Emitter contact	120	11.7	5555.5
3	N+ Si	Emitter and sub collector	te=100, tc=2500	11.7	3472.2
4	N- Si	collector	450	11.7	357.14
5	P Si	substrate	2500	11.7	5
6	SiGe	Base (here as OPWG)	120	12.724	1000.23
7	SiO_2	passivation		3.9	1.00E-12
8	TiSi	for base contact	120	3	1.98E+06

The simulation results are shown in Figure 5-3. According to the physical dimensions and to the width of the excitation port (assumed to be optical spot size), we deduce that 69% of the injected electric optical field is injected into the active region (including base ≈12%, emitter ≈12% and collector ≈45 %,). The remaining 31% is injected in to the sub-collector region. However, when light is propagating through the structure, the beam starts spreading into the sub-collector and eventually then into the substrate as shown in Figure 5-3 b). After this enlargement of the beam path, we can observe that the active region is still confining the light in its proximity. We also observe large portion of the light is attenuated near entrance of the structure.

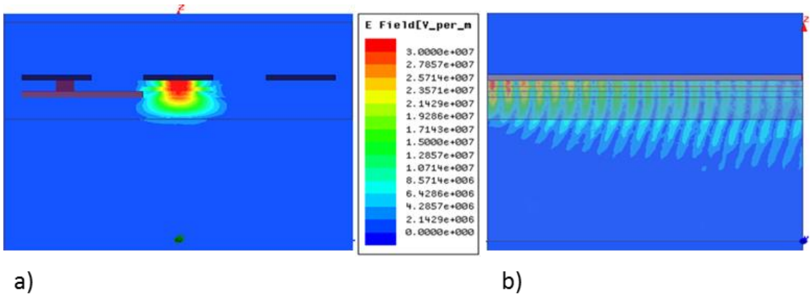

Figure 5-3: The magnitude of the electric field evaluated by HFSS at 850nm. a) at the input port, b) along the propagation axis.

This analysis validates the fact that an edge-SiGe HPT at 850nm is viable in the sense that the light can be confined in the active layers of the HPT despite an absorbing substrate. This is the purpose of the next sections to characterize experimentally such a device, in the specific condition of multimode fiber injection which is still required in home-area-networks and some other applications.

5.2.4 On-probe characterization bench setup

On-wafer bench setup described in chapter 2 is used to measure the opto-microwave performances of edge side illuminated HPT. An 850nm VCSEL is directly modulated and illuminates the HPT through a lensed multimode fiber (MMF) scanning the edge of the HPT. This VCSEL has a -3dB cutoff frequency of 12GHz. The VCSEL is biased so as to provide a 1.14mW optical beam at the end of the lensed fiber. A tilted mirror is used to monitor the alignment of the optical probe to the optical window of the HPT on the edge through the microscope as shown in Figure 2-8 b). The distance between the lensed fiber and the HPT lateral surface is set at 50µm to align the optical window with the beam waist of the lensed fiber. The angle of the fiber versus the longitudinal axis of the HPT is approaching zero, but some variation may still exist due to the difficulty of manipulation. We use a multimode light source and multimode optical probe to characterize our device as it is targeted to be implemented in Home Area Network (HAN) applications where multimode sources and MMF are largely deployed at 850nm.

The HPT is mounted in a common emitter configuration topology with two 100µm-pitch GSG pads in order to perform on wafer DC and microwave measurements. One of the ground pads of the HPT is removed during dicing so that one of the GSG ground is suspended in the air.

5.2.5 DC characteristics

Figure 5-4 shows the Ic-Vce curves of the edge illuminated HPT under illumination and dark conditions. The dark condition (blue solid curve) shows the pure electrical characteristics of the HPT. Vce is swept from 0V to 2V for Ib= 1µA, 3.5µA, 15.5µA and 80µA. Under the same condition, the HPT is illuminated by 1.14mW optical power through the edge. The result is an illuminated Ic-Vce curve (red diamond marked curve) with a noticeable increase in its output collector current. It can be observed from the plots that as Ib increases, the change in collector current (between dark and illuminated conditions) is less in absolute. It shows then the effect of the current-biasing mode of the base which was visible in the case of the top-side SiGe HPT as well, and intensively described in [235].At low Ib, especially, the HPT behaves as a 2T-HPT with a greater importance of the self-biasing of the HPT and reinjection of the photocurrent into the base-emitter junction, inducing a greater DC optical current gain as compared to higher Ib biasing case

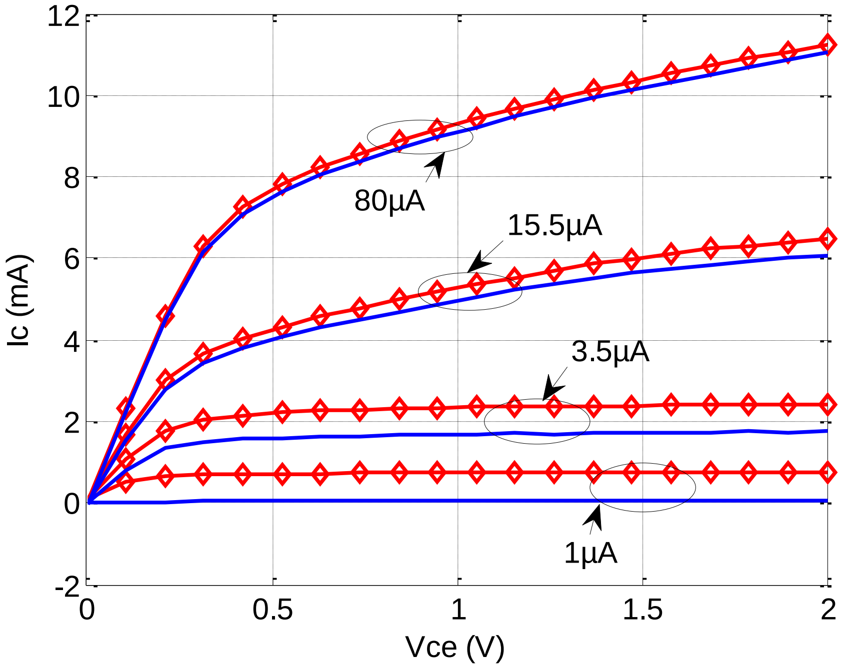

Figure 5-4: Ic-Vce curve of edge illuminated SiGe HPT with light (red curves with mark) and under dark condition (blue curves) for different Ib values.

The typical Gummel curve of the HPT with Vcb=0V is shown in Figure 5-5 in the dark condition and under illumination at 850nm with a 1.14mW optical beam. Under illuminated condition, it is observed that at high base voltage bias (>0.78V) the effect of the optical absorption is negligible as compared to the dark currents of the HPT. The top and lateral illuminated HPTs have thus comparable Ib and Ic values at high Vbe.

At low Vbe bias the base current saturates at around 1µA flowing out of the base contact and the collector current Ic saturates at around 100µA. The difference in these two currents is due to the substrate photocurrent as it was the case for top illuminated HPTs. The increase of collector current by 99µA indicates that the influence of the substrate photodiode still exists, however it has a smaller impact as compared to top illuminated HPTs having an optical window size of 10x10µm^2 for which the collector current increased by 4.95mA above the base current at low Vbe as presented in Figure 3-3 in chapter 3. Thus the substrate photodiode influence is minimized with edge illuminated structure.

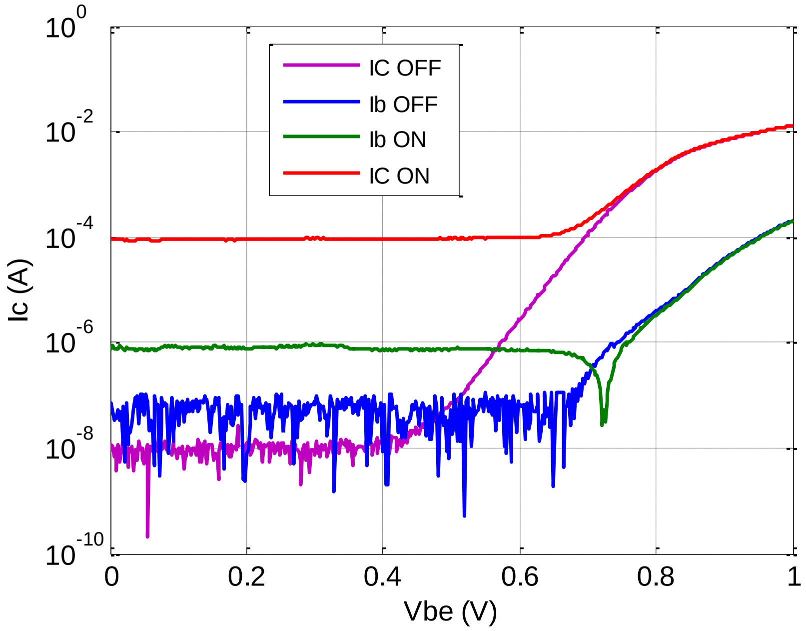

Figure 5-5: Gummel plot of edge illuminated SiGe HPTs with 1.14mW optical beam at 850nm and without light illumination.

The current gain can be extracted either from the dark Gummel curves for Vbe=0V to 1V, or dark Ic-Vce curves versus base current Ib. The extracted current gain as versus base voltage, Vbe, is presented and compared with top-side HPTs under dark conditions in Figure 5-6. The DC current gain has a comparable value for 5x5µm^2 top-HPT and the edge-HPT having nearly the same size, i.e 4.5x5µm^2.

The electrical current gain for edge-HPT starts to increase from Vbe=0.45V to reach its maximum of about 400 at Vbe =0.82V. The transistor amplification effect starts to reduce for Vbe greater than 0.82V due to high injection effects.

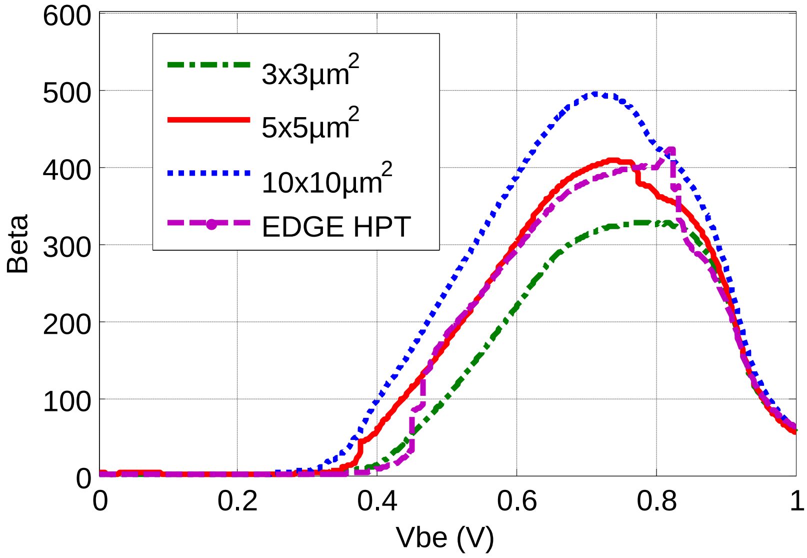

Figure 5-6: Comparison of the DC current gain from the edge-HPT or top-HPTs of various optical window sizes in dark conditions.

5.2.6 Opto-microwave characteristics

This section shows the opto-microwave behavior of the edge illuminated SiGe HPT in terms of opto-microwave cutoff frequency and responsivity in PD and HPT modes of operation. The DC biasing conditions will then be optimized according to these results before performing edge mapping. The distributions of the photocurrent and opto-microwave response across the edge section of the HPT structure are then investigated at the optimum dc biasing condition that maximizes either the low frequency responsivity or the cutoff frequency.

5.2.6.1 Optimizing the DC bias for the opto-microwave behavior

Before we perform edge SNOM investigation to look for the fastest and highest sensitive areas of the HPT as well as to see the distribution of photocurrent across the edge section of the HPT, we optimize the dc biasing conditions of the phototransistor with respect to the low frequency responsivity and the opto-microwave cutoff frequency at a given arbitrarily fixed position of the optical probe. This then provides two sets of optimum biasing conditions, depending on the selected criterion.

For this study, the opto-microwave measurements are realized using constant voltage biasing of the base. The phototransistor is operated in the forward active mode with collector-emitter voltage (Vce) values at 1V, 1.5V, 2V, 2.5V and 3V and with the base-emitter voltage (Vbe) swept from 0V to 1V.

Figure 5-7 a) shows the low frequency opto-microwave gain of the edge illuminated SiGe HPT versus Vbe at different Vce. The position of the fiber is arbitrarily chosen in the detection range of the HPT, thus at a non-optimum position. From Vbe= 0V to 0.7V, the HPT is operated in its PD mode as it is the case for top illuminated HPTs. In this region the base emitter junction is not yet efficiently biased and hence the base-collector junction pin photodiode is detecting light without any transistor amplification. Gom increases above Vbe=0.7V and eventually reaches its peak at Vbe=0.85V when Vce=1.5V, 2V, 2.5V or 3V; and at Vbe=0.92V when Vce=1V. At larger Vbe values, the fall-off of the gain is observed as the HPT is operated in a high injection regime.

The Gom is also shown as a function of Vce in Figure 5-7 b) in PD mode (Vbe=0V) and HPT mode at Vbe=0.85V and 0.92V. In PD mode, the Gom slightly increases as the collector-emitter voltage increases from 1V to 3V. However, in the HPT mode, it decreases as Vce increases either above 1V or 1.5V depending on Vbe value. We can deduce an optimum Gom when Vce is in the vicinity of 1V or eventually between 1 and 2V. More precise measurements would be needed. However, for 10x10µm^2 top illuminated HPTs the maximum Gom appears at Vce=3.5V as it is presented in chapter 3. The difference could be explained by the overall size of the phototransistor and the existence of lateral electrical field contribution in the base-collector regions, leading in a 2D electrical extended region as described in Chapter 3. As the lateral illuminated HPT is smaller and more vertical, it can be optimum at lower Vce. As well, it appears that the optimum Vbe is varying with Vce. This was not the case with top-illuminated HPT. Further investigations would be required there.

The optical gain (Gopt) enhancement between the HPT mode and PD mode of operation is presented in Figure 5-9 a) versus Vce. We reach a maximum Gopt of 12dB at Vce =1V which then falls down for higher Vce. Compared with top illuminated structure (optical window size 10x10µm^2) which has Gopt =18dB, laterally illuminated structure has smaller Gopt which is due to the smaller size of edge illuminated HPT (smaller size has lower current gain).

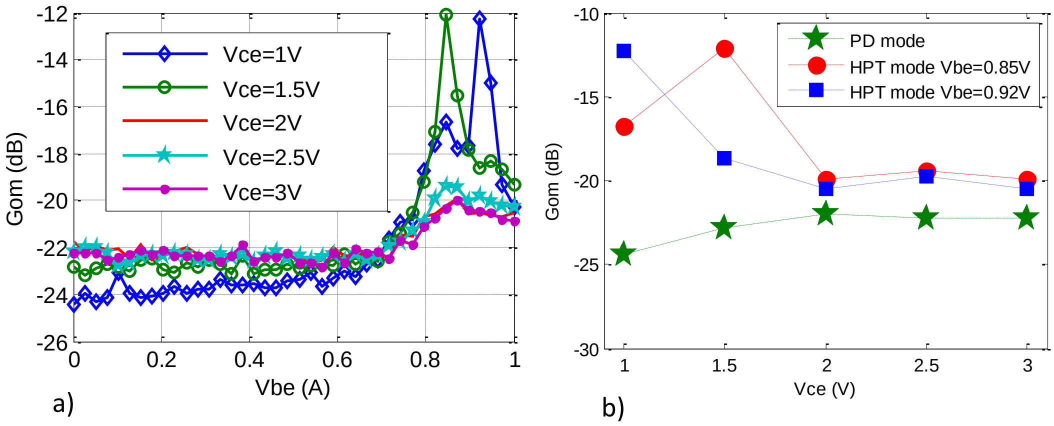

Figure 5-7: Opto-microwave gain a) versus Vbe at different Vce, b) versus Vce in PD mode and HPT moed (Vbe=0.85V and 0.92V).

The opto-microwave cutoff frequency (f_{-3dB}) versus Vbe, using 50MHz as a reference for the low frequency response, is shown in Figure 5-8. The cutoff frequency is low and constant in the PD mode (up to Vbe=0.7V) and it increases to a peak around 0.8V. We observe a maximum cutoff frequency of 480MHz at Vbe=0.8V and Vce=1.5V. The 2nd highest value is obtained at Vbe=0.85V and Vce=1V. This indicates that an optimum Vce value different from 1.5V may exist between 1V and 2V, similar to the optimization of the low-frequency gain as seen before.

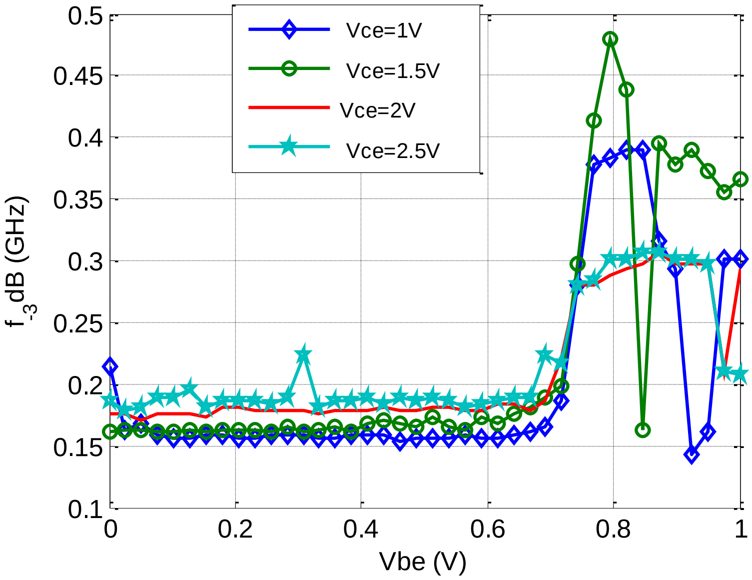

Figure 5-8: Cutoff frequency versus Vbe at different Vce.

Figure 5-9 shows the optical gain and cutoff frequency versus Vce at Vbe=0.8V. The Gopt decreases quickly as Vce increases. It indicates that the photocurrent amplification is small at Vce above 2V. The Gom in PD mode slightly increases while the Gom in HPT mode decreases (see Figure 5-7 b)). As a contrary, for top illuminated structures, the Gopt increases with Vce and its maximum appears at Vce=3.5V.

The cutoff frequency in PD mode is always smaller than the cutoff frequency in HPT mode as shown in Figure 5-9 b). This could be due to the effect of the predominant substrate photodiode, in the photodiode mode. The cutoff frequency increases with Vce in PD mode operation, whereas it decreases with Vce in HPT mode. The peak of the cutoff frequency appears at Vbe=0.8V and Vce=1.5V. We recall that with top illuminated structure, the peak appears at Vbe=0.857V and Vce=2V as presented in chapter 3. This difference is once again related to the overall size and geometry of the HPTs.

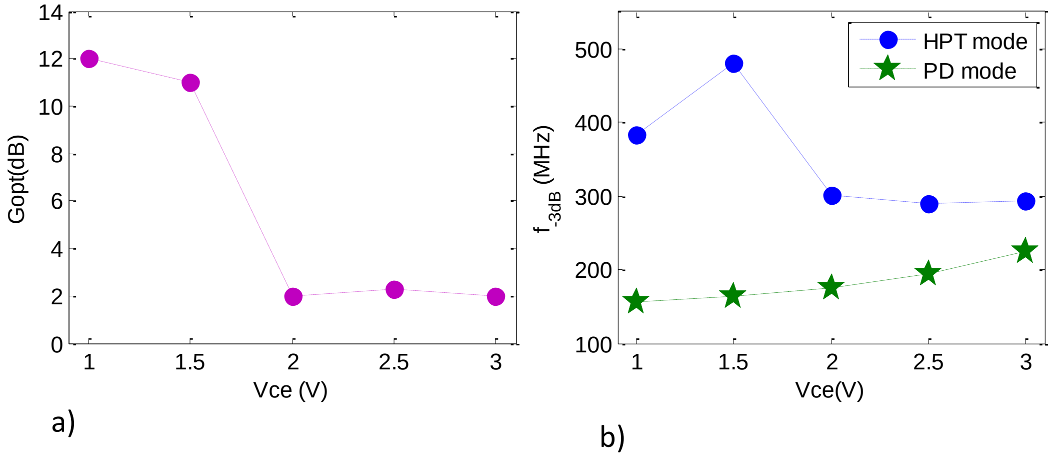

Figure 5-9: a) Optical gain versus Vce, b) cutoff frequency versus Vce in PD and HPT mode (Vbe=0.8V).

In general, from these results we conclude that:

- The optimum biasing conditions to maximize the low frequency opto-microwave responsivity are at {Vbe=0.85 V/Vce=1.5V}, with a second peak at {Vbe=0.92V/Vce=1V}.
- The optimum DC bias to maximize the cutoff frequencies are at {Vbe=0.8V/Vce=1.5V} with a second peak at {Vbe=0.85V/Vce=1V}.

Figure 5-10 shows the behavior of the opto-microwave gain versus frequency at these various optimum biasing conditions. From these curves, we understand that despite the cutoff frequency and the low frequency gain are found at different biasing conditions in a HPT mode, the high frequency part of the Gom curves become equal and have nearly the same slope at all biasing conditions.

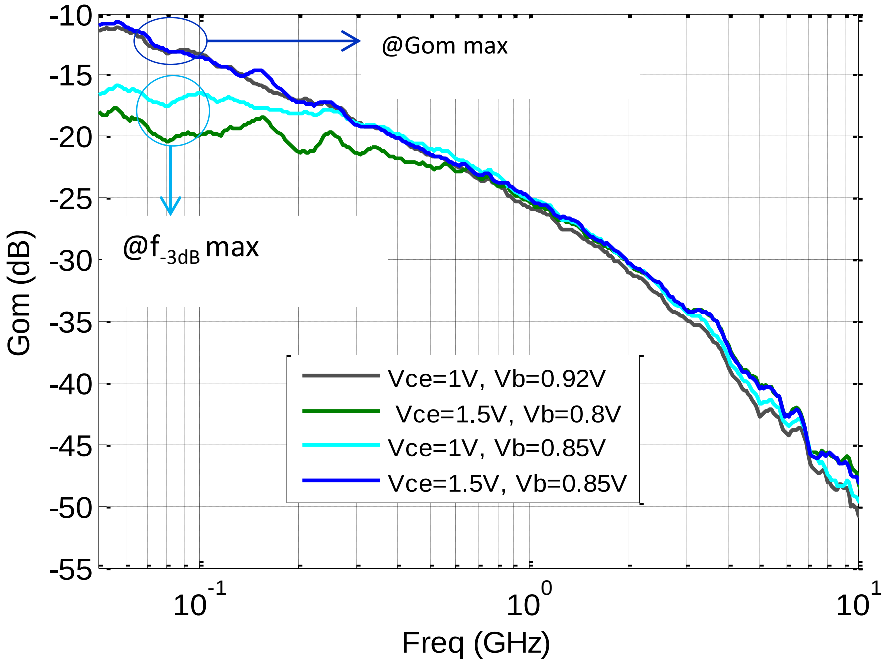

Figure 5-10: Opto-microwave gain versus frequency at low frequency Gom and cutoff frequency peak biasing conditions.

In summary, we found the optimum biasing conditions to maximize the low frequency Gom are 0.85V at the base-emitter junction and 1.5V at the collector-emitter junction; and to maximize the cutoff frequency, they are 0.8V and 1.5V at the base and collector contact respectively. We will use these dc biasing conditions for further experimental studies to perform edge OM and DC SNOM as presented in the following sections.

5.2.6.2 Edge Mapping

Figure 5-11 a) shows the simplified cross section of the edge coupled phototransistor with the optical probe aligned with the active area. The front view of the optical window is detailed in Figure 5-11 b) that shows the surface over which the edge SNOM is performed. On these figures the axes are given accordingly to the experimental results shown in the following section.

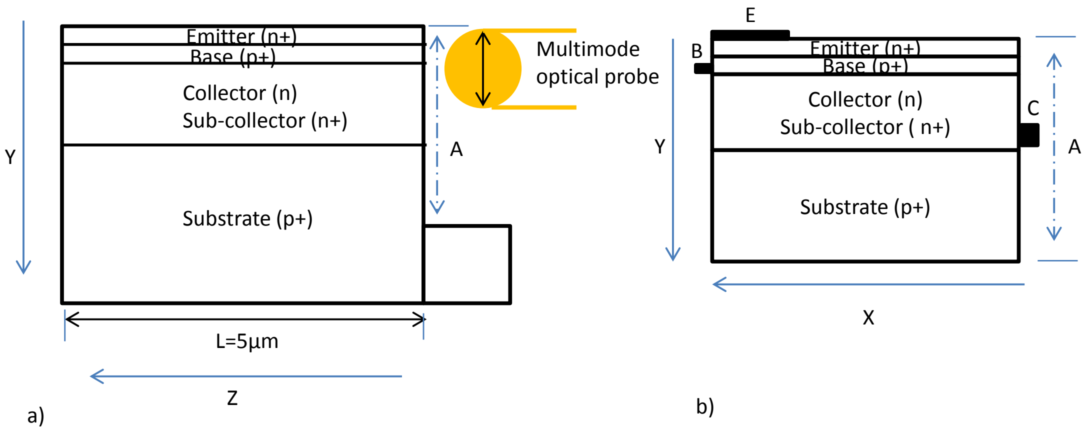

Figure 5-11: Simplified cross section of an edge illuminated HPT; a) Along the length of the HPT with the optical probe pointed to the structure, b) The front view of the edge side of the HPT where the illumination and edge mapping scan are performed.

The bench setup described in Chapter 2 section 2.3.2 is used to perform the opto-microwave and DC mapping over the edge of SiGe/Si HPT structure. The optical probe is scanned all over the HPT optical edge side. For each position, S-parameters of the optical link are measured in the [50MHz-20GHz] frequency range using the VNA. For each position the DC currents are also measured at the collector and base contacts with the help of the B1500 Semiconductor Device Parameter Analyzer. The DC currents and S-parameters are measured in both photodiode and phototransistor modes of operation. The voltage biasing conditions obtained in the previous section are used. A 2µm step (+/-20nm) is used to cover a 60µmx60µm area over the edge of the HPT. It then provides a complete OM and DC SNOM view of the HPT under test. Under this study we are able to understand the improvements of the performances of SiGe HPT under edge illumination compared to top illuminated one and it also helps to understand further the behavior of the structure, including the substrate photodiode effect.

a) DC mapping

Figure 5-12 shows the edge map of the DC current measured at the base and collector both in PD and HPT modes. The optical beam that is scanned over the HPT is assumed to have a Gaussian profile along X and *Y* axes as it was presented in chapter 3. The line at $y=0\mu m$ shows the middle of the active area (roughly around the base), for $y>0\mu m$ the optical fiber goes down to the substrate and for $y<0\mu m$ it moves to the air. The base and collector contacts are at the positive and negative sides of *x* axis respectively as shown in Figure 5-11 b).

As discussed in the previous sections, measuring the base current, either in photodiode mode or phototransistor mode, reveals the behavior of the intrinsic phototransistor, while the collector current is affected simultaneously by the intrinsic phototransistor and by the substrate photodiode.

According to Figure 5-12, the base current is symmetric along both *x* and *y* axes and its peak is used to fix our origin of axis, thus at x=y=0µm. The peak is confirmed to be simultaneously observed at his position, both in both PD (a) and HPT (c) modes. The base current map is a clear insight of the primary photocurrent, independently from the substrate.

The base current map helps to locate the intrinsic transistor. Taking into account the fact that the transistor thickness and width is very narrow compared to the Gaussian shape of the incident optical beam, it can be concluded that the SNOM map is providing a picture of this optical beam.

The active region is 4.5µm in width. Its thickness can be considered to be roughly 1µm (emitter to collector thickness) and actually less. Computing the convolution of the Gaussian beam (with an initial value of 34.8µm FWHM as obtained in Chapter 3 section 3.6.3) with the given rectangle defining the active region, it is possible to adjust the FWHM of the Gaussian beam so that the theoretical curve for Ib fits with the measurement, as shown in Figure 5-13.

It is then shown that the optimum FWHM for the optical beam is 32.2µm. This dimension is slightly different from the one obtained with the top illumination cases. This is due to eventually slight modification in the VCSEL source and to some difference in distance and angle of the lensed fiber from the scanned surface.

It is also observed that tuning the active region dimension doesn't influence much the final results, as it is much lower than the beam size.

It is then possible to sketch on the SNOM curves the rectangle related to the active region. This is done in Figure 5-12. A rectangle indicating the region of influence of the substrate is also shown in this figure. The extraction of its dimensions will be computed on a similar procedure in the following part.

The collector current has a peak centered at x=0µm and y=10µm, down into the substrate with a values 0.15mA and 1.5mA in PD and HPT mode respectively. The peak deviation from the center of the intrinsic transistor is clearly related to the substrate photodiode photocurrent which is then predominant compared to Ic from the intrinsic HPT. The peak of Ic is still in the vertical axis of the intrinsic HPT (x=0), but it is indeed shifted 10µm below where the coupling of the optical beam to the sub-collector / substrate photodiode is optimum.

Below that depth, the coupling to the substrate photodiode is stable in amplitude near to its maximum value, but the recombination losses of the photo-generated carriers are becoming predominant. It then explains the reduction of Ic below.

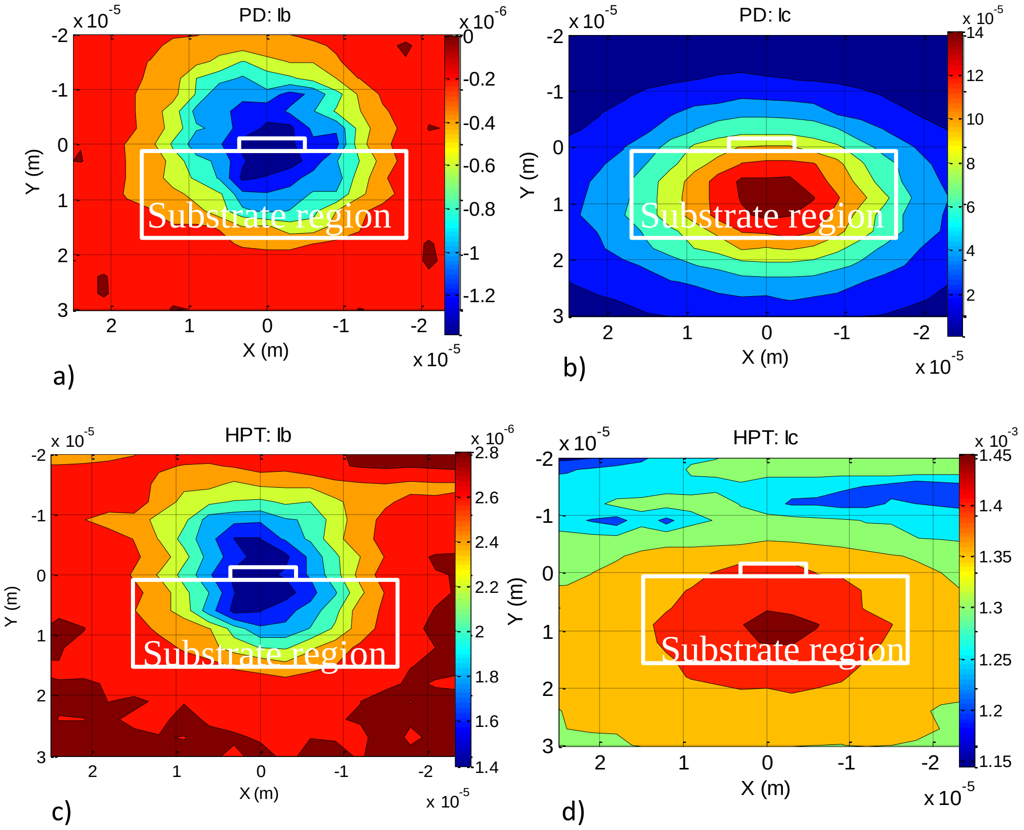

Figure 5-12:DC SNOM of edge illuminated SiGe HPT at Vce=1.5V with a) base current in PD mode, b) Collector current in PD mode, c) base current in HPT mode (Vbe=0.8V), d) collector current in HPT mode (Vbe=0.8V).

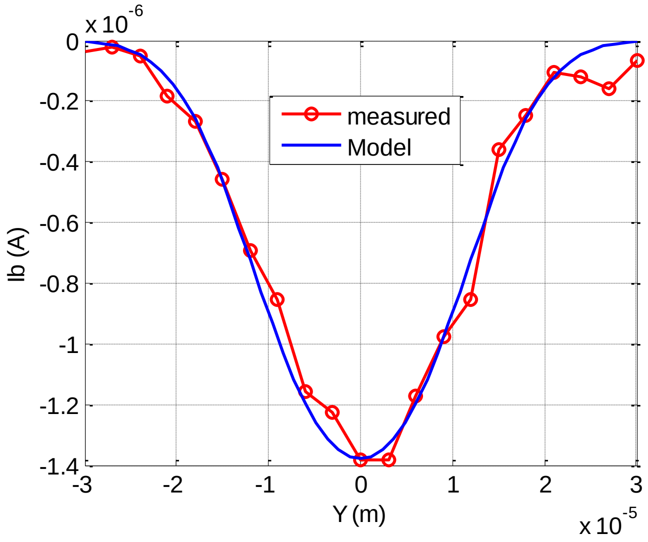

Figure 5-13: The fitting between the base current cross section along y axis with the convolution function resulted from the convolution of Gaussian beam having FWHF diameter of 32.2µm with expected rectangular shape of the active region of the HPT.

The edge map of the intrinsic photocurrent measured at the collector in PD mode is presented in Figure 5-14 a). As we can see from the figure, the peak of the collector photo-generated current is well centered to the intrinsic device and the map symmetrical to both axes. In PD mode operation, an intrinsic photocurrent of 2.2µA is measured at the collector contact at peak detection position (X=0µm and Y=0µm).

The computed intrinsic photocurrent Icph indeed confirms that the active region is very small compared to the injected optical beam and well fits with the function resulting from the convolution between the Gaussian beam and the active region rectangle of 4.5µm x1µm.

Computing the substrate current map helps to locate the substrate photodiode. It is given in Figure 5-14 b). The peaks appears around x=0µm and y=10µm, indeed outside the intrinsic area. We extract a substrate photocurrent of 110µA at the peak. It is 2.5 times less than the substrate photocurrent of top illuminated structure, i.e. 280µA. From the measurement of the base current, the substrate photocurrent peak appears 10µm below the center of the active region, so it is estimated to be approximately 9µm below the sub-collector and substrate junction if we consider a few hundred nanometer thick sub-collector.

Considering the Gaussian beam parameters as the one taken from the top illumination case described in chapter 3 section 3.6.3, it is interesting to know how thick the effective substrate absorption layer is. We assume that the effective absorption section of the substrate photodiode region has a rectangular shape. Then we perform the correlation between the Gaussian function and the rectangle function. The resulting curve is used to fit with the measured substrate photocurrent by tuning the dimensions of the rectangle. The resulting fit is achieved in Figure 5-14 d) along Y axis (at X=0µm), when the expected rectangle width dimension becomes 17µm along. This provides the effective thickness of the substrate photodiode. The fit along the X axis is also performed and hence it fits with the experimental result when the length of the rectangle becomes 32µm. This indicates that the effective substrate photodiode region has a rectangular shape with a surface area of 17µmx32µm as sketched in Figure 5-14 a) and b).

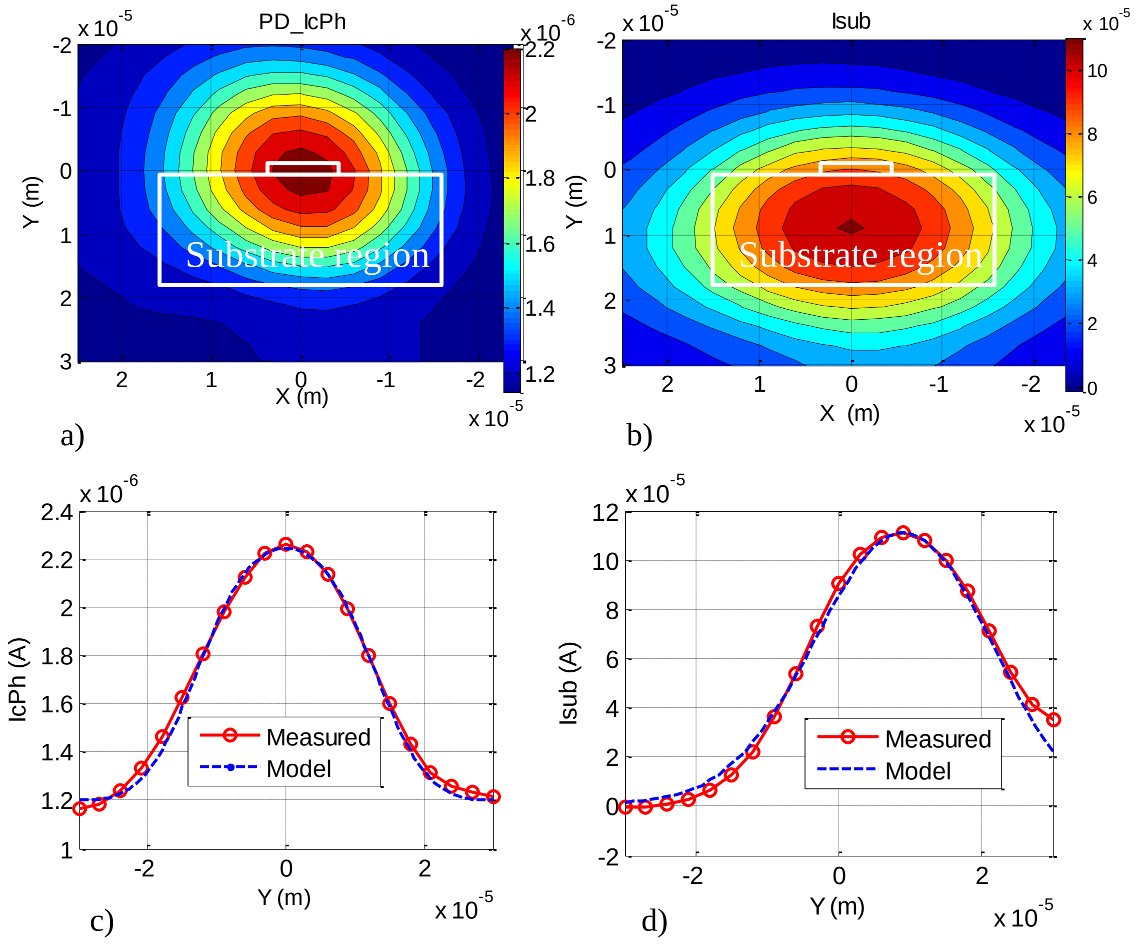

Figure 5-14: a) Intrinsic photocurrent measured at the collector contact in PD mode. b) Substrate photocurrent, c) Slice curve of intrinsic photocurrent along y-axis, d) Slice curve of substrate photocurrent along y-axis.

The edge map as a function of optical probe position of the primary photocurrent and base efficiency are shown in Figure 5-15 a) and b) respectively. Both are symmetric along the x and y axes, as Ib is. Peak values appear at the center of the active area (x=y=0µm). The maximum generated photocurrent in the edge illuminated SiGe HPT is then evaluated to be 2.6µA. This primary photocurrent is the combination of all photocurrent sources in the intrinsic photodiode mode.

Figure 5-15 b) shows the fraction of this holes photocurrent which leaks through the base contact. The rest of holes photocurrent is effectively injected into the emitter when operating in the HPT mode (in this case under Vbe=0.8V and Vce=1.5V). This part will activate the phototransistor amplification effect, while the other one will simply leak to the base contact.

When the 1.14mW optical power is injected in the active region of edge illuminated HPT, only 10% of the photo-generated holes are leaking through the base contact and 90% are used to active the transistors amplification effect. Whereas when the injection depth moves far from the active region the fraction of leakage photo-generated current increases.

The base efficiency is smaller compared with top illuminated HPTs having an optical window of 10x10µm^{2}, i.e 26%, at the peak detection (in the active region) at injected power level of 1.14mW as presented in chapter 3 section 3.6.3. This indicates a better amplification within edge-HPTs. This is attributed to be two aspects: the better localization of the optical beam all along the length of the device; a better design for the emitter contact enabling a greater proximity between the region of amplification and the region of generation of electron/hole pairs.

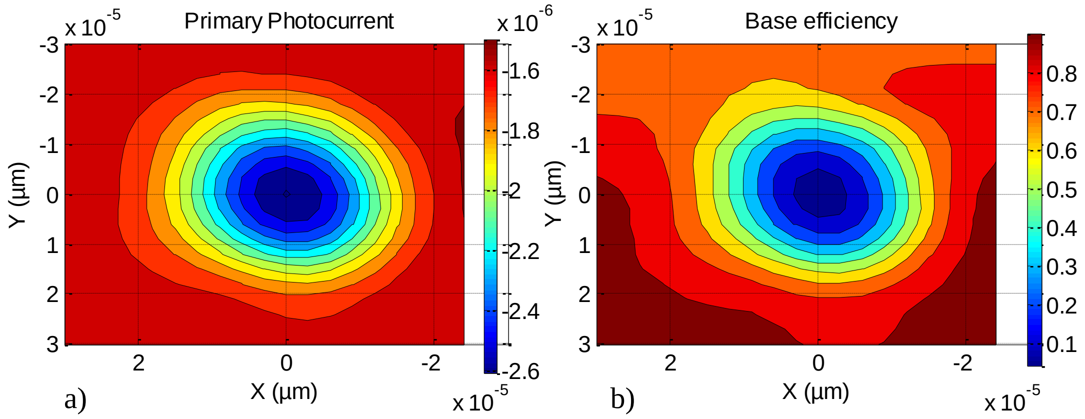

Figure 5-15: Edge map of: a) primary photocurrent generated in the structure, b) Base efficiency.

In general, at the peak detection (x=y=0µm) a complete DC responsivity of 0.48A/W in HPT mode (Vbe=0.85V and Vce=1.5V) and 0.105A/W in PD mode are observed. The DC responsivity in HPT mode for laterally illuminated device is 1.33 times larger than the top illuminated HPT of 10x10µm^2 optical window size (i.e 0.36AW). We also observe maximum DC substrate responsivity of 0.09A/W for edge illuminated structures and 0.234A/W for top illuminate case.

Thus we conclude that the substrate influence on the intrinsic HPT performance is indeed minimized in edge illuminated structures.

b) Opto-microwave mapping

Figure 5-16 a) and c) shows the OM-SNOM view of the low frequency opto-microwave responsivity and opto-microwave cutoff frequency of the edge illuminated HPT under 50Ω condition at 50MHz in HPT and PD modes, respectively. The PD modes are obtained by setting Vbe=0V and Vce=1.5V and HPT modes is obtained by setting Vbe=0.8V and Vce= 1.5V. These biasing conditions are chosen in the section 5.2.6.1 to maximize the cutoff frequency.

Thus the following observations are made from Figure 5-16:

- Figure 5-16 a): in PD mode, the highest gain at 50MHz is still located into the substrate as in the case of top illuminated HPTs but it is however closer to the intrinsic HPT with a maximum position at x=0µm and Y=5µm. This is due to the fact that the sub-collector/substrate photodiode speed is directly dependent on the distance between the points of optical injection to the sub-collector. The cutoff frequency can be lower than 50MHz and thus the signal is filtered; the amplitude at 50MHz gets lower when the light is injected far from the sub-collector.
- Figure 5-16 c): The same phenomenon is observed in the phototransistor mode. The low frequency behavior is still mostly affected by the substrate photodiode indeed. We extract a peak responsivity of 0.11A/W in HPT mode at X=0µm and Y=5µm
    - One could take advantage of the substrate photodiode to boost the overall responsivity of the device combined with the intrinsic HPT.
- Figure 5-16 b): The cutoff frequency of the photodiode mode shows two peaks. The first peak is almost centered in x, and is located at y=-9µm. This first peak is associated to the illumination of the upper part intrinsic HPT region only. This is consistent to the maximization of the f_{-3dB} when the beam is centered into the top part of the base-emitter junction. At this position, the transit time for the holes to reach the emitter is reduced, as foreseen by physical simulations conducted as simulated in [260], whose results are re-plotted in Figure 5-18. This figure shows the f_{-3dB} frequency in the lateral illumination condition versus the optical injection depth into the device when considering a theoretical beam width of 10nm injected on the edge of the device.

The second peak of the f_{-3dB} is located at x=3µm and y=0µm; for this peak it might be the base-collector junction which maximizes the speed, which then linearly decreases with y when the optical beam moves down to the substrate as shown in the cross section curve along y axis in Figure 5-17 a). The two peaks have the same f_{-3dB} value i.e. 260MHz.

- Figure 5-16 d): The f_{-3dB} of the phototransistor mode is quite different. It is mostly associated to the intrinsic HPT region with a peak value of 520MHz. Its position is located beneath the emitter metal contact around x=6µm and y close to -10µm. This shows the importance of this metal contact on the dynamic of the HPT. This emitter metal contact was initially designed only on the left hand side of the emitter to prevent from the absorption losses into the metal. These losses appear not being visible in our observation. On the counterpart, it shows to have an important effect on the f_{-3dB}. The speed decreases when the optical probe moves away from the emitter contact along x axis. From this we observe that the high doping of the emitter is not sufficient to prevent from lateral paths of the photo-carriers as observed in the top-illuminated HPT.

  We also observe that the peak is at *y* around -8µm. In this position the optical beam is illuminating above (in the air) however, the Gaussian tail excites the emitter-base region only, and thus minimizes the illumination of the substrate photodiode. We observe that when the beam is illuminating further these lower regions, the influence of the emitter metal contact is less and the f_{-3dB} is more uniform along the x axis within the volume of the intrinsic HPT. This is supporting indeed that this is due to the regions below the base, and that the toppest peak is indeed related to the emitter-base region. Figure 5-17 b) shows the f_{-3dB} frequency as the function of the optical injection location as it is moved down to the substrate. The cross section curve indeed linearly decreases as the optical injection depth moves into the active device and then down to the substrate.

A perspective of optimization of the edge-SiGe HPT would then be to fully cover the emitter with a metal contact, in order to increase the area dimension where the peak f_{-3dB} is met. In conclusion cutoff frequencies of up to520MHz and 260MHz are obtained in HPT (Vce=1.5V and Vbe=0.8V) and PD (Vce=1.5V and Vbe=0V) mode respectively.

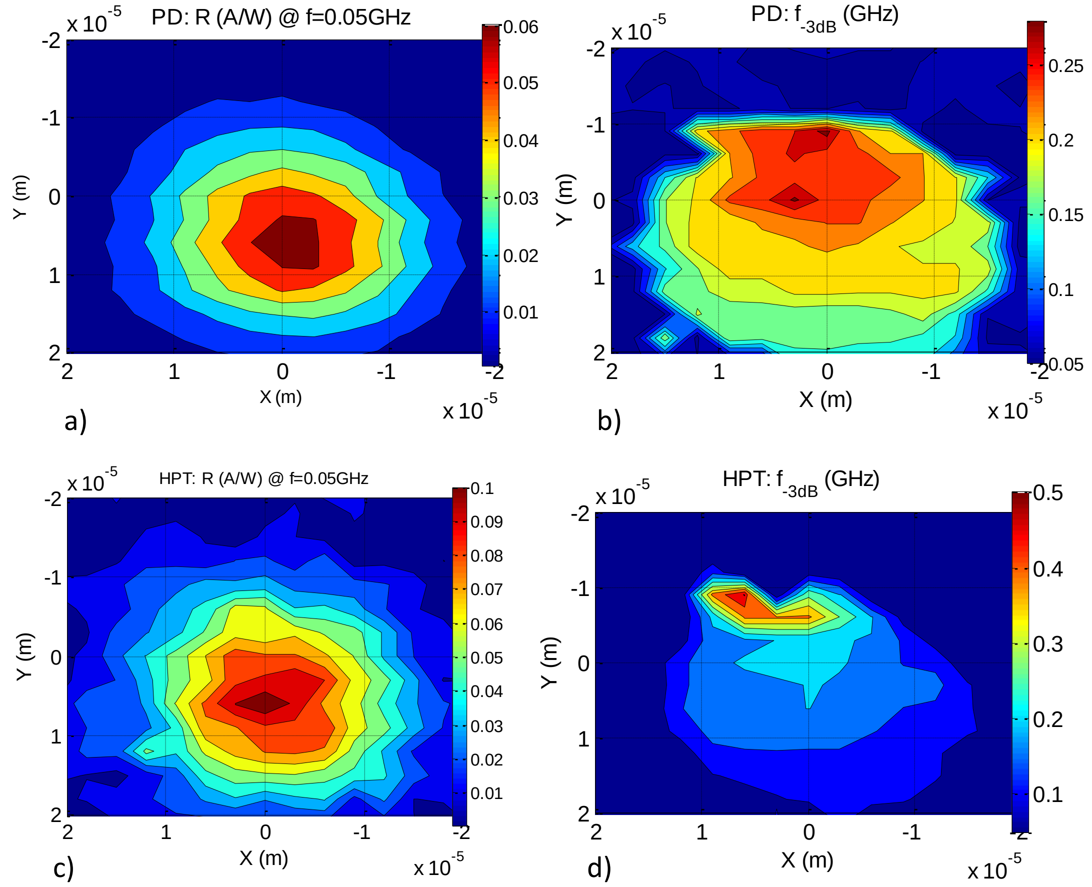

Figure 5-16: OM SNOM of edge illuminated SiGe HPT at Vce=1.5V a) Low frequency opto-microwave responsivity in PD mode (Vbe=0V), b) cutoff frequency in PD mode (Vbe=0V), c) Low frequency opto-microwave responsivity in HPT mode (Vbe=0.8V) and d) cutoff frequency in HPT mode (Vce=0.8V).

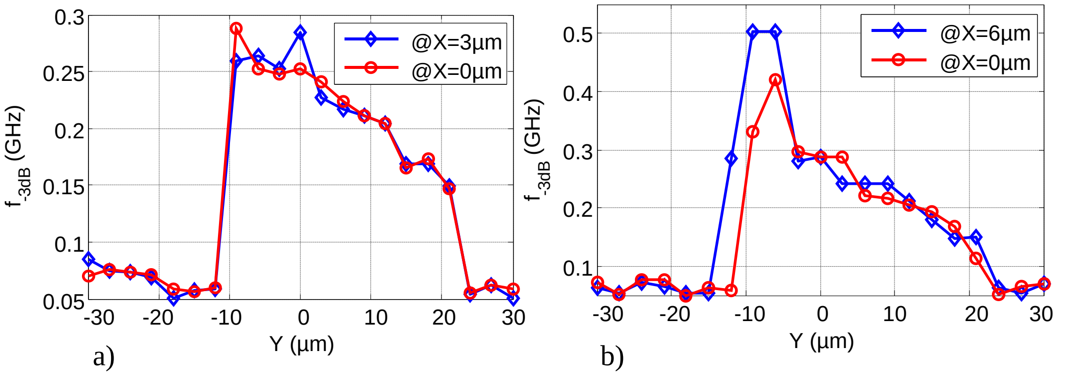

Figure 5-17: The cross section curve of the cutoff frequency along y axis (for top into the substrate) at Vce=1.5V in a) PD mode (Vbe=0.8V), b) HPT mode (Vbe=0V).

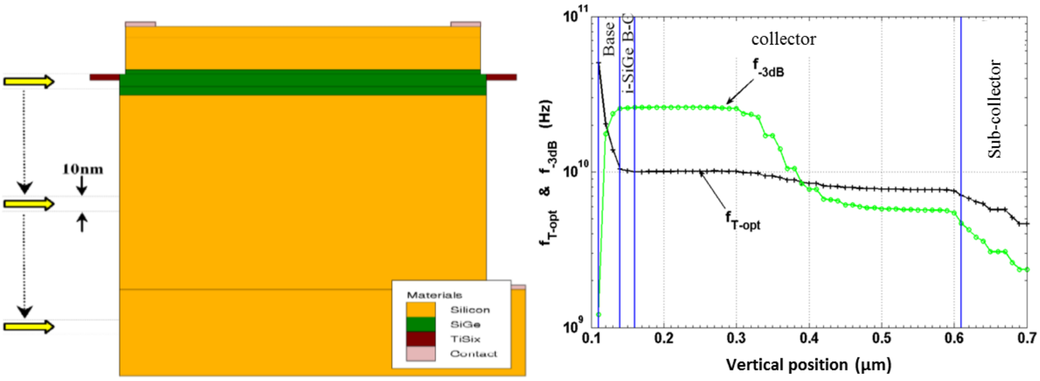

Figure 5-18: Cutoff frequency extracted from physical simulation in the lateral illumination condition versus the optical injection depth into the device when considering a theoretical beam width of 10nm [260].

Figure 5-19 shows the map of the low frequency opto-microwave responsivity and f_{-3dB} of an edge illuminated HPT under 50Ω condition at 50MHz in HPT mode obtained by setting Vbe=0.85V and Vce= 1.5V which maximizes the low frequency responsivity as studied in section 5.2.6.1. At this biasing condition the low frequency responsivity increases to 0.26A/W in HPT mode and the cutoff frequency to around 800MHz as it is also shown in the cross section curve in Figure 5-20. The peak of the cutoff frequency is shifted to the base contact due to metal contact proximity effect as described above. The peak responsivity is more than for the previous biasing points as expected (this biasing condition maximizes the low frequency responsivity). The maximum f_{-3dB} in the HPT mode is even more than for the previous biasing point. This was not expected. It indicates that the biasing optimization may be different depending on the optical injection point. We still observe two peaks. The topper one (at y~-8µm) reaches the value of 306MHz which is lower than with the previous biasing conditions as shown in Figure 5-16, i.e. 520MHz, while the peak at the bottom position (at y=0µm) is indeed increased. The top one was related to the proximity of the emitter contact and is closer to the base-emitter region whereas the bottom one is probably due to the base-collector junction within the intrinsic HPT. Both are indeed impacted by Vbe. This assumption, initiated above, is then here reinforced.

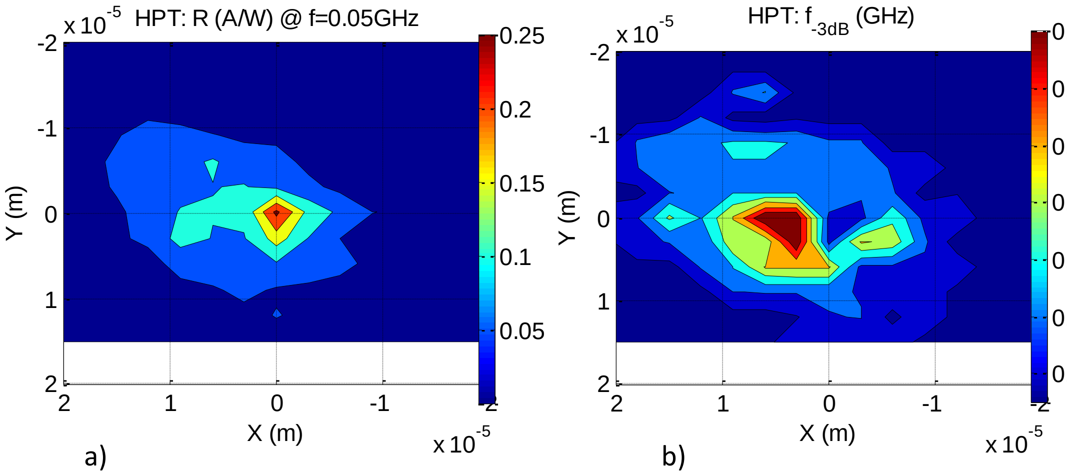

Figure 5-19: OM-SNOM of SiGe HPT with edge illumination at Vce=1.5V and Vbe=0.85V a) low frequency responsivity and b) cutoff frequency.

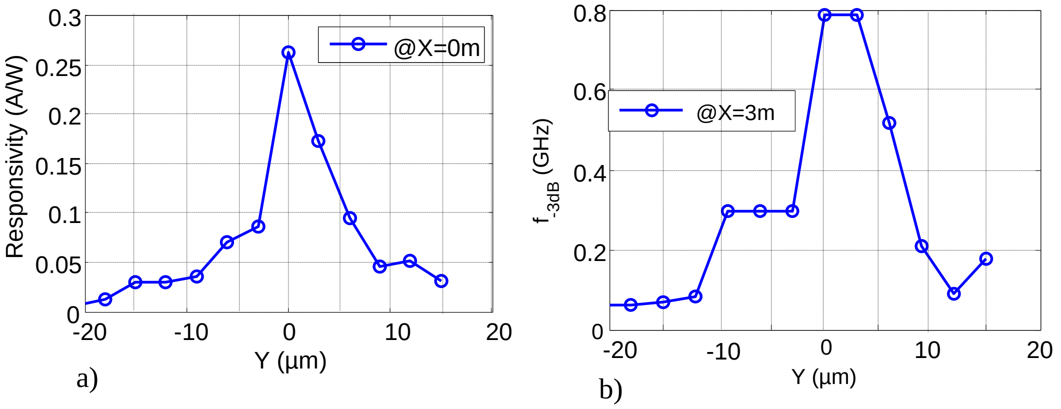

Figure 5-20: The cross section curve along y axis (with y>0 in substrate) of lateral illuminated HPTs at Vce=1.5V and Vbe=0.85V a) Low frequency responsivity, b) Cutoff frequency

The edge map of the complete optical transition frequency, f_{Topt}, at Vce=1.5V and Vbe=0.85V is presented in Figure 5-21. The maximum value of 1.01GHz of f_{Topt} is observed at y=0µm along x axis. At this position the Gaussian beam also illuminates the substrate photodiode. This explains the low f_{Topt} value. A comparison to the top-HPT would require the computation of the intrinsic f_{Topt}. Anyway, from this measurement, we indeed observe that the fTopt is indeed clear where the active region is located. However, as contrary to the f_{-3dB} curve, the peak is not at the edge of the emitter contact (spot position~-10µm), but well in the middle of the active region, thus in the base-collector junction. This is then not validating the physical simulations provided by the PhD of F.Moutier [260], but further investigations, especially with a narrower optical beam, would be required.

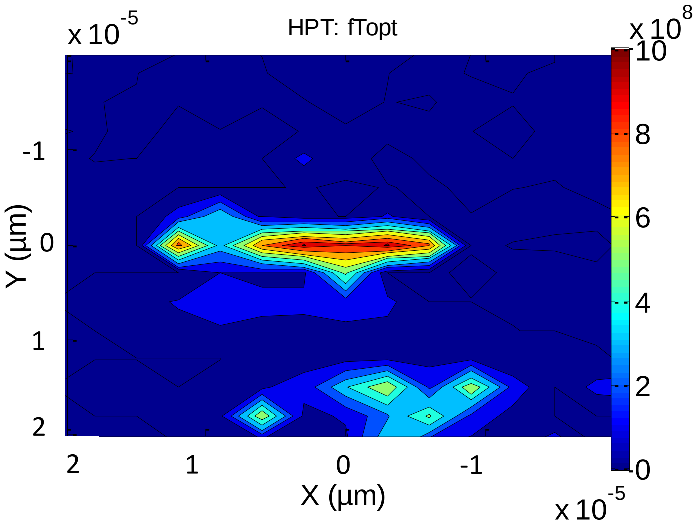

Figure 5-21: The edge map of optical transition frequency at Vce=1.5V and Vbe=0.85V.

5.2.6.3 Comparison between top-side and edge-side illuminated HPT

In order to compare the edge-illuminated HPT and the top-side illuminated HPT performances, we compare the edge HPT illuminated at its peak positions on the map with a 10x10µm^{2} top illuminated HPT, as this later leads to the best performance for top illuminated devices.

We repeat the above experiments for edge illuminated HPT by optimize the optical fiber coupling to the device by moving the fiber more closer to the HPT under Vbe =0.85V and Vce =1.5V. Thus we find that the gain and the cutoff frequency of laterally illuminated HPT, at some optical beam injection locations, are largely improved. However, the edge map is not presented here as it was too partial and focused on getting the optimum points only. Therefore we prefer to present the opto-microwave gain versus frequency at those specific points and compare with top illuminated devices.

Figure 5-22 shows the Gom versus frequency of edge and top illuminated HPTs. For the edge illuminated HPT, we present two Gom curves one extracted at the peak of the low frequency responsivity (with the substrate influence) and the other extracted where the peak of the cutoff frequency appears (the intrinsic HPT response). The intrinsic Gom is extracted close to the emitter contact at the peak is due to the illumination of the emitter base region as presented above, whereas the Gom with substrate influence is extracted when the optical beam illuminates the base-collector region and its tail illuminates the substrate photodiode.

As shown in Figure 5-22 a), we observe a low frequency (50MHz) complete opto-microwave gain of -7dB (opto-microwave responsivity of 0.45A/W) and -10dB (opto-microwave responsivity of 0.32A/W) for edge and top side illuminated HPTs respectively. The improvement in the responsivity for edge side illumination is related to the increase of the absorption length. It can be up to 5µm long whereas for top illuminated HPT the absorption length is less than 1µm (which is the total thickness of the active area including emitter, base and collector). We also note down that this increase in length could benefit both to the intrinsic HPT and to the substrate photodiode. However, at the selected beam position to optimize the f_{-3dB}, it is shown that the substrate effect is much less visible (no 10dB/dec slope). Thus the light is well confined in the intrinsic HPT all along this 5µm penetration length.

Figure 5-22 b) shows the normalized Gom versus frequency for the top and edge HPTs. We observe that the edge illuminated HPT can reach up to 890MHz cutoff frequency whereas the top illuminated one is limited to 420MHz. The cutoff frequency at the position that maximizes the HPT mode low frequency Gom (with substrate influence) is only 150MHz.

In total, it is shown that even when using a MMF, the edge-SiGe HPT is similar in performances to the top-illuminated one especially at high frequency above 1GHz (a). At frequency below 1GHz, depending on the position of injection, the substrate or the intrinsic HPT can be predominant in the case of the edge-HPT, giving thus a higher f_{-3dB} frequency when the intrinsic HPT is preferably illuminated. This may be useful to enable larger bandwidth circuits for applications below 1GHz, but doesn't limit the operation of the HPT above 1GHz in its usual 20dB/dec slope.

It is a very important result that this edge-SiGe HPT can be used without complex coupling structures and tapers. However an important perspective comes from the very high improvement potential that could bring the use of single-mode fiber (SMF) at 850nm or even reduced modes fibers such as 9µm core optical fiber operating at 850nm [259]. Indeed the previous results gives indications that the intrinsic region is capable of keeping its fraction of light confined and not getting systematically into the substrate. This is consistent with optical waveguides simulations from section 5.2.3.

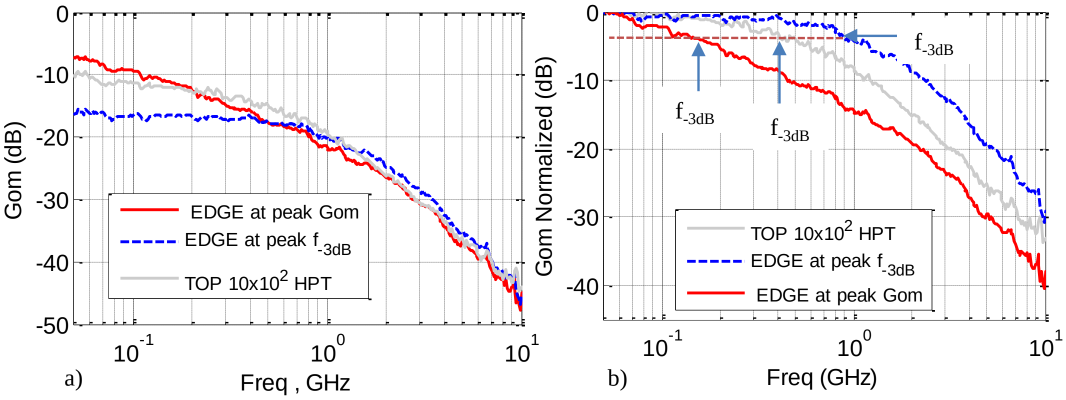

Figure 5-22: The Gom versus frequency of edge and top illuminated HPTs at their peak low frequency gain and cutoff frequency. a) Un-normalized Gom, b) the normalized Gom to indicate the cutoff frequency.

5.3 CMOS compatible Silicon Avalanche Light Emitting Diode (Si Av LED)

5.3.1 Introduction

Due to the potential for low cost and high volume production, Si has emerged as an integrated platform in recent years. However, silicon is an indirect band gap semiconductor, and, therefore, fabricating silicon based lasers is a challenge. Nevertheless, Si Avalanche Light Emitting Diodes (Si Av LED) devices which emit in the 450-750nm range are known since quite early years [112] [238] [239]. Viable CMOS compatible and avalanche based Si LEDs have however only emerged since the 1990's [111][240]. Kramer et al [111] are the first to propose the used of Si Av LEDs into CMOS technology and thoroughly illustrate some potentials of this technology. Snyman et al [112] [239] [240] have subsequently realized a series of practical first iteration to use light emitting devices in standard CMOS technology using CMOS compatible operating voltage and current levels. This was mainly achieved by using novel surface engineering, current density modeling and dynamic carrier density engineering techniques. The developed devices showed an optical output about three times higher compared to previous similar works. In particular, promising results have recently been obtained by further increasing the efficiency through depletion layer profile and carrier and momentum engineering [185] [241]. The technology is appropriately nomenclature Silicon Avalanche based Light Emitting Diode (Si Av LED) technology, as light-emission in the device occurs in reverse-biased silicon diode under avalanche breakdown.

In this section, we report an overview on the mechanisms of light emission in Silicon. We also summarize the previous works of top emitting Si AV LEDs in ESYCOM laboratory together with the Pr.Snyman team in TUT and then in UNISA. Furthermore, from the conclusion drawn from these works we design and present three different LEDs that are compatible with the existing SiGe HPT technology and we use them together to fabricate a full on chip optical link. This is presented in section 5.4.

5.3.2 Light emission mechanisms in Silicon

The avalanche light emitting diode in Figure 5-23 gives a simple but basic synopsis for the light emission process in silicon. Electrons are accelerated in the strong field of a reverse biased silicon pn junction, the energy gained by the carriers is transferred to the lattice, and electron-hole pairs are formed during the subsequent host atom ionization processes.

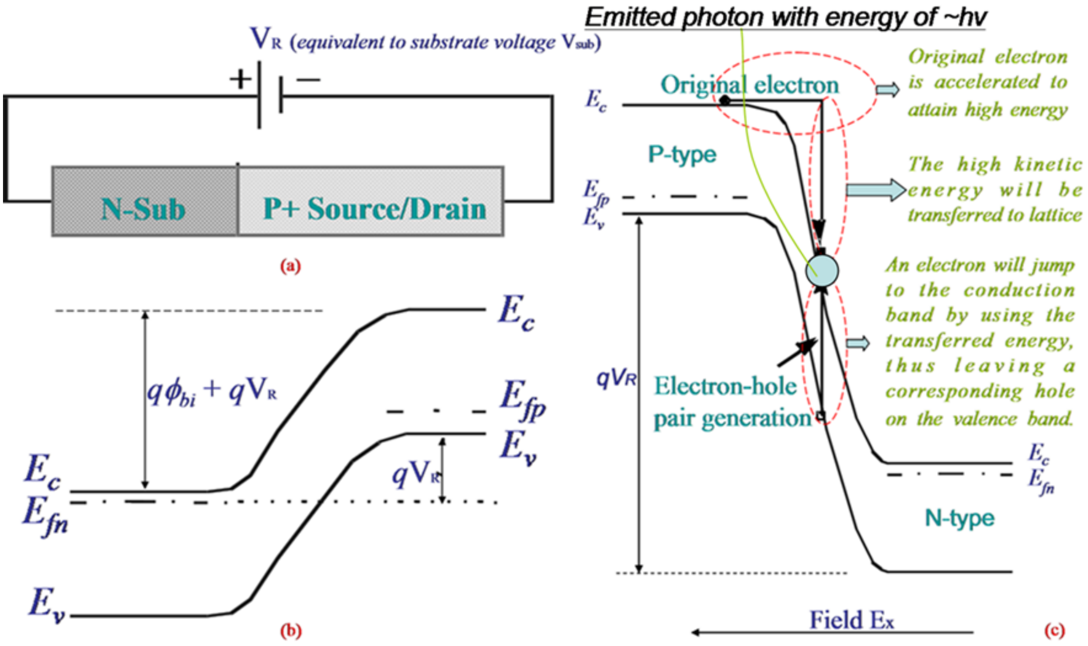

Figure 5-23: Energy band scheme for the impact ionization process for an electron in a reverse biased pn silicon junction [114]

Many perturbations are possible in the electron hole excitation process:

1. Defects such as dislocations, vacancy and interstitial complexes are responsible for electron-hole pairs generation at the sites of the defects particularly in prevailing strong E –field conditions.
2. Interstitials and dopant impurities assist with radiative recombination phenomena of electron-hole pairs.

Thus several theories have subsequently been presented for explaining light emission phenomena such as:

- Excited carriers are retarded in the crystal lattice, and according to a classical Maxwell approach, through scattering interaction with the lattice, a part of the energy may be directly converted to photons [114]
- Further theories have also been proposed that especially intra-band transitions may be responsible for the light emission processes. Such transitions may occur between the first and second conduction band for electrons as well as for the first and second bands of the valence band for holes in silicon [113]. The energy band diagram showing the various transitions in silicon was investigated [113]. At various excitation conditions specific photon transition can be enhanced as shown in Figure 5-24:
    - If electrons gain enough energies and momentums to high up in both the first and second conduction bands to 1.8 eV, direct intra-band relaxation transitions of Type A could be favored, corresponding to about 750 nm in wavelength. Similarly, intra-band transitions can also occur in the valence band, between second and first valence bands leading to transitions of about 1.5 eV (transitions of Type B), in Figure 5-24. This would lead to emissions of about 850 nm wavelength.
    - If hole energy values are sufficiently raised such that their momentum values correspond with the near momentum values of electrons excited in the conduction band, various indirect inter-band transitions of Type C, as in Figure 5-24 and with photonic emissions of approximately 2.3 eV or 650nm wavelength can occur, mainly through a process of phonon assisted carrier recombination.
    - When electron and hole momentum values correspond more precisely in the respective bands, direct type transitions of about 2.8 eV can be promoted between the conduction band and the valence band (Transitions of Type D in Figure 5-24).

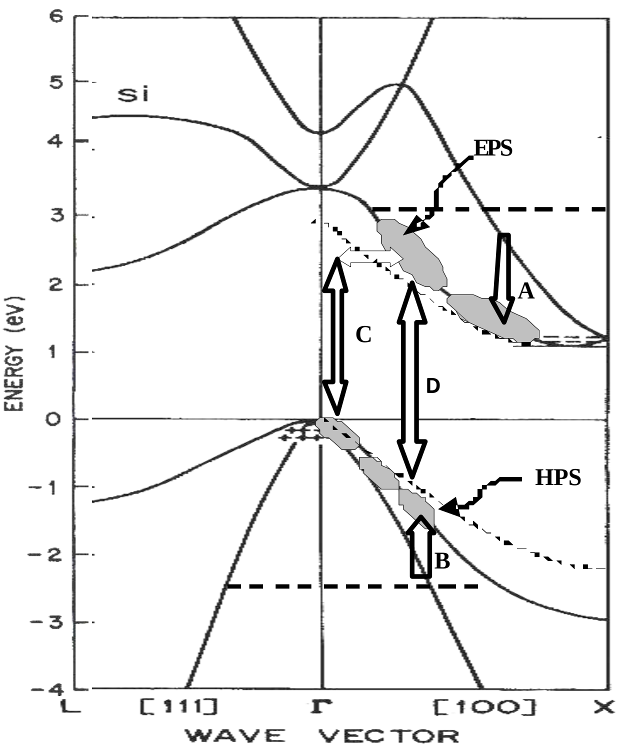

Figure 5-24: Energy distribution of populations of electrons and holes in the conduction band and valence band of silicon for various excitation conditions, momentum changes, and possible subsequent photonic transitions [113].

A series of theoretical simulations of carrier energies and momentums in the silicon band structure has been performed in [242] when a volume of crystal is subjected to high electric fields as experienced in these devices during strong reverse bias conditions. It was observed that the energy distribution of the electrons in the conduction band for this excitation field range from 1.1 to 1.7 eV, while quite a wide momentum scattering is observed for electrons. Similar tendencies were observed for holes, but the spread in both energy and momentum is less due to the heavier effective mass of holes in silicon.

During previous work and experimental analyses [228] [240] [242], some important phenomena have been observed that can provide important clues for further optimized device design.

1. Light emission was only observed on the n-side of pn junctions, indicating that electrons are primarily responsible for light emission phenomena in silicon.
2. High doping and n-type doping enhance the light emission. Strong light streaking is observed in n-material when high electron densities are injected into the avalanche junctions.
3. The emission intensity seems to be clearly related to the density of the carriers that traverse or are injected into specific crystal regions.

5.3.3 Proposed Si and SiGe Avalanche LEDs

Using our experimental and theoretical results on top emitted Si LED, we designed three different LED implemented using the SiGe2RF Telefunken GmbH technology to be used in a full on-chip optical link as shown in Figure 5-25. These structures are of course not investigated through simulation, but we use our previous work experiences on the SiGe HPT technology to implement them in a full on chip optical link for a first test.

The layouts of the three Silicon-based LEDs designed from SiGe2RF Telefunken technology are shown in Figure 5-26. The RF and DC probing contacts and the designed optical waveguides are also shown in the layout.

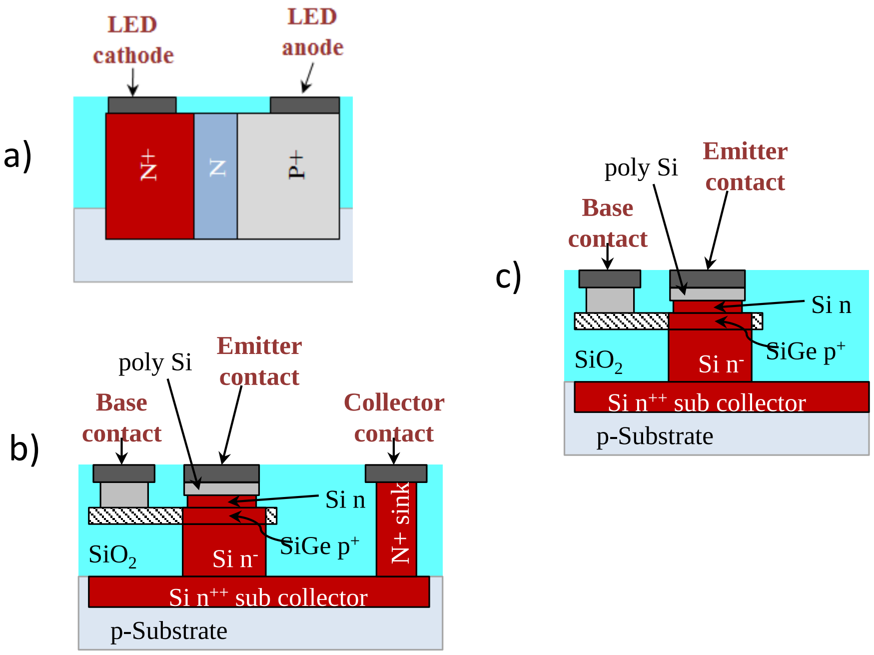

Figure 5-25: The schematic of three different Si based Av LEDs to be implemented in SiGe2RF Telefunken GmbH technology for full on chip optical link system; a) Si Av N^+NP^+ columnar, b) SiGe-N^+PN^- with collector contact and c) SiGe-N^+P without collector contact

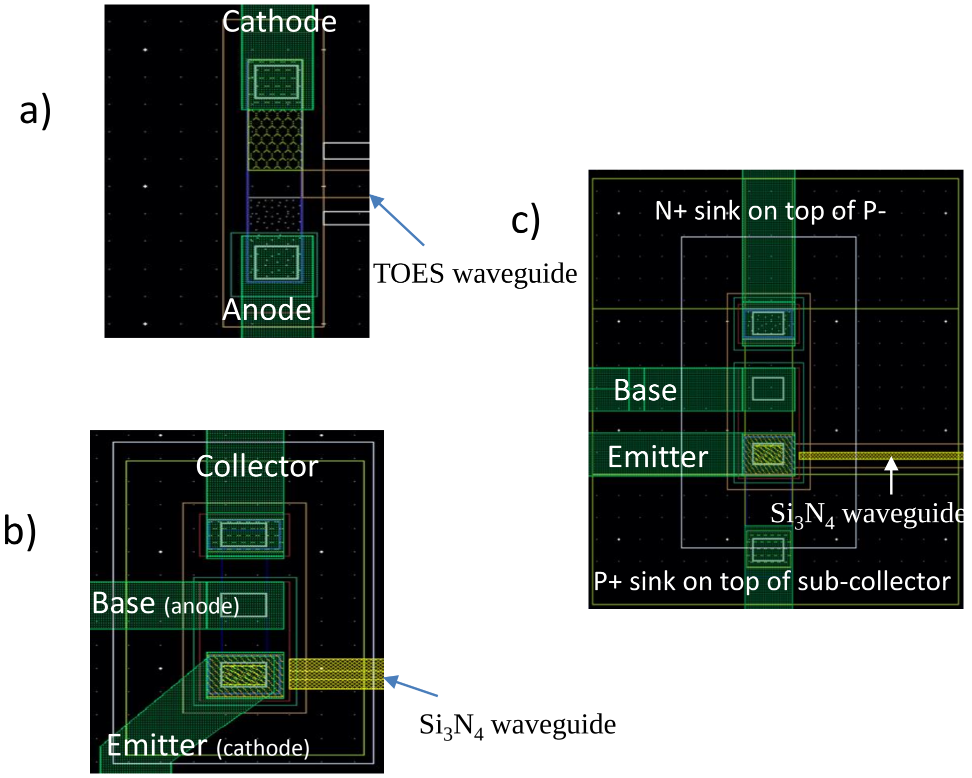

Figure 5-26: The layout of the three different Si based Av LEDs implemented in SiGe2RF Telefunken GmbH technology for full on chip optical link system; a) Si Av N^+NP^+ columnar, b) SiGe-N^+PN^- LED with collector contact and c) SiGe-N^+P LED without collector contact

The structures of these optical sources can be described as follows:

a) **Si Av N$^+$NP$^+$ columnar**: An n$^+$n-p$^+$ columnar structure is placed laterally on the semi-insulating substrate. The regions are doped as indicated in Figure 5-25 a). The regions are appropriately electrically contacted during experimental measurements in order to apply a forward bias at the first p+ n junction. Upon forward biasing, the depletion region penetrates through the n+ region in order to strengthen and confine the electric field in the lowly doped n region. According to our previous experience gained from the previously designed devices, we know that the light emission would occur near the surface region of the middle N region and extend more or less laterally across the whole region.

b) **SiGe-N$^+$PN$^-$LED with collector contact**: The basic vertical structure of a SiGe/Si HBT is used. The emitter and collector contacts are grounded as required by the RF probe bias during the measurement process and a forward biasing together with the modulation signal are applied on the base (P anode) contact. Positive voltage bias places the anode contact in forward bias mode. The depletion region lies toward the n side of either the collector or the base, as the base is highly doped. Thus light emission will be in the n regions. As it will be describe in the following section, a V-shaped groove silicon nitride waveguide with wider core is used along with this LED to realize the full optical link.

c) **SiGe-N$^+$P LED without collector contact**: A vertical cubical columnar SiGe/Si HBT like structure is used. It has four metallic contacts as shown in Figure 5-26 c) as it is designed from the HBT structure. The first two on the side are emitter and base, and the last two on top and bottom are additional N+/P-diode and P+/N+ diode sink as shown in Figure 5-26 c) which were designed for other purposes (which will not be discussed here). The base-emitter SiGe pn junction is submitted to a forward bias in avalanche regime as a positive voltage is applied through the base and thus light is emitted in the depletion region of the pn junction. As it will be describe in the following section, a silicon nitride waveguide with narrow core is used along with this LED to realize the full optical link as light emission region is expected to be very narrow (only the depletion region of the base-emitter pn junction).

Since the SiGe/Si HBT of this nature has a transition frequency of up to 80GHz, it can be assumed that this will benefit to the speed of the optical source with the base-emitter junction placed in avalanche forward bias mode. With 20%-25% Germanium doping, the emitted wavelength for this design is predicted to be about 850 nm. However the emission will be distributed among Si and SiGe regions depending on the voltage bias applied across the junction.

5.4 Complete Design of On-Chip Optical Links

Figure 5-28 illustrates the design concept of on-chip optical links making use of the features as offered by the SiGe2RF Telefunken GmbH technological process. Three different combinations of optical source, waveguide and detector are chosen by considering the technological process and theories behind for the first study (see Figure 5-28 a) to c)).

The full optical link is composed of silicon-based optical sources, waveguide and detector as describe bellow:

- ***On the detector side:*** The detector is chosen to be an edge SiGe HPT biased in a photodiode mode where the emitter and the base are short-circuited through the capacitor and grounded as shown in Figure 5-27. The capacitance is actually short-circuited as the insulator was not used in between the electrodes of the capacitor, in this specific run, and thus it results two parallel resistances of 50 Ω as shown in Figure 5-27 c). The light is injected through the edge of the HPT and the emitter metal is deposited all over the emitter. The SiGe HPT has a width of 2.4µm and a length of 2.2µm. The base-collector regions are reversed biased to separate the photo-generated electron-hole pairs.

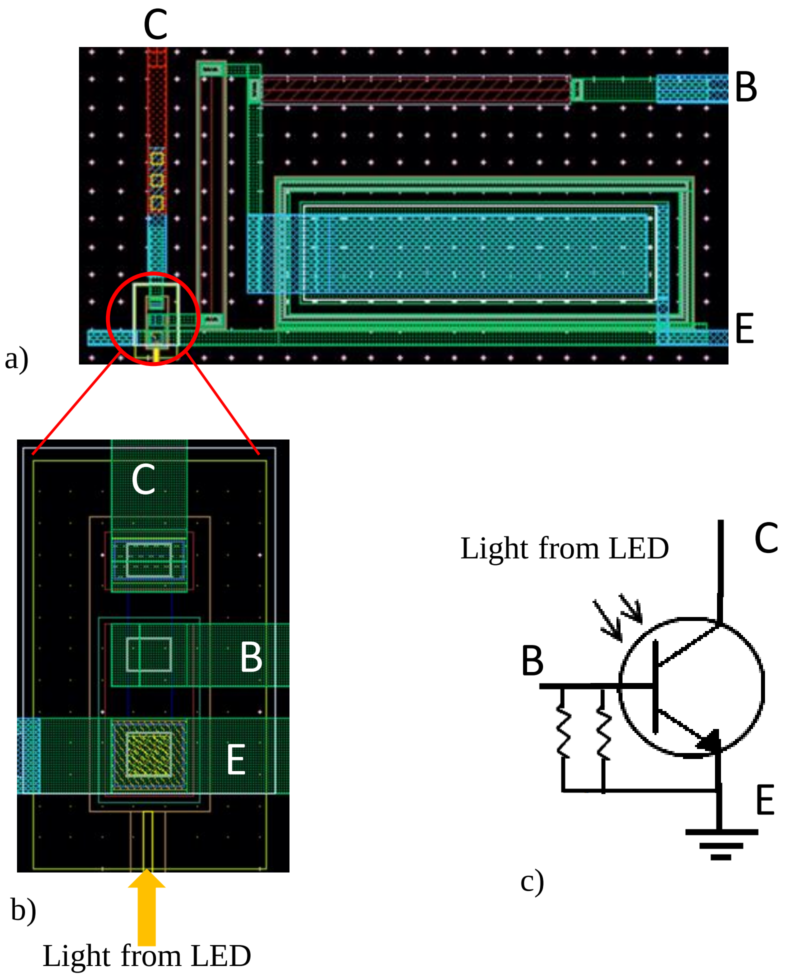

Figure 5-27: The schematic of the detector used at the receiver side of the full optical link.

- ***Optical waveguide:*** The isolation TEOS layers (usually used for RF isolation purposes between RF active components), the poly-Silicon layers and nitride layers are then used as building blocks to obtain optical wave-guiding structures between the optical sources and the detectors. Three different topologies of waveguides (OWGD1, OWGD2 and OWGD3) are envisaged as presented in Chapter 4 section 4.3.2.
- ***On the sources side:*** We implement three different Si or SiGe LEDs described in the last section.

Overall there are 3 different possible sources and 3 different waveguides, which make 9 possible combinations. According to the following table and Figure 5-28, only 3 combinations were fabricated to respect our chip surface limitations (area available for the run). Additional combinations could have been possible to vary the alignment position of the waveguide to the optical source.

Table 5-2: The possible combination of the on-chip full optical link.

LEDs	**Optical waveguide**		
	OWGD1	OWGD2	OWGD3
Si Av N^+NP^+ columnar	**Test structure 1(TS1)**	x	x
SiGe-N+PN LED with collector contact	x	**Test structure 2 (TS2)**	x
SiGe-N+P LED without collector contact	x	x	**Test structure 3 (TS3)**

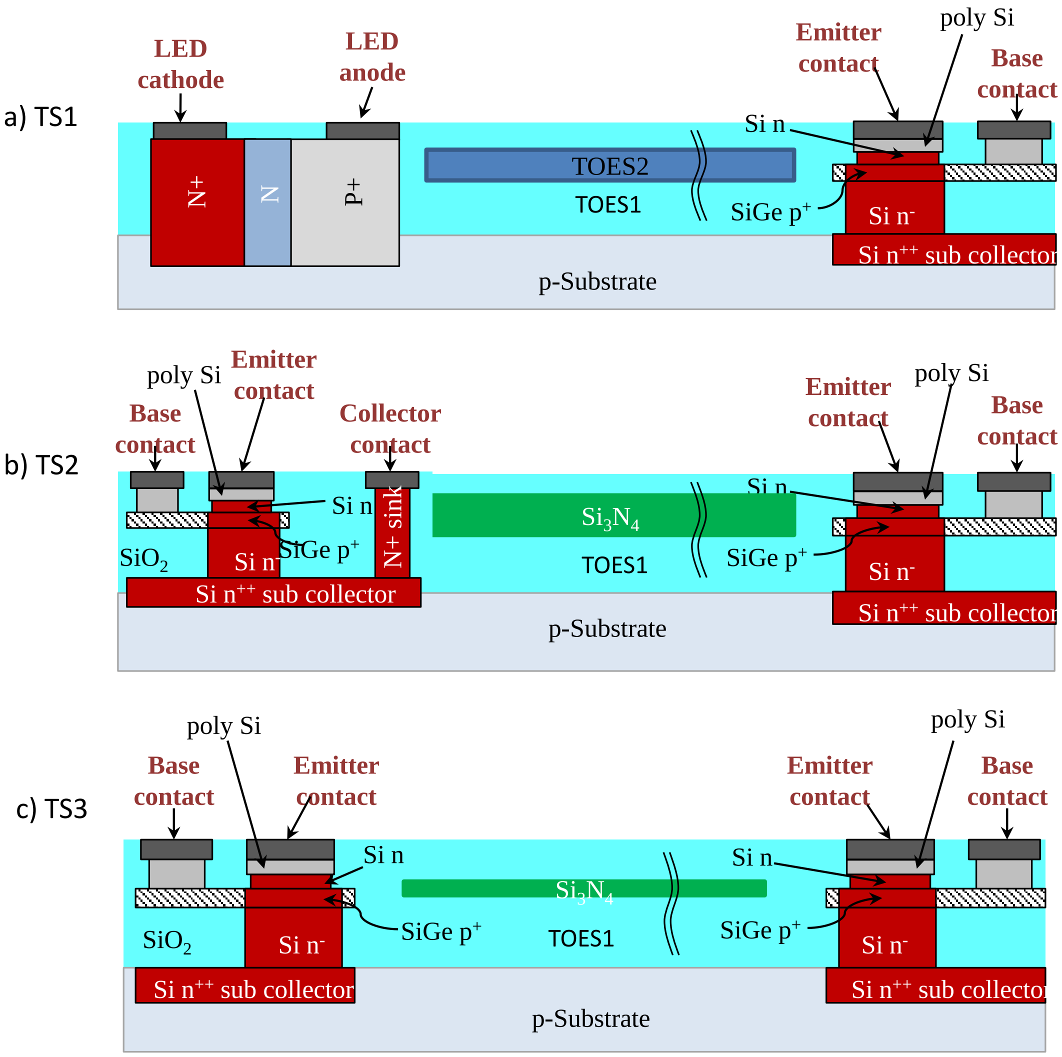

Figure 5-28: Basic designs of the optical links using Si and SiGe Av LED, waveguides and SiGe-based detectors with a) Design test structure 1 (TS1), b) Design test structure 2 (TS2) and c) Design test structure 3 (TS3).

a) Design Test Structure1 (TS1)

The first design Test Structure 1 (TS1) is shown in Figure 5-28 a). On the source side, Si Av n+np+ columnar presented in section 5.3.3 is located laterally on the semi-insulating substrate.

The region between the Si Av LED source and SiGe detector are filled with TEOS plasma deposited oxide waveguide as presented in Chapter 4 section 4.3.2 by Optical Waveguide Design 1(OWGD1).

b) Design Test Structure 2 (TS2)

In our second test structure 2 (TS2) (Figure 5-28 b)), a vertical cubical columnar HPT like structure is used to excite both the base-emitter and base-collector diode in forward avalanche regime (SiGe-N+PN LED with collector contact). A V-shaped groove silicon nitride waveguide design is used in this design, as presented in Chapter 4 section 4.3.2 (Optical Waveguide Design 2, OWGD2), in order to optimize coupling of light with the Si Av LED. The same detector structure design as in TS1 is used in this optical link.

c) Design Test Structure 3 (TS3)

In a third design test structure (TS3) (Figure 5-28 c), a SiGe-N+P LED with an open collector is used as the source. The silicon nitride optical waveguide similar to the one of TS2 but of smaller silicon nitride layer lateral thickness, as presented in Chapter 4 section 4.3.2 (Optical Waveguide Design 3, OWGD3), is used. The waveguide core size reduction enables less modal dispersion in the waveguide.

5.5 Experimental implementation and Results of the optical link

The fabricated on-chip integrated optical link is shown in Figure 5-29a). The device under test is a 750nm-850nm Silicon base avalanche LED die (Wafer) where the light is coupled from the LED optical source through the designed optical TEOS or Silicon Nitride optical waveguide to the SiGe detector.

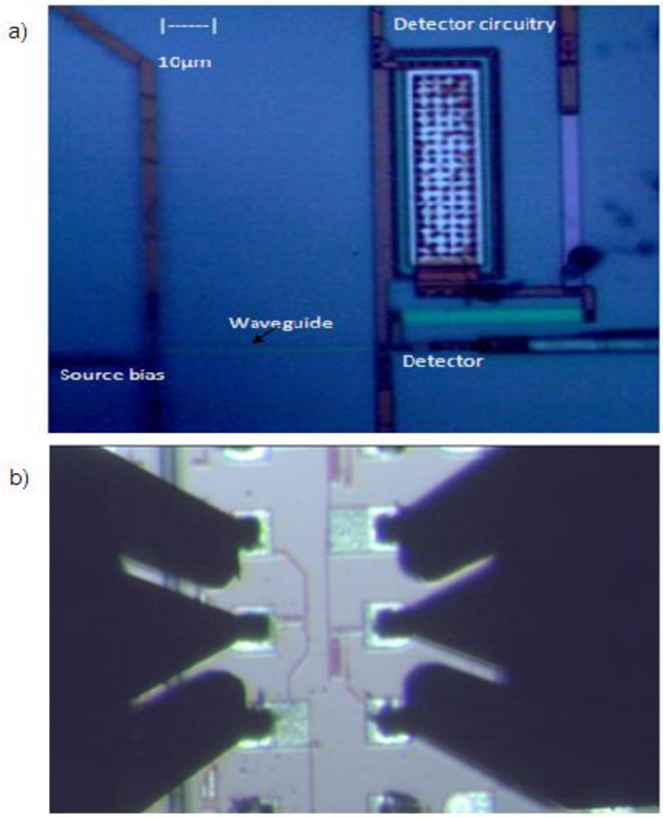

Figure 5-29: (a) Microscopic picture of the optical link device (b) Microscopic picture of G-S-G probe connection on one of the devices during measurement

The RF coupling between the source and the detector in the on-chip optical micro-links are tested and analyzed using a vector network analyzer (VNA) (50 MHz-40 GHz). The experimental setup described in Chapter 2 section 2.3.2 is used to characterize the link (from source via the designed waveguides to the detector). 200µm pitch GSG probes (shown in Figure 5-29 b)) are used to connect the DC and RF input signals to the devices on the die. RF signal and DC biasing are applied on the source and detector sides through GSG probes via VNA internal tee bias. RF signal on the source modulates the optical power emitted from the source.

The optical probing of the three test structures (TS1, TS2 and TS3) of the optical link are as shown below in Figure 5-30.

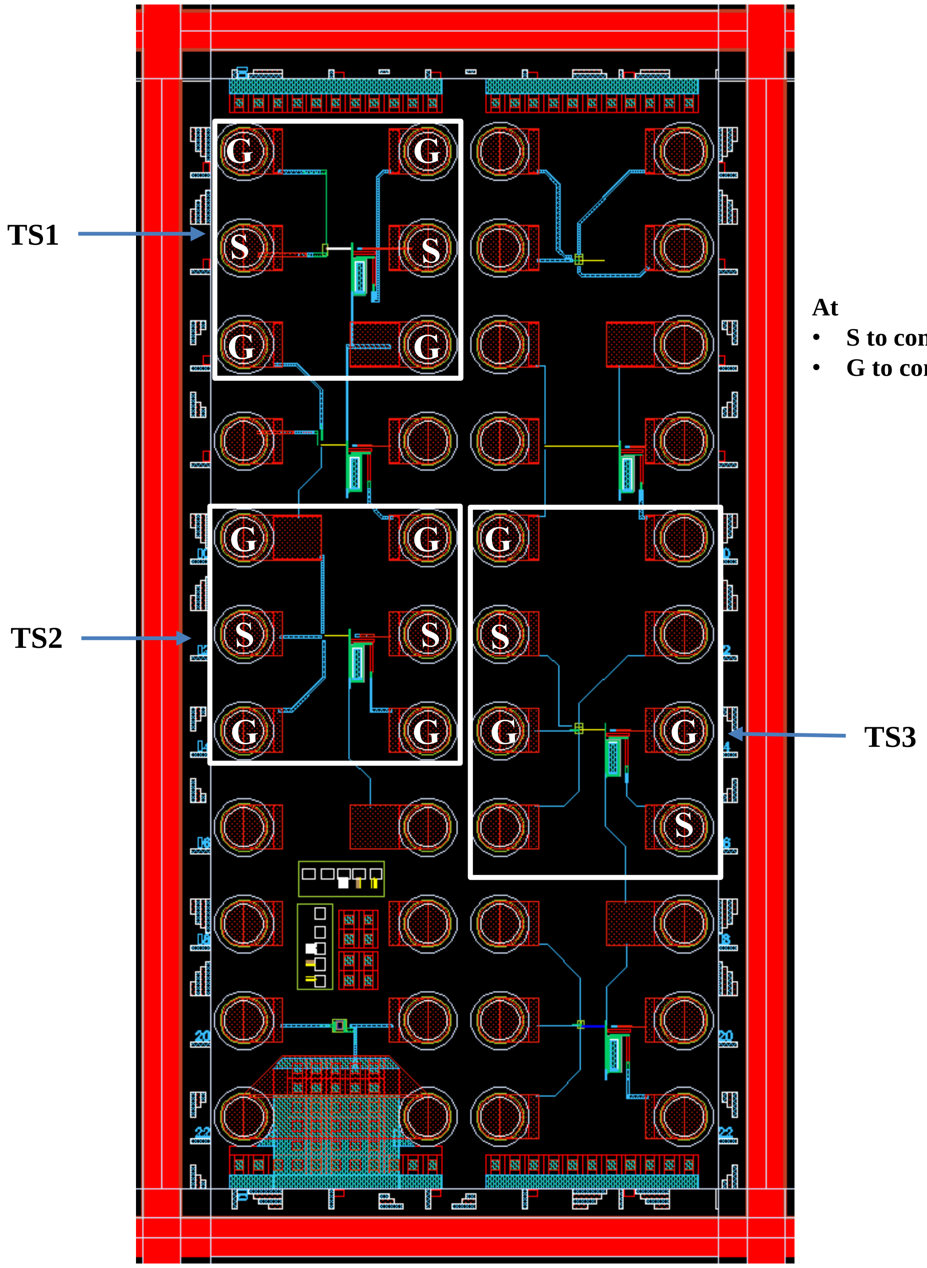

At

- **S to connect dc bias and signal**
- **G to connect the ground**

Figure 5-30: The schematic layout of the three test structures along with their appropriate GSG probe connections during link characterization.

5.5.1 Experimental Results of Test Structure 1 (TS1)

The device under test is a 750nm Silicon base avalanche LED die (Wafer), with a dimension of 1µmx1µm. The light is coupled from the LED optical source through the designed 50µm long TEOS optical waveguides to the SiGe detector. The optical probing of optical TS1 is given in Figure 5-30. The source is forward biased with the cathode (N+ region) connected to the Signal pitch of the GSG probe and the anode (P+) region grounded . The first ground of the probe is connected to the pad of a neighbor circuit on the chip. On the detector side, DC biasing and signal are applied through the collector because the detector emitter and base are short circuited.

a) DC analyses

DC measurement results for TS1 are presented in Figure 5-31. On the source side we put a forward DC bias voltage from -3.8V to 0V and on the detector side a fixed voltage of 2V. Detector link current response is observed simultaneously to the source response (Figure 5-31 b)) when the source is forward biased in avalanche mode as in Figure 5-31 a). The observed detector current is of the order of 10 to 100 nA when the Si Av LED source is activated.

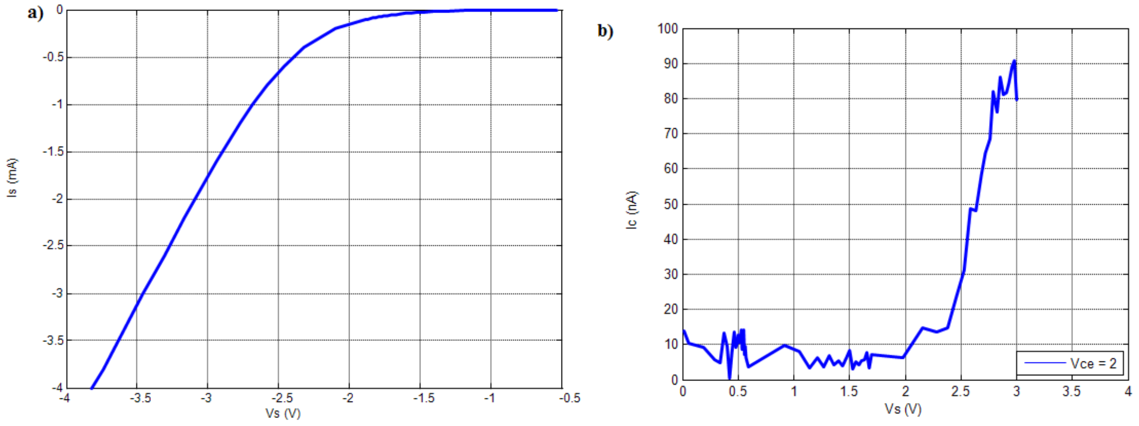

Figure 5-31: DC I-V Curves for TS1 (a) Reverse biased Optical source IV curve (b) Detector optical link current versus source voltage.

In the I-V curves monitored on the detector side, a detector current I_C of about 90nA is detected for a voltage at the source Vs =3V (Figure 5-31). This observation may suggest that the optical transmission through the designed waveguides indeed occurs from the optical source to the optical detector through the Silicon-oxide waveguide.

b) RF analyses

The experimental RF response of test structure 1 when optical source and detector are activated (biasing with Vs=-2.6V on the source and 2V on the detector) is shown in Figure 5-32. Only S21 and S12 (S-Parameters) of the two port network analyzer measurements are presented here versus frequency. It shows low and about equal values for both S21 and S12. This implies that the optical coupling is low and dominated by the substrate parasitic coupling in RF. This indicates that our design philosophy of TEOS 2 yielding higher refractive index (n = 1.48) with thermal annealing process is not successful enough or that the waveguide is misaligned with the optical source. The DC measurements show positive results, however the overall efficiency is not high enough to compete with the RF substrate coupling. However, this area of investigation could be further exploited

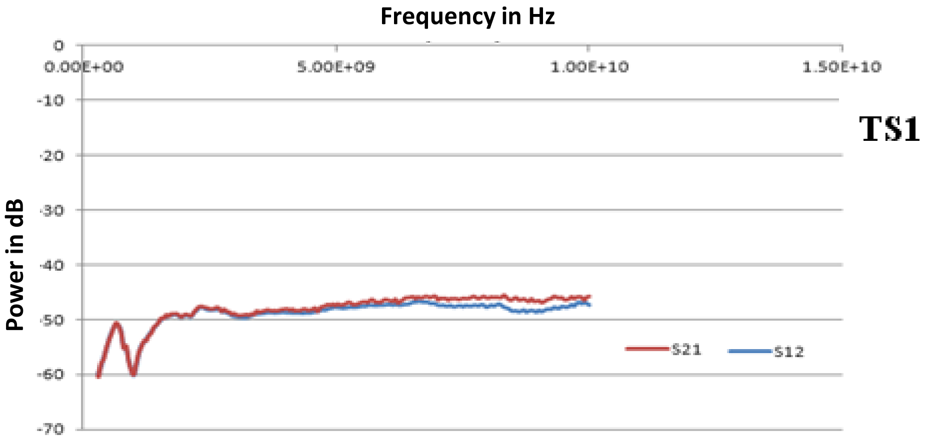

Figure 5-32: RF coupling results for the fabricated on-chip micro-optical links in TS1.

5.5.2 Experimental Results of Test Structure 2 (TS2)

In this test structure the optical source uses an 850nm SiGe-based avalanche LED die (Wafer), with a size of 1µmx1µm. It is mostly an HBT structure biased in a specific regime. The waveguide in this device is a V-shape groove silicon nitride core surrounded by a TEOS oxide of lower refractive index. The light is coupled from the LED optical source through the designed 50µm long silicon nitride optical waveguides to the SiGe detector.

The RF probing of TS2 optical link is as shown in Figure 5-30. On the source side, the emitter and collector contacts are connected to ground while the base is connected to the Signal pitch of the GSG probe. Both the base-emitter and base-collector diode are thus forward biased. On the detector side, the SiGe HPT is biased in the same condition as TS1.

a) DC analysis

To activate the devices under test, we swept on the source side the bias voltage from 0V to 1.4V on the anode (forward biasing) whereas on the detector side a fixed DC voltage of 2V is applied. In the IV curves monitored on the detector side, a detector current I_C of about 90nA is detected for the voltage Vs of 1.3V at the source (Figure 5-33). The measured curves are obtained at both source and detector sides when the optical source is forward biased. It can be seen that, when forward basing the source diode junction, current flows through the device up to about 9mA under 1.4V. The forward bias knee voltage is about 1.2V as shown in Figure 5-33 a). It can be observed that the level of current observed into the collector is similar to TS1, except that the knee voltage is shifted to lower values. This may be attributed to either the coupling substrate as in TS1, or the optical coupling.

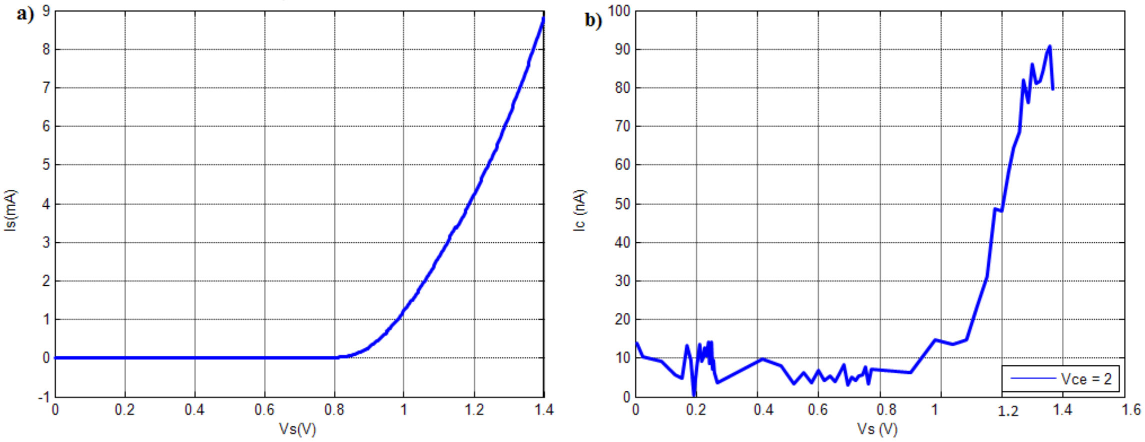

Figure 5-33: DC IV Curves for TS2 (a) Forward biased Optical source IV curve (b) Detector optical link response when source is activated.

b) RF analyses

Figure 5-34 shows the experimental results on test structure TS2 when the optical source is forward biased by 1.2V and reversed biased at the detector by 2V. Again, only S21 and S12 S-parameters are considered here. Our measurement results show a S21 somehow higher than S12 while the two ports have the same output power. This is an indication that an optical coupling is then probably present along the silicon nitride V-groove waveguide in TS2. The higher S12 value observed frequency increase is attributed to parasitic conduction along the semi-insulating substrate. The possibility of electrical coupling through the oxide layers is rejected as it would be several orders lower. Despite the fact that S21 is higher than S12, the difference is too small and as the trends of the curves is the same, it is still uncertain to attribute this to the clear demonstration of the presence of an optical coupling. However, certain design aspects of these structures (TS2) could still be improved.

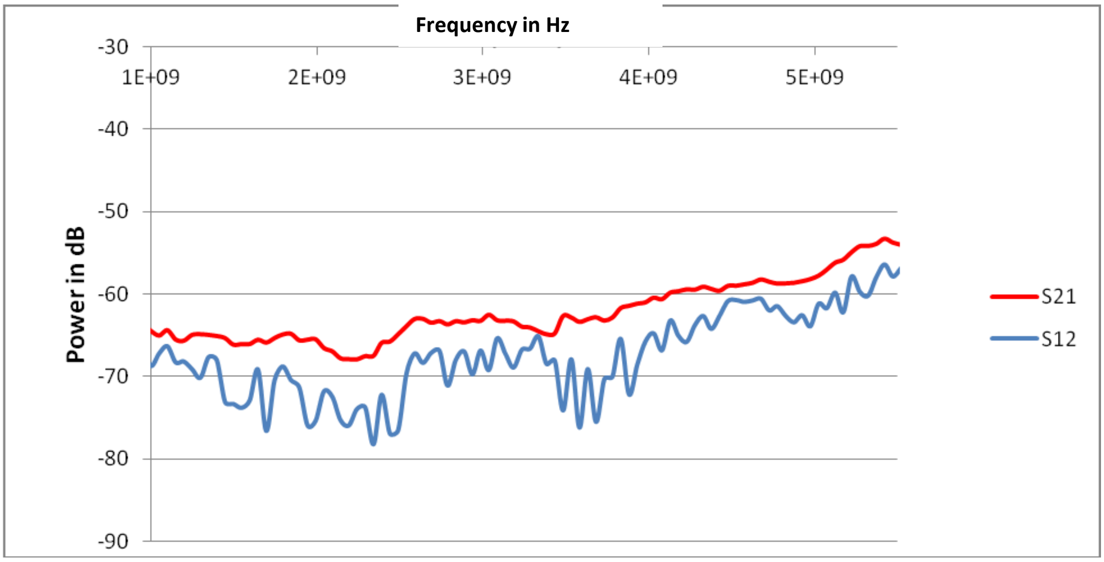

Figure 5-34: RF coupling results for the fabricated on-chip micro-optical links in TS2.

5.5.3 Experimental Results of Test Structure 3 (TS3)

The device under test is SiGe-based avalanche LED die (Wafer), with a size of 1µmx1µm. It is mostly a pn photodiode from HBT structure. The light is coupled from the LED optical source through the silicon nitride optical waveguides to the SiGe detector. The waveguide in this device is a silicon nitride with narrow core of refractive index of (n=2.4) surrounded by a TEOS1 oxide layer with lower refractive index of (n=1.46) and of 50µm length.

The RF probing of TS3 of the optical link is as shown in Figure 5-30. The source has 4 connections in order to have flexible connections. The signal and DC biasing are applied through the base, the emitter is grounded, and the n+ and p+ sink contacts are left open. The first ground of the probe is connected to the pad of a neighbor circuit on the chip. On the detector side, DC biasing and signal are applied through the base, itself short circuited to the emitter (thus emitter contact is left open). The collector is grounded as indicated in Figure 5-30. This situation is different from the previous case. It is expected to reduce the substrate coupling by ensuring a ground voltage of the N+ sub collector region.

a) DC analysis

We swept the source DC bias voltage from 0V to 1.3V (it forward-biases the base-collector junction) and fix the detector voltage at -1V though the base (it is thus +1V Vce). IV curves are shown in Figure 5-35 a) and b). A current of about +0.8mA (Ib=-0.8mA) is detected on the SiGe HPT collector side (in PD mode) at the voltage Vs of 1.3V at the source.

These DC I-V curves are obtained at both source and the detector for this test structure device when the LED source is forward biased. It can be seen that, when the device is placed in a forward bias condition, current flows through the device up to about 7mA. The forward bias knee voltage is about 1.2V as shown in Figure 5-35 a). Such currents are much higher than the 90nA measured in the previous sections. This may indeed be a clear demonstration of an optical coupling from the source to the detector, demonstrating then a good efficiency of the optical waveguides. This observation hence confirms that optical transmission through the designed nitride waveguides indeed occurs from the optical source to the optical detector through the V-groove nitride core waveguide surrounded by TEOS1 layer.

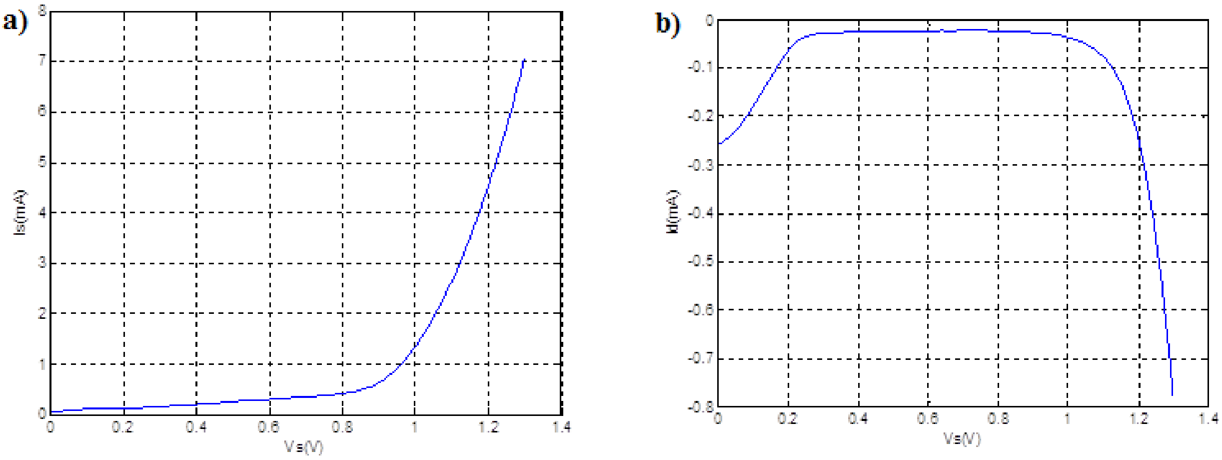

Figure 5-35: DC IV curves for TS3 (a) Forward biased Optical source IV curve (b) Detector optical link response when source was activated for TS3.

b) RF analysis

Results for the RF analysis are given in Figure 5-36. Very interesting and the most promising results are observed in the forward biasing mode of the SiGe junction LED optical source and with the waveguide configuration of Design 3 (OWGD3), when the device structure is forward biased from the SiGe p side and grounded in the n+ region. An optical link loss of only -30dB is then observed, with a sharp fall off towards higher frequencies. Very prominent is the clear difference between S21 and S12 that occurs at the lower frequencies. This large difference shows a clear unilateral transmission which is the characteristics of an optical link. This then clear demonstrate the optical transmission through the structure.

This particular result is attributed to an assumed better alignment of the optical source with the waveguide core. Figure 5-36 a), b) and c) shows the S21 (blue) and S12 (red) for 0.8V, 1.1V and 1.2V bias respectively at source (Vs) of TS3 RF experimental results. We observed that for a source bias of 0.8V S21 values attain -32dB at 100MHz frequency. At 1.1V (Figure 5-36 b), the difference between S21 and S12 is higher than at 0.8V and 1.2V source bias voltages. We then observe that the optical source emission is better at 1.1V bias voltage at source.

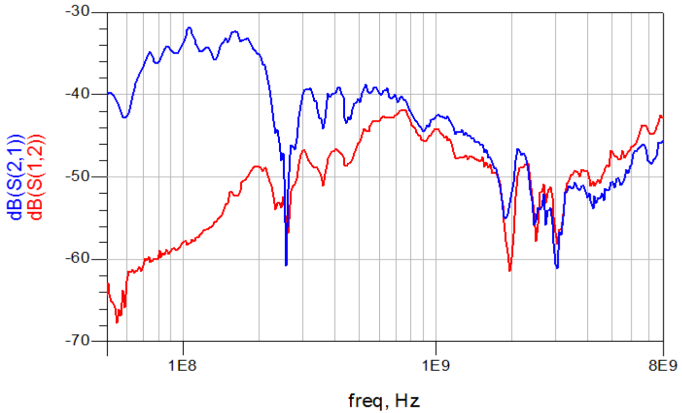

a) Vs=0.8V

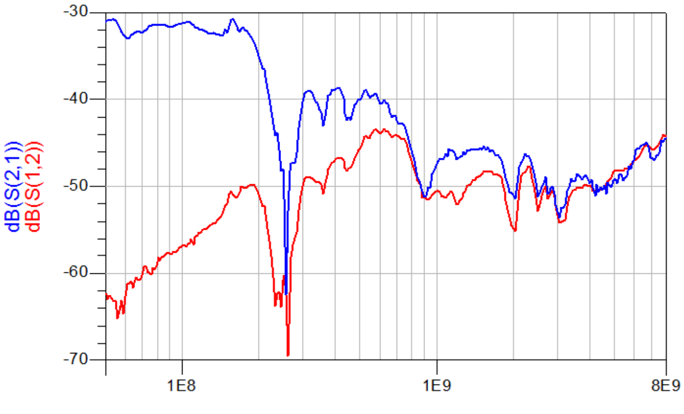

b) Vs=1.1V

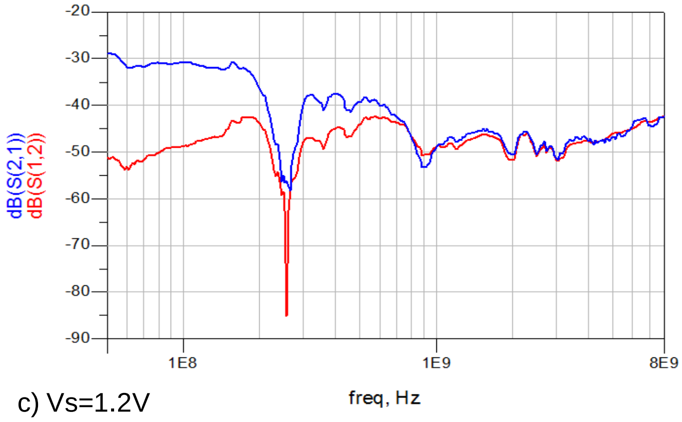

c) Vs=1.2V

Figure 5-36: RF coupling results for the fabricated on-chip micro-optical link of TS3 with the device structure forward biased from the n+ side and the SiGe p region grounded

5.5.4 Synthesis on the full optical link experimental results

We successfully observe that by using the existing SiGe bipolar technology it is possible to develop on-chip optical links that can be deployed in various opto-microwave applications such as sensors. We have studied three different test structures. Our observations are summarized in the table shown below.

Table 5-3: The observations on full optical link experimental studies

Test structure	**Performance**		**Observations**
	I_C	RF	
TS1	90nA at Vs=3V	Not successful	✚ **DC observation:** there is a dc coupling, however in the nA range only. This may be attributed to either substrate coupling or optical coupling. From the RF measurements and from the similitude to TS2 measurements, it seems to be only the substrate coupling. ✚ **RF observation:** The RF transmission is clearly dominated by the substrate coupling. No optical transmission can be demonstrated.
TS2	90nA at Vs=1.2V	Not successful	✚ **DC observation**: the dc coupling is also present. A shift in the voltage knee of the diode curve is observed, potentially due to a change in the biasing influence of the source to the substrate. The amplitude in the detected current is very similar to the TS1. This indicates that indeed only the substrate coupling is observed. ✚ **RF observation:** The RF transmission is clearly dominated by the substrate coupling. Still a slight variation is visible, which may indicate an eventual presence of an optical transmission. But no clear evidence of it can be given.
TS3	0.8mA at Vs=1.3V	successful	✚ **DC observation**: there is a clear dc optical emission, transmission and detection. Photocurrents up to 0.8mA are detected at the output of the link. ✚ **RF observation:** There is a clear and strong Opto-RF transmission through the optical link. A gain of about -30dB up to 100MHz is measured.

5.6 Conclusion

The following major conclusions can be derived from the work presented in this chapter:

The first edge illuminated SiGe/Si HPT was designed and fabricated by using the existing SiGe BiCMOS technology. A two-step post fabrication process was used to create an optical access on the edge through successive smooth and full dicing techniques. A low frequency opto-microwave responsivity of 0.45A/W and an opto-microwave cutoff frequency of 890MHz were measured. Compared to top illuminated HPT, edge illuminated HPT improves the cutoff frequency by more than a factor two and also improves the responsivity from 0.32A/W (for 10x10µm^2 HPT) to 0.45A/W. Compared to the top illuminated HPT of the same size (5x5µm^2 HPT), the edge illuminated HPT improves the f_{-3dB} by a factor of more than two and it also improves the low frequency responsivity by a factor of more than four, while using a simple lensed MMF fiber for the coupling. This phototransistor could be used in further microwave photonic applications whose operating frequency could lie in the 1-10GHz range where integration to Si Integrated Circuits (ICs) and costs are the main issues. Further optical coupling structures could improve the performances. However, these results already demonstrate that a simple etched HPT is still enough to achieve improvements compared to the top illuminated HPT without the need of complex coupling structure, even when using MMF. We have also observed the impact of the substrate photodiode and metal proximity effect on the performances of edge illuminated SiGe HPTs. These results will have a clear adding value to some further design optimization of the device. Finally, the substrate photodiode influence is minimized in laterally illuminated structure when compared with top illumined one.

The chapter then conducted some investigation toward a full integration of an optical link on the same chip. The major advantages of using 750nm wavelength are the ease of integration of optical source, waveguide and optical detector all in Silicon, thus all on the same chip.

We have demonstrated a full optical link integrated in the SiGe bipolar technology of study. Different structures were tested. A successful demonstration was obtained with a forward biased SiGe/Si avalanche LED source coupled to a SiGe HPT in photodiode mode through a Si_3N_4/SiO_2 optical waveguide., leading to total link budget to about -30dB, at even low power consumption rates, since only 1V and few mAs are required to operate these devices. However substantial further development works still need to be performed. Quite good first iteration optical coupling from source to detector has been demonstrated from this work at both DC and AC levels.

This SiGe/Si fully integrated optical link technology offers wide application possibilities for diverse micro-sensing and microwave photonic system development.

Thesis conclusion and Prospects

I. Conclusion

With the recent explosive growth of connected objects, for example in Home Area Networks (HAN), the wireless and optical communication technologies start to merge further, through the interdisciplinary domain called Microwave photonic technology (MWP). The advantage of MWP systems is that they can benefit from the strengths of both optical and wireless technologies, such as the inherently large bandwidth of optical fiber and unused bandwidth in the mm-wave wireless spectrum. For this reason, a hybrid system has the potential to provide very high data transmission rates with minimal time delay. Moreover, MWP technology has recently extended to address a considerable number of applications [11] including 5G mobile communication, biomedical analysis, Datacom, optical signal processing and for interconnection in vehicles and airplanes. Many of these novel application areas also demand high speed, bandwidth and dynamic range at the same time they require devices that are small, light and low power consuming. Furthermore, implementation cost is a key for the deployment of such MWP systems in home environment and various integrated MWP applications, becoming more and more sensitive when the application is closer to the end user. This is especially the case for Home-Area-Networks using an optical infrastructure, but also sensing applications where sensors could be widely deployed in large numbers.

This PhD work focused on the development of very cheap, Bipolar and BiCMOS integrated SiGe/Si MWP devices such as SiGe HPTs, Si LEDs and SiGe LEDs, and focused on the combined integration of mm wave and optoelectronic devices for various applications involving short wavelength links (750nm to 950nm).

Compared to bulk CMOS, the BiCMOS SiGe HBT presents a much higher cut-off frequency at a given technology node. To reach similar cut-off frequencies, bulk CMOS designs have to use much smaller process nodes, forcing compromises on the design and leading most of the time to overall lower performances and higher cost. It is also possible to develop some efficient detectors in the wavelength range from 750nm to 900nm, as high speed SiGe phototransistors were demonstrated since 2003 in bipolar and BiCMOS industrial process. Silicon is also a material of choice to integrate optical waveguides, electrical transmission lines and active devices simultaneously up to the millimetric waves. Therefore SiGe Bipolar or BiCMOS technologies are good candidates to implement MWP systems. The improvement of the SiGe HPTs, the further development and convergence of electrical transmission lines and optical waveguides for intra- and inter- chips interconnects, are steps to create complete RoF transceiver on a Silicon platform including a high speed VCSEL for the sources, ultimately targeting an monolithic integrated optoelectronic receiver and strongly integrated transmitter. A last step covered by the PhD is then the investigation of more futuristic Silicon-based optical sources directly integrated in the bipolar process. It is also important to note that, despite single mode fiber would be highly suitable to improve performances, this work kept focused on the compatibility to multimode optical fibers as this one is still yet the required standard for Home-Area-Networks.

In this research, we have chosen the SiGe2RF Telefunken GmbH SiGe Bipolar technology to implement SiGe/Si MWP devices (SiGe HPT, Si and SiGe LEDs and optical waveguide) demonstrating as well a complete on-chip optical link. The fabrication of MWP devices using this technology does modify neither the vertical stack of layers nor the masks set that is used. Only combination of existing layers and masks is done using the standard SiGe2RF HBT mask set. This ensures the direct integration with the technological process and the potential integration of complete opto-electronic radio frequency (OE-RF) circuits

SiGe HPTs have also the advantage to combine a PIN photodiode with an HBT, thus lowering the output impedance and making easier the match to the other components of the electronic circuits. Indeed, it avoids the need of a Trans-impedance Amplifier (TIA). The other advantages of HPT is the presence of three terminals (optical access, base, collector) which permits original function such as mixers and self-oscillators that are not described in this PhD, but are perspective for OE-EO circuit designers.

The basic HPT structure is designed by extending the emitter, base and collector layers of the reference HBT. The optical injection is made through the emitter for top illuminated HPT structure. The light path goes through the oxide and polysilicon layers of the emitter before entering the Si emitter, SiGe base and Si collector regions. To obtain edge illuminated SiGe HPT structure we perform a post fabrication process through smooth dicing and subsequent full dicing. Those HPT are essentially large HBTs whose emitter metallization only partially covers the emitter region. The substrate is grounded through a p+ guard ring region to control the substrate photocurrent (mainly holes) influence on the HPTs dynamic behavior.

On the source side, we implement Si and SiGe LED optical sources using the same technology with appropriate electrical contacts in order to apply a forward bias at the p+ n junction so that the light emission occur near the surface region of n region and extend more or less laterally across the whole region. We use the presence of several oxide and nitride layers in the technological process to design the Si_3N_4 or TOES optical waveguides. The full optical link was designed by interconnecting a SiGe LED and edge-SiGe HPT using an nitride optical waveguide.

Main conclusions drawn in the chapters of this PhD are synthesized as given below:

Different methods of characterizing top and edge illuminated HPTs were presented in Chapter 2. De-embedding is crucial to extract the effect of the bench fixtures like the RF probes and the optical probing link in order to know the exact opto-microwave behavior of the phototransistor. The dc photocurrent analysis of a phototransistor both in photodiode and phototransistor modes helped us to understand the physical behavior of SiGe/Si HPTs and the impact of the chosen geometrical parameters. Extracting the substrate effect from the intrinsic phototransistor response and determining the different photocurrents contribution (primary photocurrent, optical amplification, base efficiency) was also an important topic in order to observe the intrinsic behavior of the SiGe/Si HPTs. Extracting the junction capacitances and transit times was an additional important part of this work as they will be used in the future electrical/opto-microwave modeling of the SiGe phototransistors and as it provides further physical information on the behavior of photogenerated carriers for further HPT design optimizations.

In Chapter 3 top illuminated SiGe HPTs of different optical window sizes were designed and characterized in terms of DC, electrical and opto-microwave behavior at different biasing points. This analysis allowed us finding an optimum bias point that maximizes the frequency response of the HPT including opto-microwave gain, cutoff frequency and optical transition frequency. From the microwave behavioral study we measure an electrical transition frequency f_T value of 50GHz for $10x10\mu m^2$ HPT which is the same value as pure non SIC HBT technology. However, we measure an electrical transition frequency of only 26.5GHz for $3x3\mu m^2$ HPT. This unusual behavior is due to the 2D electrical extension effect which is directly related to the built in potential. This effect has been demonstrated through various mathematical models. A proper design rules is then proposed to get a symmetric contacts on the collector, base and emitters so that the electrical field will be more vertical; and also to fragment the HPT in smaller individual HPTs as the electrical extension may reach a limit in its increase. We have also carried out OM SNOM and DC SNOM analysis at their optimum biasing conditions as they are crucial to understand the impact of SiGe HPTs structure. OM SNOM analysis allowed the extraction of an opto-microwave response at each position of the optical illumination over the device. DC SNOM analysis allowed the extraction of substrate photocurrent at each optical probe position. It has a great impact on the responsivity and speed of the SiGe HPT. The substrate effect is more visible in the PD mode operation than in the HPT mode where it is hidden by the transistor effect. We observe that the intrinsic optical transition frequency f_{Topt} is much lower than the electrical transition frequency f_T. It is explained by the addition of capacitive and transit time terms related to the photodetection mechanism in the intrinsic transistor and substrate region of the structure. The opto-microwave capacitance and transit time terms are increased by more than a factor of 3.5 and 21 respectively when compared with their electrical equivalent values. We have also observed that the performance of SiGe/Si HPT is highly affected by the level of the injected optical power. This could be related to self-biasing of the HPT with the optical power and also related to the variation of the modes of the optical source under use (and thus the illumination pattern). The complete HPT opto-microwave capacitance and transit time terms are increased with decreasing the injected optical power level. We were able to demonstrate an intrinsic optical transition frequency of 6.5GHz and absolute responsivity of up to 0.8A/W for 10x10µm^2 HPT which has the best performance compared to other optical window size HPTs.

Then in Chapter 4, for future intra /inter chip hybrid interconnections, we have successfully designed polymer based low loss microwave transmission lines and optical waveguides on low resistive silicon substrate. It is a step to envisage further silicon-based platforms where SiGe HPT could be integrated at ultra-low cost and high performances with other structures such high-speed VCSEL to build up a complete optical transceiver on a silicon optical interposer. The polymer is used as dielectric interface between the line and the substrate for electrical interconnections and to design the core and cladding of the optical waveguide. Coplanar, microstrip and grounded coplanar lines based on SU8, BCB and Parlyene have been investigated and designed in the mm wave frequency range. Grounded coplanar and microstrip lines have less attenuation than coplanar line as the metallic ground prevents the propagation of electric field into the lossy silicon substrate. The targeted characteristic impedance for all types of line was 50Ω. The inclusion techniques of optical waveguide with mm microwave transmission lines are also presented. The interconnections of mm wave lines on silicon and polymer are analyzed through HFSS simulation. This study provides an input for the future integration of mm and optical waves within a single chip or for interconnections between several chips. About 1dB/mm attenuation in the millimeter wave frequency range was experimentally measured for a coplanar waveguide structure. This of course indicates that our design optimized using HFSS software is well suited even though the fabricated structure was not good enough.

In Chapter 5, the first BiCMOS compatible edge illuminated SiGe/Si HPT was then successfully designed and fabricated by using the standard SiGe Telefunken bipolar technology coupled to a multimode fiber. A two-step post fabrication process was used to create an optical access on the edge through polishing and dicing techniques. A low frequency opto-microwave responsivity of 0.45A/W and opto-microwave cutoff frequency of 890MHz was measured. Compared to top illuminated HPT, edge illuminated HPT improves the cutoff frequency by more than a factor two and also improves the complete responsivity from 0.32A/W (for 10x10µm^2 HPT) to 0.45A/W. The impact of the substrate photodiode is minimized in lateral illuminated case by a factor of 2.4 times. Compared to the top illuminated HPT of about the same size (5x5µm^2 HPT), the edge illuminated HPT improves the f_{-3dB} by a factor of more than 2.5 and also improves the low frequency responsivity by a factor of more than four while using a simple lensed multi-mode fiber (MMF) for the coupling. This phototransistor could be used in further microwave photonic applications whose operating frequency could lie in the 1-10GHz range where integration in Si Integrated Circuits (ICs) and costs are the main issues. Further optical coupling structures could improve the performances. However, these results demonstrate that a simple etched HPT is still enough to achieve improvements compared to the top illuminated HPT without requiring a complex coupling structure, even when using MMF. We have also observed the impact of the substrate photodiode and of the metal proximity on the performances of edge illuminated SiGe HPTs.

The design and fabrication of the first full optical link based on SiGe BiCMOS technological process was presented in Chapter 5 as well. It was a collaboration work between ESYCOM-ESIEE Paris and the team of Pr.Snyman in South Africa, in the University of South-Africa (UNISA) and formerly in the Tshwane University of Technology (TUT). We have designed three different optical links comprising Si or SiGe AvLED on the source side, Si_3N_4 or TSOE optical waveguide and SiGe HPT on the detector side. In particular, the use of Si-Ge technology detector in association with Si AvLEDs demonstrates potential incorporation of these devices in standard CMOS technological process. Our proposed use of TEOS and silicon nitride based waveguides which were fabricated thanks to the advanced capabilities offered by the SiGe bipolar BiCMOS process technologies, permits to design a wide variety of optimized waveguide structures between the optical source and the detector on the chip.

The designed silicon based optical waveguides use the advantage of the oxide layers existing in SiGe BiCMOS technology. The optical waveguide associated to the choice of 0.75µm to 0.85µm operating wavelength may show new routes of both developments and applications in silicon photonics technology, or at least permit an important spin-off of this technology towards low cost ease of fabrication. The major advantage of using 750nm wavelength is the integration ease of optical source, waveguide and optical detector all in a same chip; this implies a simplification of design and processing procedures.

We have shown the forward biased micro-dimensioned SiGe/Si light sources have achieved high optical emissions, leading to reduced total link budgets to about -30dB, at even low power consumption rates, since only 1V and few mA are required to operate these devices. However substantial further development works still need to be performed. Quite good first iteration optical coupling from source to detector has been demonstrated from this work at both DC and AC levels. This full optical link technology offers wide application possibilities for diverse micro-sensing and microwave photonic systems in which optical communication and data transfer play an important role.

II. Perspectives

The perspectives of this thesis are presented as follows:

Concerning the SiGe HPT:

- For the detection of optical signals in MWP systems, photodetector technologies with high responsivities, large bandwidths and high optical power handling capabilities are required. The raw SiGe phototransistor optical transition frequency (f_{Topt}) is ultimately shadowed by its substrate photodiode carriers' transient time and other intrinsic factors, such as the junction capacitances. Thus, a solution to get rid of the substrate contribution in the top illuminated HPTs could be through a proper design of the optical window with a metallic diaphragm avoiding the illumination of the substrate photodiode. Indeed, the substrate photodiode would be hidden either by metallic contacts or by upper layers of the intrinsic HPT. One could also consider in the future design that edge illuminated structures minimizes the influence of substrate diode, but still it needs extra techniques to avoid completely. Alternatively taking advantage of the substrate could be envisaged leading to combined HPT+PD structure.
- To improve the optical transition frequency (f_{Topt}) and the opto-microwave cutoff frequency (f_{-3dB}) of SiGe HPT, it would be important to reduce the electrical transit times and the optical induced terms. One direction is to consider higher f_T/f_{max} technologies like STMicroelectronics (230GHz/280GHz) or IHP (300GHz/500GHz). The second direction is to optimize the design of the HPT, and especially engineering the 2D configuration of the electrical field distribution within the HPT. A proper position of the base and collector contacts is a key direction, together with the size optimization.
- Low noise HPTs are very useful in certain MWP applications such as optoelectronic oscillators, tunable and reconfigurable filters and photonic beamforming. Further characterization of the SiGe HPT in terms of noise would be then important as well.
- These phototransistors could also be implemented in applications where a single mode fiber is used at 850nm. Characterizing the device through single mode with a smaller spot optical probe could be important for such applications. This activity is ongoing.
- Compact circuit modelling could bring clear information for future design aspects of the HPTs.
- Increasing the operating frequency of SiGe photodetectors into the millimeter wave range (60GHz) would be very useful in certain MWP applications. While being an ambitious goal, a potential direction would be to develop a phototransistor structure overcoming the frequency limitation of traveling wave HPT. For this purpose the interaction between optical and electrical waves have to be analyzed in further detail through physical and EM simulations.

Concerning the optical source and full optical link:

- We demonstrated in this thesis that the SiGe Av LEDs, the waveguide and the detector technology provides a cutoff frequency of more than 200MHz. However, this still needs to be improved through the proper design of the overall link.
- The physical behavior of Si Av LEDs and SiGe Av LEDs needs to be studied using commercial software simulators. Performing the equivalent circuit or physical modelling of the individual devices of the link will provide important information for future design. Improve the coupling efficiency to the optical waveguide is also an important issue.

Concerning the polymer based interconnections:

- We found a promising experimental result for coplanar waveguide structure even though the fabricated line was not good enough due to technical limitations. Further process developments are still needed. Thus, fabricating the waveguides (optical and electrical waveguides) with appropriate technological process using the designed layout proposed in this thesis and characterization it for its validation is crucial.

Moreover, further work is still required for the hybrid integration of VCSELs, HPTs, antenna units, and electrical and optical interconnections on silicon wafer for low cost MWP applications.

Personal scientific Publications

Journals and Articles

[1] **Z. G. Tegegne**, C. Viana, M. Rosales, J. Scheillein, J.-L. Polleux, C. Algani, M. Grzeskowiak and E. Richalot, “An 850nm SiGe/Si HPT with a 4.1GHz maximum Optical Transition Frequency and 0.805A/W Responsivity”, in International journal of microwave and wireless technologies, 2015, dio: 10.1017/S17907875001531.

[2] **Z. G. Tegegne**, C. Viana, J.-L. Polleux, M. Grzeskowiak, E. Richalot “Edge illuminated SiGe Heterojunction Phototransistor for RoF applications” in IEEE/IET Electronics Letters, Vol.51, Iss.8, p. 1906-1908, 2015.

[3] C. Viana, **Z.G. Tegegne**, M. Rosales, J.L Polleux, C. Algani, V. Lecocq, C. Lyszyk, S. Denet, “A hybrid photo-receiver based on SiGe Heterojunction Photo-Transistor for low cost 60GHz Intermediate-Frequency Radio-over-Fiber Applications” in Electronics, Vol.51, No.8, pp.640-642, 2014.

International Conferences with proceedings

[4] **Z. G. Tegegne**, C. Viana, M. Rosales, J.-L. Polleux, C. Algani, M. Grzeskowiak, E. Richalot, "Substrate diode effect on the performance of Silicon Germanium phototransistors",in IEEE International topic meeting on microwave photonic, Cyprus, 2015.

[5] **Z. G. Tegegne**, C. Viana, J.-L. Polleux, M. Grzeskowiak, E. Richalot “Improving the opto-microwave performance of SiGe/Si Phototransistor through edge illuminated structure” in PhotonicsWest 2016 conference, Paper 9752-44, San Francisco, 13-18 Feb 2016.

[6] K. Ogudo, L. W. Snyman, J.L Polleux, C. Viana, **Z.G .Tegegne,** D. Schmieder, “Towards 10 – 40 GHz on-chip micro-optical links with all integrated Si Av LED optical sources, Si N based waveguides and Si-Ge detector technology“ in PhotonicsWest 2014 conference, Paper 8991-7, San Francisco, 1-6 Feb 2014.

[7] K. Ogudo. A, L.W. Snyman, J.L. Polleux, C. Viana, **Z.G Tegegne**, “Realization of 10 GHz minus 30dB on-chip micro-optical links with Si-Ge RF Bi-Polar technology”, in Proceeding of SIPEE, Vol.9257, Republic of South Africa; May 2014

National conferences with proceedings

[8] **Z.G. Tegegne**, C. Viana, M. Rosales, J.L. Polleux, M. Grzeskowiak, E. Richalot, C.Algani “Impact du substrat sur les performances de phototransistors microondes SiGe/Si” 19emes Journees Nationales Microondes, Bordeaux, May 2015.

References

[9] IEEE 802.11 standards Tutorial http://www.radio-electronics.com/info/wireless/wi-fi/ieee- 802-11-standards-tutorial.php

[10] Carlos Viana "Technological development and system integration of VCSELs and SiGe HPT receivers for 60GHz low cost Radio-over-Fiber applications" Universite Paris-Est, Ecole Doctorale MSTIC, PhD Thesis 2014.

[11] Stavros Iezekiel and Maurizio Burla "RF Engineering Meets Optoelectronics Progress in Integrated Microwave Photonics" IEEE Microwave Magazine, 1527-3342, September 2015.

[12] http://www.radio-electronics.com/info/wireless/wi-fi/ieee-802-11n.php

[13] High Rate 60 GHz PHY, Mac and HDMI PAL, Standard ECMA-387, ECMA international December 2010.

[14] Part 15.3: Wireless MAC and PHY Layer Specifications for High Rate Wireless Personal Area Networks (WPANs): Amendment 2: Millimeterwave based Alternative Physical Layer Extension, IEEE P802.15.3c/D13 July 2009.

[15] Wireless Gigabit Alliance (WiGig), http://wirelessgigabitalliance.org

[16] NAVAIR Electronic Warfare/Combat Systems "Electronic Warfare and Radar Systems Engineering Handbook" NAWCWD TP 8347, April 1997.

[17] Christian Rumelhard, Catherine Algani, Anne Laure Billabert "Microwave Photonic Links components and circuits" Book first published 2011 in Great Britain and the United states.

[18] J. Guillory et al., "60GHz Intermediate Frequency over Fiber using a passive Multipoint-to-Multipoint architecture", 16th European conference on Networks and Optical Communications, July 2011.

[19] V. Sorianello, G. De Angelis, A. De Iacovo, L. Colace, S. Faralli, and M. Romagnoli "High responsivity SiGe heterojunction phototransistor on silicon photonics platform" Optics Express, Vol. 23, No. 22, Nov 2015.

[20] B. J. Thibeault, K. Bertilsson, E. R. Hegblom, E. Strzelecka, P. D. Floyd, R. Naone, and L. A. Coldren, 'High speed characteristics of low optical loss oxide apertured vertical cavity lasers", IEEE Photonics Technology Letters, Volume 9, pp.11–13, 1997.

[21] Y. Satuby, and M. Orenstein, "Limits of the modulation response of a single-mode proton implanted VCSEL", IEEE Photonics Technology Letters, Volume 10, pp.760–762, 1998.

[22] K. L. Lear, V. M. Hietala, H. Q. Hou, M. Ochiai, J. J. Banas, B.E. Hammons, J. C. Zopler, and S. P. Kilcoyne, "Small and large signal modulation of 850 nm oxide-confined Vertical-Cavity Surface-Emitting Lasers", Summaries of Papers Presented at the Conference on Lasers and Electro-Optics (CLEO '97), Volume 15, pp.69–74, 1997.

[23] Dyan Ali et al "High Speed SiGe pin W-Structure Photodetectors at Telecommunication Wavelengths Grown Directly on Si" Conference on Quantum Electronics and Laser Science, IET, pp.1-2, 2008 San Jose, CA.

[24] Henry C. Lee et al "A Novel High Speed Silecon MSM Photodetector oprating at 830nm wavelengh" IEEE Electronic Device Letters, Vol.16, No.5 May 1995.

[25] Papichaya Chaisakul et al "10 GB/s Ge/SiGe Multiple Quantum Well Waveguide Photodetector" IEEE Photonics Technology Letters, Vol.23, No.20, October 15, 2011.

[26] Yoshihiro Yoneda, Ryuji Yamabi, Sosaku Sawada, and Hiroshi Yano "Large-area Top-Illuminated InP-Passivated Mesa-type InGaAs pin Photodiodes for High-bit-rate Multi-mode Fiber Applications" IEEE OFC/NFOEC, pp. 1-3, San Diego, CA 2008.

[27] Lingzi Zhang et al "Wavelength Tunable Si Based InGaAs Resonant cavity enhanced photodetectors using Sol-Gel Wafer bonding technology" IEEE Photonic Technoloy Letters, Vol.23, No.13, July 1, 2011.

[28] Xiaofeng Duan, Yongqing Huang, Xiaomin Ren, Yufeng Shang, Xinye Fan, and Fuquan Hu "High-Efficiency InGaAs/InP Photodetector Incorporating SOI-Based Concentric Circular Subwavelength Gratings" IEEE Photonics Technology Letters, Vol. 24, No. 10, May 15, 2012.

[29] D.Wake, S. Dupont, C. Lethien, J.-P. Vilcot and D. Decoster, ‘‘Radiofrequency transmission of 32-QAM signals over multimode fibre for distributed antenna system applications’’, Electron. Lett., vol. 37, 1087–1089, 2001.

[30] Stavro Iezekiel "Microwave Photonics Devices and Applications" Department of Electrical and Computer Engineering, University of Cyprus, Cyp. Published 2009.

[31] R. J. Deri, "Monolithic integration of optical waveguide circuitry with 111-V photodetectors for advanced lightwave receivers," J. Lightwave Technol., vol. 11, pp. 1296-1313, 1993.

[32] J. G. Bauer, C. Lauterbach, D. Romer, N. Emeis, L. Hoffman, and G. Ebbinghaus, "Monolithic integration of a waveguide InGaAsflnP pin photodiode with a locally ion implanted JFET for receiver OEIC applications," Proc. Inst. Elect. Eng., vol. 140, pp. 66-70, 1993.

[33] P. R. Berger, N. K. Dutta, J. Lopata, S . N. G. Chu, and N. Chand, "Monolithic integration of GaAs and Ino.zGao.8As lasers by molecular beam epitaxy on GaAs," Appl. Phys. Lett., vol. 58, pp. 2698-2700, 1991.

[34] J. F. Vincbant, J. P. Vilcot, J. L. Lorriaux, and D. Decoster, "Monolithic integration of a thin and short metal-semiconductor-metal photodetector with a GaAlAs optical inverted rib waveguide on a GaAs semi-insulating substrate," Appl. Phys. L.ett., vol. 55, pp. 1966-1968, 1989.

[35] W. P. Hong, G. K. Chang, R. Bhat, C. Nguyen, and M. Koza, "Monolithically integrated waveguide-MSM detector-HEMT amplifier receiver for long-wavelength lightwave systems," IEEE Photon. Technol. Lett., vol. 3, pp. 156-158, 1991.

[36] F. J. Leonberger and J. P. Donnelly, "Semiconductor integrated optic devices," in Guided- Wave Optoelectronics, T. Tamir, Ed. New York Springer-Verlag, vol. 26, pp. 3 17-395, 1990.

[37] H. Nishihara, M. Haruna, and T. Suhara, "Passive waveguide devices," in Optical Integrated Circuits, R. E. Fischer and W. J. Smith, Eds. New York: McGraw-Hill, 19139, pp. 245-281.

[38] R.M. Barrett and M. H. Barnes "Microwave Printed Circuits" Radio and TV News (Radio-electronic Engineering section), Vo.46, pp.16-31, September 1951.

[39] Khaled Elgaid, David L. Edgar, David A. McCloy, Iain G. Thayne "CPW Interconnects for MMIC Applications on Low Resistivity CMOS Grade Silicon Using Micromachined SU8 Negative Resist" IEEE EuMA, pp.1-4, Milan, Sept 2002.

[40] D.D.Grieg and H.F. Engelmann "Microstrip –A New Transmission Technique for the Kilomegacycle Range" Proc, IRE, V.40, December 1952, pp.1644-50.

[41] K.C. GUPTA, R. GANG, J.J. BAHL. "Microstrip Lines and Slotlines". Norwood (USA): Artech House Publishers, 1996, 2nde edition, 560 pages.

[42] Laurent Martoglio, Elodie Richalot, Gaelle Lissorgues Bazin, Odile Picon "Low Cost Invertied Line in Silicon/Glass Technology for Filter in the Ka-Band" IEEE Microwave Theory and Techniques, Vol.54, No.7, pp.3084-3089, July 2006.

[43] L. Martoglio, E. Richalot, G. Lissorgues, and O. Picon "A wideband 3D-transition between coplanar and inverted microstrip on silicon to characterize a line in MEMS technology", in Microwave and Optical Technology Letters, Vol.46 (4): Pp.378 – 381, Aug 2005.

[44] George E. Ponchak, Alexandros Margomenos, and Linda P. B. Kalehi "Low Loss, Finite Width Ground Plane, Thin Film Microstrip Lines on Si Wafers" IEEE Topic meeting on Silicon Monolithic Integrated circuits in RF Systems, pp.43-47, Garmisch, Germany, April 2000.

[45] T. Quémerais, L. Moquillon, J.-M. Fournier, P. Benech, N. Corrao "TFMS Microstrip line modeling and characterization up to 110 GHz on 45 nm node silicon technology: application for CAD" IEEE Topic meeting on Silicon Monolithic Integrated circuits in RF Systems, pp.4-7, New Orleans, LA, Jan 2010.

[46] Jin Li, Xiaochuan Zhang and Jun Xu "Modeling and simulation of Silicon based Planar transimishn lines for Micromachined Filter Application" IEEE Integrated Nonlinear Microwave and Millimetre-Wave Circuits (INMMIC) workshope, pp.1-3, Dublin, 3-4 Sept. 2012.

[47] Manish Prasad, Arun Singh Gaur, Vivek Kr. Sharma and Nagendra P. Pathak “Dispersion and Attenuation Characteristics of Suspended Microstrip Line on Multilayer Lossy Silicon Substrate at 60 GHz” IEEE International conference on IRMMW-THz, pp.1-2, Pasadena, CA, Sept 2008.

[48] George E. Ponchak, Senior Member, IEEE, and Alan N. Downey “Characterization of Thin Film Microstrip Lines on Polyimide” IEEE, VOL. 21, NO. 2, MAY 1998.

[49] Om Prakash Parida and Navakant Bhat “Characterization of optical properties of SU-8 and fabrication of Optical Componenets” International Conference on Optics and Photonics CSIO, Chandigarh, India, 30 Oct.-1 Nov. 2009.

[50] L. Lalehparvar, D. Budimir, “Electromagnetic modeling of 3D multilayer CPW transmission lines on GaAs/Si substrates for MMICs”, IEEE Proc. Of MTT-S, Microwave and Optoelectronics Conference, Vol.1, pp. 253-255, August 2001.

[51] G. Six, M. Vanmackelberg, H. Happy and G. Dambrine, S. Boret, D. Gloria “Transmission Lines on Low Resistivity Silicon Substrate for MMICs Applications” IEEE EuMA, pp.1-4, London, Sept 2001.

[52] R. R. Lahiji, H. Sharifi, S. Mohammadi, and L.P. B. Katehi “Low-Loss Coplanar Waveguide Transmission Lines and Vertical Interconnects on Multi-Layer Parylene-N” IEEE SMIC, pp.1-4, San Diego, CA, Jan 2009.

[53] Roimolo Mlarcelli, Simione Catotii, Luciano Frciigtielli “Low Loss Coplanar Lines on low resistivity Silicon by SU8 thick negative Photoresist“ IEEE Microelectronics & Microsystems, Vol.1, Rome, Italy November2005.

[54] Goubau, G. “Surface waves and their application to transmission line” J. Appl. Phys, 21, pp. 1119 -1128, 1950.

[55] Goubau, G. “Single-conductor surface-wave transmission lines”, Proc. IRE, 39, pp. 619–624, 1951.

[56] Alonso, K., Hagmann, M.J. “Simulations of tapered Goubau line for coupling of microwave signals generated by resonant laser-assisted field emission”, J. Vac. Sci. Technol. B, 18, pp. 1009–1013, 2000.

[57] Xu, Y., Bosisio, R.G. “Application of Goubau lines for millimeter and sub-millimeter wave gas sensors”, IEE Proc. Microw. Antennas Propag, 2005, 152, pp. 400–405.

[58] Treizebre, A., Bocquet, B., Xu, Y., Bosisio, R.G. “New THz excitation of planar Goubau line” Microw. Opt. Technol. Lett., 2008, 50, (11), pp. 2998–3001.

[59] G. Sherman, C. Hennessy “Complex TM Modes in a Generalized Goubau Line with Arbitrary Conductivities” IEEE Trans. Ant. And Prop, 1983, Vol.31, No 4, pp. 553-562.

[60] Y. Xu, R.G. Bosisio “Study of Goubau lines for submillimetre wave and terahertz frequency applications” IEE Proceedings, Microwaves, Antennas and Propagation, IEE Proceedings, 2004, Vol.151, No. 5, pp. 460- 464.

[61] Y. Xu, R.G. Bosisio “A comprehensive study on the planar type of goubau line for millimetre and submillimetre wave integrated circuits” IET Microwaves, Antennas and Propagation, 2007, Vol. 1, No. 3, pp 681-687.

[62] Treizebre, B. Bocquet, Y. Xu, R. Bosisio “New THz excitation of planar Goubau line” Microwave and Optical Tech. Lett, Vol. 50, No°11, pp 2998-3001, 2008.

[63] Y.Xu, C. Nerguizian and R .G Bosisio “Wideband planar Goubau line integrated circut components at millimeter wave” IET Microw 2011, Vol.5, No.8, pp.882-885.

[64] J.Emond, M.Greskowiak, G.Lissorgues, S.protat, F.Deshours, E. Richalot and O.Picon “A Low loss Planar Goubau Line and a Coplanar PLG Transition on high Resistivity Silicon Substrate in the 57-64 GHz band” Microwave and optical technology letters, Vol. 54,No. 1 January 2012.

[65] Mederer, F. et al, “3-Gb/s Data transmission With GaAs VCSELs over PCB Integrated Polymer Waveguides,” IEEE Photonics Technology Letters, Vol. 12, No. 9, pp. 1032-1034, 2001.

[66] Mohammed, E. et al, “Optical interconnection system integration for ultra-short-reach applications,” Intel Technology Journal, Vol. 87, No. 2, pp. 115-128, 2004.

[67] Mohammed, E. et al, “Optical I/O technology for digital VLSI,” Proc of the SPIE, San Jose, CA, Vol. 5358, pp. 60-70, June, 2004.

[68] Jaemin Shin, et. al., “Comparision of Electrical and Optical Interconnect”, Proc 53th Electronic Components and Technology Conf, New Orleans, LA, pp.1067-1072, May, 2003.

[69] G. Kirk, D. V. Plant, M. H. Ayliffe, M. Chateauneuf, and F. Lacroix, “Design rules for highly parallel free-space optical interconnect,” IEEE J. Select. Topics Quantum Electron. vol. 9, pp. 531–547, Mar./Apr. 2003.

[70] Debaes, M. Vervaeke, V. Baukens, H. Ottevaere, P. Vynck, P. Tuteleers, B. Volckaerts, W. Meeus, M. Brunfaut, J. Van Campenhout, A. Hermanne, and H. Thienpont, “Low-cost microoptical modules for MCM level optical interconnections,” IEEE J. Select. Topics Quantum Electron., vol. 9, pp. 518–530, Mar./Apr. 2003.

[71] M. P. Christensen, P. Milojkovic, C. Kuznia, and M.W. Haney, “Design of a 160 Gbps free-space optical interconnection fabric for fully connected multi-chip applications,” in Proc. Annu. Meeting LEOS, 2002, pp. 61–62.

[72] Keishi Ohashi. et al “On-Chip Optical Interconnect” IEEE Vol. 97, No. 7, July 2009.

[73] Keren Bergman “Silicon Photonic On-Chip Optical Interconnection Networks” 20th IEEE Annual meeting on Laser and Electro-optics, pp.470-471, Lake Buena Vista, FL, Oct 2007.

[74] M. Haurylau, G. Chen, H. Chen, J. Zhang, N. A. Nelson, D. H. Albonesi, E. G. Friedman, and P. M. Fauchet, B “On-chip optical interconnect roadmap: Challenges and critical directions”, IEEE, J. Sel. Topics Quantum Electron., vol. 12, pp. 1699–1705, Jun. 2006.

[75] J. D. Meindl "Beyond Moore's Law: the interconnect era" Computing in Science & Engineering 5 (1): 20–24. doi:10.1109/MCISE.2003.1166548, 2003.

[76] T. Barwicz, H. Byun, F. Gan, C. W. Holzwarth, M. A. Popovic, P. T. Rakich, M. R. Watts, E. P. Ippen, F. X. Kärtner, H. I. Smith, J. S. Orcutt, R. J. Ram, V. Stojanovic, O. O. Olubuyide, J. L. Hoyt, S. Spector, M. Geis, M. Grein, T. Lyszczarz and J. U. Yoon "Silicon photonics for compact, energy-efficient interconnects". Journal of Optical Networking 6 (1): 63–73, 2006.

[77] J. S. Orcutt, A. Khilo, M. A. Popovic, C. W. Holzwarth, B. Moss, H. Li, M. S. Dahlem, T. D. Bonifield, F. X. Kaertner, E. P. Ippen, J. L. Hoyt, R. J. Ram, and V. Stojanovic "Demonstration of an Electronic Photonic Integrated Circuit in a Commercial Scaled Bulk CMOS Process". Conference on Lasers and Electro-Optics/Quantum Electronics and Laser Science Conference and Photonic Applications Systems Technologies, 2008.

[78] Michal Lipson "Guiding, Modulating, and Emitting Light on Silicon Challenges and Opportunities". Journal of Lightwave Technology 23 (12): 4222–4238, 2005.

[79] Lucie Robitaille, Claire L. Callender, and Julian P. Noad “Design and Fabrication of Low-Loss Polymer Waveguide Components for On-Chip Optical Interconnection” IEEE Photonics Technology Letters, Vol. 8, No. 12, December 1996.

[80] T. C. Kowalczyk, T. Kosc, K. D. Singer, P. A. Chill, C. H. Seager, M. B. Meinhardt, A. J. Beuhler, and D. A. Wargowski, “Loss mechanisms in polyimide waveguides,’’ J. Appl. Phys., vol. 76, pp. 2505-2508, 1994.

[81] IBM research “Silicon integrated Nonophotonics” http://researcher.watson.ibm.com/researcher/view_group.php?id=2757

[82] IBM “IBM integrates optics and electronics on a single chip” http://www.gizmag.com/ibm-silicon-nanophotonics/25446/?utm_source=Gizmag+Subscribers&utm_campaign=59593484e3-UA-2235360-4&utm_medium=email

[83] Intel “Intel® Silicon Photonics Technology” http://www.intel.com/content/www/us/en/research/intel-labs-silicon-photonics-research.html

[84] Fitzgerald, E.A, Kimerling, L.C., “Silicon-Based Technology for Integrated Opto electronics”, MRS, pp.39-47, Bulletin 1998.

[85] Wada, K., “Electronics and Photonics convergence on Silicon CMOS Platforms” Proc. SPIE. 5357, 16, 2004.

[86] Soref, R., “Silicon photonics technology: past, present and future “Optoelectronic Integration on Silicon” Proc SPIE 5730, 2008.

[87] G. Dang, W.S. Hobson, L.M.F. Chirovsky, J. Lopata, M. Tayahi, S.N.G. Chu, F. Ren, and S.J. Pearton, “High-speed modulation of 850-nm intracavity contacted shallow implant-apertured Vertical-Cavity Surface-Emitting lasers”, IEEE Photonics Technology Letters, Volume 13, pp.924–926, 2001.

[88] T. Tanigawa, T. Onishi, T. Nagaix, and T. Ueda, “High-speed 850 nm AlGaAs/GaAs vertical cavity surface emitting lasers with low parasitic capacitance fabricated using BCB planarization technique”, Lasers and Electro-Optics Conference, Volume 2, pp.1381–1383, 2005.

[89] N. Al-Omari, and K.L. Lear, “Polyimide-planarized Vertical-Cavity Surface Emitting Lasers with 17.0 GHz bandwidth”, IEEE Photonics Technology Letters, Volume 16, pp.969–971, 2004.

[90] N. Al-Omari, and K.L. Lear, ‘VCSELs with a self-aligned contact and copper-plated heatsink’, IEEE Photonics Technology Letters, Volume 17, pp.1767–1769, 2005.

[91] Al-Omari and K.L. Lear, “Low current density, inverted polarity, high speed, top emitting 850 nm VCSELs”, IET Optoelectronics, Volume 1, pp.221-225, 2007.

[92] Chen Chen, Zhaobing Tian, K.D. Choquette, and D.V. Plant, “25-Gb/s direct modulation of implant confined holey Vertical-Cavity Surface-Emitting Lasers”, IEEE Photonics Technology Letters, Volume 22, Issue 7, pp.465–467, 2010.

[93] Chen Ji, Jingyi Wang, D. Soderstrom, and L. Giovane, “20-Gb/s 850-nm oxide VCSEL operating at 25°c - 70°c”, IEEE Photonics Technology Letters, Volume 22, Issue 10, pp.670 –672, 2010.

[94] M. S. Alias, S. Shaari, P. O. Leisher, K. D. Choquette, “Highly confined and continuous single-mode operation of self-align photonic crystal oxide VCSEL”, Applied Physics B: Lasers and Optics, Volume 100, Number 3, pp.453-459, 2010.

[95] S.A. Blokhin, J.A. Lott, A. Mutig, G. Fiol, N.N. Ledentsov, M.V. Maximov, A.M. Nadtochiy, V.A. Shchukin, and D. Bimberg, “Oxide-confined 850 nm VCSELs operating at bit rates up to 40 Gbit/s”, Electronics Letters, Volume 45, Issue 10, pp.501–503, 2009.

[96] T. S. Kim, A. J. Danner, D. M. Grasso, E. W. Young, and K. D. Choquette, “Single fundamental mode photonic crystal vertical cavity surface emitting laser with 9 GHz bandwidth”, Electronics Letters, Volume 40, pp.1340–1341, 2004.

[97] P. Westbergh, J.S. Gustavsson, B. K. andgel, A. Haglund, A. Larsson, A. Mutig, A. Nadtochiy, D. Bimberg, and A. Joel, “40 Gbit/s error-free operation of oxide-confined 850 nm VCSEL”, Electronics Letters, Volume 46, pp.1014–1016, 2010.

[98] P. Westbergh, J.S. Gustavsson, A. Haglund, M. Skold, A. Joel, and A. Larsson, “High-speed, low-current-density 850 nm VCSELs”, IEEE Journal of Selected Topics in Quantum Electronics, Volume 15, Issue 3, pp.694–703, 2009.

[99] P. Westbergh, J.S. Gustavsson, A. Haglund, A. Larsson, F. Hopfer, G. Fiol, D. Bimberg, and A. Joel, “32 Gbit/s multimode fiber transmission using high-speed, low current density 850 nm VCSEL”, Electronics Letters, Volume 45, Issue 7, pp.366–368, 2009.

[100] P. Westbergh, J.S. Gustavsson, A. Haglund, H. Sunnerud, and A. Larsson, “Large aperture 850 nm VCSELs operating at bit rates up to 25 Gbit/s”, Electronics Letters, Volume 44, Issue 15, pp.907 –908, 2008.

[101] J. A. Lott, N. N. Ledentsov, V. A. Shchukin, A. Mutig, S. A. Blokhin, A. M. Nadtochiy, G. Fiol, and D. Bimberg, “850 nm VCSELs for up to 40 Gbit/s short reach data links”, Conference on Lasers and Electro-Optics (CLEO) and Quantum Electronics and Laser Science Conference (QELS), pp 1–2, 2010.

[102] K.L. Lear, A. Mar, K.D. Choquette, S.P. Kilcoyne, R.P. Jr. Schneider, and K.M Geib, “High-frequency modulation of oxide-confined vertical cavity surface emitting lasers”, Electronics Letters, 32, pp.457–457, 1996.

[103] G. Shtengel, H. Temkin, P. Brusenbach, T. Uchida, M. Kim, C. Parsons, W. E. Quinn, and S. E. Swirhun, “High-speed vertical-cavity surface emitting lasers”, IEEE Photonics Technology Letters, Volume 5, pp.1359–1362, 1993.

[104] K. Dutta, K. Kosaka, K. Kurihara, Y. Sugimasa and K. Kasahara, “High-speed VCSEL of modulation bandwidth over 7.0 GHz and its application to 100 m PCF datalink”, IEEE Journal Lightwave Technology, Volume 16, pp.870–875, 1998.

[105] N. Al-Omari, G. P. Carey, S. Hallstein, J. P. Watson, G. Dang and K. L. Lear, “Low thermal resistance, high speed, top emitting 980 nm VCSELs”, IEEE Photonics. Technology Letters, Volume 18, pp.1225–1227, 2006.

[106] N. Suzuki, H. Hatakeyama, K. Yashiki, K. Fukatsu, K. Tokutome, T. Akagawa, T. Anan, and M. Tsuji, “High-speed InGaAs VCSELs”, Lasers and Electro-Optics 19th Annual Meeting, 2006.

[107] H. Hatakeyama, T. Akagawa, K. Fukatsu, N. Suzuki, K. Tokutome, K. Yashiki, T. Anan and M. Tsuji, “25 Gbit/s 100 °C operation of highly reliable InGaAs/GaAsP-VCSELs”, Electronics Letters, Volume 45, Issue 1, pp.45–46, 2009.

[108] T. Anan, N. Suzuki, K. Yashiki, K. Fukatsu, H. Hatakeyama, T. Akagawa, K. Tokutome, and M. Tsuji, “High-speed 1.1- µm range InGaAs VCSELs” presented at the OFC, San Diego, CA, 2008.

[109] Bude, J., Sano, N, and Yoshii,A, “Hot carrier luminescence in silicon,” Phys. Rev. B 45 (11), pp5848–5856, 1992.

[110] Akil, N. , Houstma, V.E., LeMinth, P., Holleman, J., Zieren, V., DeMooij, D., Woerlee, P.H., van den Berg, A., and Wallinga, H., “Modelling of light-emission spectra measured on silicon nanometer-scale diode antifuses”, J. Apl. Phys. 88 (4), 1916-1922, 2000.

[111] Kramer J., Seitz. P., Steigmeier, E. F., Auderset H., and Delley B., “Light-emitting devices in Industrial CMOS technology” Sensors and Actuators (A37-38), 527-533 (1993).

[112] Snyman, L.W. , Aharoni, H , du Plessis, M., Marais, J.F.K , van Niekerk, D. and Biber, A., "Planar light emitting electro-optical interfaces in standard silicon complementary metal oxide semiconductor integrated circuitry" Optical Engineering (SPIE-USA) (41), Issue 12, 3230 – 3240 (2002).

[113] Snyman , L. W. , du Plessis, M., and Bellotti, E., “Photonic transitions (1.4 eV- 2.8 eV) in Silicon p+np+ injection-avalanche CMOS LEDs as function of depletion layer profiling and defect engineering”, IEEE Journal of Quantum Electronics 46 (6), 906-919 (2010).

[114] Xu, K., and Li, G.P, “A three terminal silicon PMOSFET light emitting device (LED) for optical intensity modulation” IEEE Photonic J (4) 6, 2159 – 2168 (2013).

[115] Massimo Ghioni. et al “A VLSI-Cimpatible High Speed Silicon Photodetector for optical Data Link Applications” IEEE Transaction on Electron Devices, Vol.43,No.7, July 1996.

[116] Dyan Ali et al “High Speed SiGe pin W-Structure Photodetectors at Telecommunication Wavelengths Grown Directly on Si” Conference on Quantum Electronics and Laser Science, IET, pp. 1-2, 2008 San Jose, CA.

[117] Sebastian M. Csutak et al “CMOS Compatible High Speed Planar Silicon Photodiodes Fabricaled on SOI Substrates” IEEE Journal of Quantum Electronics, Vol, 38, No.2, February 2002.

[118] Johann Osmond et al “High speed Ge Photodetector Integrated on SOI operating at very low bias voltage” 5th IEEE international conference on Group IV Photonics, Sept 2008, pp.164-166, Cardiff.

[119] Buwen Cheng et al “Silicon based long wavelength photodetectors” IEEE communication and photonic conference, pp.1-9, Shanghai, Nov 2011.

[120] S.S.Agashe et al “Integrated High Linearity and High Bandwidth Compact Tapered Photodetector” IEEE Photonics Technology Letters, Vol.18, No.24, December 15, 2006.

[121] L. Vivien, L. Virot, D. Marris-Morini, J-M. Hartmann, P. Crozat1, E. Cassan, C. Baudot, F. Boeuf, J-M. Fédéli “40Gbit/s Germanium Waveguide Photodiode” OFC/NFOEC Technical Digest, 2013 OSA.

[122] Giovanni Ghione “Semiconductor Devices for High-Speed Optoelectronics” Politecnico di Torino, Torino, Italy, published 2009 (book).

[123] Jeong Woo Park et al “Traveling wave type photomixer with a high responsibility and a high 3dB bandwidth” IEEE, 37th International conference on Infrared, Millimeter, and Terahertz Waves, Sept 2012, pp.1-2, Wollongong, NSW.

[124] Andreas Beling et al “High speed Miniatured Photodiode and parallel Fed Traveling wave Photodetectors based on InP” IEEE Journal of Selected Topics in Quantum Electronics, Vol.13, No.1, Januwary/February 2007.

[125] Andrean Beling et al “Parallel Fed Traveling wave photodetector for >100GHz Application” Journal of Lightwave Technology, Vol.26, No.1. January1, 2008.

[126] Asher Mardjar et al “ A Novel Analytical Model as a Design Tool for Uni Traveling Carrier Traveling Wave Photo Detector Approaching 1 THz” IEEE Transation on Microwave Theory and Techniques, Vol. 57,No.1, January2009.

[127] Kirk Steven Giboney “Travelling-Wave Photodetectors” A dissertation submitted in partial satisfaction of the requirements for the degree of Doctor of Philosophy in Electrical and Computer Engineering. University of California, Santa Barbara.

[128] Kato K. “Ultrawide-bandhigh-frequency photodetectors”, IEEE Trans. on Microwave Theory Tech., 1999, Vo1.47,no.7, Part 2, pp.1265-1281.

[129] R. S. Tucker, A. J. Taylor, C. A. Burms, G. Eisenstein, and J. M. Wiesenfeld, “Coaxially mounted 67 GHz bandwidth InGaAs PIN photodiode,” Electron Lett., vol. 22, pp. 917-918, Aug. 1986.

[130] Sergei Malyshev and Alexander Chizh “STATE OF THE ART HIGH-SPEED PHOTODETECTORS FOR MICROWAVE PHOTONICS APPLICATION” 15th International Conference on Microwaves, Radar and Wireless Communications, Vol.3, pp765-775, 2004.

[131] Y. S. Wang, S. J. Chang, Member, IEEE, C. L. Tsai, M. C. Wu, Y. Z. Chiou, Y. H. Huang, and W. Lin “High-Speed InGaAs P-I-N Photodetector With Planar Buried Heterostructure” IEEE Transactions on Electron Devices, Vol. 56, No. 6, June 2009.

[132] C. S. Whelm, P. F. Marsh, R. E. Leoni 111, J. Hunt, M. Grigas,W. E. Hoke, KC Hwang and T. E. Kazior “Metamorphic PIN Photodiodes for the 40 Gb/s Fiber Market” IEEE 23rd Annual Technical Digest, pp. 251-254, Baltimore, MD, SUA Oct 2001.

[133] D. WAKE, L. C. BLANK, R. H. WALLING, AND I. D. HENNING” Top- Illuminated InGaAs/InP p-i-n Photodiodes with a 3-dB Bandwidth in Excess of 26 GHz” IEEE Electron Device Letters, Vol. 9, No. 5, May 1988.

[134] Tuo Shi, Bing Xiong, Changzheng Sun, and Yi Lu “Novel Back-to-Back Uni-Traveling-Carrier Photodiodes with High Responsivity, High Saturation Current and Wide Bandwidth” IEEE OFC/NFOEC, pp. 1-3, Anaheim, CA, March 2013.

[135] Sanjeev Murthy, Seong-Jin Kim, Thomas Jung, Zhi-Zhi Wang, Wei Hsin and Ming C. Wu “Backward-Wave Cancellation in Distributed Traveling-Wave Photodetectors”, Journal of Light wave technology, Vol. 21, No. 12, December 2003.

[136] Asher Madjar, Navya Koka, Jeffry Bloch, Paul K. L. Yu, Andreas Stoehr and Dieter Stefan Jaeger “A Novel Analytical Model as a Design Tool for Uni-Traveling-Carrier Traveling Wave Photo Detectors Approaching 1 THz”, IEEE Transactions on Microwave Theory And Techniques, Vol. 57, No. 1, January 2009.

[137] Xiaofeng Duan et al “Long Wavelength Multiple Resonant Cavities RCE Photodetectors on GaAs substrates” IEEE Transactions on Electron Devices, Vol.58, No.11, November 2011.

[138] Ding Li et al “Analysis and optimization of a dual absorption RCE photodetector for high speed applications” IEEE communication and photonic conference, pp.1-7, Shanghai, Nov 2011.

[139] Lingzi Zhang, Yuhua Zuo, Quan Cao, Chunlai Xue, Buwen Chen, Jinzhong Yu, and Qiming Wang “High performance of silicon-based resonant-cavity-enhanced (RCE) photodetectors using sol-gel bonding” 7th IEEE international conference on Group IV photonics, pp.272-274, Beijing, Sept 2010.

[140] D. Kuhl, F. Hieronyme “High speed Metal Semiconductor Metal Photodetector on InP:Fe” IEEE Photonocs Technology Letters, Vol.2, No.8, August 1990.

[141] R. A. Norwood, G. Khanarian “Very High-Speed Metal-Semicondaactor-Metal InGaAs Photodetectors with InP barrier enhancement layer grown by Low Pressure Metalorganic Chemical Vapour Deposition” Ellectronic letters, Vol. 26 No. 25, December 1990.

[142] W. A. Wohlmuth, P. Fay, K. Vaccaro, E. A. Martin, and I. Adesida “High speed InGaAs Metal-Semiconductorotodetectors Metal Photodetector with thin absorption Layers” IEEE Photonics Technology Letters, Vol. 9, No 5, May 1997.

[143] Zefram Marks, Bart Van Zeghbroeck “High-Speed Nanoscale Metal-Semiconductor-Metal Photodetectors with Terahertz Bandwidth” 10th IEEE international conference on NUSOD, pg.11-12, Atlanta, GA, Sept 2010.

[144] Ven dier O. Jokerst N. Leavitt R.. “Thin-film inverted MSM photodetectors”, IEEE Photon. Technol. Lett.. 1996, Vo1.8, no.2, pp.266-268.

[145] Sang-Woo Seo, Sang-Yeon Cho, Sa Huang, Jeng Jung Shin, Nan Marie Jokerst, April S. Brown, and Martin A. Brooke “High-Speed Large-Area Inverted InGaAs Thin-Film Metal–Semiconductor–Metal Photodetectors” IEEE Journal of Selected Topics in Quantum Electronics, Vol. 10, No. 4, July/August 2004.

[146] L. Ding, T.-Y. Liow, A. E.-J. Lim, N. Duan, M.-B. Yu, and G.-Q. Lo “Ge Waveguide Photodetectors with Responsivity Roll-off beyond 1620 nm Using Localized Stressor” IEEE OFC/NFOEC, p p.1-3, Los Angeles, March 2012.

[147] Dyan Ali1, Phillip Thompson, Julius Goldhar, Joseph DiPasquale Christopher J.K. Richardson “High-Speed SiGe p-i-n W-Structure Photodetectors at Telecommunication Wavelengths Grown Directly on Si” IET Confrence on Quantum Electronics and Laser Science, pp.1-2, San Jose, CA, May 2008.

[148] Shiyang Zhu1, G. Q. Lo1, D. L. Kwong1, H. S. Chu2, P. Bai2, and E. P. Li2 “Silicon Waveguide Infrared Photodiodes Based on Embedded Nickel Silicide Particles” IEEE OFC/NFOEC, pp.1-3, Los Angeles, March 2012.

[149] K. Kato, A. Kozen, Y. Muramoto, Y. Itaya, T. Nagatsuma, and M. Yaita1 “10-GHz, 50%-Efficiency Mushroom-Mesa Waveguide p-i-n Photodiode for a 1.55-pm Wavelength” IEEE Photonics Technology Lelters, Vol. 6, No. 6, June 1994.

[150] Guido Torrese, Isabelle Huynen, Marc Serres, Dominic Gallagher,Matthew Banham, and André Vander Vorst, “An Analytical Small-Signal Bias-Dependent Nonuniform Model for p-i-n Traveling-Wave Photodetectors”, IEEE Transactions on Microwave Theory and Techniques, Vol. 50, NN. 11, November 2002.

[151] Kuhl D., Hieronymi F., Bottcher E.H., Wolf T., Bimberg D., Kuhl I., Klingenstein M. “Influence of space charges on the impulse response of IuGaAs metal-semiconductor-metal photodetectors”, J. Lightwave Technol., 1992, Vol.10, 110.6, 1’992, pp.753-759.

[152] Guido Torrese, Cailin Wei, Matthew J. Frank, Isabelle Huynen, André Vander Vorst, and Patrice Mégret “Embedded Grating n+-i-n+ Traveling-Wave Photodetectors” IEEE Transactions On Microwave Theory and Techniques, Vol. 57, No. 5, May 2009.

[153] Jin-Wei Shi, Gan-Giap Gan, Yi-Jen Chiu, Yen-Hung Chen’ Chi-Kuang Sun, Ying-Jay Yang, and John E. Bowers “Ultra-high bandwidth (570GHz) Metal-Semiconductor-Metal Traveling-Wave-Photodetectors” IEEE Microwave conference, Vol.1, pp.358-361, Taipei, 2001.

[154] Jin-Wei Shi, Yen-Hung Chen, Tzu-Ming Lid, Ming-Che Chan’, Kian-Giap Can’, Yi-Jen Chid, John. E. Bowers’, and Chi-Kuang Sun “Metal-Semiconductors-Metal Traveling Wave Photodetetcors” IEEE Photonics Technology Letters, Vol.13, No.6, pp.623-625, June 2001.

[155] Ebrahim Mortazy and Ke Wu CREER and Poly-Grames Research Center Ecole Polytechnique de Montreal Montreal, Canada” Integration of Traveling-Wave Photodetector and Coplanar-Fed Log-Periodic Antenna for Terahertz Source Generation”, IEEE MWP, pp.107-110, Montreal, QC, Oct 2010.

[156] P. R. A. Binetti, X. J. M. Leijtens, T. de Vries, Y. S. Oei, L. Di Cioccio, J.-M. Fedeli, C. Lagahe, J. Van Campenhout, D. Van Thourhout, P. J. van Veldhoven, R. Notzel, and M. K. Smit “InP/InGaAs Photodetector on SOI Photonic Circuitry” Photonic journal, IEEE, Vol 2, No 3, pp.299-305, June 2010.

[157] John Wiley and Sons “Physics of semiconductor Devices” 2nd edition, New York, 1981

[158] L. E. M, J. DeBarros, A. Paolella, P. R. Herczfeld, and A. A. A. De Salles, “Noise Performance of HBT as photodetector in analog fiber optic communication link,” Proceedings, 1997 SBMO/IEEE MTT-S International, 1997, vol. 1, pp.338–343.

[159] Marc D. Rosales, Jean-Luc Polleux,Julien Schiellein, Carlos Viana Catherine Algani “Full area Emiter SiGe Phototransistor for Opto-Microwave circuit applications” 9th IEEE international conference on Group IV Photonic, pp. 294-296, San Diego, CA, Aug 2012.

[160] S. A. Bashar and A. A. Rezazadeh, “Optically transparent ITO emitter contacts in the fabrication of InP/InGaAs HPT's,” Microwave Theory and Techniques, IEEE Transactions on, vol. 43, no. 9, pp.2299–2303, 1995.

[161] Marc D. Rosales, Jean-Luc Polleux, Catherine Algani “Design and Implementation of SiGe HPTs using an 80GHz SiGe Bipolar Process Technology” 8th IEEE international conference on Group IV Photonic, pp. 243-245, London, Sept 2011.

[162] C. Gonzalez, M. Muller, J. L. Benchimol, M. Riet, P. Jaffre, and P. Legaud, “A 28 GHz HPT/HBT monolithically integrated photoreceiver for hybrid fibre radio distribution systems,” High Performance Electron Devices for Microwave and Optoelectronic Applications, 2000 8th IEEE International Symposiumon, Jan. 2000.

[163] P. Freeman, Xiangkun Zhang, I. Vurgaftman, J. Singh, and P. Bhattacharya, “Optical control of 14 GHz MMIC oscillators based on InAlAs/InGaAs HBTs with monolithically integrated optical waveguides,” IEEE Trans. Electron Devices, vol.43, no.3, pp.373–379, Mar. 1996.

[164] Peter Ashburn “SiGe Heterojunction Bipolar Transistors” University of Southampton, Southampton, UK 2003.

[165] T. Mitsuyu, S. Fujita, and A. Sasaki, “InGaAsP/InP wavelength selective Heterojunction phototransistors,” IEEE Trans. Electron Devices, vol. 31, no. 6, pp. 812–817, 1984.

[166] K. H. Ha, Y. H. Lee, J. I. Song, C. Caneau, C. Y. Park, and K. H. Park, “High-speed Ga In P/GaAs heterojunction phototransistors,” Electron. Lett., vol. 31, no. 16, pp. 1386–1387, Aug. 1995.

[167] Z.Pei, L. Lai, H. Hwang, Y.Tseng, C. Liang, and M. J. Tsai, “Si1− x Ge x/Si Multiquantum well phototransistor for near infrared operation,” Physica E: Low dimensional Systems and Nanostructures, vol. 16, no. 3, pp. 554–557, 2003.

[168] T. Yin, A. Apsel, A.M. Pappu, C. Reungsinpinya, and A. Khimani, “Optical interconnects in commercial BiCMOS,” Proceedings of SPIE, vol. 5357, p.1, 2004.

[169] D. Fritzsche, E. Kuphal, and R. Aulbach, “Fast response InP/InGaAsP Heterojunction phototransistors,” Electron. Let. vol.17, no.5, pp.178–180, 1981.

[170] S. Chandrasekhar, M. K. Hoppe, Dentai, “Demonstration of enhanced Performance of an InP/InGaAs heterojunction phototransistor with a base terminal,” Electron Device Letters, IEEE, vol. 12, no.10, pp.550–552, 1991.

[171] S.W.Tan, H.R.Chen, W.T.Chen, M.K.Hsu, A.H.Lin, and W.S.Lour, “Characterization and Modeling of Three Terminal Heterojunction Phototransistors Using an InGaP Layer for Passivation”, vol.52, no. 2, pp.204–210, Feb. 2005.

[172] Julien Schiellein “Etude de Phototransistors bipolaires à hétérojonction InP/InGaAs pour applications d’oscillateurs photoinjectés très faible bruit de phase” Thèse de doctorat de l’université Paris-Est.

[173] Yuqing Zhu, Qinqing Yang, Qiming Wang “Resonant Cavity SiGe/Si MQW Heterojunction Phototransistor Grown on the SIMOX Substrate for 1.3pm Operation” IEEE Electronic Components and Technology Conference, pp.1199-1204, San Jose, CA, May 1997.

[174] N.B.Lukyanchikova, N.P.Garbar and M.V.Petrichuk “Noise Properties of AlGaAs/GaAs HPTs with transparent ITO emitter contact “IEEE EDMO, pp50-55, Leeds, Nov 1996.

[175] H. R. Chen, S. W. Tan, W. T. Chen, T. S. Lin, and W. S. Lour, “The Effect on Base Bias for InGaP/GaAs Heterojunction Phototransistors,” IEEE Optoelectronic and Microelectronic Materials and Devices, pp241-244, Brisbane, Qld, Dec 2004.

[176] S.W.Tan, W.T. Chen, M.Y. Chu and W.S.Lour “A new model for the phototransistor” 4th IEEE IWJT, pp.232-235, March 2004.

[177] H.R. Chen, S.W. Tan, W.T. Chen, T.S. Lin and W.S.Lour “The effect on base biase for InGaP/GaAs Heterojunction Phototransistor” IEEE CSIC’08, pg.1-4, Monterey, CA, Oct 2008.

[178] Hassan A. Khan and Ali A. Rezazadeh “Analytical Modeling of the Spectral Response of Heterojunction Phototransistors” IEEE Electronic Device Letters, Vol.30, No.11, pp.1158-1160, Oct 2009.

[179] Shih-Wei Tan, Hon-Rung Chen,Wei-Tien Chen, Meng-Kai Hsu, An-Hung Lin, andWen-Shiung Lour, Member, “Characterization and Modeling of Three-Terminal Heterojunction Phototransistors Using an InGaP Layer for Passivation” IEEE Electronic Device Letters, Vol.52, No.2, pp.204-210, Feb 2005.

[180] Min Su Park and Jae Hyung Jang “Enhancement of Optical Gain in Floating-Base InGaP–GaAs Heterojunction Phototransistors” IEEE Photonics Technology Letters, Vol. 22, No. 16, August 15, 2010.

[181] Zingway Pei, C. S. Liang, L. S. Lai, Y. T. Tseng, Y. M. Hsu, P. S. Chen, S. C. Lu, M.-J. Tsai, and C. W. Liu, “A High-Performance SiGe–Si Multiple-Quantum-Well Heterojunction Phototransistor” IEEE Electron Device letters, Vol.24, No.10, pp.643-645, Oct 2003.

[182] J.L. Polleux, F. Moutier, A.L. Billabert, C. Rumelhard1, E. Sönmez, H. Schumacher “A Strained SiGe layer Heterojunction Bipolar Phototransistor for Short-Range Opto-Microwave Applications” IEEE international Topical Meeting on MWP, pp.113-116, Sept 2003.

[183] J.L. Polleux, F. Moutier, A.L. Billabert, C. Rumelhard, E. Sönmez, H. Schumacher “An SiGe/Si Heterojunction Phototransistor for Opto-Microwave Applications: Modeling and first Experimental Results” 11th GAAS symposium-Munich 2003.

[184] Yin T, Pappua.M, Apel A.B “Low cost high effieciency, and high speed SiGe phototransistors in commercial BICMOS” IEEE photonics Technology latters, vol.18,no 1,pp55-57, 2006.

[185] Z.Pie, J.W. Shi, Y-M.Hsu, F.Yuan. C.S.Lu “Bandwidth Enhancement in an Integrated SiGe Phototransistor by Removal of Excess carriers” IEEE Electronics Device Letter Vol.25 No. 5 May 2004.

[186] M.Egels and B. Delacressonniere, “Design of an optically frequency or Phase controlled oscillator for hybrid fiber radio LAN at 5.2 GHz,” Microwave and Optical Technology Letters, Vo.45 (2), pp.104-107, Wiley, 2005.

[187] Marchlewski and H. Zimmermann, “BiCMOS phototransistors,” Proceedings of SPIE, vol. 7003, pp.70030J, 2008.

[188] S. Chandrasekhar, L. M. Lunardi, A. H. Gnauck, R. A. Hamm, and G. J. Qua, “High-speed monolithic p-i-n/HBT and HPT/HBT photoreceiver implemented with simple phototransistor structure,” IEEE Photon. Technol. Lett., vol. 5, no. 11, pp. 1316–1318, Nov. 1993.

[189] D. W. E. Allsopp, M. S. Stern, and E. Strobel “Analysis of Edge-Coupled Heterojunction Phototransistors” IEEE Transactions on Microwave Theory and techniques, Vol. 47, No. 7, July 1999.

[190] Julein Schiellein, Marc Rosales, Jean Luc Polleux, Catherine Algani, Thomas Merlet “ Analysis of Opto Micro wave path in to an InP/InGaAs UTC-HPT” Proceeding of the 41st European Microwave conference, 2011.

[191] J. Thuret, C. Gonzalez, J.L. Benchimol, M. Riet and P. Berdaguer “High-speed InP/InGaAs Heterojunction Phototransistor for Millimetre- Wave Fibre Radio Communications” 11th IEEE International Conference on Indium Phosphide and Related Materials, pp.389-392, Davos, Switzerland, May 1999.

[192] P. Kostov, W. Gaberl, M. Hofbauer, H. Zimmermann “PNP PIN bipolar phototransistors for high-speed applications built in a 180 nm CMOS process” An International journal of Solid-State Electronics Vol.74, pp.49–57, 2012.

[193] Z. Pei, C.S. Liang, L.S. Lai, Y.T. Tseng, Y.M. Hsu, P.S. Chen, S.C. Lu, C.M. Liu, M.-J. Tsai and C.W. Liu “High efficient 850 nm and 1,310 nm multiple quantum well SiGe/Si heterojunction phototransistors with 1.25 plus GHz bandwidth (850nm)” Electron Devices Meeting, 2002. IEDM '02. Digest. International, pp.297–300, 2002.

[194] A.B. Apsel, T. Yin, and A.M.Pappu, “Photonic VLSI for on chip computing architectures,” Society of Photo Optical Instrumentation Engineers (SPIE) Conference Series, vol.5597, pp. 1–12, 2004.

[195] K. Kato, “Ultrawide-band/high-frequency photodetectors,” IEEE Trans. Microwave Theory Tech., vol. 47, no. 7, pp. 1265–1281, 1999.

[196] W.K. Ng, C.H. Tan, P.A. Houston and A. Krysa “High current InP/InGaAs evanescently coupled waveguide phototransistor” IEE Proc.-Optoelectron., paper 152 (2), 140-144 (2005).

[197] Wake, D., Newson, D.J., Harlow, M.J., and Henning, I.D: ‘Optically biased, edge coupled InP/InGaAs heterojunction phototransistor’, Electron. Lett, paper 29, 2217–2219 (1993).

[198] D. C. Scott, D. P. Prakash, H. Erlig, M. A. Bhattacharya, and H. R. Fetterman, “High power, high frequency traveling wave heterojunction phototransistors with integrated polyimide waveguide,” in Proc. IEEE Int. Microw. Symp., 1998, pp. 1237–1240.

[199] G. Rangel-Sharp, R. E. Miles, and S. Iezekiel, “Physical Modeling of Traveling-Wave Heterojunction Phototransistors” Journal of lightwave technology, Vol. 26, No. 13, July 1, 2008.

[200] Jean-Luc Polleux, Laurent Paszkiewicz, Anne-Laure Billabert, Jacques Salset, and Christian Rumelhard, “Optimization of InP–InGaAs HPT Gain: Design of an Opto-Microwave Monolithic Amplifier” IEEE Transactions on Microwave Theory and Techniques, Vol. 52, No. 3, March 2004.

[201] F. Moutier, J.L. Polleux and C. Rumelhard “Numerical Results Of The Uni-Traveling-Carrier Effect Of A SiGe/Si Heterojunction Bipolar Phototransistor” ESYCOM.

[202] J. Kim, S. Kanakaraju, W.B. Johnson and C.-H. Lee” InP/InGaAs uni-travelling carrier heterojunction phototransistors” Electronics Letters, Vol. 45, No. 12, June 2009.

[203] Tae Woung Jeong, Koichi Iiyama and Sabro Takamiya “Two Terminal InP/InGaAs Heterojunction Phototransistor with Lateral Photodiode as Sensing Section” IEEE International Conference on Indium Phosphide and Related Materials, pp.250-253, May 2005.

[204] J.-W. Shi, Y.-S. Wu, F.-C. Hong, and W.-Y. Chiu “Separate Absorption-Charge Multiplication Heterojunction Phototransistors with the Bandwidth-Enhancement Effect and Ultrahigh Gain-Bandwidth Product under Near Avalanche Operation” IEEE Electronic device Letters, Vol. 29, No. 7, JULY 2008.

[205] F. Moutier, J.L. Polleux, C. Rumelhard, H. Schumacher” Frequency Response Enhancement of a Single Strained Layer SiGe Phototransistor Based on Physical Simulations” IEEE EGAAS, pp.113-116, Oct 2005.

[206] Payam Rabiei, William H.Steier, Cheng Zhang, and Larry R.Dalton “Polymer Micro-Ring Filters and Modulators” Journal of Lightwave Technology, Vol. 20, No. 11, November 2002.

[207] Hidehisa Tazawa and William H. Steier “Linearity and Ultra-Linearization ofRing Resonator Based Modulators for Sub-Octave Bandpass Analog Optical Links” IEEE OFC, dio. 10.1109/OFC.2006.215804, March 2006.

[208] Guoliang Li, Xuezhe Zheng, Jin Yao, Hiren Thacker, Ivan Shubin, Ying Luo, Kannan Raj, John E. Cunningham, and Ashok V. Krishnamoorthy “High-efficiency 25Gb/s CMOS ring modulator with integrated thermal tuning” IEEE 18th international conference on Group IV Photonics, pp8-10, London, Sept.2011.

[209] Yangjin Ma, Zhe Xuan, Yang Liu, Ran Ding, Yunchu Li, Andy Eu-Jin Lim, Guo-Qiang Lo, Tom Baehr-Jones, and Michael Hochberg “Silicon Microring Based Modulator and Filter for High Speed Transmitters at 1310 nm” IEEE optical interconnects conference , pp.23-24, San Diego, CA, May 2014.

[210] T. Latchu, M. Pochet , N. G. Usechak , C. D e Ro se , A . Len t in e , D. C. Trotter , and W. Zo rtman “Power-Penalty Comparison of Push-Pull and Traveling-Wave Electrode Silicon Mach–Zehnder Modulators” IEEE optical interconnects conference , pp.25-26, San Diego, CA, May 2014.

[211] Michael R. Watts, William A. Zortman, Douglas C. Trotter, Ralph W. Young,and Anthony L. Lentine “Low-Voltage, Compact, Depletion-Mode,Silicon Mach–Zehnder Modulator” IEEE Journal Of Selected Topics In Quantum Electronics, Vol. 16, No. 1, January/February 2010.

[212] A. Brimont, D.J. Thomson, P. Sanchis, J. Herrera, F.Y. Gardes, J.M. Fedeli, G.T. Reed, J. Martí “Enhancing the Performance of Carrier Depletion Based Silicon Electro-optical Modulators via Slow Light Propagation” IEEE 18th international conference on Group IV Photonics, pp1-3, London, Sept.2011.

[213] Mohamed Saïd Rouifed, Delphine Marris-Morini, Xavier Le Roux, Papichaya Chaisakul,1 Jacopo Frigerio, Daniel Chrastina, Giovanni Isella, and Laurent Vivien “Advances towards the demonstration of a Ge/SiGe modulator integrated on SOI” IEEE 11th international conference on Group IV Photonics, pp75-76, Paris, Sept.2014.

[214] S.Gupta al et “50GHz Ge Waveguide Electro-Absorption Modulator Integrated in a 220nm SOI Photonic Platform” IEEE OFC, pp1-3, Los Angeles, CA, March 2015.

[215] Papichaya Chaisakul, Delphine Marris-Morini, Giovanni Isella, Daniel Chrastina, Mohamed-Saïd Rouifed,Xavier Le Roux, Samson Edmond, Eric Cassan, Jean-René Coudevylle, and Laurent Vivien “10-Gb/s Ge/SiGe Multiple Quantum-Well Waveguide Photodetector” IEEE Photonics Technology Letters, Vol.23, No.20, pp.1430-1135, July 2011.

[216] Nagatsuma T. “Photonic measurement technologies for high-speed electronics”, Meas. Sci. Technol., 2002, Vo1.13, pp.1655-1663.

[217] Mourad Chtioui, Francois Lelarge, Alain Enard, Frederic Pommereau, Daniele Carpentier, Alexandre Marceaux, Frédéric van Dijk, and Mohand Achouche” High Responsivity and High Power UTC and MUTC GaInAs-InP Photodiodes” IEEE Photonics Technology Letters, Vol.24, No.4, pp.318-320, Dec 2011.

[218] Ho-Jin Song, Member, IEEE, Katsuhiro Ajito, Member, IEEE, Yoshifumi Muramoto, Atsushi Wakatsuki, Tadao Nagatsuma, Senior Member, IEEE, and Naoya Kukutsu, Member, IEEE” Uni-Travelling-Carrier Photodiode Module Generating 300 GHz Power Greater Than 1 mW” IEEE Microwave And Wireless Components Letters, Vol. 22, No. 7, July 2012.

[219] Guido Torrese, , Isabelle Huynen, Marc Serres, Dominic Gallagher, Matthew Banham, and André Vander Vorst, “An Analytical Small-Signal Bias-Dependent Nonuniform Model for p-i-n Traveling-Wave Photodetectors” IEEE Transactions On Microwave Theory and Techniques, Vol. 50, No. 11, November 2002.

[220] Abdolber Mallah Livani, Hassan Kaatuzian “Improving Bandwidth of Parallel-Fed Travelling Wave Photo Detectors” 20th IEEE Iranian Conference on Electrical Engineering, pp.267-269, Tehran, May 2012.

[221] R. People, “Physics and Applications of GexSi1-x/Si Strained-Layer Heterostructures”, in IEEE Journal of Quantum Electronics, Vol. QE-22, N°9, September 1986.

[222] Z. Matutinovic-Krstelj, V. Venkataraman, E. J. Prinz, J. C. Sturm and C. W. Magee, “Base Resistance and Effective Bandgap Reduction in n-p-n Si/Si1-xGex/Si HBT's with Heavy Base Doping”, in IEEE Transactions on Electron Devices, Vol. 43, N°3, pp. 457-466, March 1996.

[223] J.L. Polleux and C. Rumelhard “Optical Absorption Coefficient Determination and Physical Modelling Of Strained Sige/Si Photodetectors” 8th IEEE international symposium, pp167-172, Glasgow, 2000.

[224] R. Braunstein, A. R. Moore and Frank Herman, “Intinsic Optical Absorption in Germanium Silicon Alloys”, in Physical Review,, Vol. 109, N°3, pp. 695-710, February 1958.

[225] Jean-Luc Polleux “Contribution à l'étude et à la modélisation de phototransistors bipolaires à hétérojonction SiGe/Si pour les applications opto-microondes” These Docteur du Conservatoire National des Arts et Métiers, oct 2001.

[226] Y. Ding, W. J. Fan, D. W. Xu, C. Z. Tong, Y. Liu, L. J. Zhao, "Low threshold current density, low resistance oxide-confined VCSEL fabricated by a dielectric-free approach", Applied Physics B: Lasers and Optics, Volume 98, Issue 4, pp.773-778, 2010.

[227] Y.-C. Chang, C.S. Wang, and L.A. Coldren, “High-efficiency, high-speed VCSELs with 35 Gbit/s error-free operation”, Electronics Letters, Volume 43, Issue 19, pp.1022 –1023, 2007.

[228] Snyman, L. W. , Aharoni , H., and du Plessis, M ., “Two order increase in the quantum efficiency of silicon CMOS n+pn avalanche-based light emitting devices as a function of current density” IEEE Photonic Technology Letters . 17 (10), 2041 – 2043 (2005).

[229] Jin Li, Xiaochuan Zhang, and Jun Xu “Modeling and Simulation of Silicon-Based Planar Transmission Lines for Micromachined Filter Applications” IEEE Work shop on INMMIC, pp1-3, Dublin, Sept 2012.

[230] D. Lin, B. Schleicher, A. Trasser, and H. U.-W. I. 2. I. I. C. O. Schumacher, “A highly compact SiGe HBT differential LNA for 3.1–10.6 GHz ultra-wideband applications,” IEEE International Conference ICUWB, vol. 1, pp1-4, Nanjing, Sept 2010.

[231] H. Kamitsuna, “Direct Optical Injection Locking of InP/InGaAs HPT Oscillator Circuits for Millimeter Wave Photonics and Optoelectronic Clock Recovery,” pp.1–4, Jun. 2003.

[232] G. Liu, A. Trasser, and H. M. T. A. T. I. T. O. Schumacher, “A 64–84-GHz PLL with Low Phase Noise in an 80-GHz SiGe HBT Technology,” IEEE Microwave Theory and Techniques, IEEE Transactions on, vol. 60, no. 12, pp.3739-3748, Sept 2012.

[233] Ç. Ulusoy, G. Liu, A. Trasser, and H. Schumacher, “Hardware efficient receiver for low-cost ultra-high rate 60 GHz wireless communications,” Int. J. Microw. Wireless Technol., vol. 3, no. 2, pp. 121–129, Mar. 2011.

[234] G. Liu, A. Trasser, and H. Schumacher, “33–43 GHz and 66–86 GHz VCO With High Output Power in an 80 GHz SiGe HBT Technology”, in IEEE Microwave And Wireless Components Letters, Vol. 20, No. 10, pp.557-559, Oct. 2010.

[235] Marc ROSALES “Study of SiGe HPT for Radio over Fiber Applications” Ph.D THESIS, UNIVESITÉ PARIS-EST, June 16, 2014.

[236] Agilent, “Measuring noninsertable devices, agilent 8510-13 product note,” Agilent Technologies, Tech. Rep., 1999.

[237] Carlos VIANA, Jean-Luc POLLEUX, Catherine Algani “VCSEL characterizations at the circuit- and system-levels for low-cost RoF applications” IEEE MMS 13th Mediterranean, pp1-4, Sept 2013.

[238] Snyman, L.W. , Aharoni, H ., du Plessis, M. , and Gouws, R.B.J., “Increased efficiency of silicon light emitting diodes in a standard 1.2 micron complementary metal oxide semiconductor technology” SPIEE Optical Engineering Vol.37, Isu.7, 2133 – 2141, February 1998.

[239] Snyman, L.W. , du Plessis, M., Seevinck, E. , and Aharoni, H. , “An efficient, low voltage, high frequency silicon CMOS light emitting device and electro-optical interface”, IEEE Electron Device Letters, Vol.20, No.12, pp.614-617, Dec 1999.

[240] Snyman, L.W. , Auderset, H., Derendinger, M. , Patterson, B.D. , and Von Lanthen, A "Efficient electroluminescence from 2- and 3-junction silicon structures" Applied physics, Annual Report 1996/Annex.111B of the Paul Scherrer Institute, Switzerland, Vol.28, 1996.

[241] K.A. Ogudo, D. Schmieder, D. Foty and L. W. Snyman. "Optical propagation and refraction in silicon complementary metal-oxidesemiconductor structures at 750nm: toward on chip optical links and microphotonic systems" Journal of Micro and Nano Lithography, MEMS, MOEMS, 12 (1) 013015, 1 -13 (2013).

[242] Lukas W. Snyman , Jean-Luc Polleux , Kingsley A. Ogudo , Carlos Viana and Sebastian Wahl "High Intensity 100 nW 5 GHz Silicon Avalanche LED utilizing carrier energy and momentum engineering" Proc. of SPIE Vol. 8990 89900L-1, SPIE 2014; doi: 10.1117/12.2038195.

[243] P.J. Venter, M. du Plessis, A.W. Bogalecki and C.J. van Rensburg, " Nanoscale SOI silicon light source design for improved efficiency, Proc. SPIE 8628, Optoelectronic Integrated Circuits XV, 86280A (2013); doi:10.1117/12.2004235.

[244] L. Y. Lin, M. C. Wu, T. Itoh, T. A. Vang, R. E. Muller, D. L. Sivco, and A. Y. Cho "High-Power High-Speed Photodetectors—Design, Analysis, and Experimental Demonstration" IEEE Microwave Theory and techniques, Vol. 45, No.8. pp. 1320-1331, Aug 1997.

[245] M. D. Rosales, F. Duport, J. Schiellein, J.-L. Polleux, C. Algani, C. Rumelhard, "Opto-microwave experimental mapping of SiGe/Si phototransistors at 850nm", International Journal of Microwave and Wireless Technologies, Volume 1, Issue 06, pp 469-473, 2009.

[246] A. W. Fang, H. Park, O. Cohen, R. Jones, M. J. Paniccia, and J. E. Bowers, "Electrically pumped hybrid AlGaInAs-Silicon evanescent laser," Opt. Express, vol. 14, no. 20, pp.9203–9210, 2006.

[247] W.Shockley, M. Sparks, and G. Teal, "p---n Junction Transistors," Physical Review, vol.83, no.1, pp.151–162, Jul. 1951.

[248] J. N. Shive, "The Properties of Germanium Phototransistors," J. Opt. Soc. Am., vol. 43, no.4, p.239, 1953.

[249] Helme.J.P, Houstron.P.A,"Analytical modeling of speed response of heterojunction bipolar phototransistors". Lightwave Technology. 25(5) (20007), 1247-1255.

[250] Feng Yuan, Jin-Wei Shi, Zingway pei, and Chee Wee Liu "MEXTRAM Modeling of Si-SiGe HPTs" IEEE Transactions On Electronics Devices, Vol.51, No.6, June 2004.

[251] J.-W. Shi, Z. Pei, F. Yuan, Y.-M. Hsu, C.-W. Liu, S. C. Lu, and M.-J. Tsai, "Performance enhancement of high-speed SiGe based heterojunction phototransistor with substrate terminal," Appl. Phys. Lett., VOL.85, NO.14, Oct. 2004.

[252] Mohammed El-Gibari, Yann Mahe, Dominique Averty, Cyril Lupi and Hongwu Li "Ultra-Wideband Coplanar Microstrip Transitions for Connectorizing Microwave Photonic Components Based on Thin Polymer and Driven by Microstrip Electrode" Proceedings of the 6th German Microwave Conference, 14–16 March 2011, Darmstadt, Germany.

[253] Hasan Sharifi, Rosa R. Lahiji, Han-Chung Lin, Peide D. Ye, Linda P. B. Katehi, and Saeed Mohammadi, "Characterization of Parylene-N as Flexible Substrate and Passivation Layer for Microwave and Millimeter-Wave Integrated Circuits" IEEE Transactions On Advanced Packaging, Vol. 32, No. 1, February 2009.

[254] Felix D. Mbairi & Hjalmar Hesselbom "High Frequency Design and Characterization of SU-8 based Conductor Backed Coplanar Waveguide Transmission Lines" IEEE International Symposium on Advanced Packaging Materials, pp.243 – 248, 16-18 March 2005.

[255] http://memscyclopedia.org/su8.html

[256] Roberto Machorro, Luis E. Regalado, and Jesus M. Siqueiros "Optical properties of parylene and its use as substrate in beam splitters" APPLIED OPTICS , Vol. 30, No. 19, 1 July 1991.

[257] Julien ÉMOND "Contribution a L'etude des Structures Passives Verre-Silicium dans le Domaine Millimetrique" Ph.D Thesis, Univesité Paris-Est, Jully 02, 2010.

[258] Gorin, A., Jaouad, A., Grondin, E., Aimez, V. and Charette, P "Fabrication of silicon nitride waveguides for visible-light using PECVD: a study of the effect of plasma frequency on optical properties" Optics Express, Vol.16, No.18, pp.13509-13516, September 2008.

[259] Jacopo Nanni, Giovanni Tartarini, Simone Rusticelli, Federico Perini, Carlos Viana, Jean-Luc Polleux, Catherine Algani, "Modal noise in 850nm VCSEL-based Radio over Fiber systems for manifold applications", FOTONICA 2015, Turin, Italy, May 6-8 2015.

[260] Frederic Moutier “Modélisation et ´Evaluation des Performances des Phototransistors Bipolaires à Hétérojonction SiGe/Si pour les Applications Optique-microondes Courtes Distances” Ph.D THESIS, Université de Marne-La-Vallée, December 2006.

[261] José Capmany al et“Innovative Concepts in Microwave Photonics” Waves - 2012 - year 4/ISSN 1889-8297.

[262] M. Reisch “High-Frequency Bipolar Transistors” Springer edition, ISBN 978-3-642-63205-1, 2003.

[263] Sasa Radovanovic “High-speed Photodiodes in Standard CMOS Technologies” Published 2004, Netherlands, ISBN 90-365-2115-7.